ELECTRONIC STRUCTURE AND QUANTUM CONTROL OF NICKEL VACANCY DEFECTS IN DIAMOND

By

Ian Morris

A DISSERTATION

Submitted to
Michigan State University
in partial fulfillment of the requirements
for the degree of

Doctor of Philosophy - Physics and Electrical Engineering

2026

ABSTRACT

ELECTRONIC STRUCTURE AND QUANTUM CONTROL OF NICKEL VACANCY DEFECTS IN DIAMOND

By

Ian Morris

This thesis seeks to make the negatively charged nickel vacancy center, NiV^-, in diamond, accessible as a resource for quantum information processing. To achieve this, we experimentally determine its electronic structure using cryogenic magneto-optical spectroscopy, finding it in agreement with our own group-theoretical model as well as density functional theory. We assess its spectral properties, measuring a Debye-Waller factor of ~0.6 and an excited state lifetime of 10.5 ns. Further, we perform photoluminescence excitation spectroscopy and are able to achieve lifetime-limited linewidths critical for indistinguishable single photon emission. We probe its charge states over a broad range of optical excitation frequencies as well as under electrical bias in ion implanted p-i-p junction devices. With these results, we develop a charge state model for the NiV^-, finding that the NiV^{2-} serves as the dark shelving state. Moreover, we set a lower bound for its ground state coherence time by performing coherent population trapping, being limited by the ^{13}C nuclear spin bath. Lastly, we demonstrate all-optical control via two-photon Raman transitions, observing Rabi oscillations, Ramsey fringes, and successfully decouple from the ^{13}C spin bath using Hahn-Echo and Carr-Purcell-Meiboom-Gill sequences. Overall, this work provides a variety of fundamental information about the NiV^- and provides a pathway for remote entanglement of NiV's and use in quantum networking applications.

Dedicated to my loving parents.

TABLE OF CONTENTS

LIST OF TABLES

LIST OF FIGURES

Chapter 1

Introduction

1.1 Motivation

The development of quantum mechanics in the early 1900s transformed society's understanding of light and matter by creating a mathematical framework to describe the behavior of particles and light at the atomic scale. Since then, this understanding has led to the creation of a wide range of technologies which now underpin modern life. These include devices such as the transistor, the laser, magnetic resonance imaging machines, and atomic clocks. These advances are often grouped under the general umbrella of the "first quantum revolution", an era in which quantum mechanical concepts were used to explain and engineer the behavior of novel quantum systems. Presently, the current era is often described as the "second quantum revolution"[1]. Where in the first era devices relied on the average behavior of a large number of quantum states, this new era is defined by attempts to prepare, control, and measure individual quantum states directly. Indeed, more than just explaining behavior, individual quantum states can be created and controlled coherently, featuring uniquely quantum properties. While this new level of control is still developing, wide ranging near-term applications in computation, communication, and sensing are being actively explored [1]. To understand this, it is useful to first describe the simplest quantum state: a two-level system. This is typically referred to as a quantum bit, or qubit and, unlike classical bits, which can take on one of two values, 0 or 1, a qubit can be in either of those states or in a superposition of both,

$$|\Psi\rangle = \alpha\,|0\rangle + \beta\,|1\rangle\,, \qquad |\alpha|^2 + |\beta|^2 = 1. \tag{1.1}$$

The coefficients α and β are complex amplitudes whose squared magnitudes give the probabilities of obtaining the corresponding measurement outcomes. In particular, if $|\alpha|^2 = 1/2$, there is a 50% chance of finding the qubit in the $|0\rangle$ state. The normalization condition guarantees that the qubit is in either of the two states. The probabilistic nature of qubits is what can give them an advantage over classical bits in certain applications. With two classical bits, the system can occupy only one

of four possible configurations at a given time, namely $|00\rangle, |01\rangle, |10\rangle$, or $|11\rangle$. In contrast, two qubits can exist in a coherent superposition of all four configurations simultaneously,

$$|\Psi\rangle = \alpha\,|00\rangle + \beta\,|01\rangle + \gamma\,|10\rangle + \delta\,|11\rangle\,, \qquad |\alpha|^2 + |\beta|^2 + |\gamma|^2 + |\delta|^2 = 1. \tag{1.2}$$

With three qubits, this grows to eight total states and for the general case of n-qubits, the system can be in 2^n states. Because all of these states are possible configurations, operations performed on the system apply to all the configurations, enabling a parallelism inaccessible to classical bits. Importantly, however, a measurement on the system only reveals the qubit in one of the many possible states. To determine the individual coefficients for each state, one would need to measure many times to obtain an accurate probability distribution. The trick then is to use the fact that these quantum states are wave functions, consistent with Schrodinger's equation, and can therefore exhibit interference, similar to classical waves. One can then manipulate the state in such a way as to constructively interfere the states of interest and destructively interfere the ones not of interest, so that only the relevant states and their coefficients remain. This allows less measurements while still revealing the information of interest and can then be used for calculating interesting quantities. Moreover, multiple qubits can also exist in entangled states, in which operations on one qubit affect the other [2]. A typical example is one of the Bell states (of which there are four total)

$$|\Phi^+\rangle = \frac{1}{\sqrt{2}}\left(|00\rangle + |11\rangle\right), \tag{1.3}$$

in which if one qubit is found in the state $|0\rangle$, the other qubit is also found in the state $|0\rangle$; likewise for $|1\rangle$. As will be described below, entanglement along with superposition provide the uniquely quantum ingredients which underlie the second quantum revolution.

There are three main areas being explored, which seek to exploit these quantum phenomena: quantum computing, quantum sensing, and quantum networking [1]. Quantum computers first started receiving serious interest in 1994 when Peter Shor discovered that quantum computers could factor large integers in polynomial time; something for which the best known classical algorithm can achieve in sub-exponential time [3]. Quantum computers take advantage of the large number of accessible states, parallelism and interference described above to explore large computational spaces more efficiently compared to classical algorithms for certain classes of problems [4]. In particular, quantum computers are suited to logistics and other optimization problems, but can also simulate quantum systems, which is an intractable task for classical computing even with relatively small system sizes. This has applications across a variety of sectors, but in particular, in the study of novel molecules, drugs or new materials [5]. Quantum sensors on the other hand seek to use carefully prepared quantum states to measure a variety of physical quantities such as

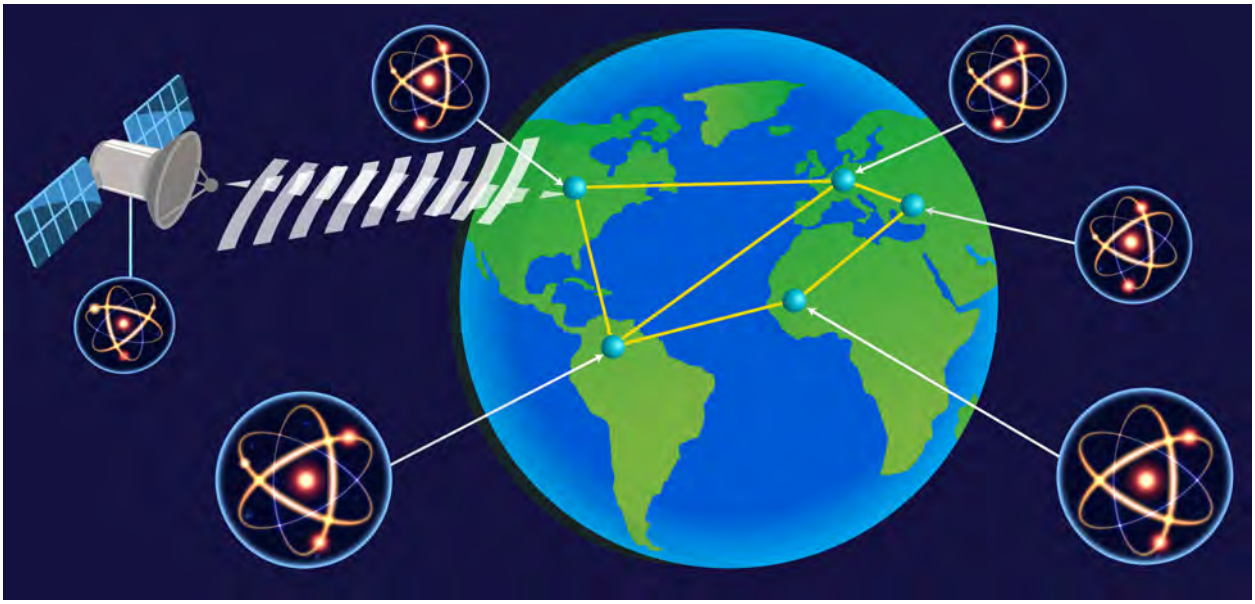

Figure 1.1 Cartoon representation of quantum network nodes scattered over earth, communicating via both land and satellite based links using atom-like qubits. Reprinted from https://www.nist.gov/pml/productsservices/quantum-networks-nist.

electric and magnetic fields, gravity, forces, or time with extremely high sensitivity [6, 7]. Because individual quantum states respond strongly to small environmental fluctuations, they can be orders of magnitude more sensitive compared to classical sensors [6]. Additionally, quantum sensors can potentially self-calibrate because they involve measuring quantized levels which do not drift with time, in contrast to classical sensors which can erode over time [8]. This potential for zero drift, however, is still limited by the host of supporting classical equipment such as lasers, detectors etc. which do suffer from irreversible drift or degradation. Furthermore, quantum sensors can achieve higher levels of precision than classical sensors. Indeed, for a classical sensor performing N independent measurements, the precision scales as $1/\sqrt{N}$, commonly referred to as the standard quantum limit (SQL), but it has been shown that entangled states can in principle achieve a precision that scales as $1/N$ [9]. Because of these advantages, quantum sensors have found use in a wide variety of fields from position, timing and navigation to medical imaging and geological mapping [6, 7]. Lastly, quantum networks aim to distribute quantum information between distant locations, allowing remote quantum devices to share entanglement and operate together rather than as isolated systems [10]. This thesis focuses primarily on quantum networks because the novel defect explored here is suitable as a node in such a network. However, it should be noted that there is much overlap between the different areas, and so qubits developed for quantum networks can also usually have functionality within a quantum computer or as a sensor and vice versa.

To understand quantum networks, it helps to first understand classical networking. Classical

networking, in the most general sense involves sending and receiving classical information over long distances. Classical networking, includes, for example, the modern Internet, which grew out of a DARPA project initiated to ensure that critical information could still be shared over long distances even in the event of a catastrophe [11]. Since then, the Internet has ballooned into the global backbone for sending and receiving information. A central challenge for any network is how to support secure communication between users, even in the presence of untrusted, malicious third parties. Classical networks solve this problem by using cryptography, which is a set of encryption and decryption algorithms relying on mathematical functions that are easy to perform but computationally infeasible to reverse, even on the largest supercomputers [12]. For example, RSA encryption schemes rely on the computational difficulty of factoring a large integer generated from the product of two large prime numbers. It is easy to multiply two numbers, it is hard to figure out the factors of that number. For RSA-2048, a secure key is generated using 2048 bit length numbers, or about 617 decimal digits, and no polynomial-time classical algorithm is known for recovering its prime factors. As a result, breaking such keys by known classical methods is considered computationally infeasible in practice [13]. Crucially, however, the security of this protocol is not guaranteed by a proof of inherent classical hardness, but instead on the empirical absence of an efficient classical factoring algorithm. Improvements in factoring algorithms and available computing power have accordingly driven repeated increases in recommended RSA key lengths, from 512-bit keys in early deployments to the 2048-bit keys widely used today [14]. It was in this area of cryptography that interest in quantum networks was first ignited. In 1984, Charles Bennett and Gilles Brassard created the BB84 quantum key distribution protocol, a provably secure encryption technique based on quantum physics [15]. This was the first protocol to demonstrate an advantage gained by using quantum based communication protocols for protecting information. The main idea is that measuring a quantum state disturbs it, and arbitrary copying of a quantum state is forbidden by the no-cloning theorem [16]. As a result, any eavesdropping attempts can, in principle, be detected. This is the basis for quantum key distribution, in which two parties establish a shared secret key with security guaranteed by the properties of quantum mechanics rather than by assumed limits on an adversary's computing power [10] as in the case of RSA. The generated keys can then be used to securely encrypt one's message. Importantly, even if eavesdropping does occur, it only affects the key, and because such eavesdropping can be detected, the subsequent key can be discarded and a new one can be created to replace it. This is all done prior to the message ever being transmitted, so it is never in danger of being revealed. Since then, this idea of provably secure communication using quantum properties has been extended even further. Examples include quantum secure direct communication in which the message is encoded directly within the quantum states themselves and sent securely without the need for a secret key [17]; quantum fingerprinting, in which n-bit messages can be encoded with exponentially fewer qubits compared to classical bits

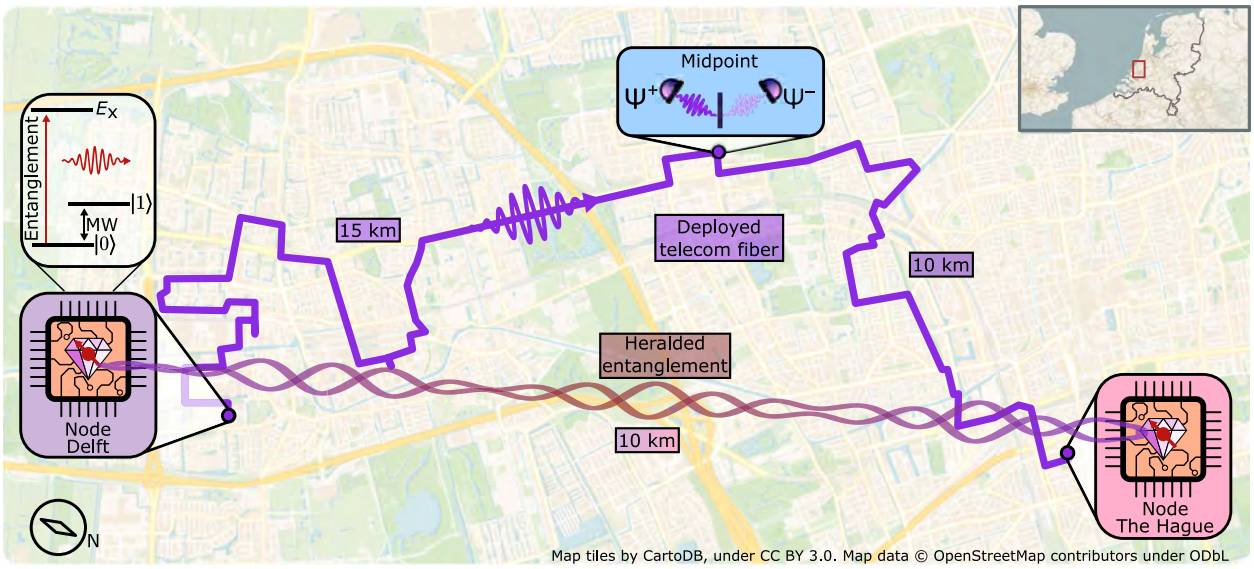

Figure 1.2 Graphic of multi-node quantum network using defects in diamond with nodes, entanglement, Bell state measurement displayed across metropolitan scale distances. Reprinted from [25] under the Creative Commons CC BY license.

[18]; and device independent entanglement based schemes, in which the nodes of the network can be compromised, but provably secure communication is still maintained [10].

The importance of quantum networks, however, extends beyond just secure communication. A quantum network could, for example, connect remote quantum processors, allowing many smaller quantum devices to function together as a larger modular system. This is of particular interest for quantum computers because it would relax the challenging scaling requirements current quantum computers face. Instead of requiring a large monolithic device, which may be infeasible to cool or control properly, one could connect many smaller quantum computers together to achieve a large utility-scale system [19]. Furthermore, quantum networks could enable secure access to quantum computers, so that users can submit a computational job, but the contents and results of the job remain hidden from others [20]. It can also support enhanced clock synchronization [21, 22] which can improve GPS, distributed sensing [7], secure identification [18], and networked protocols that reduce the amount of communication required for certain tasks [23]. Another possibility includes linking distant telescopes with shared quantum states to extend effective measurement baselines [24], which would allow for higher resolution images. Taken together, these possibilities demonstrate the enormous potential for quantum networking as a fundamentally new platform for communication, computation, and metrology.

Having reviewed the various applications of a quantum network, the question remains how such a system can be physically realized. Any practical implementation requires platforms that can both process quantum information locally and transmit it over long distances. The field typically divides

this into two different roles: matter based quantum systems for storing and manipulating qubits locally, and "flying" qubits capable of traversing long distances [26]. A quantum network must be able to do both and the two qubit types must be able to interact efficiently. A node in a quantum network must therefore contain a local matter qubit, which can store quantum information for long enough to perform useful operations, and it must be able to interface with a flying qubit so that quantum states can be transmitted and entanglement can be distributed between distant nodes [26]. Whenever a signal is sent through a fiber, it experiences loss. Classical networks deal with this problem using amplifiers, which boost the attenuated signal. Quantum networks cannot use this because quantum states cannot be copied [16] and entanglement is fragile. This is to a large extent why quantum networks can be ultra-secure compared to classical networks, however, it still poses a challenge for implementation. As such, the concept of a quantum repeater was created which can store and teleport entanglement across long distances. To achieve this; however, the matter qubit must remain coherent for long enough that entanglement can be transferred. Additionally, there is a tradeoff because while having more quantum repeaters can extend the distance that quantum information can be transmitted, it also introduces additional noise with each node. For a more thorough review of quantum repeaters, the reader is referred to [27]. The focus of this thesis is the development of a novel matter-based qubit as a quantum network node. In particular, it explores a novel defect in diamond for quantum networking applications. These systems are attractive because they can host localized spin states that have long coherence times while also possessing optical transitions that enable interaction with light [28]. In addition to their relevance for quantum communication, such defects may also find use in quantum sensing and, more broadly, as components of future quantum information processors. Here, however, the emphasis is on their role as quantum network nodes.

The organization for the rest of this chapter is as follows. First, the general requirements for a quantum node are introduced. Next, the current state of the art in terms of different physical architectures are discussed. Then, solid state spin qubits are examined in more detail, before introducing diamond defects and their unique advantages. Lastly, the diamond defect studied in this thesis is reviewed, namely, the nickel vacancy center, along with its advantages.

1.2 Requirements for a Quantum Network Node

As stated above, a quantum network relies on both flying qubits and matter qubits interacting strongly. In most network architectures, optical photons serve as the flying qubits that carry quantum information between nodes, while matter-based qubits provide local storage and processing. Photons are especially well suited to this role because they propagate quickly, interact only weakly with their environment, and can be transmitted at relatively low-loss in optical fibers [19]. The central challenge

is therefore to identify a matter-based qubit that can interface efficiently with light while preserving its quantum coherence long enough to support network operations. Below, a non-exhaustive but key set of requirements are outlined for which any potential quantum node candidate must be able to meet to be useful in a real quantum network.

1.2.1 Light-Matter Interface

The first, most basic, requirement is that the matter qubit must be able to interface with light. This was already mentioned above, but a quantum network relies on converting stationary quantum information, stored in localized degrees of freedom, into propagating photonic degrees of freedom and back again [26]. This means the node must possess an internal degree of freedom that can couple to an optical field. Depending on the platform, this degree of freedom may correspond to an electron spin, nuclear spin, orbital state, charge state, or another long-lived quantum degree of freedom. In all cases, however, the system must provide an optical interface through which light can be used for state preparation, coherent control, readout, or entanglement generation. This could be achieved a number of ways, including emission and absorption, Raman scattering, or cavity-mediated interactions. The key point, however, is that without such a light-matter interface, there is no mechanism to map quantum information onto a flying photonic qubit or to mediate remote interactions between distant nodes [27].

1.2.2 Telecom Band Wavelength

The next main requirement relates to the wavelength of light which the matter qubit can interact with. In particular, the wavelength of light used to carry quantum information throughout the quantum network should be near 1310nm or 1550nm. Both of these wavelengths correspond to the ultra low loss regimes for standard silica optical fibers used in the telecommunications industry [27, 29]. 1550 nm, also called the telecom-c band has the lowest loss at 0.2 dB/km while 1310 nm has a slightly higher 0.35 dB/km [30] (Figure 1.3, although researchers are actively pursuing even lower loss fiber designs [31]. The primary reason for loss of light in optical fibers is Rayleigh scattering, which arises from microscopic differences in glass density and refractive index. These "defects" can cause scattering of the guided light out of the mode, which then results in attenuation [32]. This scattering depends inversely on the fourth power of the wavelength of light, so the longer the wavelength the better. This is only up to a point, however, as eventually long enough wavelength light will start to be absorbed as vibrations by the atomic bonds in the fiber itself. This starts picking up around 1.6 microns. Furthermore, there are also absorption mechanisms from water molecules and other impurities which have diffused into the fiber. The low loss windows are regions where there is significantly less absorption from such water molecules [33] while also minimizing Rayleigh

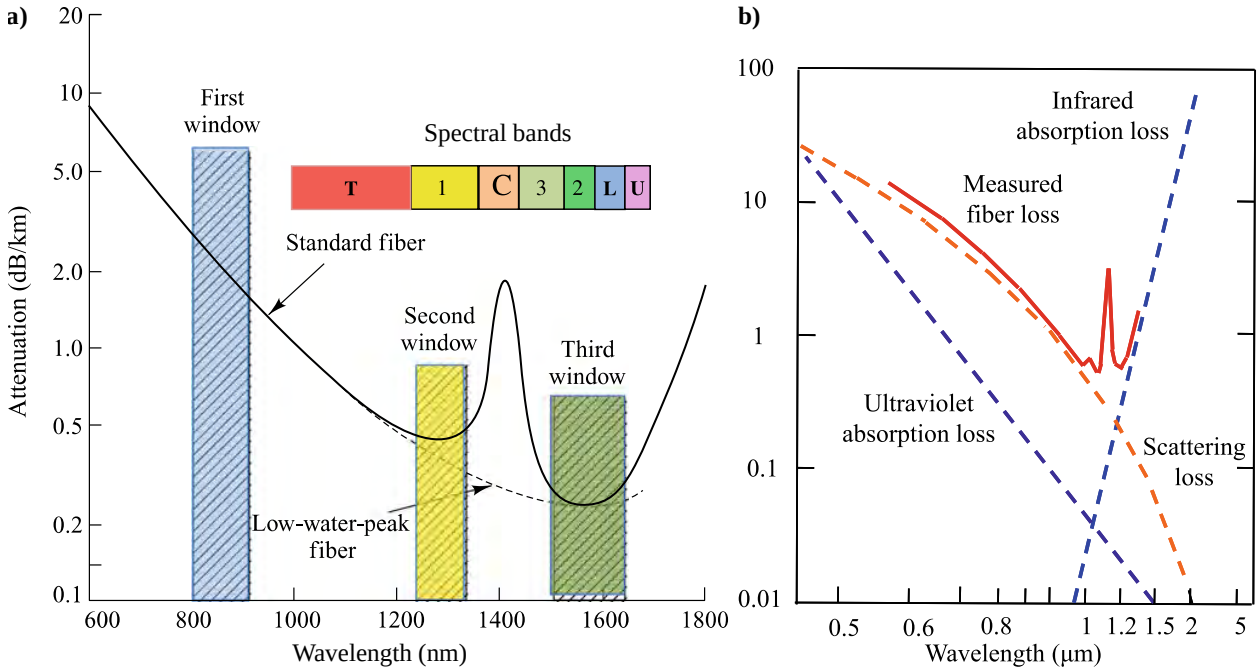

Figure 1.3 **a)** Dependence of fiber attenuation on wavelength; the dashed curve shows attenuation from water absorption. The three main telecom ranges are also highlighted, with 850 nm corresponding to the first telecom window, 1260-1360 nm corresponding to telecom O-band (stands for original band) and 1550 nm telecom C-band (stands for conventional band). **b)** Further fiber attenuation dependence along with loss mechanisms labeled. The images are both reprinted from Chapter 3 of [34], Copyright 2021 The Author(s), under exclusive license to Springer Nature Singapore Pte Ltd..

scattering and vibrational bond absorption. Minimizing unnecessary photon losses will be critical to maintaining long distance entangled nodes.

The matter qubit can interface with telecom band light in two ways: (1) natively possess a telecom transition which can be used for entanglement, or (2) be able to convert telecom band light efficiently to the native operating frequency. The second approach is generally referred to as quantum frequency conversion (QFC). In these schemes, single photons emitted by a quantum node are translated to a new wavelength, often in the telecom band, while preserving the quantum information they carry [35–38]. In practice, this is commonly achieved with a strong pump field in a nonlinear medium such as periodically poled lithium niobate, where the medium's second-order nonlinearity enables either sum-frequency generation or difference-frequency generation. In sum-frequency generation, the photon to be converted and the pump combine to produce a higher-frequency photon, with $\omega_{\text{out}} = \omega_{\text{sig}} + \omega_{\text{p}}$, whereas in difference-frequency generation the output is shifted to lower frequency according to $\omega_{\text{out}} = \omega_{\text{sig}} - \omega_{\text{p}}$. For solid-state emitters, difference-frequency generation is often used to convert visible or near-infrared photons to the telecom band, since it allows the original photon to interact coherently with a strong classical pump and emerge at a longer wavelength more suitable for fiber transmission [36, 39]. QFC is attractive because it relaxes the requirement that

the quantum emitter itself operate at a low-loss fiber wavelength. This is particularly relevant for color centers in diamond, whose zero-phonon lines typically lie in the visible or near-infrared, such as the NV center at 637 nm, the SiV center at 737 nm, and the SnV center at 619 nm. The main drawbacks of QFC are added loss and noise. Loss can arise from imperfect coupling into the nonlinear device, poor internal conversion efficiency of the nonlinear crystal, and propagation loss or absorption. Noise is often generated by the strong pump beam required for conversion. In particular, spontaneous Raman scattering can produce broadband photons near the target wavelength, while other pump-induced processes, including parasitic spontaneous parametric fluorescence and pump leakage through the filters, can also contaminate the single-photon channel [37, 39, 40]. To combat this, a minimal number of conversion steps and the so called 'long pump wavelength regime' are usually desired, in which the pump wavelength is at an even lower frequency than the desired telecom band target frequency. Difference frequency generation can then be used to convert the signal light in a single step to the desired telecom light [41]. This ensures that any Raman noise does not interfere with the telecom converted light. However, depending on the signal wavelength, the phase matching conditions can be challenging to meet [42]. As such, while quantum frequency conversion can enable long distance transport via the telecom band, they can also be quite deleterious, especially when one requires single photons in which even a small background contribution can degrade nonclassical correlations.

1.2.3 Indistinguishable Photons

The photons transmitted throughout the network must also be identical in all relevant degrees of freedom, including frequency, polarization, temporal profile, and spatial mode [30]. If any of these properties differ enough that, even in principle, one could determine which photon came from which source, then the photons are distinguishable.

This indistinguishability is essential because it enables two-photon interference, a key resource in many quantum networking architectures. Its best described by the Hong-Ou-Mandel (HOM) effect, first observed by Hong, Ou, and Mandel [43, 44]. In the HOM effect, two indistinguishable photons enter the two input ports of a 50:50 beamsplitter. Then, denoting the input photon creation operators by $a^\dagger$ and $b^\dagger$, and the output operators by $c^\dagger$ and $d^\dagger$, the beamsplitter transformation may be written as

$$a^\dagger \to \frac{c^\dagger + d^\dagger}{\sqrt{2}}, \qquad b^\dagger \to \frac{c^\dagger - d^\dagger}{\sqrt{2}}. \tag{1.4}$$

Thus, for one photon in each input port of the beamsplitter, the input state is

$$a^\dagger b^\dagger \left|0\right\rangle . \tag{1.5}$$

Applying the beamsplitter transformation gives

$$a^\dagger b^\dagger |0\rangle \rightarrow \frac{1}{2}\left[(c^\dagger + d^\dagger)(c^\dagger - d^\dagger)\right]|0\rangle = \frac{1}{2}\left[(c^\dagger)^2 - (d^\dagger)^2\right]|0\rangle\,, \tag{1.6}$$

where the terms proportional to $c^\dagger d^\dagger$, corresponding to one photon exiting each output port, cancel by destructive interference. Therefore, the two photons "bunch" and leave together through the same output port. This effect only occurs only when the two photons are truly indistinguishable. In a quantum network, this interference is valuable because it removes information about which node emitted which photon. This is often called erasing "which-path" information.

This quantum effect is frequently used to achieve remote entanglement of two matter qubits. In such a scheme, each matter qubit first becomes locally entangled with a photon. In this example, consider spin-photon entanglement. Then if matter qubits A and B each emit a photon whose photonic qubit is entangled with a local spin, the joint states may be written as

$$|\Psi\rangle_A = \frac{1}{\sqrt{2}}\left(|\uparrow_A\rangle|0_A\rangle + |\downarrow_A\rangle|1_A\rangle\right), \qquad |\Psi\rangle_B = \frac{1}{\sqrt{2}}\left(|\uparrow_B\rangle|0_B\rangle + |\downarrow_B\rangle|1_B\rangle\right), \tag{1.7}$$

where $|0\rangle$ and $|1\rangle$ denote two photonic basis states, for example two time bins, frequencies, or polarizations. The two photons are then interfered on a central beamsplitter. Because HOM interference erases which-path information, a suitable coincidence detection event projects the two-photon state onto an entangled Bell state, such as

$$|\Psi^-\rangle_{\text{ph}} = \frac{1}{\sqrt{2}}\left(|0_A 1_B\rangle - |1_A 0_B\rangle\right). \tag{1.8}$$

Thus, depending on the detection event, the two remote spins are projected into the corresponding entangled state

$$|\Psi^-\rangle_{\text{spin}} = \frac{1}{\sqrt{2}}\left(|\uparrow_A\downarrow_B\rangle - |\downarrow_A\uparrow_B\rangle\right), \tag{1.9}$$

In this way, a measurement on the photons entangles two distant matter qubits that have never interacted directly. In practice, achieving high indistinguishability usually requires photons that are close to lifetime-limited, meaning that their spectral linewidth is as narrow as allowed by the time they spend in the excited state [45, 46].

1.2.4 Single Photon Source

Thus far, the requirements are that the photons be indistinguishable and at a certain wavelength. The next requirement is the ability for on-demand generation of individual photons. This is particularly important because two photon interference by definition requires one and only one photon at each

input port. If the source occasionally emits more than one photon, then the detection outcomes can become ambiguous, which reduces the fidelity of the generated entangled state. Likewise, if the source fails to emit when required, then entanglement cannot be generated [26, 30]. Furthermore, single photons are also important for quantum communication more broadly. In particular, multi-photon emission can create security vulnerabilities. In some protocols, one particular vulnerability is the photon-number-splitting attack, in which an eavesdropper takes advantage of pulses containing more than one photon by diverting one photon while allowing the others to continue to the intended receiver. This way, they could avoid detection while also stealing information about the message or key being sent [47]. For these reasons, a quantum network node should ideally emit exactly one photon per excitation attempt, with high probability and at a well-defined time.

1.2.5 Brightness and Quantum Efficiency

Related to the ability to emit single photons, a useful quantum network node must do so efficiently. Here, efficiency has two closely related aspects: how rapidly the node can produce a photon and how likely it is to emit a photon into the desired optical channel. The latter is commonly described by the quantum efficiency [30, 48].

The excited-state lifetime sets the characteristic timescale over which an emitter remains in its excited state before returning to a lower-energy state. In the case of spontaneous emission, it therefore gives the average time before a photon is emitted following excitation. More generally, this timescale helps determine how quickly the optical interface can be reused and thus influences the achievable repetition rate and brightness of the source, although the precise limit can be modified in schemes based on stimulated emission, cavity-enhanced emission, or Raman processes [49]. For photon-mediated entanglement protocols, shorter emission times are generally desirable because they allow entanglement attempts to be repeated more rapidly.

Equally important is the probability that excitation of the node actually produces a photon in the desired mode. In practice, an emitter may have multiple decay pathways, and not all of them lead to emission at the wavelength or into the optical channel relevant for networking. As a result, both the internal quantum efficiency of the emitter and the efficiency with which photons are emitted into a useful mode play a central role in determining the overall source performance [48]. Since remote-entanglement protocols succeed only when photons are generated, transmitted, and detected successfully, a source that emits photons both rapidly and with high probability will generally support higher entanglement generation rates.

The brightness of a source can be further improved by placing the emitter inside an optical cavity. In this case, the spontaneous emission rate into a desired optical mode can be enhanced through the Purcell effect, which arises from modifying the photonic environment of the emitter [49]. Cavity

coupling can therefore increase the fraction of photons emitted into the mode relevant for networking and, in many cases, shorten the effective radiative lifetime associated with that channel. More broadly, cavities can also improve spectral and spatial mode control, which helps direct photons into a well-defined output mode and can assist in producing photons with the properties required for interference-based networking protocols.

1.2.6 Long Coherence Times

In order to perform remote entanglement, the matter qubit must be able to maintain a coherent superposition state long enough for the flying qubit to entangle with other flying qubits [26]. Otherwise, by the time the flying qubits meet, there may be nothing left to entangle. This is where the idea of quantum repeaters comes in, as mentioned above. In theory, one can simply add more quantum repeaters in between but this makes the platform less scalable and more costly and, ideally, a system can be identified which is not limited by coherence times [27]. Consider this example: a beam of light with a wavelength of 1550nm experiences 20dB of loss when traveling through a 100km fiber. That means only 1% of the original light beam will reach the end. On the other hand, 1550nm light travels through fiber at a speed of $v = c/n \approx 2 \cdot 10^5$ km/s, where $n = 1.47$ corresponds to the index of refraction for silica fibers at that wavelength. That means that for a qubit which possesses 1ms long coherence times, light could travel 200 km. This should make it clear that in such a regime, the largest limiting factor is no longer the coherence time of the qubit but instead losses from the fiber.

1.2.7 Device Integrability

Beyond long coherence times and optical properties, ideal matter qubits should be compatible with scalable device integration. This includes the ability to incorporate emitters into photonic structures to enhance photon collection efficiency, as well as into devices that enable efficient control, e.g. electrical control and stabilization of the emitter charge state [29]. For solid state emitters like the one studied in this thesis, it is particularly important to be able to deterministically place emitters within photonic circuits and the prospect of scalable, wafer-level fabrication akin to that achieved in the semiconductor industry [50]. In particular, integration with planar photonic structures and waveguides, on-demand emitter production, and reproducible large-scale fabrication are key requirements for practical quantum photonic technologies [28]. Finally, for spin-based quantum emitters, long electron spin coherence times (T_2^*) and the ability to tune optical transitions using strain or electric fields are highly desirable, as they enable both stable operation and spectral matching between multiple devices [12, 29].

1.3 Current state-of-the-art

Having reviewed the key requirements for a matter qubit, the leading physical architectures are discussed and compared including trapped ions, neutral atoms, photonic qubits, superconducting circuits, semiconductor quantum dots, and spin defects in solids. Comparing these platforms provides a picture of the current field while also motivating the interest in the diamond-based defect studied in this thesis. As there is no clear winner across the various architectures, the strengths and weaknesses of each will be highlighted along with opportunities for hybrid integration, when applicable.

1.3.1 Trapped ions

Trapped ions are among the most mature physical platforms for quantum information processing and have played a central role in the development of quantum networking. In these systems, individual atoms are first ionized, and are then confined in space using electromagnetic fields, typically rapidly oscillating radio-frequency fields in combination with static electric potentials. Because the particles are charged, they can be held in ultra-high-vacuum traps for long periods of time with very little disturbance from the surrounding environment. Quantum information can then be encoded in two long-lived internal states of the ion, which may be electronic spin states, orbital states, or hyperfine states, depending on the ion species and the application. Lasers are used to initialize the ion into a known state, manipulate the qubit, and read out its final state through state-dependent fluorescence, in which the ion scatters light differently depending on which qubit state it occupies [51].

The main advantages of trapped ions for quantum networking stem from their exceptional uniformity, coherence, and control. Because these qubits are defined by atomic energy levels, ions of the same species are fundamentally identical and therefore exhibit identical transition frequencies and level structures. This ensures high spectral stability for photons emitted and consequently, high indistinguishability. Trapped ions also exhibit extremely long coherence times, often extending to seconds or longer. In addition, trapped-ion systems support some of the highest-fidelity quantum gates and state preparation and measurement operations achieved in any platform [19].

In terms of challenges, most are technical rather than fundamental, but still highly challenging. First, many of the optical transitions used lie in the visible or ultraviolet spectral range rather than in the telecom bands near 1.3-1.5 μm. Quantum frequency conversion can be used to shift them to telecom bands, however, because most readily accessible transitions lie within the UV and visible bands, they are also suffer high absorption and strong dispersion in nonlinear crystals needed for frequency conversion [42]. Additionally, direct or single step conversion in the so called long pump wavelength regime is generally not possible [41]. Despite these challenges, much work has been done to overcome these challenges. In particular, an 854nm transition for Ca atoms has been shifted to

telecom O-band [37] and telecom C-band [42] and a visible transition in Ba was successfully shifted to telecom C-band [52]. The second main challenge trapped ions face is photon collection. This is because the emitter is effectively suspended in free space and radiates into a wide solid angle. Only a small fraction of the emitted light is then naturally captured by collection optics. This limits the efficiency of remote entanglement generation, although optical cavities and integrated nanophotonic structures are being developed to enhance light collection and improve coupling into waveguides or fibers. Third, trapped-ion platforms require substantial infrastructure, including ultra-high vacuum, stable trapping potentials, multiple laser systems, and precise control electronics [19]. While these requirements are manageable in laboratory environments, they complicate miniaturization and large-scale deployment.

1.3.2 Neutral atoms

Neutral atoms provide a conceptually similar but architecturally distinct platform. Here, individual atoms are trapped in optical tweezers, optical lattices, or cavity QED systems, and qubits are encoded in hyperfine or Zeeman states. Like ions, neutral atoms benefit from the intrinsic uniformity of atomic transitions and from long-lived internal states [19]. They can also be manipulated and measured optically with high precision. In recent years, neutral-atom arrays have emerged as a powerful platform for quantum simulation and computing, particularly through the use of Rydberg-mediated entangling gates. As spin-photon interfaces, neutral atoms are compelling in cavity-based architectures, where a single atom coupled to a high-finesse optical cavity can efficiently absorb and emit photons with well-defined spatial modes. This makes them attractive for quantum memories and remote entanglement generation. Neutral atoms have also been used in repeater-style demonstrations and in protocols where photonic qubits are mapped onto collective atomic excitations [27].

For networking, the principal strengths of neutral atoms are again their optical uniformity, long coherence, and the possibility of deterministic atom-photon coupling in cavities. Their limitations are similar in spirit to those of trapped ions: operation typically requires substantial laser and vacuum infrastructure, and many of the most useful transitions are not generally at telecom wavelengths [19]. Despite this, there are proposals to use quantum frequency transition and there are some less explored inherently telecom band transitions in certain neutral atom schemes [53, 54]. Outside of this, standalone neutral-atom emitters also do not naturally offer the same degree of chip-scale photonic integration as nanofabricated solid-state platforms. Thus, neutral atoms are highly attractive for high-fidelity quantum memories and cavity interfaces, but less naturally suited to compact integrated network nodes unless substantial photonic and vacuum engineering is added.

1.3.3 Photonic qubits

Photonic qubits occupy a somewhat different role in the quantum-network landscape. In this case, the qubit is encoded directly in a photonic degree of freedom such as polarization, time bin, path, or frequency, and the photon itself serves as the information carrier. As noted at the beginning of this section, photons are naturally well suited to communication because they can propagate long distances with relatively low decoherence, particularly in optical fiber at telecom wavelengths. The principal strength of photonic platforms is therefore transmission rather than long-lived storage. Single photons and multiphoton entangled states can be generated, manipulated, interfered, and measured using mature optical technologies, while integrated photonic circuits have enabled low-loss routing, phase control, and multiplexing on chip [19].

The central limitation of a purely photonic platform is that it does not by itself provide a long-lived stationary memory. Photons are excellent carriers of quantum information, but they are not naturally suited to local storage: if one attempts to delay or hold them for extended periods, loss generally accumulates unless an additional memory element is introduced. Moreover, because photons typically do not interact strongly with one another, deterministic two-qubit operations are difficult to realize in all-photonic architectures. For this reason, such approaches often rely on probabilistic measurement-induced gates, extensive multiplexing, or the prior generation of large entangled resource states such as cluster states. This is a powerful and active approach, particularly for communication and measurement-based quantum information processing, but it addresses a somewhat different challenge from that of a node built around a matter-based qubit.

For a repeater or quantum network node, one generally still desires a matter-based memory that can store quantum information while entanglement is being established across lossy links. Photonic qubits are therefore indispensable for quantum networking as flying qubits, but in most architectures they are not, by themselves, a complete substitute for a stationary quantum memory.

1.3.4 Superconducting Qubits

As the name implies, superconducting qubits are based on superconductors and in particular, electrical circuits whose dynamics, resemble that of a harmonic oscillator, with a necessary quantum twist. For a typical quantized harmonic oscillator, an infinite ladder of equally spaced energy levels exists, which makes accessing any two such levels, as required for qubit operations, difficult, because it will excite the rest of the levels as well. This means that excitation of one level causes continuing excitations to higher and higher states. Superconducting qubits get around this by adding a nonlinear circuit element which breaks this equal level spacing, allowing individual transitions to be addressed without exciting the rest of the ladder [55]. This nonlinearity is provided by a Josephson junction, which consists of two superconductors separated by a thin insulating barrier. Below the critical

temperature, Cooper pairs of electrons can tunnel through this barrier, giving rise to the Josephson effect and a nonlinear relationship between between current and phase across the junction [56].

The primary application of superconducting qubits has largely been in quantum computing, owing to their fast gate speeds and compatibility with lithographic fabrication. Because they are manufactured using techniques closely related to those developed for the semiconductor industry, including mask patterning, lithography, and liftoff, they benefit from substantial design flexibility and precise fabrication control [55]. They also support extremely fast operations, with typical single-qubit gate times on the order of 20-40 ns and two-qubit gate times on the order of tens of nanoseconds [56].

In the context of quantum networking, however, their advantages and limitations look somewhat different. Their fast control and strong coupling to microwave resonators make them promising for short-range modular links, local quantum buses, and deterministic communication between nearby nodes housed in cryogenic environments. At the same time, their native photonic interface lies in the microwave rather than optical domain. This is a major limitation for long-distance networking, since microwave photons experience high propagation loss and are highly susceptible to thermal noise outside cryogenic environments [57, 58]. As a result, superconducting qubits are not naturally suited to direct transmission over long optical fibers in the way that optically active emitters are. Long-distance networking therefore generally requires microwave-to-optical transduction, so that quantum information encoded in microwave excitations can be converted into telecom-band photons for low-loss fiber transmission, although this remains technically challenging.

Superconducting qubits also face important constraints related to coherence and infrastructure. While superconductivity itself can be maintained at liquid-helium temperatures (2-4K) for many materials, high-coherence qubit operation generally requires much lower temperatures, typically in the tens of millikelvin range, to suppress thermal excitations and other decoherence processes. Their coherence times are often on the order of microseconds, although continued improvements in materials, circuit design, and fabrication have pushed some devices into the millisecond regime [59, 60]. Achieving such performance therefore typically requires dilution refrigeration, which adds substantial engineering complexity and cost. For networked architectures, this implies that each node must operate within a millikelvin cryogenic environment, complicating deployment relative to platforms that interface more directly with room-temperature optical systems [61].

1.3.5 Solid-State Defects and Quantum Dots

Solid-state platforms are among the most promising candidates for quantum network nodes because they offer a combination of optical addressability, spin-based quantum memories, and compatibility with nanophotonic integration. Unlike trapped atomic systems, they do not require vacuum

trapping architectures, and many can be directly incorporated into photonic structures such as waveguides, cavities, resonators, and photonic crystal devices. From the perspective of quantum networking, this is especially attractive because it raises the possibility of combining spin qubits, single-photon generation, and on-chip photonic control within a scalable material platform. At the same time, however, solid-state systems are embedded in a condensed-matter environment, making them susceptible to decoherence from phonons, fluctuating electric fields, and materials inhomogeneity. Broadly speaking, the solid-state emitters most relevant here fall into two main classes: semiconductor quantum dots and atomic-like defects embedded in solid hosts.

1.3.5.1 Semiconductor quantum dots

Semiconductor quantum dots are engineered nanostructures that are often described as artificial atoms. In these systems, electrons and holes are confined by band-structure engineering, typically by embedding a lower-bandgap material within a higher-bandgap semiconductor host [62]. This creates a localized potential well in which charge carriers can be trapped. Upon optical excitation, the confined carriers may form a bound exciton which subsequently recombines and emits a photon [19]. Depending on the implementation, the relevant quantum degree of freedom may be associated with an electron, a hole, or an optically excited state such as an exciton or trion. Quantum dots are particularly attractive for quantum networking as sources of single photons. This is because of their strong optical transitions, fast radiative emission, and compatibility with semiconductor nanofabrication. They can be integrated into micropillars, photonic crystal cavities, waveguides, and related photonic devices to enhance brightness and collection efficiency [63]. Among the various candidate quantum network platforms, quantum dots have been especially successful as bright, nearly deterministic, and highly indistinguishable single-photon sources.

Their main limitations arise from the fact that they are engineered nanostructures rather than naturally identical atomic systems. Variations in dot size, composition, and local strain lead to substantial inhomogeneity from device to device, so remote emitters are usually not naturally frequency matched [19]. In practice, external tuning using strain, electric fields, magnetic fields, or temperature is often required to bring distinct dots into resonance. In addition, charge noise and coupling to the surrounding solid-state environment can cause spectral diffusion and reduce photon indistinguishability if not carefully controlled. For spin-based applications, the surrounding nuclear-spin environment in many semiconductor hosts can also limit coherence. Thus, quantum dots are especially compelling when brightness, fast operation, and photonic integration are prioritized, while spectral uniformity and long-lived memory remain challenging.

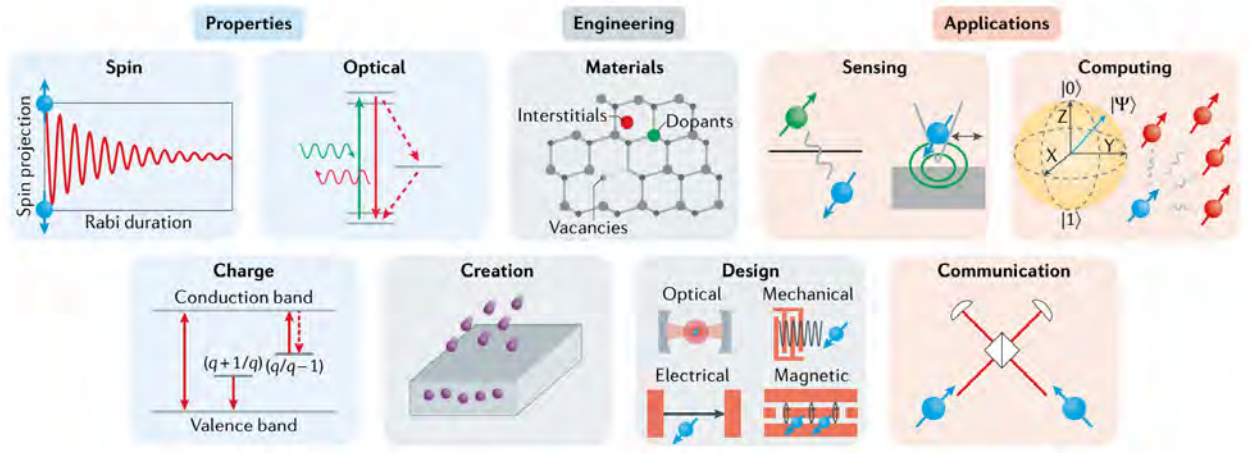

Figure 1.4 Overview of spin defects in wide bandgap materials highlighting defect properties, engineering considerations and the major quantum applications. The image is reprinted from [66] with license to reprint obtained from Springer Nature.

1.3.5.2 Atomic-like defects in solids

A second major class of solid-state quantum emitters consists of atomic-like defects embedded within a host crystal or other solid material [29, 64]. These systems are formed by impurity atoms, vacancies, or more complex defect structures that introduce localized electronic states within the band gap of the host. In this sense, they resemble isolated atoms embedded in a solid-state environment. Depending on the defect and host, the relevant quantum degree of freedom may be an electronic spin, nuclear spin, charge state, orbital state, or an optically excited bound exciton. Compared with semiconductor quantum dots, an important distinction is that individual atomic defects tend to have a more reproducible microscopic structure. Because quantum dots are composed of many atoms and depend sensitively on growth conditions, they exhibit substantial device-to-device variation. By contrast, single atomic defects in a crystal often show more well-defined transition energies and reduced inhomogeneous broadening, more closely resembling the spectral uniformity of atomic systems [65]. For this reason, defect-based qubits are often viewed as an attractive middle ground between trapped atoms and more strongly engineered semiconductor nanostructures.

Spin-based defects are especially important for quantum information because spin degrees of freedom typically couple more weakly to the environment than charge or orbital states, often enabling longer coherence times [29]. These defects can be introduced by ion implantation, incorporation during growth, high-energy irradiation, or pulsed laser writing, with each method offering different tradeoffs in placement accuracy, concentration control, and induced damage [67, 68]. From the standpoint of quantum networking, their appeal lies in the possibility of combining atom-like coherence with solid-state integrability. Many defects support optical initialization and readout, spin-selective transitions, and in favorable cases spin–photon entanglement. In addition, host

materials such as diamond, silicon, and silicon carbide are compatible with modern nanofabrication, enabling integration with waveguides, resonators, and optical cavities. In some defect platforms, exceptionally long coherence times have been demonstrated: for example, electron-spin coherence times in NV centers can reach the millisecond regime under ambient conditions and extend to seconds under dynamical decoupling in high-purity diamond, while associated nuclear-spin memories can reach seconds to minute-scale coherence times [69–72].

Within this broad class, two especially important subclasses for quantum networking are rare-earth ions in solids and color centers in wide-bandgap materials. Rare-earth ions are attractive for quantum networking because their optical transitions originate from shielded inner-shell 4f electronic transitions. Because they are shielded, they can possess long optical coherence times and exceptionally long spin or hyperfine coherence times, making rare-earth ions strong candidates for quantum memories and repeater nodes. They are especially promising in fiber-based networks because some species, most notably erbium, have telecom-band transitions near 1.5 μm, reducing the need for frequency conversion, and they can be integrated into a variety of solid-state photonic hosts. The main tradeoff in these systems arises from the weak transition dipole moments associated with their native $4f$-shell optical transitions. As a result, although rare-earth ions in glass hosts are attractive for long-lived storage and telecom-band compatibility, they are generally less well suited to bright and fast spin-photon interfaces unless cavity enhancement is employed [19, 73]. Color centers in wide-bandgap materials refers to impurities or defects which create localized electronic states within the energy gap of the semiconductor. These states can then be optically interfaced with and can possess spin states, which allow for control over that degree of freedom with optical or microwave application. This class of qubits will be elaborated further below, as the defect explored in this thesis falls into this category.

1.3.5.3 The importance of the host material

For atomic-like defects in solids, the properties of the host material are often just as important as the properties of the defect itself. A useful framework for evaluating candidate hosts is given in [74]. First, the host should possess a sufficiently wide band gap to support localized electronic states associated with defects or impurities within the gap. The wideband gap also ensures that the material is transparent and as such can support optical interfacing. Second, weak spin-orbit coupling is often desirable because it suppresses unwanted spin flips and can help preserve spin coherence. Typically, this favors host materials composed of lighter elements, since lower atomic number is generally associated with weaker spin-orbit coupling due to the weaker atomic potential and reduced relativistic effects. Third, the host should be available in high-quality single-crystal form and be compatible with nanofabrication, so that scalable photonic devices can be realized. Finally, the constituent elements should ideally have zero or near-zero nuclear spin, or at least the ability to be

isotopically purified, in order to reduce decoherence arising from hyperfine interactions.

1.3.5.3.1 Deep Defects Deep defects refer to well-isolated electronic states of a defect far from the valence and conduction band edges of the host material it resides in. This separation ensures that the defect behaves as a localized atom-like system. If one of the levels is too close to the valence or conduction band, then optical or thermal excitation can potentially ionize the defect or lead to uncontrolled switching between charge states, reducing the stability of the emitter. Hence, the requirement for a wide band gap host material tends to be thought of as especially important as it provides more freedom for a defect's energy levels [66, 74]. This is one reason why materials such as diamond and silicon carbide are so prominent in the search for quantum useful defects. Recently, however, there has been work pointing out that many of the defect candidates currently being studied do not meet the deep defect criteria and yet can still be used to perform many quantum node experiments [66, 75]. Indeed, the silicon vacancy complex in diamond contains an energy level within the valence band, however, despite this, the desired negative charge state remains remarkably stable. This has been attributed to the fact that the transition is between two localized electronic states, and so even if one is in the valence band, it remains robust to ionization [75]. Similarly, many defects of interest in silicon involve bound exciton states in which a valence or conduction band state is excited to an intra gap localized defect state. The downside with exciting a highly delocalized wavefunction to a localized defect state; however, is that the overlap between the two and hence the transition dipole moment is very low, leading to weak radiative rates [75] typically on the order of μs. This is in contrast to the SiV, which has a strong transition dipole moment and an excited state on the order of ns [75]. Furthermore, depending on the binding energy of the bound exciton, it can be broken by thermal excitations and as such temperature induced fluorescence quenching can occur, potentially limiting such defects to low temperature operation. Lastly, it should be mentioned that one additional reason for deep defects typically being the recommended choice, outside of their intuitive advantage, is because the NV center in diamond was so successful and it lies well within the diamond band gap [76].

1.3.5.3.2 Nuclear Spin Decoherence The nuclear spin environment of the host is also crucial. Although nearby nuclear spins can themselves serve as useful quantum resources, for example as long-lived memory qubits [77], an uncontrolled bath of nuclear spins is one of the main sources of decoherence for electronic spin qubits. This is especially important because only a limited number of materials can be isotopically purified so that most or all host nuclei carry zero spin [74]. Diamond is particularly attractive in this regard because isotopic purification can greatly suppress the nuclear-spin bath, leading to dramatic improvements in coherence time. By contrast, in some rare-earth host materials the surrounding nuclear-spin environment can be much denser. As such,

even though the rare-earth ions themselves may possess very appealing optical properties, the hosts which can accept them can severely limit coherence times and as such novel host materials with potentially novel incorporation methods are required.

1.3.5.3.3 Non-Radiative Decay Another host-dependent issue is nonradiative decay, in which an excited state relaxes by transferring its energy to lattice vibrations rather than emitting a photon. Since quantum networking relies on efficient optical initialization, readout, and spin-photon interfacing, strong nonradiative decay is highly undesirable [78, 79]. Whether nonradiative decay is severe depends inversely on the size of the optical transition energy (energy gap law), the phonon spectrum of the host, and strength of the electron phonon coupling of the defect wavefunctions to lattice vibrations [80–83]. If the transition energy is small, relaxation can occur efficiently through the emission of only a few phonons, making multiphonon nonradiative decay more likely. By contrast, larger transition energies require the simultaneous emission of many phonons, which is much less probable [82]. This creates an important tradeoff for telecom-band quantum emitters: although emission near 1.3-1.5 μm is highly desirable for fiber transmission, such low-energy optical transitions are often more vulnerable to nonradiative loss. Diamond provides a useful example of this tradeoff. Despite its many advantages, it is generally difficult for defects in diamond to emit brightly in the telecom band. One reason is that diamond has a high maximum phonon energy, so relatively few phonons are needed to bridge a small transition energy, which enhances nonradiative decay [84]. Since telecom-band transitions already have relatively low photon energy, this problem becomes even more severe [78]. As a result, even if a telecom-wavelength defect can be realized in diamond, it may not be intrinsically bright. Nanophotonic cavities via cavity quantum electrodynamics can help increase the radiative decay rate by increasing the coupling strength between the defect and the excitation light. Furthermore, phononic band-gap engineering can suppress the non-radiative rate by making structures in which the phonon modes needed to cause non-radiative relaxation are strongly inhibited or completely removed [85]. Interestingly, telecom-emitting defects in diamond have been reported, including one near 1200 nm of unknown origin [86] and erbium-related emission near 1550 nm [87]. More broadly, this has motivated ongoing interest in host materials with lower maximum phonon energies, which may better suppress phonon-mediated nonradiative decay.

1.3.5.4 Zero-phonon-line emission and its importance

Before covering the specific diamond color centers, it is important to introduce the idea of the zero phonon line. Because these emitters are embedded in a crystal, their electronic states are inevitably coupled to lattice vibrations. As a result, optical transitions generally do not occur in isolation from the host lattice. This can be understood with the help of the Franck-Condon principle. First, within the Born-Oppenheimer approximation, electronic motion can be treated as much faster than

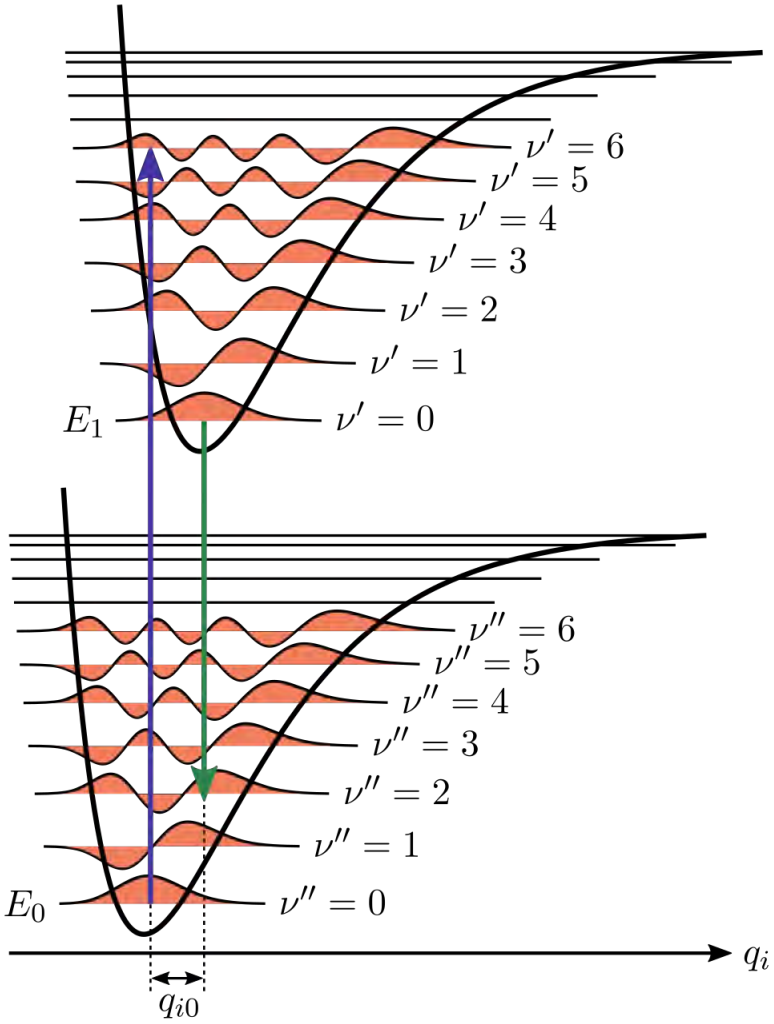

Figure 1.5 Energy diagram illustrating the Franck-Condon principle, reprinted from `https://en.wikipedia.org/wiki/Franck-Condon_principle`.

nuclear motion because the masses are orders of magnitude apart. That means that during an optical transition, the nuclei are effectively frozen. The consequence of this is that optical excitation and emission can occur between different vibrational states associated with the electronic ground and excited manifolds [88]. In a crystalline solid, the atoms oscillate about equilibrium positions, and for small displacements these motions can be approximated as harmonic. The vibrational degrees of freedom can therefore be described in terms of quantized lattice modes, or phonons. Since the equilibrium nuclear configuration generally differs between the electronic ground and excited states of a defect, the associated vibrational wavefunctions are not identical. Optical transitions may therefore occur either without changing the vibrational state or together with the creation or annihilation of phonons.

This leads to two main contributions in the optical spectrum. The first is the zero-phonon

line (ZPL), which corresponds to a purely electronic transition that leaves the vibrational state unchanged. The second is the phonon sideband (PSB), which consists of transitions in which electronic excitation or emission is accompanied by one or more phonons. In photoluminescence, the phonon sideband typically appears at lower photon energy than the ZPL because some of the transition energy is carried away by lattice vibrations. Photons emitted into the phonon sideband are generally unsuitable for entanglement protocols because electron-phonon coupling causes the emitted photon to become entangled with the vibrational environment, resulting in decoherence and reduced photon indistinguishability after the phonon degrees of freedom are traced out [89]. As such, emitters which radiate a large fraction of their light into the ZPL [78, 79] are desirable. A standard figure of merit then is the Debye-Waller factor, defined as the fraction of total emission that occurs in the ZPL.

$$\mathrm{DW} = \frac{I_{\mathrm{ZPL}}}{I_{\mathrm{ZPL}} + I_{\mathrm{PSB}}} \tag{1.10}$$

A larger Debye-Waller factor indicates weaker electron-phonon coupling and a greater proportion of spectrally coherent photons. As a quick explanation, the strength of the phonon sideband depends strongly on the specific defect and host material. For example, the nitrogen-vacancy center in diamond exhibits a relatively strong phonon sideband, commonly attributed to its stronger electron-phonon coupling and the large spatial character of its electronic wavefunction as well as the big difference in charge distribution between ground and excited state [90, 91].

1.4 Diamond Defects as Qubits

Having reviewed the general requirements for solid-state spin qubits and single photon emitters, we now turn to a concrete material platform which satisfies many of these criteria: diamond. Among the various solid-state hosts, diamond has emerged as one of the most successful and versatile systems for realizing optically addressable spin qubits and spin–photon interfaces. In particular, color centers in diamond, most notably the nitrogen-vacancy (NV) center and the group-IV vacancy centers (SiV, GeV, and SnV), have become leading qubit candidates and have been used in numerous proof-of-principle experiments in quantum sensing, quantum communication, and quantum information processing [92]. Each of these defect systems exhibits distinct advantages and limitations, which are reviewed below, together with a brief historical perspective on their discovery and development.

1.4.1 Diamond as a Host

Diamond offers many advantages as a host material for quantum defects as well as some drawbacks. It is a wide-bandgap semiconductor with an indirect bandgap of approximately 5.48 eV and a direct

bandgap near 7.2 eV [84] and as such it can host a wide range of deep defect levels, which can remain isolated from the bulk electronic structure. Further, owing to its wide band gap, even at room temperature, the thermal population in the conduction band is negligible, strongly suppressing unwanted interactions between free carriers and defect states [93]. In addition, the strong covalent bonds in diamond result in a very high Debye temperature (exceeding 1800 K), which is why diamond is so hard and heat dissipating, but also that few phonons will disturb the qubit [94]. Diamond's wide band gap makes such optical interfacing easy because diamond is transparent from the UV to far infrared and as such one can relatively easily excite and collect fluorescence from any defect of interest without the diamond absorbing that light. That being said, diamond's high refractive index of $n = 2.4$ means that most light emitted from defects in bulk diamond experience total internal reflection, limiting total light extraction efficiency. However, various fabrication methods can be used to create nanophotonic structures to combat this low light extraction efficiency such as solid immersion lenses, nanopillars, and cavity waveguides.

In terms of magnetic spin noise, natural diamond consists predominantly of ^{12}C which has zero nuclear spin, with only about 1.1% of ^{13}C which has nuclear spin of $I = 1/2$. However, thanks to advancements in chemical vapor deposition growth, this residual nuclear spin bath can be largely eliminated by growing diamonds with ^{12}C enriched precursors, dramatically reducing spin noise [95]. Other sources of decoherence can arise from paramagnetic impurities which incorporate during the growth process such as substitutional nitrogen (N_s); however, these can also be limited to below 5 ppb in high-purity material. Furthermore, because diamond is composed of the relatively small C atom, the inherent spin orbit coupling is quite weak, limiting any spin flips from that. Additionally, since the crystal structure of diamond is inversion symmetric, it can, by definition, host defects which are themselves inversion symmetric, meaning they have no permanent static electric dipole and thus up to first order do not experience energy level shifts from stray electric field noise. Moreover, many diamond color centers are bio-compatible, enabling applications for quantum sensing in the life sciences [96].

Defects in diamond can also possess long spin relaxation times (T_1) owing to diamond's high Debye temperature and weak spin-orbit coupling. The Debye temperature relates to how high an energy is required to move the lattice atoms around and because diamond has very stiff carbon covalent bonds (which is what makes diamond the hardest material on earth), it is hard to for thermal energy to supply energy for lattice vibrations. Second, because carbon is a light atom, it has weak spin-orbit coupling, which is the dominant spin relaxation mechanism, e.g. via spin phonon lattice relaxations. However, the low coupling make that challenging. As such, seconds long spin relaxation times have been observed in diamond. Importantly, however, SiV- experiences shortened T_1 times even at low temperatures because of dynamic Jahn-Teller effect which can couple it to low energy phonons which because the spin quantization axes in upper and lower ground state orbital

branches is different, absorption of phonons at 50GHz can cause a spin flip.

Defects in diamond can also possess long spin-relaxation times (T_1), owing to diamond's high Debye temperature and the relatively weak spin-orbit coupling associated with carbon. The Debye temperature is defined as the temperature above which all phonon modes are populated and below which certain phonon modes get frozen out or severely depopulated. As such, it sets the energy scale for lattice vibrations, and because diamond is composed of very strong carbon-carbon covalent bonds, its lattice is exceptionally stiff. As a result, thermal occupation of lattice vibrations is suppressed compared with many other solids, especially at low temperature. In addition, carbon is a light element, so spin-orbit coupling is relatively weak. Since spin-orbit interaction often mediates spin-lattice relaxation, this weak coupling helps suppress phonon-induced spin relaxation. Consequently, spin-relaxation times as long as seconds have been observed in diamond.

Importantly, however, not all diamond defects retain such long T_1 times. In the case of the SiV^- center, the spin-relaxation time can be strongly shortened even at low temperatures because of the dynamic Jahn-Teller effect, which couples the electronic orbital states to low-energy phonons. In the ground state, the upper and lower orbital branches have different spin quantization axes. As a result, phonon-mediated transitions between these orbital branches can also change the spin character of the state, enabling spin relaxation. For SiV^-, this process is particularly efficient because the orbital splitting is on the order of tens of gigahertz, so phonons at these energies are sufficient to drive the transition. Importantly, this only happens when an off-axis magnetic field is applied

Comparison with Si and SiC Silicon and silicon carbide are also leading candidate host materials, and several defects in these systems have been identified as spin qubits and single-photon emitters [97]. Because the bandgaps of these materials are smaller than that of diamond, their defects tend to emit at longer wavelengths, and in some cases in or near the low-loss telecommunications bands [98]. A major practical advantage of Si and SiC is the extraordinary maturity of their fabrication ecosystems: industrial semiconductor foundries can routinely produce extremely pure, high-quality material and complex nanophotonic structures, enabling straightforward integration with photonic integrated circuits [99]. Such integrated photonic platforms are widely viewed as a key enabling technology for scalable quantum computing and quantum networking, as they allow optical signals to be routed on-chip between multiple quantum emitters and functional components.

1.4.2 Nitrogen vacancy center

Having discussed the advantages of diamond as a host material, the current defects of interest for quantum information processing applications will now be explored. We start with the one that started it all: the Nitrogen Vacancy (NV) center. The NV center consists of a substitutional nitrogen atom occupying a carbon lattice site, adjacent to a vacant carbon lattice site in the diamond crystal

[100]. Its optical and spin properties were first characterized in the 1970s [101, 102], but it was not until the late 1980's that optically detected magnetic resonance (ODMR) was performed [103, 104]. The extension of ODMR to single defects was achieved in 1997 [105], marking a major mileston and firmly establishing the NV center as a leading spin qubit platform.

The negatively charged NV^- exhibits a zero phonon line at 637 nm and possesses an orbital singlet, spin triplet ground state. While it can take on neutral and positively charged charge states, it is the NV^- charge state - with its spin triplet ground state - that underpins its most remarkable properties and has attracted the greatest interest over the past several decades. In particular, ground state spin coherence times of milliseconds at room temperature can be achieved, limited primarily by the roughly $\sim$1.1% of ^{13}C nuclear spins in natural diamond. This limitation can be mitigated via isotopic engineering or dynamical decoupling sequences. The first removes the nuclear spin bath by using ^{12}C precursors during diamond growth. The second cancels out the random and slowly varying spin flips using coherent pulse sequences. Both can result in coherence times reaching seconds even at room temperature [106–108]. These excellent spin coherence properties gave hope to the idea of a near term room temperature quantum computer. However, this was not to be. While the NV^- has long spin coherence times even at room temperature and allows for easy microwave control thanks to its electronic structure, it faces a number of challenges which limit its use in quantum computers and networks.

Before discussing these challenges, it is worth examining the origin of the NV center's unusually long spin coherence times at room temperature. A central reason is that the NV^- ground state is an orbital singlet, which strongly suppresses first-order spin–phonon coupling. The 2.87 GHz zero-field splitting of the ground-state spin triplet arises from the intrinsic spin–spin interaction [109]. In systems with orbital degeneracy, phonons can efficiently couple different orbital branches through vibronic interactions, leading to strong spin dephasing [110]. By contrast, the absence of orbital degeneracy in the NV ground state greatly reduces such phonon-mediated decoherence channels. As a result, even at room temperature, long coherence times are observed.

There are two main challenges the NV faces when it comes to its use as a qubit. The first is the NV's susceptibility to electric field noise [111]. This comes from the nitrogen sitting off-symmetry in a carbon lattice site, resulting in a permanent electric dipole. As such, any stray electric field noise from other defects within the diamond or from the surface for example can shift the energy of light it emits due to the DC Stark effect. This shifting of the ZPL energy is usually referred to as spectral diffusion [112]. The emitted photons are then no longer indistinguishable as they each have different frequencies. As stated in section 1.2.3, this makes two-photon entanglement challenging as indistinguishable photons are the key ingredient. Now, while it is challenging, it's not impossible. This is because one can intentionally apply electric fields to tune the NV ZPL to a specific energy. Tuning on the order of tens of GHz has been achieved with moderate electric fields

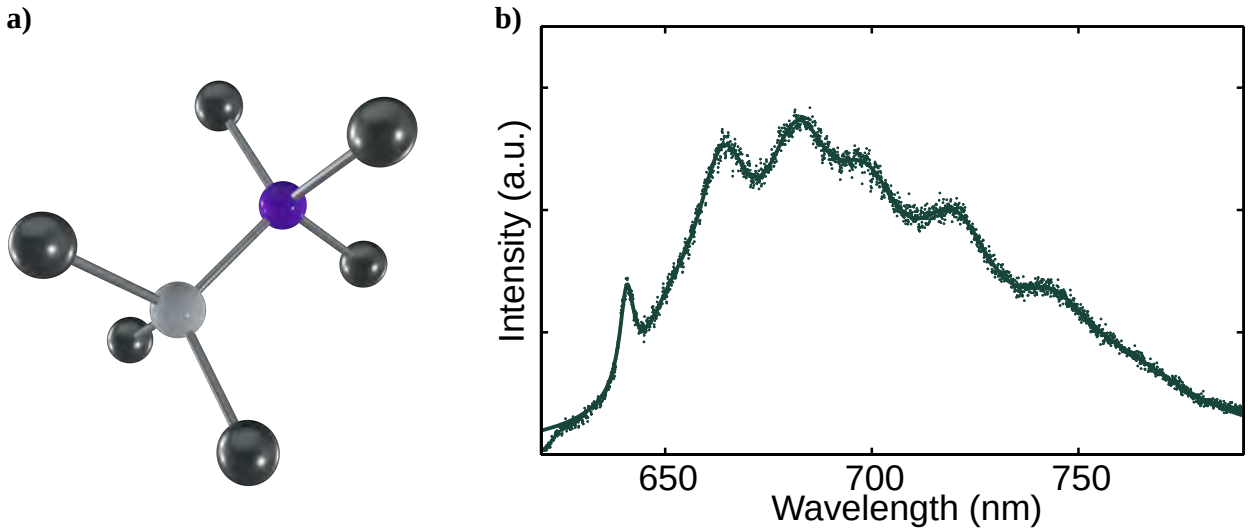

Figure 1.6 a) shows the geometric structure of the NV center with the dark grey spheres representing carbon atoms, the light grey a vacancy, and the purple, a nitrogen atom. b) shows a typical photoluminescence spectrum of an NV center.

[113]. This enables frequency matching of detuned NV's via separate electrodes [114]. That being said, this requires further nanofabrication and can be at odds with nanophotonic structures, which are necessary to improve light collection efficiency. As such, it is generally considered better to have defects which don't have permanent electric dipoles. The second disadvantage is the NV's weak emission into the zero phonon line (~3%). This is a result of strong electron-phonon coupling, which makes the phonon sideband responsible for ~97% of the NV's emission (see Figure 1.7). As stated in section 1.3.5.4, this limits entanglement rates because one has to wait long times before a coherent photon is emitted, as most are coupled to phonons which decay on pico-second time scales [111]. One can boost this ZPL emission by using nanophotonic cavities; however, this is challenging because the NV's are placed near surfaces and as such experience strong electric field noise which as stated before causes spectral diffusion [115]. Microcavities are an alternate solution to this; however, they scale poorly and perform worse than nanocavities because their mode volumes aren't as small and thus can't offer the truly increased spin-photon interaction that nanocavities can.

It faces two additional hurdles, which are generally viewed as less fundamentally limiting but are still worth mentioning. First, while not unique to the NV center, is that it can take on other charge states. As mentioned above, while the negatively charged NV^- is the desired charge state with its favorable spin-1 ground state, it can also convert to the neutral charge state, NV^0, so charge state stability is an important consideration [116]. As a result, protocols are needed to check which charge state the defect is in, and further protocols to repump the system back into its negative charge state if needed [117–119]. Ultimately, this overhead can take on the order of hundreds of μs, a large fraction of the total sequence time [119], decreasing the amount of time available for the actual

quantum protocol to be applied, which can limit both scalability and which quantum protocols can be implemented due to already limited coherence times [120]. Furthermore, limitations in single shot readout of nuclear spins has been observed due to stochastic charge state transitions [121, 122] owing to a reduced spin flip probability. It should be noted; however, that this is a problem faced by many defects embedded in solid-state hosts and there are a variety of different techniques which have been developed to combat it [120, 123–128]. A fourth disadvantage is that its ZPL is at 1.94 eV, or 637 nm, which is a wavelength not directly compatible with long-distance photon propagation [86] as it isn't in any of the telecom bands. As such, some form of quantum frequency conversion would be needed to convert the NV photons to a telecom band. This typically results in losses and is not guaranteed to convert to the lowest loss telecom-c band.

Despite these challenges, many amazing proof-of-principle experiments have been performed [129] including both two-photon entanglement [130] and a three-qubit quantum network [131]. quantum sensor [132], quantum register [133], and quantum communication node [134]. Outside of computing and networking applications, the NV has been established as a world leading magnetometer and quantum sensor for pressure, temperature, and electric fields. This follows to some extent, but generally, the best sensors are not usually the greatest quantum bits as one wants a quantum bit that is insensitive to its environment. As a result of the weaknesses of the NV, researchers began looking for alternative defect systems which might be able to build upon the NV's weaknesses while still capturing its benefits.

1.4.3 Silicon vacancy center

The next promising defect to be explored as an alternative to the NV center, was the silicon vacancy center (SiV^-), which is opposite to the NV^- in many ways [112]. Much like the NV, it consists of an impurity atom plus a carbon vacancy. However, unlike the NV, the larger silicon atom sits in the center between two carbon vacancy sites. This is its most stable configuration as moving out of the center can result in strain to the lattice. Although silicon-related defects were first observed many decades ago, they were originally thought to be very dim with low photon counts. This changed in 2011, when Neu et al. published results showing millions of counts from SiV^-s in nanodiamonds [135], sparking intense interest across the scientific community. In stark contrast to the NV's weak emission into the ZPL, the SiV offers between 70 to 80% emission into the ZPL with much weaker electron phonon coupling [136]. Additionally, in contrast to the NV^-, the SiV^- is in the split vacancy configuration, where the silicon atom is located between two vacant lattice sites (see Figure 6 center). This gives it D_{3d} point group symmetry, which is inversion symmetric, and thus eliminates first-order Stark shifts as a result of not having a permanent electric dipole [112]. Consequently, the SiV^- has extremely limited spectral diffusion. Already, this represents a major

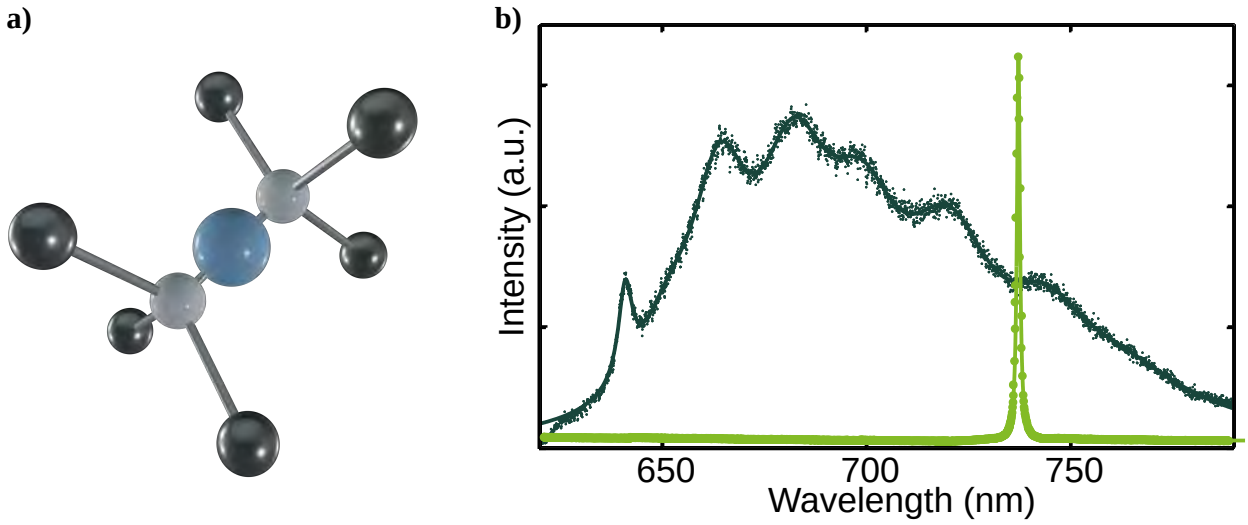

Figure 1.7 a) shows the geometric structure of the SiV center with the dark grey spheres representing carbon atoms, the light grey are vacancies, and the light blue is a silicon atom. b) shows a typical photoluminescence spectrum of for an SiV center compared to the previously shown NV spectrum.

improvement over the NV^- center.

On the other hand, where the NV^- excels in terms of long coherence time at room temperature, the SiV^- is quite poor, limited to the nanosecond regime even at liquid helium temperatures (~2-4K). Even at these temperatures, the relevant phonon modes needed for resonant absorption and emission (~50GHz) between the SiV^- ground state orbital branches remain populated, resulting in phonon-induced dephasing [**roger**, 109, 137]. Even though the orbital transition is spin conserving, and so long T_1 spin lifetimes can be observed, the splitting between $|\uparrow\rangle$ and $|\downarrow\rangle$ are different for the two orbital branches, and so the spin precession frequency is different. This means that a random phase will be accumulated whenever a phonon is absorbed and this is measured as decoherence. Hence, the orbital relaxation time puts an upper bound on the spin coherence time [109]. Such phonon-induced dephasing can be limited by cooling the system to mK temperatures in a dilution refrigerator [138]. However, while such an approach has been found to extend the SiV^-'s coherence time into the millisecond regime, it is extremely costly and not as scalable. This is because dilution refrigerators are large, expensive cryostats which require both helium-3 (expensive) and helium-4 (more common isotope). A color center or configuration in which the same coherence times could be achieved at temperatures > 1 K would be preferable as these temperatures can be achieved with simpler ^{4}He cryostats, which are accessible to more groups and considered to be more scalable than dilution refrigerators.

Strain has been demonstrated to improve the coherence of the SiV as it can increase the ground state orbital branch splitting, reducing phonon induced decoherence, however, it is at the cost of modifying the original inversion symmetric structure. Despite that, strain based techniques

have been implemented to a great degree of success for the SiV. Another method to suppress the phonon-induced dephasing is to find a system which has a larger ground state spin-orbit splitting, and thus a lower phonon occupation [28]. The problem with introducing transverse strain, however, is that it will mix the spin orbit states, so that while microwave transitions can be driven efficiently, the T_1 times for the spin states will be shortened. Researchers thus began to look for systems which have similar electronic and geometric structures to the SiV^-, so as to retain the SiV^-'s favorable optical properties, but which have larger ground state spin-orbit splittings. This leads us to the next primary color centers of interest.

1.4.4 Heavier Group-IV Centers

The heavier group-IV centers, in particular germanium, tin, and lead, follow the SiV naturally. These impurities share the same group as silicon and thus have the same number of valence electrons. Accordingly, the vacancy complexes containing these atoms were expected to have similar electronic properties as the SiV. In particular, the GeV, SnV, and PbV complexe were expected to largely share the SiV's properties. The main difference however is that these atoms have larger atomic numbers and as such the spin orbit coupling strength should be stronger. This corresponds to a larger ground state spin orbit splitting and hence reduced phonon induced decoherence owing to the higher energy required for phonon absorption at similar temperatures. As such, the coherence times are expected to be extended at liquid helium temperatures. This has also been observed experimentally with T_2^* times on the order of a microsecond being reported for SnV's even at 1.7K [139]. Further, these times are primarily limited by slowly varying magnetic field noise and can be dynamically decoupled from, resulting in coherence times on the ms time scales [139]. Moreover, these defects retain the inversion symmetric D_{3d} point group as well as narrow optical linewidths and strong emission into the ZPL [140–142]. However, these defects are not without their challenges. In particular, both GeV and SnV feature zero phonon lines (ZPLs) in the 600 nm regime, which are challenging laser wavelengths, requiring complex and costly systems such as dye lasers or frequency mixing systems. Additionally, the stronger SOC makes spin control of these defects highly challenging, as it strongly pins the spin quantization axes of the ground and excited states. Spin control can be achieved using either all-optical two-photon Raman transitions or direct microwave driving; however, in both cases, the strong SOC makes it challenging to access the nominally spin-forbidden transitions necessary for optical pumping and coherent control.

Optical spin control is typically implemented using two-photon Raman transitions in a Λ-type scheme (see Chapter 2), in which the qubit is encoded in two ground-state spin sublevels and coupled via a common excited state. In a Raman process, coherent population transfer between the two ground states is driven by two laser fields, each resonant with one of the two spin transitions to the

excited state. Moreover, both lasers are detuned from the excited state to ensure the system evolves through a virtual intermediate state rather than via the excited state itself. This greatly suppresses spontaneous emission or optical scattering off the excited state. However, the excited-state still mediates the interaction, so residual off-resonant scattering can occur. These scattering events can lead to decoherence by either flipping the spin state or randomizing the phase of the qubit state. Efficient optical control requires a nonzero branching ratio between spin-conserving and spin-flipping optical transitions. In an unperturbed state, the spin quantization axes of the ground and excited states are aligned, so the spin-forbidden transition vanishes and the branching ratio becomes effectively infinite. To overcome this, an off-axis magnetic field is applied to tilt the spin quantization axes and generate finite overlap between the two legs of the Λ system [143]. For the heavier group-IV centers, however, the Zeeman interaction must compete with very large ground- and excited-state SOC splittings, so comparatively large magnetic fields are required before appreciable spin mixing is obtained. Thus, while all-optical control has been demonstrated, it is challenging [112]. Despite this, all-optical control has been achieved for the SnV^- [139] and GeV^- [144].

Microwave control provides an alternative but still trap-laden route to victory. Here, a microwave magnetic field is used to drive transitions between two spin sublevels usually within one of the ground-state orbital branches (typically the lower one). This transition, however, is magnetic-dipole forbidden because the relevant states differ in spin and also feature the same orbital character. To relax this selection rule, transverse strain can be introduced which mixes the orbital branches and makes the qubit states more spin-like, enabling microwave driving. Indeed, coherent microwave control has been demonstrated with the SiV^- with fidelities reaching near 99% [145, 146]. For the heavier group-IV centers, the story is more complicated. Because the ground state splitting is generally an order of magnitude larger, higher microwave driving powers are required to achieve similar off-axis strain values. This is due to the fact that the strain-induced orbital mixing is related to the strength of the spin–orbit coupling and thus, for the large ground state spin-orbit splitting of the heavier group-IV centers, the overlap between orbital states is reduced [28]. Consequently, stronger strain or higher microwave power is generally required to obtain comparable control fidelities. Both strategies introduce tradeoffs. First, increasing strain can change the intrinsic symmetry of the defect, potentially altering its ZPL as well as inversion symmetry and thus increasing the probability for spectral diffusion. Furthermore, too much mixing from strain can also limit coherence time because of spin-mixing. Second, microwave delivery can produce sample heating, which may itself become a source of decoherence [147]. This can be limited by the use of relatively low Rabi frequencies (on the order of 10 MHz); however, that can result in the qubit dephasing during microwave pulses [28]. Moreover, microwave fields are difficult to localize on the scale of individual emitters, leading to cross-talk in multi-defect architectures, whereas optical fields offer much higher spatial selectivity.

Importantly, one advantage of microwave control over optical control is the increased flexibility afforded to the orientation of the magnetic field with respect to the defect's symmetry axis. In particular, microwave control can allow the magnetic field axis to be brought close to alignment with the defect axis, thus providing access to cycling optical transitions [137] for single-shot read-out of the spin state [117].

1.4.5 Neutral charge states and other defects

The defects described above are by no means an exhaustive list of all the defects in diamond that have been explored. Here, I discuss some others which also have nice properties but for which there are fewer works focusing on in the research community. The group-III elements, Al, Ga, In, and Tl, have been theoretically predicted to have NV^- like properties in their single negative charge state [148]. However, there has been no experimental observation of the predicted defects reported as of yet. There was a telecom band emitter reported in a silicon ion implanted diamond, although its origin was unknown [86]. This would get around any sort of quantum conversion scheme to get to low loss telecom fiber bands. There are also the MgV and PbV, which are potentially thought to be more charge stable, as in, truly deep defects [149, 150]. Further, higher than 4K operating temperature has been reported while maintaining narrow linewidths and long coherence times for the PbV [151].

Additionally, there are also alternate charge states that one can look into. For example, the SiV^0 has a near-infrared ZPL at 946 nm and is a spin S=1 state similar to the NV^- [152]. This enables easy spin control and longer coherence times, like the NV^-, but it retains the high ZPL emission of the SiV^- [152]. Indeed it has been reported that the neutral SiV^0 has spin lifetimes of $T_1 = 43$s and coherence time of $T_{2,\text{echo}} = 954\mu$s at temperatures below 20K. The primary problem for the neutral defects in diamond is that they are historically hard to create in intrinsic diamond without the use of specialized doping. This is particularly true for the SiV0 as there has been much difficulty in reproducing samples which show it owing to charge state instability [153]. It has been reported that it requires a very specific concentration of boron doping between 1 and 3 parts per million to achieve a charge stabilized SiV0. One potential reason for this is its narrow window of formation with respect to Fermi level compared to the other charge states that SiV can take on. That said, despite these challenges, there is ongoing work to improve the formation yield of this center as well as to charge stabilize it [154].

1.5 The Nickel Vacancy Center

Having reviewed the leading diamond color centers, including the NV and group-IV vacancy centers, we now turn to the defect that is the focus of this thesis: the nickel-vacancy center in diamond (NiV).

1.5.1 NiV^- History and Motivation

Nickel has a long and somewhat complicated history in diamond spectroscopy. It is a common impurity which shows up in both chemical vapor deposition (CVD) and high-pressure high-temperature (HPHT) diamond growth environments, and a variety of nickel-related optical and electron paramagnetic resonance (EPR) signatures have been reported over several decades [155–158]. The first EPR center conclusively associated with nickel in diamond, the so-called W8 center, was identified as early as 1966 and later confirmed using isotopically enriched ^{61}Ni samples [159, 160]. Subsequent studies established a substitutional nickel defect model for this particular center, associated with optical features near 2.5 eV [161–165]. In parallel, optical studies in the near-infrared revealed narrow emission lines around 883–885 nm, most notably in the work of Nazaré et al. in 1991, who reported sharp low-temperature features, isotope-dependent splittings, and preferential alignment along the $\langle 111 \rangle$ directions [166, 167]. Despite these observations, the microscopic origin of this near-infrared emitter remained unclear for many years. Limited experimental resolution and incomplete theoretical understanding meant that key aspects of its fine structure were not resolved, and most theoretical work was split between that of a trigonally distorted interstitial nickel complex [161, 168–170]. Under this assumption, the center would not possess inversion symmetry, making it less attractive from the perspective of spectral stability and quantum optics. At the same time, the rapid rise of the NV center as a dominant experimental platform likely further reduced interest in nickel-related defects, which remained comparatively underexplored.

This picture changed significantly with the density functional theory study by Thiering and Gali in 2021, which compiled and synthesized much of the previous work while also identifying the split-vacancy NiV^- configuration as the most likely origin of the 883 nm zero-phonon line and providing a detailed prediction of its electronic structure using state of the art DFT methods [171]. In this model, the nickel atom sits between two vacant carbon sites, forming a structure analogous to that of the SiV^- center. Crucially, this split-vacancy configuration possesses inversion symmetry, which suppresses first-order Stark shifts and therefore strongly reduces spectral diffusion, similar to the group-IV centers. The predicted level structure of the NiV center consists of a ground-state orbital doublet and an excited-state orbital singlet, with a ground-state spin–orbit splitting comparable in magnitude to that of the heavier group-IV centers (see Fig. 1.9) [171]. As in the SiV, GeV, and SnV centers, this large spin–orbit splitting implies that extended spin coherence times should be achievable at readily accessible liquid-helium temperatures. At the same time, the

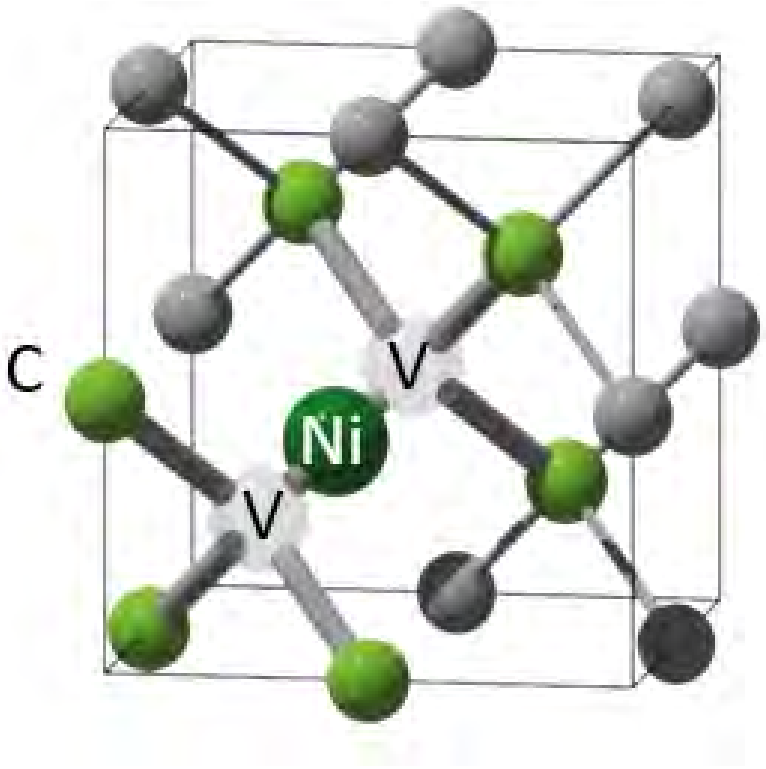

Figure 1.8 Geometric structure of an NiV defect with the six nearest carbon atoms shown in green, the rest in grey, the nickel atom in dark green and the vacancies as slightly transparent.

presence of an excited-state singlet, rather than a doublet as in the group-IV centers, provides an important additional advantage: because singlet states are not subject to spin–orbit or Jahn–Teller interactions, the excited-state structure is greatly simplified, and the spin quantization axis aligns directly with an applied magnetic field. This enables more efficient and robust optical spin-pumping protocols at lower magnetic fields, which is highly desirable for practical implementations [171].

The NiV center also offers an attractive zero-phonon line wavelength near 885 nm, which is readily accessible using compact and inexpensive diode lasers, in contrast to the 600–750 nm range typical of the NV and group-IV centers. Moreover, photons at this wavelength can be frequency converted to the telecom C band around 1550 nm in a single step with low added noise using difference-frequency generation driven with commercially available thulium lasers at 2050 nm [37, 172]. This provides direct compatibility with ultra-low-loss optical fibers, a key requirement for scalable quantum networks. While telecom networking via frequency conversion of the SiV center has recently been demonstrated [173], that approach is currently limited to the higher-loss telecom O-band due to Raman noise from the pump laser, making the NiV wavelength particularly appealing from a systems-engineering standpoint.

Finally, the NiV center exhibits photoelectrical activity. In 2018, it was shown that such defects can generate photocurrent signals [174], opening the door to photoelectric readout schemes for

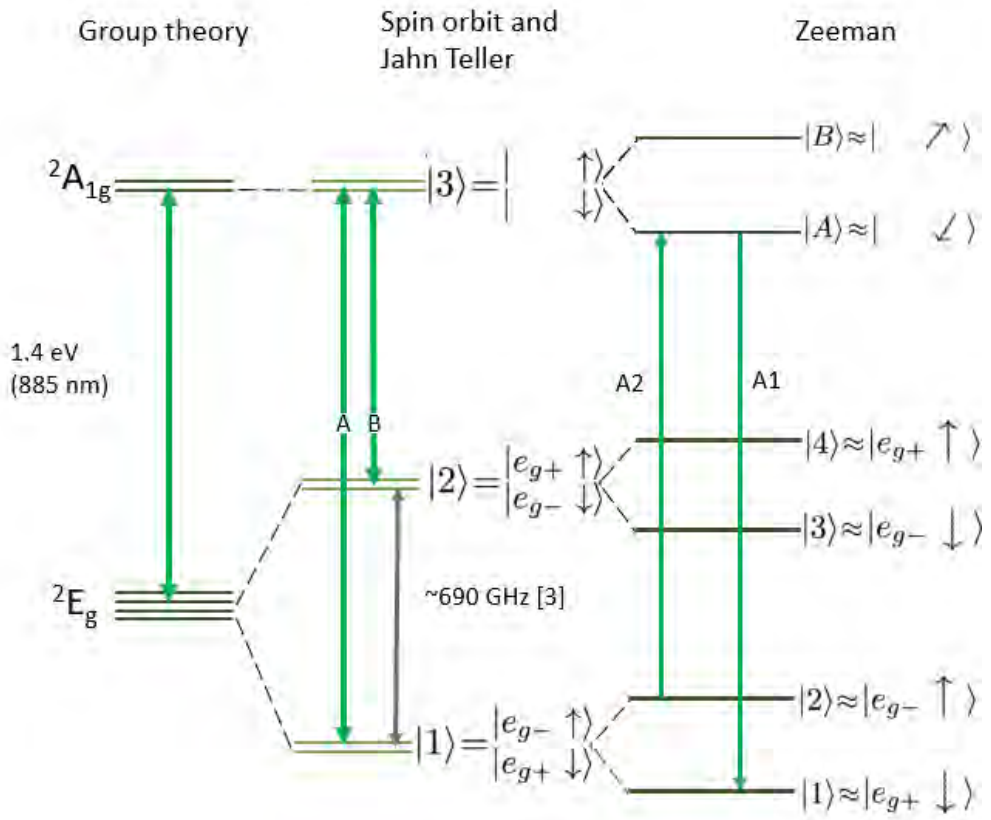

Figure 1.9 Proposed electronic structure of the NiV^- as predicted and proposed in Thiering and Gali's work [171]. Optical transitions are shown as green arrows while the ground state spin orbit splitting is shown in grey.

both electronic [175–178] and nuclear spins [179, 180]. This capability provides a promising alternative or complement to purely optical detection and may prove advantageous for integrated device architectures. Taken together, the combination of inversion symmetry and spectral stability, a favorable electronic level structure, a convenient near-infrared emission wavelength compatible with low-noise telecom conversion, and the prospect of photoelectric spin readout strongly motivates a detailed experimental investigation of the NiV center as a platform for quantum photonics and spin–photon interfaces.

1.5.2 Alternate Nickel Defects and Charge States

The neutral nickel vacancy charge state has the potential to be NV^-like in that it has a spin-1 ground state, so spin control should be favorable [171]. Furthermore, there may be two potential ways to excite it; either a) through the first acceptor state at roughly 1000 nm or b) at the 716 nm ZPL transition [171]. One challenge however, is that the true ZPL energy is higher than the ionization

threshold, so in theory it should be very challenging to excite NiV^0 without ionizing it to NiV^-. That being said, it may be possible using carefully boron doped diamond. In general, using neutral defects in diamond has been challenging, as seen with the neutral SiV, and generally requires much work on exactly how much boron doping is necessary. Hence, diamond growth techniques which utilize high precision in situ doping control are highly valuable to identify which doping conditions support neutral defects. This could be achieved for example by adjusting the rate of impurity gas introduced as growth occurs [181, 182], thereby creating a sample with a gradient doped profile. It was also found that substitutional nickel might be interesting to study as it might form a decoherence free subspace [183]. Like the NiV, it is also quite stable and potentially able to form based on formation energy calculations. The challenges associated with it, however, include the high energy UV excitation required, which might also excite a bunch of other defects and thus could degrade coherence.

1.6 Summary

To conclude, this chapter has reviewed the motivation and interest behind solid state defects for use in quantum networks. The chapter began by discussing the second quantum revolution, highlighting certain advantages quantum information processing possesses over classical information processing, especially with regard to computing, sensing, and networking. Then, quantum networking was highlighted as a platform for secure communication, distributed sensing, and modular quantum computing. The requirements for a useful quantum node were identified, including an efficient light-matter interface, which can interact with low-loss telecom band photons, generate indistinguishable single photons on demand, remain coherent for long periods of time and be integrated scalably into a device. The leading physical platforms were then compared against these metrics, with no clear winner yet identified. Solid state defects housed within wide-band gap semiconductors were then discussed and ideal host material properties were reviewed. Diamond was identified as a particularly promising host material due to its wide band gap, low nuclear-spin background, nanofabrication compatibility, and ability to host deep, optically active defects. Diamond color centers, in particular, the nitrogen vacancy, and group-IV vacancy centers were reviewed, providing context as to why novel defect centers are being pursued before finally touching on the topic of this thesis: the nickel vacancy center in diamond. The history of the NiV was then discussed along with its potential advantages as a qubit, providing a picture for what the rest of the thesis hopes to confirm: namely, that the NiV can address some of the remaining challenges other defects face in realizing a practical quantum network.

Chapter 2

Light Matter Interactions

This chapter presents the necessary theoretical background for understanding the experiments performed in this thesis. In particular, this chapter introduces the light-matter interaction model used to describe coupling between the levels in two- and three-level systems and radiation. This model has been successful at describing the behavior of interactions in which lasers are coupled to electronic transitions in defect systems. Then, decoherence processes are Furthermore, decoherence processes are introduced using a master equation approach. More complex phenomena can then be described with this approach such as the spectrum observed under resonant excitation of a two level system, saturation power, transition linewidths, and linewidth broadening mechanisms. Then, autocorrelation functions, used to describe single photon sources are covered. Next, three-level systems are described, with phenomena including coherent population trapping, optical spin pumping, and Raman based transitions reviewed. These are particularly important for the description of coherent optical control over our qubit system. Lastly, Hahn-Echo sequences and dynamical decoupling techniques such as Carr-Purcell-Meiboom-Gill sequences are reviewed. These can be used to extend the coherence time of spin qubits coupled to slowly varying noise sources and as such are very important.

2.1 Two-Level System

To start, consider a two-level system consisting of a lower-energy state $|1\rangle$ and a higher-energy state $|2\rangle$, separated by an energy $\hbar\omega_0$. If the energy of $|1\rangle$ is referenced to zero, the Hamiltonian of the undriven system, or bare Hamiltonian, can be written as

$$H_0 = \hbar \begin{pmatrix} 0 & 0 \\ 0 & \omega_0 \end{pmatrix}, \tag{2.1}$$

where the basis $\{|1\rangle, |2\rangle\}$ has been used.

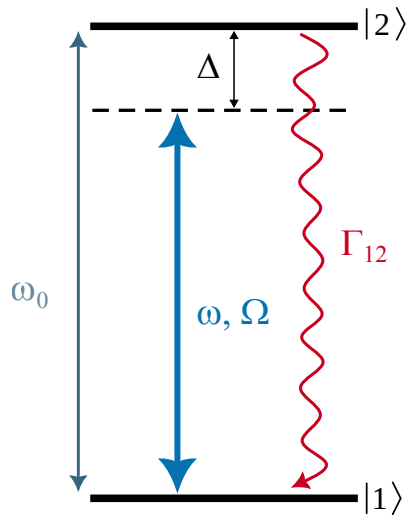

Figure 2.1 Diagram of two level quantum system with energy separation $\hbar\omega_0$ and resonant beam detuned.

2.1.1 Dipole Approximation

For atom-like defects in solid state hosts, the eigenstates of the bare Hamiltonian are electronic wavefunctions, that is, spatial distributions of charge. Hence, an applied electric field can couple to this charge distribution, causing it to move, and as such can cause transitions between different eigenstates. In particular, if a classical electric field of the form $\mathbf{E}(t) = \mathbf{E}_0 \cos(\omega t)$ is added, the field can interact with the system via its electric dipole moment, with the interaction Hamiltonian written as

$$H_I = -\mathbf{d} \cdot \mathbf{E}(t), \tag{2.2}$$

where $\mathbf{d} = q \sum_i \mathbf{r}_i$ is the electric dipole operator. For a general charge distribution interacting with a general electromagnetic field, this interaction can be expanded into the dipole, quadrupole, and even higher-order terms. However, in our case, we neglect the higher order terms and only use the dipole term because of the electric dipole approximation. This approximation assumes that the field is uniform across the defect, so that the dipole term dominates. This arises from the fact that the higher order terms depend on the spatial variation of the field over the charge distribution. However, if the wavelength of the field is far larger than the spatial charge distribution, it can safely be assumed that it is uniform. For defects in diamond, this is well justified because the defect is only a few lattice spacings (a=3.567 Å) on the order of angstroms whereas the optical wavelengths used are hundreds of nanometers [184].

2.1.2 Rabi Oscillations

With the electric field interaction in hand, the full Hamiltonian can be written as

$$H(t) = H_0 + H_I(t). \tag{2.3}$$

To write this in matrix form, we must evaluate the matrix elements of the Hamiltonian:

$$H_I^{ij} = \langle i| H_I |j\rangle = -\langle i| \mathbf{d} \cdot \mathbf{E}_0 |j\rangle \cos(\omega t), \qquad i, j \in \{1, 2\}. \tag{2.4}$$

From here, it is convenient to define the Rabi frequency as [184]

$$\Omega_{ij} = -\frac{1}{\hbar} \langle i| \mathbf{d} \cdot \mathbf{E}_0 |j\rangle , \tag{2.5}$$

which determines the strength of the coupling between the optical field and the transition dipole moment. From the definition, it is clear that Ω_{ij} increases when either the transition dipole or the driving field increases.

Importantly, for atomic or defect systems featuring symmetric electric potentials, parity is said to be conserved. This is because, owing to the fact that the potential is symmetric, an electron at **r** will experience the same potential when it is at **-r** as well. Hence, the electronic wavefunctions will be the same at those two points up to a difference in the phase. This means that the parity of the wavefunction is well-defined (see section 2.5 for more discussion of this) and we can use it to determine which matrix elements are zero by symmetry arguments. In particular, for parity conserving transitions, states will not couple to themselves because that results in an odd function integrated over infinity [184]. This is because the position operator **r** is odd under parity and the product of the same parity will always be even, thus resulting in an odd function overall. Therefore, only the coupling between different states needs to be retained, in this case, $|1\rangle$ and $|2\rangle$. Also, for simplicity, Ω is taken to be real. With this, the full Hamiltonian can be written as

$$H = \hbar \begin{pmatrix} 0 & \Omega \cos(\omega t) \\ \Omega \cos(\omega t) & \omega_0 \end{pmatrix}. \tag{2.6}$$

To simplify this even further, we move into the rotating frame, which rotates at the frequency of the applied field. This removes the fast time oscillation ω of the driving field and can be achieved with the unitary transformation

$$U(t) = \begin{pmatrix} 1 & 0 \\ 0 & e^{i\omega t} \end{pmatrix}, \tag{2.7}$$

under which the Hamiltonian becomes

$$H_{\text{rot}} = U^{\dagger} H U - i\hbar U^{\dagger} \dot{U}. \tag{2.8}$$

Evaluating this expression gives

$$H_{\text{rot}} = \hbar \begin{pmatrix} 0 & \Omega \cos(\omega t) e^{i\omega t} \\ \Omega \cos(\omega t) e^{-i\omega t} & \omega_0 - \omega \end{pmatrix}. \tag{2.9}$$

At this point, a detuning can be defined

$$\Delta = \omega_0 - \omega, \tag{2.10}$$

which measures how far the drive frequency is from resonance. Then, using Euler's formula, $\cos(\omega t) = \frac{1}{2}\left(e^{i\omega t} + e^{-i\omega t}\right)$, the rotating-frame Hamiltonian becomes

$$H_{\text{rot}} = \hbar \begin{pmatrix} 0 & \frac{\Omega}{2}\left(1 + e^{i2\omega t}\right) \\ \frac{\Omega}{2}\left(1 + e^{-i2\omega t}\right) & \Delta \end{pmatrix}. \tag{2.11}$$

From here, the rotating-wave approximation (RWA) can be applied, in which the rapidly oscillating terms $e^{\pm i2\omega t}$ are neglected. These oscillations occur on a much faster time scale compared to how the state amplitudes c_1 and c_2 evolve, so their net effect is to average to zero. This leaves a Hamiltonian which is much easier to solve while still retaining the relevant physics

$$H_{\text{RWA}} = \hbar \begin{pmatrix} 0 & \Omega/2 \\ \Omega/2 & \Delta \end{pmatrix}. \tag{2.12}$$

Having reduced the Hamiltonian to such an extent, we can now look to observe how the state evolves in time. To do this, we can write the general state of the two-level system as a linear combination of the original stationary states of the undriven system $|\psi(t)\rangle = c_1(t)\,|1\rangle + c_2(t)\,|2\rangle$, where $|c_1(t)|^2$ and $|c_2(t)|^2$ are the probabilities of finding the system in $|1\rangle$ and $|2\rangle$, respectively. The time evolution of this state is determined by the time-dependent Schrödinger equation [184],

$$i\hbar \frac{d}{dt} |\psi(t)\rangle = H\,|\psi(t)\rangle\,. \tag{2.13}$$

Substituting H_{RWA} and the state vector into this equation gives

$$i\hbar \frac{d}{dt} \begin{pmatrix} c_1 \\ c_2 \end{pmatrix} = \hbar \begin{pmatrix} 0 & \Omega/2 \\ \Omega/2 & \Delta \end{pmatrix} \begin{pmatrix} c_1 \\ c_2 \end{pmatrix}, \tag{2.14}$$

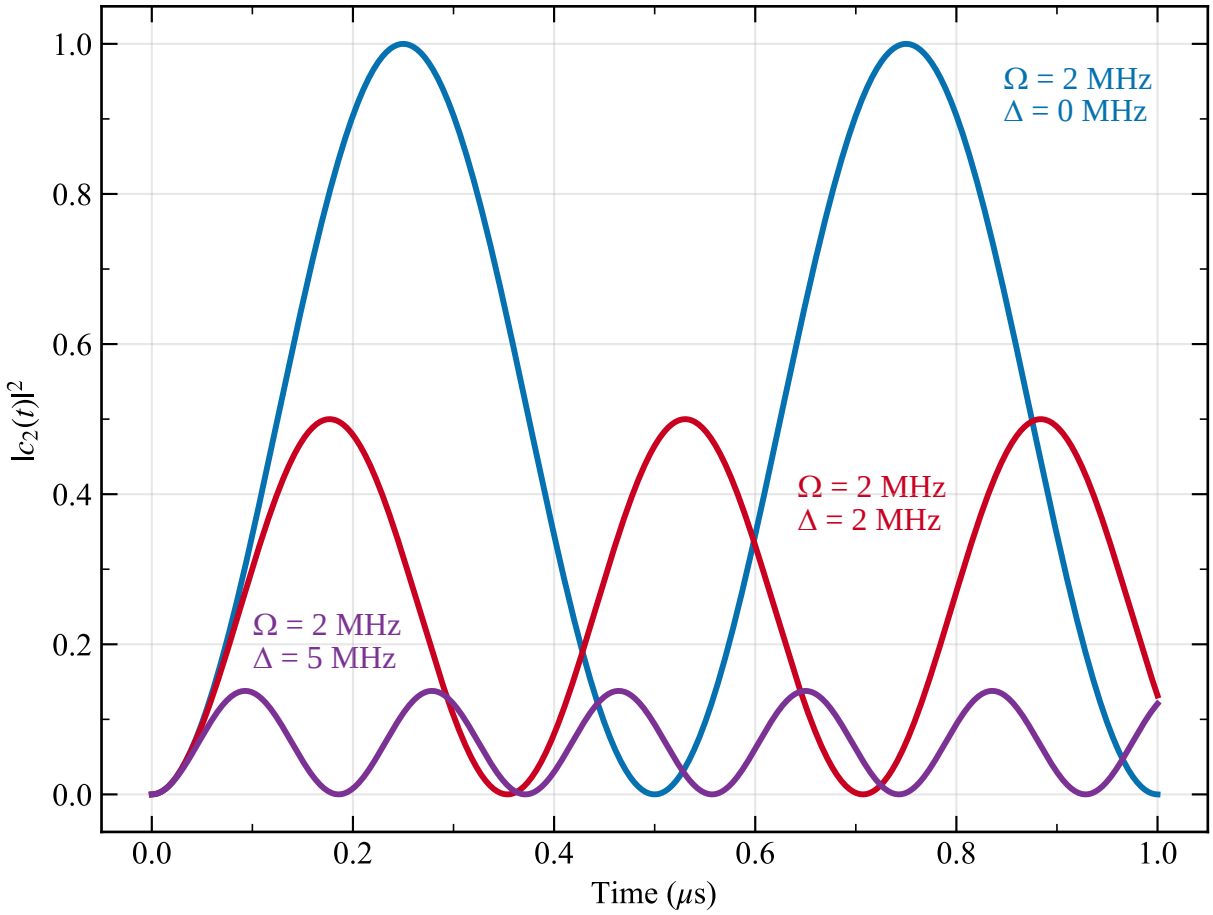

Figure 2.2 $|c_2(t)|^2$ at a Rabi frequency $\Omega = 2$MHz with different detunings labeled, clearly displaying higher frequency as detuning increases but lower population transfer.

where, after canceling $\hbar$ and multiplying through, we find

$$i\dot{c}_1 = \frac{\Omega}{2}c_2, \tag{2.15}$$

$$i\dot{c}_2 = \frac{\Omega}{2}c_1 + \Delta c_2. \tag{2.16}$$

This is a pair of coupled differential equations for the amplitudes $c_1(t)$ and $c_2(t)$. They can be solved by differentiating a second time and then substituting c_2, so that an equation only in terms of c_1 is left. Then, choosing the initial conditions $c_1(0) = 1$ and $c_2(0) = 0$, we can solve and find the population probability as a function of time.

$$|c_1(t)|^2 = 1 - \frac{\Omega^2}{\Omega_R^2}\sin^2\left(\frac{\Omega_R t}{2}\right), \tag{2.17}$$

$$|c_2(t)|^2 = \frac{\Omega^2}{\Omega_R^2}\sin^2\left(\frac{\Omega_R t}{2}\right), \tag{2.18}$$

where

$$\Omega_R = \sqrt{\Omega^2 + \Delta^2} \tag{2.19}$$

is the generalized Rabi frequency [184]. From these solutions, we see that the populations oscillate between the two states and these are known as Rabi oscillations. If the applied field is detuned, the population transfer is reduced but the Rabi frequency increases as can be seen in Figure 2.2. Rabi oscillations are a key signature of coherent control of a two level system.

These dynamics also define the standard pulse operations used in coherent control experiments. In particular, when $\Delta = 0$, a resonant pulse of duration t_π satisfying

$$\Omega t_\pi = \pi \tag{2.20}$$

is called a π pulse and transfers the system entirely from $|1\rangle$ to $|2\rangle$. Similarly, a pulse of duration $t_{\pi/2}$ satisfying

$$\Omega t_{\pi/2} = \frac{\pi}{2} \tag{2.21}$$

creates an equal superposition of the two states. This will be described further in the section on Ramsey and Hahn-Echo measurements.

2.1.3 AC Stark Shift

In addition to driving population transfer between the two states, the oscillating field also shifts the energies of the states. This is known as the AC Stark shift and it is called this because it is derived from an oscillating electric field [184]. There is also the DC Stark shift, which is derived from a static electric field. We can determine the amount the states shift by solving for the eigenenergies of the RWA Hamiltonian

$$H_{\mathrm{RWA}} = \hbar \begin{pmatrix} 0 & \Omega/2 \\ \Omega/2 & \Delta \end{pmatrix}, \qquad \det(H_{\mathrm{RWA}} - \lambda \mathrm{I}) = 0. \tag{2.22}$$

The resulting eigenenergies of these new states are

$$E_\pm = \frac{\hbar}{2}\left(\Delta \pm \sqrt{\Delta^2 + \Omega^2}\right) = \frac{\hbar}{2}\left(\Delta \pm \Omega_R\right). \tag{2.23}$$

Additionally, the eigenstates are also no longer pure stationary states but instead mixtures of them and are generally called dressed states, meaning states of the combined system plus driving field [184, 185].

2.1.4 Coupling to the Environment

Thus far, we have only described pure quantum states, which can evolve in a perfectly isolated way. In this case, all the dynamics are unitary and reversible, and we can use the Schrödinger equation to determine evolution. In a real-world system, however, the quantum state is not perfectly isolated. Indeed, a quantum state can interact with a number of different degrees of freedom which can affect its state in the form of irreversible processes such as spontaneous emission or energy dissipation, and dephasing. To describe such irreversible dynamics, it is useful to introduce the density operator,

$$\rho = \sum_i P_i \left|\psi_i\right\rangle \left\langle\psi_i\right|, \tag{2.24}$$

in which P_i is the probability of being in the pure state $|\psi_i\rangle$. For the pure state above, this takes the form

$$\rho = \begin{pmatrix} |c_1|^2 & c_1 c_2^* \\ c_2 c_1^* & |c_2|^2 \end{pmatrix}. \tag{2.25}$$

The diagonal elements of ρ represent the populations of the two basis states, while the off-diagonal elements represent coherences, that is, the phase relationship between the two states. The density matrix formalism is more general than the state-vector description because it can also describe mixed states, in which the system is not in a single pure state but is instead represented by a statistical ensemble of possibilities. In principle, the total state of the system plus environment, usually referred to as the bath, evolves unitarily under a Hamiltonian

$$H_{\text{tot}} = H_S + H_B + H_I, \tag{2.26}$$

where H_S describes the system of interest, H_B describes the environment or bath, and H_I describes the interaction between them. In practice, however, the bath contains an enormous number of degrees of freedom and is not practical to model explicitly. Because information can be lost from the system into the environment, the resulting system dynamics are generally no longer purely unitary. This can still be modeled though as long as the coupling to the bath is both weak and the bath only depends on its current configuration. This is also known as a Markovian approximation. Then, the system can be described with the Gorini-Kossakowski-Sudarshan-Lindblad master equation [186, 187],

$$\frac{d\rho}{dt} = -\frac{i}{\hbar}[H, \rho] + \sum_i \left(L_i \rho L_i^\dagger - \frac{1}{2} \left\{ L_i^\dagger L_i, \rho \right\} \right). \tag{2.27}$$

The first term,$-\frac{i}{\hbar}[H, \rho]$ is the density-matrix version of the Schrödinger equation and describes the coherent, unitary part of the motion. The second term accounts for non-unitary processes arising

from coupling to the environment. For convenience, we define the Lindblad dissipator as

$$\mathcal{D}[L]\rho = L\rho L^\dagger - \frac{1}{2}\left\{L^\dagger L, \rho\right\}. \tag{2.28}$$

This allows us to write the master equation as

$$\dot{\rho} = -\frac{i}{\hbar}[H, \rho] + \sum_i \mathcal{D}[L_i]\rho. \tag{2.29}$$

The operators $\{L_i\}$, are called collapse or jump operators and they represent specific dissipative channels such as spontaneous emission or dephasing. We now describe these channels.

2.1.4.1 Dissipation

The first irreversible process to cover is energy dissipation, which manifests as population transferring between levels as energy is exchanged with the bath. In general, if population decays from a state $|j\rangle$ into a state $|i\rangle$ at a rate Γ_{ij}, the corresponding collapse operator is

$$L_{ij} = \sqrt{\Gamma_{ij}}\ |i\rangle\langle j|. \tag{2.30}$$

For a two-level system, there can generally be transfer between upper and lower states via spontaneous emission or absorption of resonant energy (phonons, photons etc.). If we consider an example in which the sample has been cooled to a low enough temperature so that there is only decay in one direction from the upper level $|2\rangle$ down to the lower level $|1\rangle$, then the collapse operator is $L_{12} = \sqrt{\Gamma_{12}}\ |1\rangle\langle 2|$. If we plug this into the Lindblad dissipator, we find

$$D[L_{12}] = \Gamma_{12}\begin{pmatrix} \rho_{22} & -\rho_{12}/2 \\ -\rho_{21}/2 & -\rho_{22}. \end{pmatrix} \tag{2.31}$$

This makes sense because the ground state will then gain population from the excited state at a rate Γ_{12} and the excited state will lose it at that rate. An important timescale then is how long it takes for these levels to go from being in a well-defined level to (polarized state) to a thermal equilibrium of both. This is known as the T_1 time, which is also often referred to as the longitudinal relaxation or energy-relaxation time [184] and it is equal to the inverse of the decay rate, $T_1 = 1/\Gamma_{12}$. Interestingly, the coherence or relative phase between the two states also decays as seen by the non-zero off-diagonal terms. As such, population transfer can limit coherence times at a rate $\Gamma_{12}/2$. We will discuss coherence times more in the next section.

2.1.4.2 Decoherence

The next important process is decoherence. This involves the decay of the relative coherence or phase between the two states. In particular, even without population transfer between $|1\rangle$ and $|2\rangle$, the relative phase between the two states can become randomized as a result of environmental fluctuations. This process is often referred to as pure dephasing and it leaves the diagonal elements ρ_{11} and ρ_{22} unchanged while modifying ρ_{12} and ρ_{21} [184]. A convenient way to represent this process within the Lindblad formalism is through collapse operators with respect to the individual eigenstates themselves,

$$L_{\phi,1} = \sqrt{\Gamma_\phi}\,|1\rangle\langle 1|\,, \qquad L_{\phi,2} = \sqrt{\Gamma_\phi}\,|2\rangle\langle 2|\,. \tag{2.32}$$

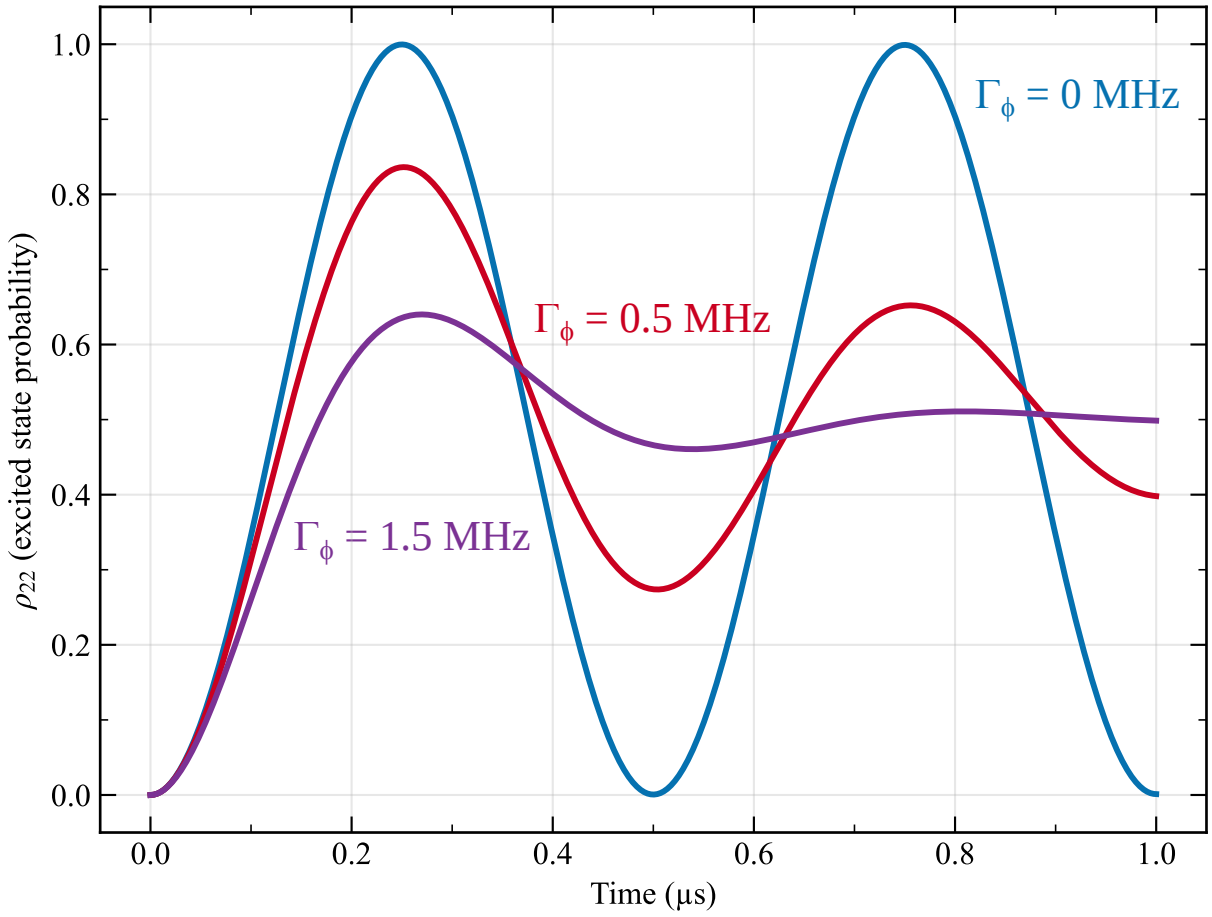

Figure 2.3 Excited state probabilities having solved the Lindbladian master equation. Each of the graphs used a different Γ_ϕ value. Γ_{12} was fixed at 0.5 kHz which corresponds to a $T_1 = 2$ms which is realistic for certain diamond color centers depending on the temperature. $\Omega = 2$MHz was also fixed along with $\Delta = 0$ MHz. The simulation was performed by numerically solving the Lindblad master equation using a Python ODE solver with the Runge-Kutta integration technique. The normalization condition of $\rho_{11} + \rho_{22} = 1$ was also employed.

Similar to the population transfer, we can identify what the Lindblad dissipator looks like for one of these collapse operators to determine how it affects the state of the system. In particular, we find for $L_{\phi,1}$

$$D[L_{\phi,1}] = \Gamma_\phi \begin{pmatrix} 0 & -\rho_{12}/2 \\ -\rho_{21}/2 & 0 \end{pmatrix}. \tag{2.33}$$

From this, it is clear that these operators do not transfer population between $|1\rangle$ and $|2\rangle$. This is because if we plug the resulting matrix entries into the rate of change of ρ, and solve the differential equation, we find that for the Lindblad dissipator

$$\rho_{12}(t) = \rho_{12}(0)e^{-\Gamma_\phi t/2}, \qquad \rho_{21}(t) = \rho_{21}(0)e^{-\Gamma_\phi t/2}. \tag{2.34}$$

From this, it is clear that the decay of coherence of the system is governed by two distinct mechanisms. The first is energy relaxation in which population transfer at a rate $\Gamma_{12} = 1/T_1$ causes decoherence at a rate $\Gamma_{12}/2$. The second mechanism is pure dephasing, which contributes an additional rate Γ_ϕ, multiplied by two here because we have dephasing on both states [139]. The total decoherence rate is therefore

$$\Gamma_2 = \frac{1}{T_2} = \frac{\Gamma_{12}}{2} + \Gamma_\phi, \tag{2.35}$$

or equivalently,

$$\frac{1}{T_2} = \frac{1}{2T_1} + \frac{1}{T_\phi}, \tag{2.36}$$

where

$$T_\phi = \Gamma_\phi^{-1}. \tag{2.37}$$

Here, T_2 refers to the homogeneous coherence time, while T_ϕ is the pure-dephasing time. There is another quantity, which we will see later on called T_2^*, which is the inhomogeneous coherence time. It is called this because it refers to a spin system experiencing an inhomogeneous magnetic field . It was born out of the nuclear magnetic resonance community, which focused on ensemble measurements of spin systems and as such would frequently experience field inhomogeneities across the ensemble. Consequently, T_2^* is generally shorter than T_2. T_2^* sets the timescale over which the off-diagonal elements of the density matrix remain appreciable, and thus the timescale over which a well-defined phase relationship between $|1\rangle$ and $|2\rangle$ is preserved.

2.1.5 Resonance Fluorescence of a Two-Level System

With the Lindblad formalism, we can now describe some commonly observed experimental phenomena with atomic-like defects. To start, we will consider the fluorescence spectrum of a

two-level system under resonant excitation. Similar to above, we will consider only spontaneous decay from $|2\rangle$ to $|1\rangle$ at a rate Γ_{12}. This is reasonable as many measurements are carried out at sufficiently low temperatures for which thermal excitation from $|1\rangle$ to $|2\rangle$ is negligible. In addition, we include a pure dephasing term at a rate Γ_ϕ. The corresponding collapse operators can then be written like so

$$L_{12} = \sqrt{\Gamma_{12}}\,|1\rangle\langle 2|\,, \qquad L_\phi = \sqrt{\frac{\Gamma_\phi}{2}}\,(|1\rangle\langle 1| - |2\rangle\langle 2|)\,, \tag{2.38}$$

where the factor of $1/2$ is chosen so that the off-diagonal density-matrix elements decay at a rate Γ_ϕ. We start by evaluating the unitary evolution term

$$-\frac{i}{\hbar}[H_{\mathrm{RWA}}, \rho] = \begin{pmatrix} \frac{i\Omega}{2}\rho_{21} - \frac{i\Omega}{2}\rho_{12} & \frac{i\Omega}{2}(\rho_{11} - \rho_{22}) + i\Delta\rho_{12} \\ \frac{i\Omega}{2}(\rho_{22} - \rho_{11}) - i\Delta\rho_{21} & \frac{i\Omega}{2}\rho_{12} - \frac{i\Omega}{2}\rho_{21} \end{pmatrix}, \tag{2.39}$$

Then, we evaluate the Lindblad dissipators for both collapse operators, finding

$$\mathcal{D}[L_{12}]\rho = \begin{pmatrix} \Gamma_{12}\rho_{22} & -\frac{\Gamma_{12}}{2}\rho_{12} \\ -\frac{\Gamma_{12}}{2}\rho_{21} & -\Gamma_{12}\rho_{22} \end{pmatrix}, \tag{2.40}$$

and

$$\mathcal{D}[L_\phi]\rho = \begin{pmatrix} 0 & -\Gamma_\phi\rho_{12} \\ -\Gamma_\phi\rho_{21} & 0 \end{pmatrix}. \tag{2.41}$$

Combining these results, the master equation becomes

$$\dot{\rho} = \begin{pmatrix} \Gamma_{12}\rho_{22} + \frac{i\Omega}{2}\rho_{21} - \frac{i\Omega}{2}\rho_{12} & \frac{i\Omega}{2}(\rho_{11} - \rho_{22}) + \left(i\Delta - \frac{\Gamma_{12}}{2} - \Gamma_\phi\right)\rho_{12} \\ \frac{i\Omega}{2}(\rho_{22} - \rho_{11}) + \left(-i\Delta - \frac{\Gamma_{12}}{2} - \Gamma_\phi\right)\rho_{21} & -\Gamma_{12}\rho_{22} + \frac{i\Omega}{2}\rho_{12} - \frac{i\Omega}{2}\rho_{21} \end{pmatrix}. \tag{2.42}$$

Equivalently, the individual matrix elements satisfy

$$\dot{\rho}_{11} = \Gamma_{12}\rho_{22} + \frac{i\Omega}{2}\rho_{21} - \frac{i\Omega}{2}\rho_{12}, \tag{2.43}$$

$$\dot{\rho}_{22} = -\Gamma_{12}\rho_{22} - \frac{i\Omega}{2}\rho_{21} + \frac{i\Omega}{2}\rho_{12}, \tag{2.44}$$

$$\dot{\rho}_{12} = \frac{i\Omega}{2}(\rho_{11} - \rho_{22}) + \left(i\Delta - \frac{\Gamma_{12}}{2} - \Gamma_\phi\right)\rho_{12}, \tag{2.45}$$

$$\dot{\rho}_{21} = \frac{i\Omega}{2}(\rho_{22} - \rho_{11}) + \left(-i\Delta - \frac{\Gamma_{12}}{2} - \Gamma_\phi\right)\rho_{21}. \tag{2.46}$$

These are the well-known optical Bloch equations [184] and they describe the full dynamics of a two-level system with spontaneous decay and dephasing. In this case, we are interested in the

steady-state response under continuous excitation and so we set the time derivative equal to zero. An analytic solution for the upper state population can be found and it is

$$\rho_{22}^{(\mathrm{ss})}(\Delta) = \frac{\frac{\Omega^2}{4}\Gamma_2}{\Gamma_{12}\left(\Delta^2 + \Gamma_2^2\right) + \frac{\Omega^2}{2}\Gamma_2}, \tag{2.47}$$

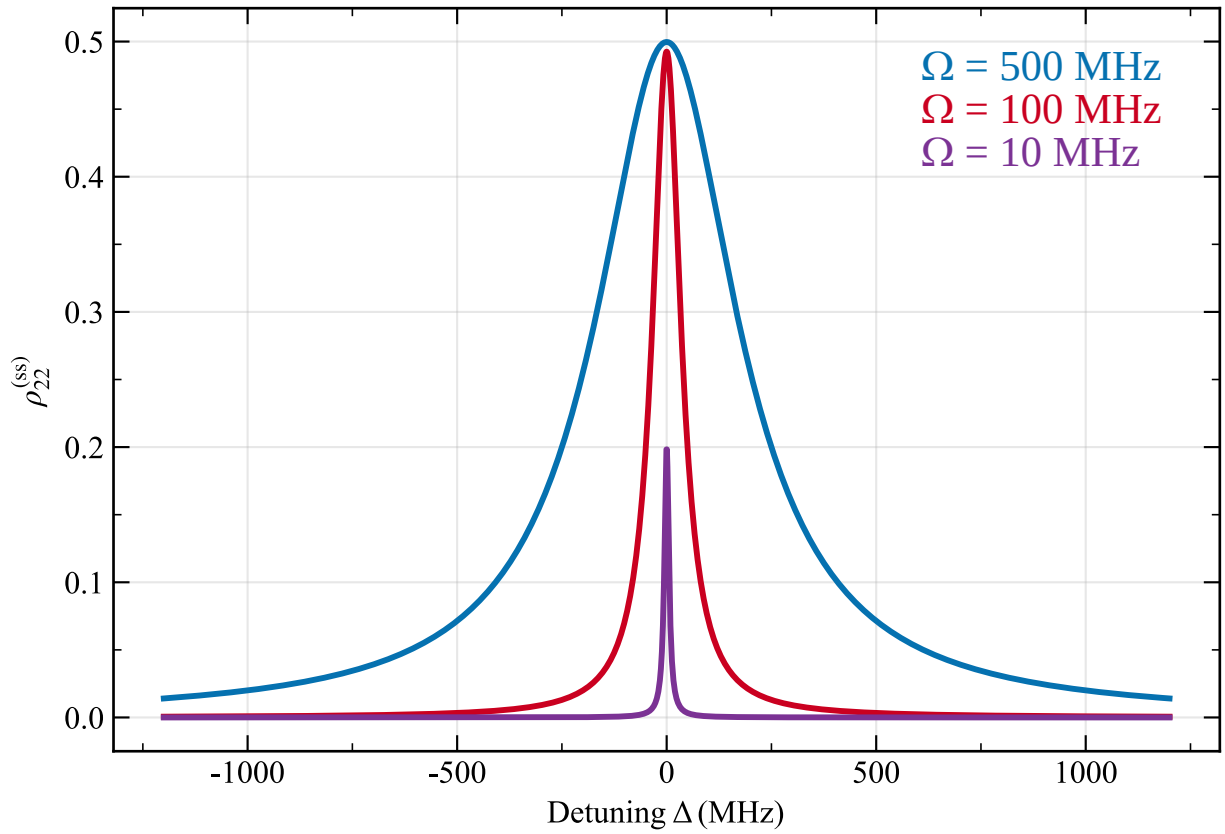

Figure 2.4 Steady state population of the upper level under resonant excitation as the detuning is changed. Three different graphs each with a different Rabi frequency are shown.

This is useful because we can use this to compare to experimental data. In particular, whenever the system is excited to the upper state and decays back down, energy is emitted. This can be radiative in the form of photons or non-radiative via e.g. phonons. Importantly, though, this means the fluorescence response of the system is proportional to the excited-state population. As such, the derived expression can be used to model what happens experimentally in the case of a laser being slowly scanned over a transition frequency. As it is scanned, the detuning changes and as long as the measurement is long enough so that a steady state is reached, the excited state profile can be observed. The shape of this function is that of a Lorentzian with the center at zero detuning. If we define the saturation parameter as $s = \Omega^2/(2\Gamma_{12}\Gamma_2)$, the full width half maximum is $2\Gamma_2\sqrt{1+s}$.

With this, we can see that driving the system with a larger Rabi frequency will cause the transition to broaden (see Figure 2.4). Physically, this arises because stronger driving increases the range of detunings over which the transition responds, and so the resonance therefore becomes wider. On the other hand, at zero power, the full width half maximum is limited by $\Gamma_2 = \frac{\Gamma_{12}}{2} + \Gamma_\phi$. The spontaneous decay rate is the excited state lifetime which although it can be modified by nanophotonic structures is largely constant. On the other hand, the pure dephasing term can also broaden the linewidth. Such dephasing can arise because the upper state couples to the environment differently than the lower state. Then, fluctuations in the local nevironment, including phonons, strain, and electric field noise, can then cause the transition energy to shift in time resulting in dephasing. In the limit $\Gamma_\phi \ll \Gamma_{12}/2$, the linewidth is determined primarily by the excited-state lifetime and this is what is meant by a lifetime-limited linewidth.

On resonance, when $\Delta = 0$, Eq. (2.47) reduces to

$$\rho_{22}^{(\mathrm{ss})}(0) = \frac{1}{2}\frac{s}{1+s}. \tag{2.48}$$

A graph of $\rho_{22}^{(ss)}$ as a function of s is shown in Figure X and we can see that when s is small, the excited state population increases linearly with s. Whereas, when s is large, the population saturates at 0.5. This is an important result: quantized two level systems cannot emit arbitrarily strong amounts of fluorescence. Moreover, because the detected fluorescence is proportional to $\rho_{22}^{(\mathrm{ss})}(0)$, the measured count rate as a function of optical power P can be fit to

$$I(P) = I_\infty \frac{P}{P + P_{\mathrm{sat}}}, \tag{2.49}$$

where I_∞ is the asymptotic count rate and P_{sat} is the saturation power. This follows from Eq. (2.48) together with the proportionality $\Omega^2 \propto P$, such that $s = P/P_{\mathrm{sat}}$. Hence, over a limited power range, the linewidth can therefore appear approximately linear in power. Experimentally, one often measures the linewidth at several excitation powers and extrapolates to $P \to 0$ to estimate the intrinsic homogeneous linewidth $\Delta\nu_0$, while the corresponding fluorescence counts are fit to Eq. (2.49) to determine the saturation power.

When interpreting such measurements, it is important to distinguish between homogeneous and inhomogeneous contributions to the observed optical linewidth. Homogeneous broadening arises from processes that act on the timescale of the optical coherence itself, including radiative decay, phonon-induced pure dephasing, and rapid spectral diffusion. These mechanisms enter through Γ_2 and produce a Lorentzian lineshape. Power broadening is likewise a homogeneous effect, since it originates from strong coherent driving of the same optical transition. Inhomogeneous broadening, by contrast, arises from static or slowly varying variations in the local environment.

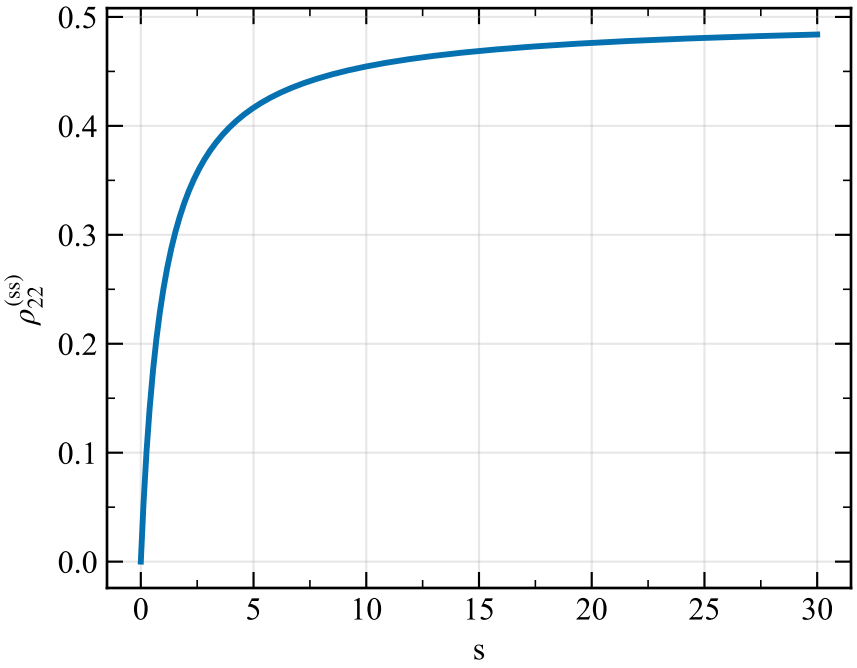

Figure 2.5 Steady state population of the upper level under resonant excitation as a function of the saturation parameter s.

In an ensemble, different emitters may experience slightly different strain fields, electric fields, or charge environments, leading to a distribution of transition frequencies. Even for a single emitter, sufficiently slow spectral diffusion can produce a similar effect when the signal is averaged over long measurement times. In this case, the measured linewidth no longer directly reflects the intrinsic coherence time T_2, but also the influence of environmental fluctuations. These shifts in frequency also show up typically as a Gaussian distribution and hence when fitting spectral data, if it fits better to a Gaussian profile, it is more likely inhomogeneous broadening. This is in contrast the Lorentzian profile indicative of homogeneous broadening.

2.2 Three-Level System

Having introduced the two-level system along with coupling to the environment, we now turn to the three-level system. Such systems are ubiquitous in atomic and solid-state physics and are especially important because they can enable all-optical control of qubits, critical for spin photon interfaces and quantum networking applications. In particular, we focus on the case of two ground states that are each optically coupled to a common excited state, forming a so-called Λ configuration [185].

This level structure supports a range of important and interesting phenomena, including optical pumping, coherent population trapping, and Raman transitions.

Using the notation introduced earlier, we consider two ground states, $|1\rangle$ and $|2\rangle$, coupled to a common excited state $|A\rangle$. One optical field drives the $|1\rangle \leftrightarrow |A\rangle$ transition with a Rabi frequency Ω_1, and a second optical field drives the $|2\rangle \leftrightarrow |A\rangle$ transition with Rabi frequency Ω_2. The single-photon detuning is denoted by Δ and it measures how far off of the excited state both drive frequncies are, while the two-photon detuning δ measures the detuning from the exact two-photon resonance between the two ground states. A diagram can be seen in Figure 2.6.

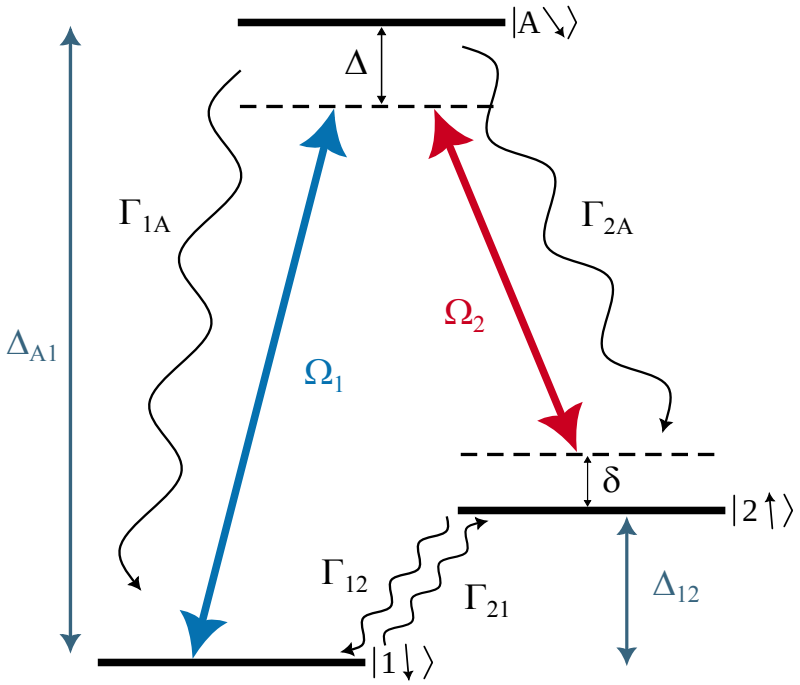

Figure 2.6 Diagram for a three-level Λ system with both optical drives displayed as straight arrows and decay mechanisms shown as squiggly arrows.

As in the two-level case, it is convenient to move into a rotating frame in order to remove the rapid optical time dependence. Using the unitary transformation

$$U = \begin{pmatrix} 1 & 0 & 0 \\ 0 & e^{-i(\delta+\Delta_{12})t} & 0 \\ 0 & 0 & e^{-i(\Delta_{A1}-\Delta)t} \end{pmatrix}, \tag{2.50}$$

where Δ_{A1} is the energy splitting between $|1\rangle$ and $|A\rangle$, and Δ_{12} is the splitting between the two

ground states, the Hamiltonian in the rotating frame under the rotating-wave approximation becomes

$$H = \begin{pmatrix} 0 & 0 & \Omega_1/2 \\ 0 & -\delta & \Omega_2/2 \\ \Omega_1/2 & \Omega_2/2 & \Delta \end{pmatrix}, \tag{2.51}$$

written in the basis $(|1\rangle, |2\rangle, |A\rangle)$. Different sign conventions or basis orderings are sometimes used in the literature, but the physical structure is the same: both ground states are coupled to a common excited state.

2.2.1 Optical Pumping

The first property we will discuss is that of optical pumping. Because the two ground states are coupled via a common excited state, when one of the drives is resonant with a transition, population in that state will be excited and there will be a non-zero chance for it to decay into the other state. Hence, population is pumped from one state to the other. This is a very important property as it enables initialization and readout of qubit states. The efficiency with which the system is pumped is determined by the branching ratio $\eta = \frac{P_{\mathrm{A1}}}{P_{\mathrm{A2}}}$, where P_{A1} and P_{A2} are the transition dipole overlap for the $A1$ and $A2$ transitions respectively. This was briefly discussed in Chapter 1, but a small branching ratio means that optical pumping can occur relatively quickly because the probability of decaying into the other state upon excitation to the excited state is relatively high compared to decaying back into the original ground state. On the other hand, a large branching ratio makes optical pumping slower because even if the probability to decay into the other state is high, if the excitation probability is low, that also slows the process down. Lastly, it should be noted that the optical pumping process is an incoherent one because when the state is excited, all phase information is lost and a spin flip can be induced.

2.2.2 Coherent Population Trapping

Optical pumping involves the use of one field on a particular transition. We now consider when both fields are utilized. In particular, when both fields are exactly on resonance with their corresponding transitions, optical pumping goes in both directions, but a quantum interference effect also happens in which the two fields destructively interfere and a beat frequency equal to their difference is generated. This beat frequency is equal to the ground state splitting and can cause coherent oscillations between the ground state. This phenomenon is referred to as coherent population trapping and it occurs when the two-photon detuning vanishes, $\delta = 0$. To see this, we can substitute the rotating wave Hamiltonian into the time-dependent Schrodinger equation along with the general

state $|\psi(t)\rangle = c_0 |1\rangle + c_1 |2\rangle + c_2 |A\rangle$. Doing this we get

$$i\frac{d}{dt}|\psi(t)\rangle = H|\psi(t)\rangle,$$

$$\begin{pmatrix}\dot{c}_0\\ \dot{c}_1\\ \dot{c}_2\end{pmatrix} = \begin{pmatrix}0 & 0 & \Omega_1/2\\ 0 & -\delta & \Omega_2/2\\ \Omega_1/2 & \Omega_2/2 & \Delta\end{pmatrix}\begin{pmatrix}c_0\\ c_1\\ c_2\end{pmatrix}. \tag{2.52}$$

which leaves us with

$$\dot{c}_0 = \frac{\Omega_1}{2}c_2 \tag{2.53}$$

$$\dot{c}_1 = -\delta c_1 + \frac{\Omega_2}{2}c_2, \tag{2.54}$$

and lastly

$$\dot{c}_2 = \frac{\Omega_1}{2}c_0 + \frac{\Omega_2}{2}c_1 + \Delta c_2, \tag{2.55}$$

In the case of both two-photon and single-photon resonance in which both optical fields are resonant with their respective transitions $\delta = 0$, and $\Delta = 0$, the equations simplify. Similar to the two-level system, these equations can be solved by differentiating the last equation and then substituting the other two in to get an equation only in terms of c_2. Then, initial conditions can be used to constrain the solutions further. Moreover, it can be shown that a dark state can form which does not couple to the excited state

$$|D\rangle = \sin\theta |1\rangle - \cos\theta |2\rangle, \tag{2.56}$$

where $\cos\theta = \Omega_1/\Omega$ and $\sin\theta = \Omega_2/\Omega$ and $\Omega = \sqrt{\Omega_1^2 + \Omega_2^2}$. This is a coherent superposition state of the two ground states and is formed by optically pumping on resonance. It traps population in a coherent state, hence the name.

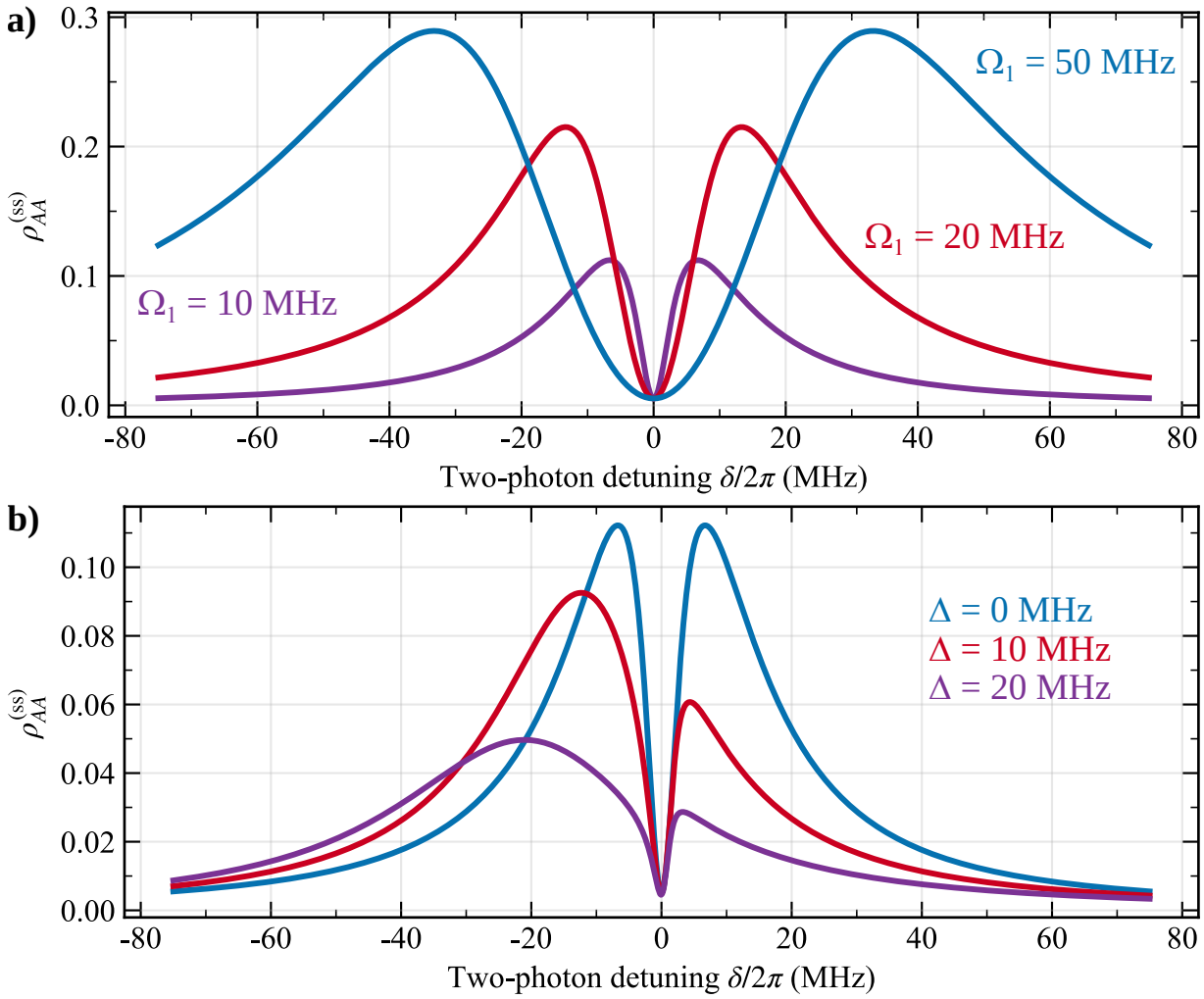

Figure 2.7 **a)** Shows a characteristic coherent population trapping simulation with two photon detuning swept over a range and the the Ω_1 varied across the three graphs. The other parameters were kept constant, namely: $\eta = 4$ $\Delta/2\pi = 0$MHz, $\Gamma_{1A}/2\pi = 15$MHz $\Gamma_\phi/2\pi = 0.1$MHz, and $\Gamma_{12,21}/2\pi = 0.5$kHz. **b)** Shows a similar graph except Ω_1 was now fixed at 10 MHz and the single photon detuning Δ was varied.

To describe dissipative and decoherence terms that may affect the coherent dark state, we use the same Lindblad master equation approach as we did for the two-level system. In this case, we include spontaneous emission from the excited state down to either ground state as well as depolarization terms between the ground states. Lastly, we include a ground state decoherence term. Thus, the

collapse operators can be written as

$$L_{1A} = \sqrt{\Gamma_{1A}}\ |1\rangle\langle A|\,, \tag{2.57}$$

$$L_{2A} = \sqrt{\Gamma_{2A}}\ |2\rangle\langle A|\,, \tag{2.58}$$

$$L_{12} = \sqrt{\Gamma_{12}}\ |1\rangle\langle 2|\,, \tag{2.59}$$

$$L_{21} = \sqrt{\Gamma_{21}}\ |2\rangle\langle 1|\,, \tag{2.60}$$

$$L_{\phi} = \sqrt{\Gamma_{\phi}/2}\,(|1\rangle\langle 1| - |2\rangle\langle 2|)\,. \tag{2.61}$$

With the collapse operators and Hamiltonian, we can numerically solve the Lindblad master equation. However, instead of calculating the transient response, for coherent population trapping, it is sufficient to simply compute the steady state solution by solving

$$\frac{d\rho}{dt} = 0. \tag{2.62}$$

In particular, the excited state population is what we're interested in as it determines the fluorescence emitted by the sample and so can be observed experimentally. By evaluating P_A as a function of the two-photon detuning δ, we can obtain the theoretical CPT spectrum. On exact two-photon resonance, destructive interference suppresses excitation into $|A\rangle$, producing a dip in $P_e(\delta)$ characteristic of the coherent population trapping dip. In Figure 2.7, we can see that increasing the Rabi frequency broadens the CPT dip and furthermore that shifting the single photon detuning causes the transition to shift around the dip.

2.2.3 Two-Photon Raman Transitions

CPT enables the creation of superposition states between the two ground states. Next, we discuss two-photon Raman transitions which will allow us to coherently transfer population between these two ground states. With CPT, the two laser fields are close to resonance ($\Delta \sim 0$) such that population will scatter off the excited state. This optical scattering; however, is undesirable because each scattering event introduces the possibility of decoherence or a spin flip between the two ground states. Thus, although CPT is a powerful method for preparing and probing coherent superpositions, it only provides a lower bound on the coherence time of the system. To mitigate optical scattering, the excitation fields can be detuned from the excited state such that $|\Delta| \gg |\Omega_1|,\ |\Omega_2|,\ \Gamma_{1A}$. In this far-detuned regime, population transfer between the two ground states no longer occurs via occupation of the excited state $|A\rangle$, but instead through a virtual intermediate state. This is the Raman transition regime. Within this regime, the excited state can be adiabatically eliminated [184, 188] and the original three-level problem reduces to an effective two-level system consisting of only

the two ground states.

Importantly; however, the excited state has not been eliminated completely. Because the detuning is finite, there remains a small probability for optical scattering and this can limit the coherence of the two level system. In particular, spontaneous decay contributes an additional decoherence channel, since each scattering event randomizes the phase of the ground-state superposition and can also induce spin flips by decaying into a state of the opposite spin. This scattering rate can be quantified as [188]

$$\Gamma_{\text{os}} = \frac{s\Gamma_{1A}^3}{32\Delta^2}\left(1+\frac{1}{\eta}\right)^2, \tag{2.63}$$

where s is the saturation parameter and η is the branching ratio. This residual scattering adds to the pure dephasing rate such that $\Gamma_2 = \Gamma_\phi + \Gamma_{\text{os}}$. Moreover, on average, one spin flip occurs after η scattering events, thus limiting the T_1 time to $T_{1,\text{os}} = \frac{\eta}{\Gamma_{\text{os}}}$.

In terms of Rabi frequency, the effective Raman Rabi frequency is described by [184]

$$\Omega_R \approx \frac{\Omega_1\Omega_2}{2\Delta}. \tag{2.64}$$

As such, increasing either optical drives to either of the transitions or reducing the detuning can increase the rate at which the system is driven. Recall from the two level system, the Rabi frequency can also be defined using the saturation parameter, $s = \frac{P}{P_{\text{sat}}}$, where P is the applied optical power and P_{sat} is the saturation power. The Rabi frequency can then be written as

$$\Omega_1 = \sqrt{\frac{s}{2}}\,\Gamma_{1A}, \tag{2.65}$$

where Γ_{1A} is the excited state decay rate. Importantly, the two ground state optical transitions likely have different dipole strengths and as such their Rabi frequencies will differ in general. This can be described with the branching ratio η, giving [139]

$$\Omega_2 \approx \frac{\Omega_1}{\sqrt{\eta}}. \tag{2.66}$$

Experimentally, the branching ratio η can be determined independently, for example by measuring the initialization time as a function of optical power. Likewise, once the saturation power is known, the saturation parameter $s = P/P_{\text{sat}}$ provides a direct way to estimate Rabi frequencies.

2.3 Ramsey Interference and Dynamical Decoupling

2.3.1 Ramsey Interferometry

Rabi oscillations and the corresponding decay that comes with them can provide a baseline measure for the coherence time of the system; however, it is still limited by optical scattering as it requires continuous driving. To mitigate this even further, beyond just increasing the detuning, a technique known as Ramsey interferometry can be employed. Whereas a Rabi pulse sequence involves continuous driving, a Ramsey sequence applies a $\pi/2$ pulse to create a superposition state in the equatorial plane, then lets the system freely evolve, before applying a second $\pi/2$ pulse. The advantage over Rabi oscillations is gained by reducing the interaction time between the driving field and the spin [189]. Because the optical field is absent during the free-precession interval, this measurement isolates the intrinsic spin coherence more cleanly than the driven Rabi measurement and more directly reveals the extent to which the qubit is limited by slowly varying noise rather than optical scattering. Below, the relevant results are derived.

If the initial condition is such that the state starts in the spin up state, we can write it as

$$|\psi_0\rangle = |\uparrow\rangle = \begin{pmatrix} 1 \\ 0 \end{pmatrix}. \tag{2.67}$$

Then, if a pulse of duration t is applied with a phase of ϕ, the state will be rotated a polar angle $\theta = \Omega t$ with respect to the z-axis around an equatorial axis determined by $\hat{n}_\phi = \cos\phi\,\hat{x} + \sin\phi\,\hat{y}$ on the Bloch sphere. Thus, phases of 0, π, and 2π correspond to rotations about the x, -x, and x axes while phases of π and $3\pi/2$ correspond to rotations about the y and -y axes. As was mentioned in the two-level system section before, π and $\pi/2$ pulses correspond to pulses of length $t = \frac{\pi}{\Omega}$ and $t = \frac{\pi}{2\Omega}$. The operator for such a pulse can be written as

$$R_\phi(\theta) = \exp\left[-\frac{i\theta}{2}\left(\cos\phi\,\sigma_x + \sin\phi\,\sigma_y\right)\right], \tag{2.68}$$

where $\sigma_{x,y}$ are the Pauli spin matrices. In matrix form, this can be written as

$$R_\phi(\theta) = \begin{pmatrix} \cos\left(\frac{\theta}{2}\right) & -ie^{-i\phi}\sin\left(\frac{\theta}{2}\right) \\ -ie^{i\phi}\sin\left(\frac{\theta}{2}\right) & \cos\left(\frac{\theta}{2}\right) \end{pmatrix}. \tag{2.69}$$

In a typical Ramsey sequence, the first $\pi/2$ pulse is applied with a phase of 0 . Using 2.69, we can write this as

$$R_0\left(\frac{\pi}{2}\right) = \frac{1}{\sqrt{2}}\begin{pmatrix} 1 & -i \\ -i & 1 \end{pmatrix}. \tag{2.70}$$

This transforms the initially spin up state into an equal superposition state

$$R_0\left(\frac{\pi}{2}\right)|\psi_0\rangle = \frac{1}{\sqrt{2}}\begin{pmatrix}1\\-i\end{pmatrix} = \frac{1}{\sqrt{2}}(|\uparrow\rangle - i\,|\downarrow\rangle). \tag{2.71}$$

Then, the state is allowed to freely precess. Importantly, the superposition state represents a state in which both spin up and down have a 0.5 probability of being measured, and it is only the relative phase between the two spin states which evolves as the spin precesses. This relative phase is imaginary and as such doesn't contribute to the amplitude squared probabilities. Hence, the probability of measuring either spin state remains the same at 0.5 during this process unless a T_1 spin flip event occurs. In particular, this relative phase accumulation can be written as a factor on one of the two spin states

$$|\psi_1\rangle = \frac{1}{\sqrt{2}}\left(|\uparrow\rangle - ie^{-i\phi_{\text{rel.}}}\,|\downarrow\rangle\right), \tag{2.72}$$

where $\phi_{\text{rel.}} = \phi_\downarrow - \phi_\uparrow$ is the relative phase.

In the lab frame, this relative phase is accumulated at a rate determined by the splitting between the spin ground states $\phi_{\text{rel.}} = \omega_0\tau$ where τ is the free precession time and ω_0 is the ground state splitting between spin sublevels. However, in the rotating frame (rotating at a frequency equal to the ground state splitting) the phase accumulates at a rate of $\phi_{\text{rel.}} = \delta\tau$ where $\delta = \omega - \omega_0$ is the detuning of the drive frequency off of the two photon transition or ground state splitting. Assuming a perfect resonant in which $\delta = 0$, then $\phi_{\text{rel.}} = 0$.

Then, after letting the system freely precess, another $\pi/2$ pulse is applied, this time with some variable phase ϕ which will largely determine the experimental observations. The rotation operator can be written as

$$R_\phi\left(\frac{\pi}{2}\right) = \frac{1}{\sqrt{2}}\begin{pmatrix}1 & -ie^{-i\phi}\\ -ie^{i\phi} & 1\end{pmatrix} \tag{2.73}$$

and it evolves our system into the state

$$R_\phi\left(\frac{\pi}{2}\right)|\psi_1\rangle = \frac{1}{2}\begin{pmatrix}1-e^{-i\phi}\\ -ie^{-i\phi}-i\end{pmatrix}. \tag{2.74}$$

The corresponding probabilities of measuring either the spin up or spin down state are then

$$P_\uparrow = |\frac{1}{2}(1-e^{-i\phi})|^2, \qquad P_\downarrow = |\frac{1}{2}(-ie^{-i\phi}-i)|^2. \tag{2.75}$$

We can expand the exponential terms using Euler's formula $e^{-i\phi} = \cos(-\phi) + i\sin(-\phi) = \cos(\phi) -$

$i\sin(\phi)$. Substituting this in, we find

$$P_{\uparrow} = \frac{1}{2}(1 - \cos\phi), \qquad P_{\downarrow} = \frac{1}{2}(1 + \cos\phi). \tag{2.76}$$

Thus, if we were reading out the $|\downarrow\rangle$ state, then maxima near 0 and 2π and minima at π are expected. This is because when the second $\pi/2$ pulse has a phase of 0 and 2π, these correspond to the same axis of rotation (x) as the first $\pi/2$ pulse and as such maximize population in the $|\downarrow\rangle$ state. On the other hand, rotations with a phase of π correspond to rotation about the $-x$ axis, which reverses the action of the initial $\pi/2$ pulse and thus minimizes the readout signal. Phases of $\pi/2$ and $3\pi/2$ correspond to rotations about the y axis, thus keeping the state in a superposition state and thus correspond to 50% in either spin state.

Next, consider a scenario in which the free precession time is varied and the phase of the second $\pi/2$ is changed such that it evolves according to $\phi = \omega_s\tau$ where $\omega_s/2\pi = 5$ MHz for example and τ is the free precession time. Then, the probability of measuring the state in the $|\downarrow\rangle$ state is

$$P_{\downarrow} = \frac{1}{2}[1 + \cos(\omega_s\tau)]. \tag{2.77}$$

From this, it is clear that one can observe oscillations in population equal in frequency to the chosen evolution rate ω_s.

In addition to oscillations, a decay envelope will also be observed. This decay envelope comes from the fact that from measurement to measurement, small fluctuations in the ground state splitting or magnetic field can cause the accumulated relative phase to be slightly different, which, averaged over many repetitions, can wash out oscillations. The result is that the Ramsey contrast decreases with increasing free precession time. As such, the original probability function can be modified to account for such decoherence

$$P_{\downarrow} = C(\tau)[1 + \cos(\omega_s\tau)], \tag{2.78}$$

where $C(\tau)$ is a function that accounts for the decaying contrast. Now the choice of this function depends on the source of the noise. If the noise is Markovian, i.e. random phase flips with no memory of previous interactions, then the envelope is usually modeled by an exponential

$$C(\tau) = e^{-(\tau/T_2^*)}. \tag{2.79}$$

However, if the fluctuations are quasistatic and follow a Gaussian distribution as is typical with slowly varying noise sources, then the average gives a Gaussian decay envelope

$$C(\tau) = e^{-(\tau/T_2^*)^2}. \tag{2.80}$$

Even higher order functions exist and can describe different types of noise sources providing a useful method to potentially narrow down what's causing decoherence.

At this point, it is also worth revisiting the difference between T_2^*, and T_2. T_2 refers to the true coherence time or transverse relaxation because it is the time over which the relative phases decay. T_2^* on the other hand is generally referred to as the "observed" coherence time under an inhomogeneous magnetic field, which originated from the NMR research community and ensemble measurements in which different spins experienced different magnetic fields. For single spins, randomly varying magnetic field noise such as from nuclear or electronic spins in the host material can also fulfill this role. Hence, Ramsey measurements mitigate optical scattering but cannot correct for the dephasing under inhomogeneous magnetic field noise. As such, Ramsey measurements provide a measure of T_2^*. In contrast, if one were to remove these inhomogeneities and measure the true coherence time, this is what is referred to as the T_2 time. This is why T_2 is what is quoted when dynamical decoupling sequences are used as they make the magnetic field more homogeneous.

At this point, it is also worth covering how full-qubit control and or arbitrary Bloch sphere initialization can be achieved. We've already covered how rotations can be done. In particular the microwave generated signal contains a phase which is imprinted onto the sidebands which then imprint on the defect and that sets the axis of rotation in the equatorial plane. Additionally, however, one can use the two-photon detuning to set the rotation axis component along the z-axis. In particular, different two-photon detuning values will cause the system to rotate using a tilted z-axis; however, it will also make population transfer less efficient.

2.3.2 Hahn-Echo and CPMG

Having discussed how Ramsey sequences can extend coherence time by minimizing optical scattering and extracting the T_2^*, we now review the Hahn-echo pulse sequence. A Hahn-Echo involves inserting a refocusing π pulse halfway through the free-evolution interval of a Ramsey sequence. This refocusing pulse serves to counteract slowly varying magnetic field noise. Specifically, a Hahn-Echo sequence can be described as a $\pi/2$ pulse with phase 0°, then wait for the system to evolve over a time $\tau/2$; then, apply a π pulse with phase 0° so that the fast dephasing components are reversed and the slow components skip ahead; then another free evolution time $\tau/2$, before finally applying a $\pi/2$ with phase dependent on which state is desired to be readout. If the phase of the second pulse is swept similar to the Ramsey, a phase map that is shifted in phase by π should be seen. One can also define the visibility to determine the degree to which the state has decohered as

$$v(\tau) = \frac{S_{\max} - S_{\min}}{S_{\max} + S_{\min}}. \tag{2.81}$$

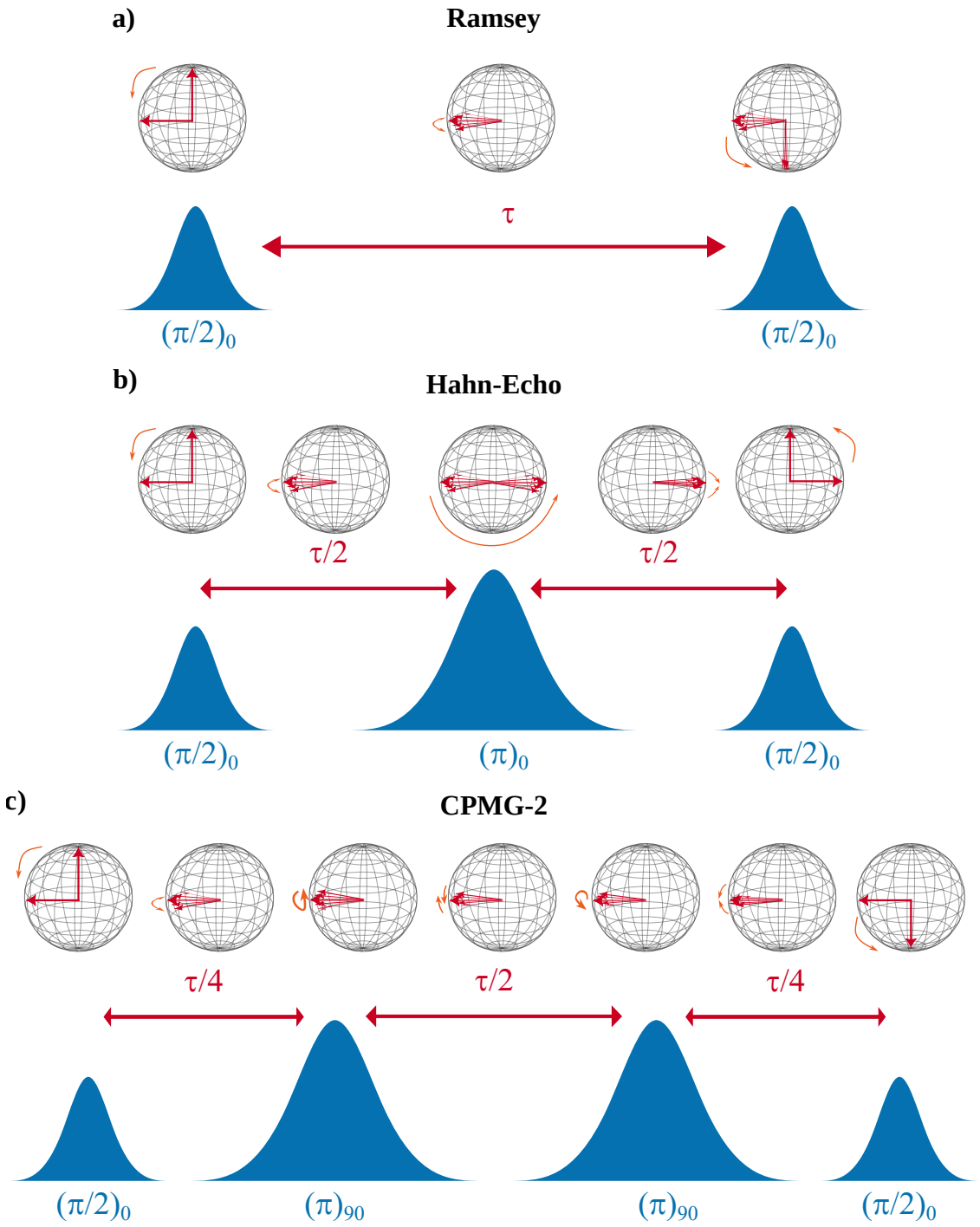

Figure 2.8 **a)** Shows a characteristic Ramsey pulse sequence in addition to Bloch sphere evolution. **b)** Shows a characteristic Hahn-Echo pulse sequence. **c)** Shows a characteristic CPMG-2 sequence.

This visibility can then be fit to a stretched exponential

$$v(\tau) = v_0 \exp\left[-\left(\frac{\tau}{T_2^{\text{echo}}}\right)^n\right] + v_\infty, \tag{2.82}$$

where v_0 is the initial contrast, v_∞ is a long-time offset, T_2^{echo} is the Hahn-echo coherence time, and n is the stretching exponent. The value of n provides information about the noise environment: $n = 1$ corresponds to exponential decay characteristic of Markovian noise; $n = 2$ on the other hand corresponds to Gaussian decay typical of quasi-static fluctuations. Higher order terms mean the noise itself may have correlations or periodicity, and so fitting the Hahn echo decay can yield not only a characteristic, longer coherence time but also reveal information about the microscopic origin of the decoherence. Carr-Purcell-Meiboom-Gill sequences are a natural extension of the echo dynamical decoupling sequence. They involve adding more and more refocusing pi-pulses with the general structure shown in Figure 2.8. Moreover, instead of using X-rotations, they employ Y-rotations, which lock the spin to a particular axis and reduce the probability of pulse length errors effecting rephasing.

2.4 Correlation and Photon Statistics

Thus far, the discussion has focused on how two- and three-level systems respond to optical driving in terms of coherence time, linewidth of transition and steady state population dynamics. Another property of interest is how the emitted photons are distributed in time. This is the subject of photon statistics and is important for determining whether an optical signal comes from a single two level system or from multiple two level systems emitting simultaneously. A defining feature of a single-photon emitter is that it cannot emit two photons at the same time. By contrast, a classical light source or an ensemble of independent emitters can produce simultaneous detection events with nonzero probability. These differences can be quantified with the second-order intensity autocorrelation function, denoted $g^{(2)}(\tau)$, which measures correlations between photon detection events separated by a time delay τ.

For a stationary light source with a constant average intensity, the normalized second-order correlation function is defined classically as [190]

$$g^{(2)}(\tau) = \frac{\langle I(t)I(t+\tau)\rangle}{\langle I(t)\rangle^2}, \tag{2.83}$$

where $I(t)$ is the detected intensity and $\langle\cdots\rangle$ denotes a time average. Experimentally, $g^{(2)}(\tau)$ gives the probability for detecting a photon at time $t + \tau$, after a photon has already been detected

at time t. The denominator is used to normalize this probability to that which is expected for completely uncorrelated events. Thus, for completely uncorrelated photon arrivals $g^{(2)}(\tau) = 1$. This corresponds to completely random time spacing between detected photons. Any deviations from this result indicate temporal correlations from the light. In particular, light can be categorized based on the value of their autocorrelation function at $\tau = 0$. For ideal coherent light, such as an ideal laser, the photon arrivals are completely random and can be described with a Poisson distribution (generally used to describe discrete, random events). Thus, for an ideal laser

$$g^{(2)}(0) = 1. \tag{2.84}$$

On the other, for thermal or chaotic light, photons tend to arrive in bunched clusters and one can measure

$$g^{(2)}(0) > 1. \tag{2.85}$$

For sub-Poissonian light, the value is below that of the ideal laser and this describes light which has some degree of temporal correlation or non-randomness and

$$g^{(2)}(0) < 1. \tag{2.86}$$

Individual quantum emitters fall into this last category in which emission is anti-bunched or spread out in time in a correlated way. For an ideal single emitter, one usually finds

$$g^{(2)}(0) = 0. \tag{2.87}$$

Intuitively, this makes sense. For a two-level system, after a photon is emitted, the emitter returns to its lower state $|1\rangle$. Once in $|1\rangle$, the system must be re-excited before another photon can be emitted. There is thus a finite interval following each emission during which a second emission cannot occur. This is fundamentally different from a classical wave picture, and it leads directly to a dip in the $g^{(2)}(\tau)$ function.

This can be derived by using the quantum optics definition for the second order correlation function. In particular, we can redefine the classical definition to [191].

$$g^{(2)}(\tau) = \frac{\langle \hat{a}^\dagger(t)\hat{a}^\dagger(t+\tau)\hat{a}(t+\tau)\hat{a}(t)\rangle}{\langle \hat{a}^\dagger(t)\hat{a}(t)\rangle^2}, \tag{2.88}$$

where $I \propto E^2$ has been used and $E \propto \hat{a}(t)$ where $\hat{a}$ is the annihilation operator for the emitted

photon mode and $\hat{a^\dagger}$ is the creation operator. From this, for $\tau = 0$,

$$g^{(2)}(0) = \frac{\langle \hat{a}^\dagger \hat{a}^\dagger \hat{a}\hat{a} \rangle}{\langle \hat{a}^\dagger \hat{a} \rangle^2}. \tag{2.89}$$

Moreover, if we use the number operator $\hat{n} = \hat{a}^\dagger \hat{a}$, to rewrite the numerator as

$$\hat{a}^\dagger \hat{a}^\dagger \hat{a}\hat{a} = \hat{n}(\hat{n} - 1), \tag{2.90}$$

so that

$$g^{(2)}(0) = \frac{\langle \hat{n}(\hat{n} - 1) \rangle}{\langle \hat{n} \rangle^2}. \tag{2.91}$$

Hence, for a perfect number state containing exactly N photons,

$$\hat{n} \left| N \right\rangle = N \left| N \right\rangle, \tag{2.92}$$

the zero time delay value we find is

$$g^{(2)}(0) = \frac{N(N-1)}{N^2} = 1 - \frac{1}{N}. \tag{2.93}$$

This shows clearly that values below one can be obtained and in particular, for a single-emitter state, in which $N = 1$, we find that $g^{(2)}(0) = 0$. For two independent emitters, we find $g^{(2)}(0) = 0.5$, and larger numbers of emitters approach the classical limit $g^{(2)}(0) = 1$. This is also the origin of the commonly used experimental criterion that observing

$$g^{(2)}(0) < 0.5 \tag{2.94}$$

provides evidence that the detected light originates from a single emitter.

Beyond the value at zero delay, the full time dependence of $g^{(2)}(\tau)$ contains additional information about the emitter. In particular, for a continuously driven two-level system, the system must be re-excited after each emission and so one can fit these curves to the characteristic anti-bunching curve [190, 191]

$$g^{(2)}(\tau) = 1 - e^{-|\tau|/\tau_c}, \tag{2.95}$$

where τ_c is the excited state lifetime of the quantum state.

2.4.0.1 Resonant $g^{(2)}(\tau)$ Coherent Oscillations

The previous section considered the case of incoherent excitation of a two-level system. For a resonantly and coherently driven two-level system, the emitter can undergo coherent oscillations

between $|1\rangle$ and $|2\rangle$ while also experiencing population decay and dephasing. In that case, the normalized second-order correlation function takes the form [192]

$$g^{(2)}(\tau) = 1 - e^{-\eta|\tau|}\left[\cos(\mu|\tau|) + \frac{\eta}{\mu}\sin(\mu|\tau|)\right], \tag{2.96}$$

where

$$\eta = \frac{1}{2}\left(\frac{1}{T_1} + \frac{1}{T_2}\right) \tag{2.97}$$

and

$$\mu = \sqrt{\Omega^2 + \left(\frac{1}{T_1} - \frac{1}{T_2}\right)^2}. \tag{2.98}$$

Here, T_1 is the population relaxation time, T_2 is the coherence time, and Ω is the Rabi frequency introduced earlier. The exponential factor describes the decay of correlations in time, while the oscillatory terms reflect coherent Rabi oscillations of the driven emitter. Thus, antibunching at short delay reveals the single-photon nature of the source, while oscillations in $g^{(2)}(\tau)$ provide direct evidence of coherent optical control. These oscillations happen because while the system is undergoing Rabi oscillations, it can only be in one of the two states, and so photon emission must wait until it oscillates from the excited state back down to the ground state. This is determined by the Rabi frequency, and so one observes an imprint of these oscillations on the normal $g^{(2)}(\tau)$.

2.5 Role of Inversion Symmetry on Transitions and Spectral Diffusion

If a defect is inversion symmetric, then inverting the spatial coordinates of the defect, $\mathbf{r} \to -\mathbf{r}$, leaves the atomic configuration unchanged. Because the electronic potential arises primarily from the Coulomb potentials of the nuclei, this symmetry implies that the electronic potential experienced by an electron satisfies

$$V(\mathbf{r}) = V(-\mathbf{r}). \tag{2.99}$$

This is important because it means that the potential an electron sees is symmetric under inversion, and so if an eigenstate $\psi(r)$ exists, then $\psi(-r)$ is the same except for a change of sign from a phase difference. In particular, the inversion operation is represented by the parity operator P, which acts on a wavefunction as

$$P\psi(\mathbf{r}) = \psi(-\mathbf{r}). \tag{2.100}$$

So for an inversion symmetric defect, the Hamiltonian is left unchanged under parity,

$$PHP^{-1} = H, \tag{2.101}$$

so that $[H, P] = 0$. Parity is therefore a conserved quantity, or equivalently, a good quantum number. This means that the electronic eigenstates of the defect can be chosen to have definite parity:

$$P\,|\psi\rangle = \pm\,|\psi\rangle\,. \tag{2.102}$$

States satisfying $P\,|\psi\rangle = +\,|\psi\rangle$ are even parity states, referred to as *gerade* (g), while states satisfying $P\,|\psi\rangle = -\,|\psi\rangle$ are odd parity states, referred to as *ungerade* (u). For inversion-symmetric defects such as the NiV center, whose symmetry includes inversion, the electronic eigenstates may therefore be classified according to their parity. If a defect does not possess inversion symmetry, then the potential is not symmetric under $\mathbf{r} \to -\mathbf{r}$, and the Hamiltonian no longer commutes with the parity operator. In that case parity is not conserved, and the eigenstates generally cannot be assigned a definite parity. Instead, they may be written as mixtures of even and odd parity components,

$$|\psi\rangle = \alpha\,|\psi_{\text{even}}\rangle + \beta\,|\psi_{\text{odd}}\rangle\,. \tag{2.103}$$

This distinction has important consequences for the interaction of the defect with electric fields. The electric dipole operator is

$$\mathbf{d} = -e\sum_i \mathbf{r}_i, \tag{2.104}$$

which is odd under parity because $\mathbf{r}$ changes sign under inversion. The dipole matrix element between two states is

$$\langle\psi_f|\,\mathbf{d}\,|\psi_i\rangle = -e\int \psi_f^*(\mathbf{r})\,\mathbf{r}\,\psi_i(\mathbf{r})\,d^3\mathbf{r}. \tag{2.105}$$

If the initial and final states have the same parity, then the product $\psi_f^*(\mathbf{r})\psi_i(\mathbf{r})$ is even. Multiplication by the odd function $\mathbf{r}$ then makes the full integrand odd, and its integral over all space vanishes. Therefore,

$$\langle\psi_f|\mathbf{d}|\psi_i\rangle = 0 \tag{2.106}$$

for states of the same parity. By contrast, if the two states have opposite parity, then the integrand is even and the matrix element can be nonzero. This gives the electric-dipole parity selection rule: electric dipole transitions are allowed only between states of opposite parity. This has two important implications. First, an optically allowed electric dipole transition requires that the two states involved have opposite parity. Second, for an inversion-symmetric defect, the expectation value of the dipole

operator in any eigenstate vanishes,

$$\langle\psi|\,\mathbf{d}\,|\psi\rangle = 0. \tag{2.107}$$

Thus inversion-symmetric defects do not possess a permanent static electric dipole moment. This strongly suppresses their sensitivity to static or slowly varying electric fields. The interaction of a static electric field with a dipole is described by the Stark Hamiltonian,

$$H_{\text{Stark}} = -\mathbf{d}\cdot\mathbf{E}, \tag{2.108}$$

where $\mathbf{E}$ is a static electric field. In first-order perturbation theory, the corresponding shift of an energy level $|n\rangle$ is

$$\Delta E_n^{(1)} = \langle n|\,H_{\text{Stark}}\,|n\rangle = -\langle n|\,\mathbf{d}\,|n\rangle\cdot\mathbf{E}. \tag{2.109}$$

For an inversion-symmetric defect, this vanishes because $\langle n|\,\mathbf{d}\,|n\rangle = 0$. Therefore, inversion-symmetric defects do not experience a first-order DC Stark shift.

For defects without inversion symmetry, however, the eigenstates need not have definite parity and may possess nonzero permanent dipole moments. Their energies can therefore shift linearly with electric field. For an optical transition of frequency

$$\omega_{eg} = \frac{E_e - E_g}{\hbar}, \tag{2.110}$$

the resulting shift in transition frequency is

$$\Delta\omega = \frac{\Delta E_e - \Delta E_g}{\hbar} = -\frac{(\mathbf{d}_e - \mathbf{d}_g)\cdot\mathbf{E}}{\hbar}. \tag{2.111}$$

As a result, electric-field noise arising from charge traps, surface effects, or other stray local fields leads directly to linear fluctuations in the optical transition frequency. This spectral diffusion broadens the optical line and reduces photon indistinguishability, which is highly detrimental for entanglement generation in quantum networking applications.

Although the first-order Stark shift vanishes for inversion-symmetric defects, second-order shifts remain. From second-order perturbation theory,

$$\Delta E_n^{(2)} = \sum_{m\neq n} \frac{|\,\langle m|\,\mathbf{d}\,|n\rangle\,|^2 E^2}{E_n - E_m}. \tag{2.112}$$

These shifts are generally nonzero because the dipole operator can connect states of opposite parity. However, because the dependence is quadratic in the electric field rather than linear, small electric-field fluctuations produce much smaller changes in transition frequency. This is why inversion-symmetric defects experience strongly reduced spectral diffusion.

Importantly, the absence of a permanent dipole moment does not prevent optical transitions. Even though the average charge distribution of a given eigenstate is inversion symmetric, the ground and excited states can still have different spatial symmetries and opposite parity. The transition dipole matrix element between such states can therefore be nonzero, allowing strong optical transitions while maintaining insensitivity to electric-field noise at first order.

Chapter 3

Experimental methods and sample fabrication

This chapter describes the experimental methods and sample fabrication processes used throughout this thesis. To identify and probe both individual and ensembles of NiV centers, we employ confocal fluorescence microscopy. We therefore begin by reviewing the principles of confocal microscopy and its practical advantages over conventional widefield imaging for isolating single emitters. Then, we describe how we realize such a confocal microscope in the lab along with other experimental setups used to carry out e.g. single photon statistics measurements, coherent population trapping, Rabi oscillations, Ramsey interference, Hahn Echo and dynamical decoupling sequences. Finally, we detail the samples studied in this thesis and their preparation. As most of the samples were created via ion implantation, we briefly describe that concept. Moreover, due to the difficulty of extracting light from diamond (owing to its high refractive index), we fabricate nanophotonic structures in the form of nanopillars to improve photon collection; the associated nanofabrication processes are therefore also described.

3.1 Confocal Microscopy

The basic idea of confocal microscopy is to spatially filter both the excitation light shining on a sample and the detection light coming out of the sample, so that out of focus light is both weakly exciting and suppressed in detection. The defects of interest fluoresce and hence we are interested in collecting that fluorescence. As such, we use confocal fluorescence microscopy, but there are also other types, such as Raman based or reflectance based techniques, among others. Here we review the basic concepts of confocal microscopy, but for a more thorough review, we recommend [193] and [194] for an explicit focus on imaging color centers.

A useful starting point for understanding confocal fluorescence microscopy is conventional widefield fluorescence microscopy. In a widefield configuration, the sample is illuminated uniformly

throughout, hence the name, widefield. Fluorescence emitted from the sample is then collected by an objective lens and imaged onto a detector such as a camera or photodetector. The objective lens is the primary light-collecting element of the microscope. Its ability to gather light is characterized by its numerical aperture (NA), defined as

$$\mathrm{NA} = n \sin \theta, \tag{3.1}$$

where n is the refractive index of the medium between the sample and the objective, and θ is the half-angle of the largest cone of light that can enter the objective. As such, when imaging in air, the maximum NA one can achieve is 1. To achieve higher NA values, one needs to use alternative mediums, for example, oil which has a larger index of refraction. Widefield microscopy is useful because it enables rapid imaging of a sample. This is because the entire field of view is illuminated and recorded simultaneously. However, if the sample being imaged is thick, fluorescence is generated throughout the illuminated volume. The detector therefore collects light not only from the plane in which excitation light is focused (also called the focal plane), but also from regions above and below it. Because the detector is two-dimensional, all of the light from different depths will be integrated together. The resulting image then looks blurry because it contains out-of-focus background light that reduces the image contrast. The ability of a microscope to distinguish structures separated along the optical axis is referred to as the axial resolution or optical sectioning capability. Widefield microscopes do not have the ability to optically section however because they collect light from the entire illuminated volume.

Before going any further, it helps to understand the so-called point spread function (PSF). In optical microscopy, the goal is to form images of objects using light. Ideally, each point in that object would map to a single point in the image. In practice, however, the wave nature of light prevents perfect focusing, as the waves interfere and one approaches the diffraction limit. That means that even for an infinitesimally small object or emitter, we will observe some non-infitesimal intensity distribution in the image. This response of the imaging system to such an ideal point emitter is known as the PSF and understanding the PSF is essential for describing the spatial resolution of a microscope. Indeed, the measured image can be written as a convolution of the actual object with the microscope PSF, where each point in the object will contribute a copy of the PSF to the final image. Therefore, the smaller the PSF, the sharper the image will be, and thus the better one will be able to resolve two distinct point objects, which defines the spatial resolution of the microscope. The exact size of the PSF depends on the wavelength of light and the numerical aperture of the objective. When the objective back aperture is completely filled or fully illuminated, the system reaches the diffraction limit, meaning that the focal spot is as small as physically allowed. This diffraction limit forms a characteristic pattern known as an Airy pattern, which consists of a bright central dot

surrounded by concentric rings of decreasing intensity. The central bright region is called the Airy disk and its size determines the smallest separation between two points that can be distinguished by the microscope. For a circular aperture, the lateral radius of the Airy disk is approximately

$$r_{\text{Airy}} \approx 0.61 \frac{\lambda}{\text{NA}}, \tag{3.2}$$

where λ is the wavelength of the light being sent into the objective lens. This sets the lateral resolution, which describes the ability to distinguish two points in the transverse (x–y) plane. The axial extent of the focal region is larger and scales approximately as

$$\Delta z \approx \frac{2n\lambda}{\text{NA}^2}. \tag{3.3}$$

Both widefield and confocal microscopy are subject to the diffraction limit, but confocal microscopy improves image contrast and optical sectioning. It achieves this by spatially restricting both the excitation and the detection volumes. The term confocal refers to the fact that the focal point of the illumination and the focal point of the detection optics are the same. To do this, a spatial filter, such as a pinhole or single-mode optical fiber, ensures that the excitation or illumination light behaves as an effective point source. This produces a tightly localized excitation region within the sample, so that only emitters in focus will be strongly excited, whereas points nearby will experience a far lower power density. Then, in the detection arm, a pinhole or fiber is placed in a position with the same focus as that of the excitation light to ensure that only in focus fluorescence can pass through, while out of focus light is rejected. Fluorescence originating from the focal region is imaged sharply onto this pinhole and is transmitted efficiently. Light emitted from out-of-focus planes forms a larger spot at the pinhole and is thus largely rejected. Together, these two mechanisms strongly suppress out-of-focus background and allow the microscope to isolate a thin optical slice of the sample. The detected signal in a confocal microscope depends on both the excitation intensity distribution and the detection efficiency. As a result, the effective confocal PSF is given by the product of the excitation and detection PSFs. Because both functions are peaked at the focal point, their product is narrower than either function alone. This leads to improved spatial selectivity compared with widefield detection. For an ideal confocal system with a small pinhole, the approximate resolutions are

$$\Delta r_{\text{lat}}^{\text{confocal}} \approx 0.37 \frac{\lambda}{\text{NA}}, \tag{3.4}$$

and

$$\Delta z_{\text{axial}}^{\text{confocal}} \approx 1.4 \frac{n\lambda}{\text{NA}^2}. \tag{3.5}$$

While the improvements in resolution compared to a widefield configuration are modest at best, the

axial response is significantly sharper as a result of both suppressing out of focus excitation and rejecting out of focus light, neither of which can be done in a widefield configuration.

In this work we employ a laser-scanning confocal fluorescence microscope, in which a diffraction-limited excitation spot is scanned across the sample while the fluorescence signal is recorded at each position using a single-photon detector. Spatial filtering in both the excitation and detection arms is implemented with a single-mode optical fiber, which acts as an effective pinhole while simultaneously coupling light into photon-counting detectors. Additional spectral filtering, such as dichroic mirrors and bandpass filters, is used to separate fluorescence from reflected excitation light. Confocal microscopy is particularly well suited for studying individual colour centres in diamond. Because the fluorescence originates from a single atomic-scale defect, suppressing background emission from nearby defects or the host crystal is essential for achieving high signal-to-noise ratios.

3.2 Experimental Setup

To characterize the NiV samples studied in this thesis, we used a home-built confocal fluorescence microscope attached to a closed-cycle helium cryostat (attocube attoDRY 2100) with a 9T superconducting magnet (see Figure 3.1). Unless otherwise stated, all measurements were performed at 1.65K. In the following, the experimental setup is described by first detailing the excitation lasers used to "power" the confocal microscope, then the confocal microscope setup itself, and lastly on the various exit points the collected fluorescence could be sent to for analysis.

3.2.0.1 Excitation Lasers

Throughout this thesis, we employ four main laser excitation sources which are used to excite the diamond samples. The first laser source is a continuous-wave (cw) titanium-sapphire laser (ti:sapph, Sirah Matisse CS), which can be tuned from 670 nm to 1100 nm. This is the primary laser we used for confocal scanning of NiV samples. We employed a variety of excitation wavelengths from off-resonant 690 nm to on-resonant 883 nm and various in between wavelengths to probe excitation wavelength dependence. The Ti:sapphire laser was actively frequency stabilized using a side-of-fringe locking scheme referenced to a cavity, yielding a spectral linewidth of approximately 35 kHz. In addition, a small portion of the laser output was directed to a HighFinesse wavemeter, which was used to monitor the laser wavelength with an absolute accuracy of approximately 15 MHz. This provided a convenient reference for tracking relative frequency changes during laser scans. The laser is pumped using a cw, diode-pumped Nd:YVO4 solid state laser (Specra-Physics Millennia eV 15) emitting at 1064 nm. This is then frequency doubled to 532 nm using a beta-barium borate (BBO) non-linear crystal and operates at a maximum output power of 15 W at λ = 532 nm. With

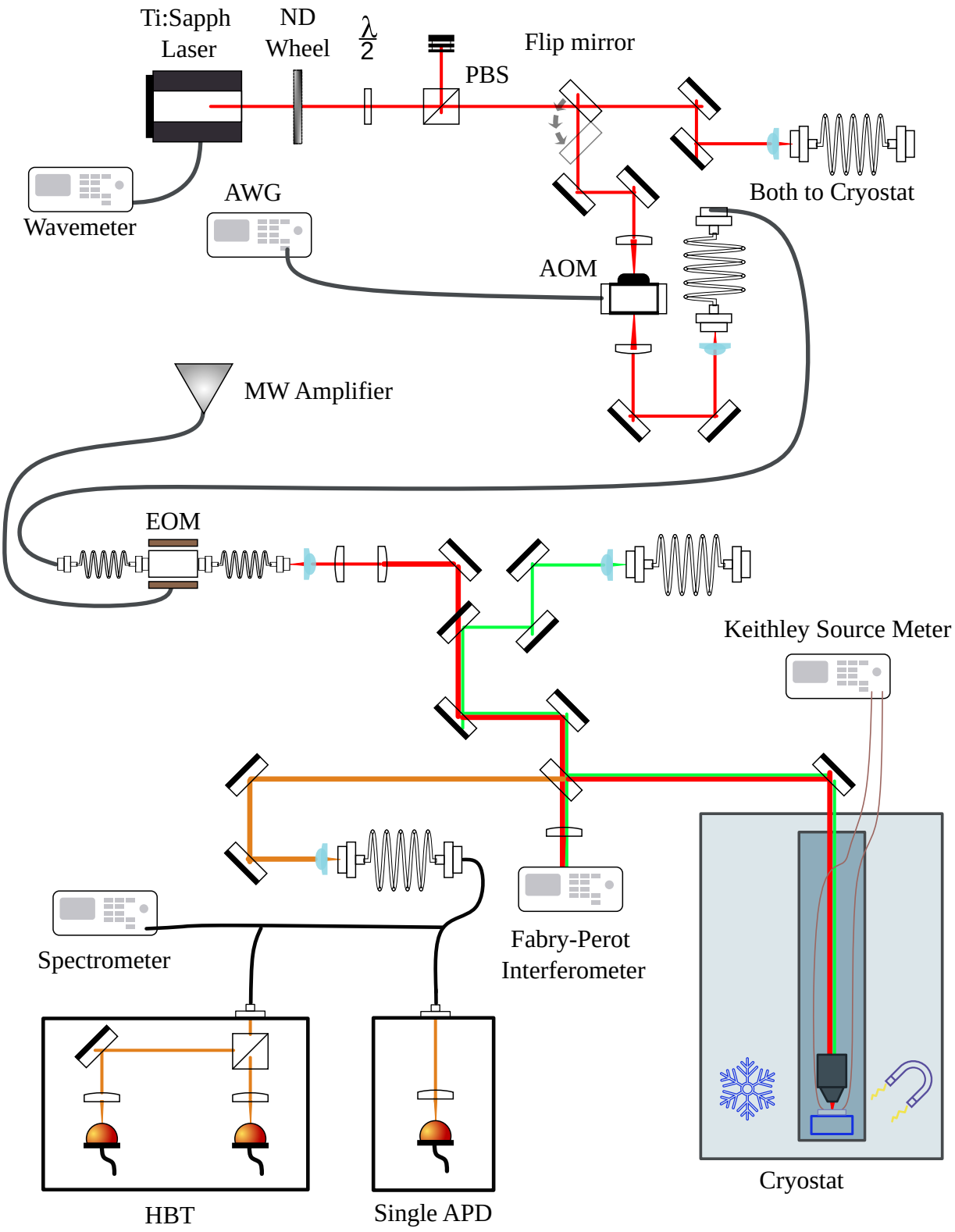

Figure 3.1 Diagram of optical setup with Ti:Sapph laser heading to confocal attached to cryostat, along with spectrometer and apd exit points included as well. Full description can be found in the main text.

15 W pump power, the ti:sapph laser at λ = 690 nm gives an output power of 6 W. Before being coupled into the confocal microscope, the output beam is passed through a neutral density filter wheel, which is used to adjust the input laser power. The laser is then coupled into a single mode fiber (SMF, core diameter ~ 5 μm, Thorlabs SM600), using two mirrors and an aspheric lens of focal length f = 11mm. The fiber serves as a spatial filter to suppress higher transverse laser modes, and this allows us to approximate the laser excitation as a point-like illumination source, critical for confocal imaging. The second laser source which is frequently employed for confocal scanning is a 532 nm diode-pumped solid-state laser (Spectra-Physics Millennia eV 15), which normally would be used to pump a pulsed ti:sapph laser, but which we frequently split off and use as a repump laser for the NiV. Similar to above, it is coupled to a single mode fiber after being passed through a variety of beam splitters which enable multiple different setups within the lab access to green light. Neutral density filters are used for coarse power adjustment.

The remaining lasers were used for specific measurements and not general confocal scanning. In particular, we used a different ti:sapph laser (Spectra Physics Tsunami), which was configured to emit 300ps pulses using an active mode locking technique. It should be noted that it can emit femtosecond pulses using a passive Kerr-lens mode locking technique as well. Similar to the previous ones described, it is fiber coupled to the confocal setup with neutral density filters and a 90/10 beam sampler as power adjustment. This laser was employed to measure the fluorescence lifetime of NiV centers using TCSPC. Lastly, we also occasionally used a 405 nm UV diode laser (Thorlabs) as a repump laser to compare to 532 nm light. This was also fiber coupled into the confocal and joined with the main resonant beam using a dichroic mirror.

3.2.0.2 Confocal Microscope

The coupled single mode fibers guide the excitation light to a closed cycle helium cryostat upon which a medium sized optical breadboard sits which contains the optics for the confocal microscope. The light emerges from the SMF and is collimated to a beam waist of about 3 mm, using an aspheric lens of f = 14 mm focal length. The light is then sent through a 2x magnifier using a Galilean beam expander setup comprised of two achromatic plano convex lenses of focal lengths 40mm and 80mm respectively. This beam waist overfills the entrance aperture of the microscope objective used, which is necessary because otherwise the full NA of the objective lens will not be used. This is due to the fact that the beam has a Gaussian intensity distribution and as such unless the objective lens is overfilled, the full NA of the lens will not be taken advantage of because beam waists are typically defined as the point at which the beam intensity is $1/e^2$ or ~13.5% of its maximum value. The light then goes through a spectral band pass filter meant to clean up or remove any light shifted in frequency due to Raman scattering while traveling through the excitation SMF, also known as fiber Raman light. This ensures that we only excite the sample with laser light. So, for 690 nm

excitation, for example, we use a 700 nm short pass, transmitting wavelengths shorter than 700 nm. Thus, it would let 690 nm through, but any higher wavelengths are cut off. For 532 nm excitation, we use a bandpass filter centered around 532 nm (Thorlabs FL05532-10).

The light is then sent through a dichroic mirror with a cut-on or transmission wavelength at 552 nm (LaserMux) followed by a 90/10 beam sampler both at 45 degree angles with respect to the beam. Usually, only a beam sampler is needed to allow for excitation and collection of fluorescence; however, we use the additional dichroic to couple in a second excitation source. This is useful for adding in repump lasers and for trying different combinations of excitation wavelengths. The dichroic will transmit red light but will reflect any light below 552nm. We can then overlap the two beams to ensure they excite the same part of the sample. We have two mirrors after each excitation source before the dichroic for overlapping the beams and an additional two mirrors before the beam sampler to adjust for any astigmatism. The 90:10 beam sampler reflects 10% of the incident light, and lets 90% transmit through. While this means that most of the input laser power before the objective is lost, this is done in order to maximize the fluorescence exiting from the sample. This is because while we only get 10% of the power, we get 90% of the fluorescence, and because we can always compensate with more input laser power, but never with fluorescence, the tradeoff is favorable.

A 100x cryogenic apochromatic objective lens (attocube LT-APO/VISIR) with NA=0.82 and working distance of 600 μm placed inside the cryostat was used for optical excitation and collection. The sample was mounted on stages and is cooled by a static exchange gas (helium) within a closed-cycle helium cryostat (attocube attoDRY 2100). Both coarse and fine positioners were used to move the sample in the x, y, and z directions, allowing for movement across the sample as well as control over the focus. The sample was coarse positioned using a set of three piezoelectric slip-stick stages (attocube ANPX101, ANPz102). The coarse positioners (controlled by attocube APS100 Magnet Power Supply) have a minimum stepping size of 500 nm and a max range of 3.5mm while the fine positioners (controlled by attocube ANC300 Piezo Controller) have a maximum range of 30 microns but can move in steps of 20 nm. Confocal scanning was achieved using piezo scanners (attocube ANSxy100, ANSz100). The sample is located at the center of a superconducting solenoid coil which allowed for the application of a vertical (Faraday configuration) magnetic field of up to 9 T.

The emitted fluorescence of the sample was collected using the objective lens and was then sent back through the beam sampler to the detection path of the confocal microscope. Using a second aspheric lens of focal length f = 18.4 mm, the fluorescence light was coupled into another SMF (Thorlabs SM780), through which it was guided to the grating spectrometer or the avalanche photodiodes. To suppress laser light reflected or scattered on the sample surface, a dielectric longpass filter (Thorlabs FELH0850), which transmits only wavelengths above λ = 850 nm, was

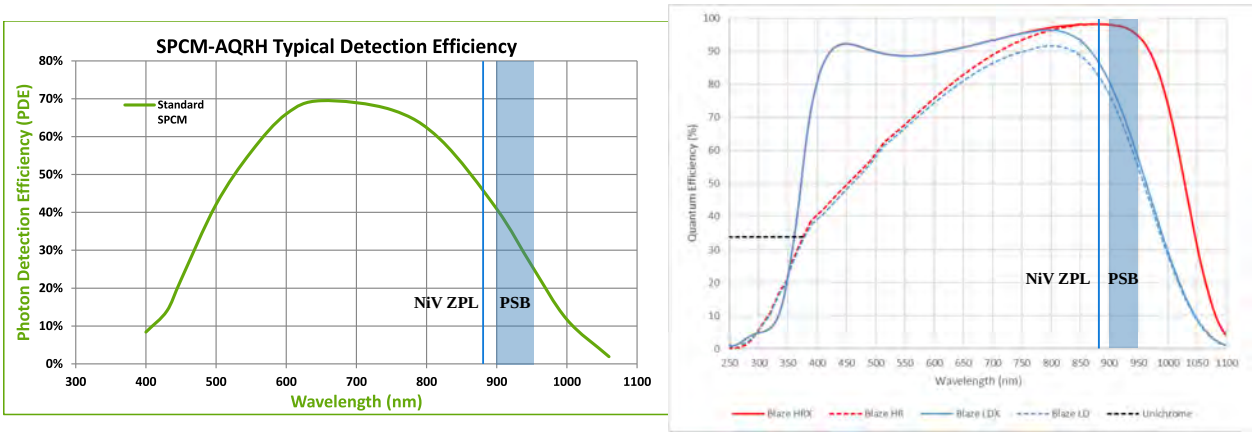

Figure 3.2 Both images show detection efficiency as a function of wavelength along with the 883/885 nm ZPL and 925 ± 25 nm phonon sideband. The left image shows the photon detection efficiency as a function of wavelength, reprinted from the manufacturer website: www.excelitas.com/product/spcm-aqrh. The right image shows the quantum efficiency for the spectrometer camera, also reprinted from the manufacturer website: www.teledynevisionsolutions.com/products/blaze

employed whenever trying to detect the characteristic 883/885 nm light from NiV^-.

3.2.0.3 Detection Systems

Here we describe the different exit points which were used to analyze the emitted fluorescence from the NiV samples.

3.2.0.3.1 Spectrometer Fluorescence light emitted by the defects could be guided to a spectrometer using an optical fiber attached to a "fiber port" featuring two aspheric lenses (f = 11 mm) used to focus the fluorescence onto the entrance slit of the fiber. These lenses were mounted in xy-translation mounts to further maximize the signal and resolution on the camera. Spectral analysis was performed using a grating spectrometer (Teledyne-Princeton Instruments SpectraPro HRS-750), which is an imaging spectrometer, i.e., it images the entrance slit onto its detector, with an imaging focal length of 750 mm. The detector is a charge-coupled device (CCD) with 1340 x 400 pixels (pixel width 50 microns). To decrease the noise-level of the recorded spectra, the CCD was electrically cooled down to -85 degrees Celsius. The CCD camera is specified by the manufacturer to provide a detection efficiency of 90% at a wavelength of 602nm and 95% at 737nm; however, it is lower at longer wavelengths, as seen in Figure 3.2. The spectrometer comprises three interchangeable diffraction gratings with 600, 1200 and 1800 grooves/mm, respectively. The resulting maximum resolution for the three gratings is approximately 0.22 nm for 600 grooves/mm, 0.1 nm for 1200 grooves/mm and 0.04 nm for 1800 grooves/mm. Spectrum are recorded using a spectral analysis software (Teledyne Princeton Instruments LightField).

3.2.0.3.2 Single Photon Detectors and Timetagging Fluorescence light could also be guided to an avalanche photon diode (APD, Excelitas Technologies SPCM-AQRH-16) instead of the grating spectrometer. The APD features a detection efficiency of 65% at 602 nm and 70% at 737 nm according to manufacturer specifications; however, like the spectrometer it is lower at longer wavelengths as seen in Figure 3.2. Dark count levels are quoted at ~20 counts per second. The detection window was limited to a specific spectral interval by placing bandpass filters in front of the APD in order to allow fluorescence from only SiV or only GeV to be detected. An IDQ900 timetagger was used to count the signals sent from the detectors where they could be read off and analysed. For off-resonant imaging, an 850 nm long-pass filter (Thorlabs FELH0850) and a 880 nm band-pass filter (Semrock FF01-880/11-25) were used in front of the detection fiber and single photon avalanche photodiodes (Excelitas SPCM-AQRH-16), respectively. For resonant excitation, the 880 nm band-pass was used in excitation, and a 900 nm long-pass (Thorlabs FELH0900) and 925 nm band-pass (Edmund Optics 87-797, 50 nm bandwidth) was used to detect on the weak phonon sideband. The Ti:Sapphire was then scanned across resonant transitions and the wavelength of the laser was read out using a wavelength meter (Highfinesse WS7-30).

3.2.0.3.3 Hanbury Brown-Twiss Setup The collected fluorescence could also be directed to a Hanbury Brown and Twiss (HBT) interferometer for measurements of the second-order intensity autocorrelation function $g^{(2)}(\tau)$ (see Figure 3.1). In this configuration, the light is split by a 50:50 beam splitter into two spatially separated paths, each of which is directed to an independent single-photon detector of the same type as described above. Detection events from the two detectors are time-stamped and correlated using time-tagging electronics (IDQ900) to build up a histogram of coincidence counts as a function of the time delay τ between detection events. The measured quantity $g^{(2)}(\tau)$ provides direct information about the photon statistics of the emitter. In particular, for an ideal single-photon source, the probability of detecting two photons simultaneously vanishes, leading to $g^{(2)}(0) = 0$, a signature known as photon antibunching. In practice, background counts and detector timing jitter lead to a nonzero but suppressed value at zero delay, and the depth and shape of the antibunching dip can be used to extract information about the emitter dynamics.

In our setup, the two optical paths after the beam splitter are not identical in length, resulting in a fixed relative time offset between the two detection channels. This path-length difference appears as a constant shift in the measured correlation histogram. Aside from this offset, the HBT configuration provides a straightforward and robust method to verify single-photon emission and to characterize the temporal statistics of the emitted light.

3.2.0.4 Control Electronics

3.2.0.4.1 Bias Voltage Control To perform voltage control for the p-i-p device, we utilized a Keithley 2400 source meter connected to the cryostat. When applying 20V, the total specified source uncertainty is ± 6.4mV. The output of the source meter was routed through the cryostat feedthroughs and connected to the attocube electrical wiring (stick) assembly, which provides direct electrical access to the sample mounted inside the cryostat. This configuration allowed us to apply well-defined DC bias voltages across the device. Furthermore, we could measure the current as we applied different voltages allowing us to measure IV-curves of the device.

3.2.0.4.2 Coherent Control Measurements Coherent population trapping (CPT), Raman, and pulsed spin-control experiments were implemented using microwave modulation of the optical excitation. An arbitrary waveform generator (AWG, Tektronix 700001A) with a tunable sampling rate of up to 50 GSamples/s, microwave generation range of up to 20GHz, and 16GSamples of waveform memory enabling sequences as long as 320 ms provided the microwave signals. These were then amplified (ix Blue) with 30dB gain and applied to a fiber-coupled electro-optic modulator (EOSpace EOM) through which the Ti:sapphire laser was passed. This phase modulation generates optical sidebands at frequencies $\omega_{\mathrm{L}} \pm \omega_s$ relative to the carrier frequency ω_{L}, where ω_s is the applied microwave modulation frequency.

For CPT measurements, the carrier laser was tuned to one optical transition (e.g., A1), while the AWG frequency ω_s was scanned such that one of the sidebands was swept across the second transition (A2). When both transitions were simultaneously addressed, a coherent dark state formed, which was observed as a reduction in fluorescence. After identifying the relevant transitions, Raman control was implemented by driving the EOM with a sinusoidal microwave signal, producing symmetric sidebands of equal amplitude about the carrier. In this configuration, the carrier frequency was simply shifted to set the desired single-photon detuning, while the two sidebands drove the two optical transitions. Initialization and reset pulses were generated using serrodyne modulation (i.e., a sawtooth or ramp waveform applied to the EOM), with the ramp frequencies chosen to shift the laser light to the respective A1 and A2 transitions. This enabled optical pumping into the desired spin state followed by coherent Raman manipulation.

For Ramsey measurements, phase control of the optical pulses was achieved by adjusting the phase of the microwave signal driving the EOM. This phase is imprinted onto the optical sidebands. Because a sinusoidal modulation produces both $+\phi$ and $-\phi$ sidebands, any applied microwave phase results in an effective factor-of-two phase shift between the two Raman fields, which must be taken into account when programming phase-sensitive pulse sequences.

For measurements involving controlled dark times, such as Ramsey, Hahn-echo, and CPMG sequences, it was necessary to completely extinguish the optical excitation during the free-evolution

intervals. Initially, we only used phase modulation and so the carrier remained present during the delay, which led to artificially shortened T_1 times and limited the achievable coherence, particularly when attempting to decouple from the ^{13}C spin bath. To resolve this, an acousto-optic modulator (AOM) was added to provide fast amplitude gating of the laser. The AOM was pulsed using one of the AWG marker outputs, while a second marker output was used to trigger the time-stamping electronics for photon counting. Because the AWG marker outputs provide a maximum voltage of 1V, which is insufficient for direct digital modulation of the AOM (requiring $\gtrsim$3.3V), a high-frequency comparator was used. This comparator compared the marker signal to a 0.5V reference and output a 5V TTL signal whenever the marker exceeded the threshold, thereby reliably switching the AOM on and off.

The performance of the EOM and the generated sidebands was monitored using a scanning Fabry-Pérot interferometer. We used the 90% arm of the beamsampler to measure this. This allowed direct visualization of the phase-modulated optical spectrum and was used to optimize the microwave drive power and amplifier settings to achieve the desired sideband-to-carrier ratios.

Finally, initial longitudinal relaxation (T_1) measurements were performed by pulsing the first-order beam of the AOM on and off while the laser was tuned to one of the optical transitions. The delay between the pump and probe pulses was controlled using a digital delay generator (SRS DG645), enabling measurement of the population recovery as a function of time. Later, when the EOM was put in place, we were able to replace thermalization wait times with the reset pulse, which ensured our starting population was the same for each measurement.

3.2.0.5 Stability of the Optical Setup

Maintaining the stability of an optical setup is critical for all experiments, but particularly for long measurements (>12 hours) that rely on precise optical powers and stable coupling between the excitation laser and the emitter. In measurements of single solid-state defects, even small fluctuations in beam pointing or optical power can significantly affect the excitation rate and therefore the Rabi frequency and detected photons. The primary source of instability in our setup arises from temperature fluctuations. While the Ti:Sapphire laser itself is enclosed in a temperature-stabilized housing with active HVAC control, the optical breadboard mounted above the cryostat is exposed to ambient laboratory conditions. As a result, small variations in temperature can introduce mechanical drift in the optical components.

One mechanism for this drift is the thermal expansion and contraction of optomechanical mounts. Mirror mounts, for example, rely on finely threaded adjustment screws to control beam alignment. Changes in temperature can cause these screws and the surrounding mount to expand or contract slightly, leading to small angular shifts in the mirror orientation. Even minute changes in mirror angle can alter the beam pointing, which in turn changes the spatial overlap between the laser beam

and the emitter, ultimately affecting the optical power density experienced by the defect.

Temperature variations can also influence the polarization state of light propagating through optical fibers. Because our setup uses a polarization-dependent beam sampler to monitor the optical power delivered to the microscope objective, changes in the fiber polarization state can translate into fluctuations in the measured power. In addition, the fiber coupling optics themselves can undergo thermal expansion or contraction, which may modify the coupling efficiency into or out of the fiber and introduce further power fluctuations. Furthermore, the electro-optic modulator is sensitive to polarization changes and so the modulation efficiency of the sidebands can fluctuate as well. To mitigate these effects, several measures could be implemented. The Ti:Sapphire laser could be coupled to the cryostat optical breadboard using a polarization-maintaining (PM) fiber in order to stabilize the polarization state of the delivered light. In the event that a PM-fiber is unavailable, a 3-paddle system can be used to induce strain to the fiber effectively pinning the polarization state. Furthermore, the number of free-space optical components between the fiber output and the cryostat objective were minimized, reducing the number of alignment-sensitive elements that could drift over time. Lastly, a box enclosing the system was used to mitigate large temperature swings and drafts from the air circulation on mirror drift. These steps helped improve long-term stability during extended measurements.

3.3 Fabrication Methods and Samples

This section describes the different samples investigated in this thesis and the fabrication methods used to produce them. The primary technique employed to create NiV centers is ion implantation. We therefore begin with a brief review of ion implantation before discussing the specific samples in detail. More broadly, such a review is useful because ion implantation is a widely applied and highly successful method for introducing controlled concentrations of impurity atoms and point defects into solid-state materials.

3.3.1 Ion Implantation

Ion implantation has been used extensively over the past several decades as a means of incorporating impurity atoms that cannot be readily introduced during crystal growth [195]. In diamond, this technique has enabled the creation of a wide range of color centers, including the NV^-, SiV^-, GeV^-, SnV^-, and PbV^- centers [196]. In a typical implantation process, an ion beam is accelerated to a chosen kinetic energy and directed onto the target material, where the ion energy determines the approximate implantation depth [136]. As the ions penetrate the crystal, their energy is dissipated through collisions with both electrons and nuclei in the lattice [195]. These collisions can displace

carbon atoms from their lattice sites, creating vacancies and interstitials, and can ultimately allow the implanted impurity atoms to occupy energetically favorable positions in the lattice [197].

Two primary parameters control the outcome of the implantation process. The first is the ion fluence, typically specified in ions/cm^2, which determines the areal density and thus the concentration of implanted impurities. The second is the ion energy, which sets the stopping range of the ions and therefore the depth distribution of the implanted species. Together, these parameters also influence the amount of lattice damage introduced during implantation [136]. While ion implantation provides a powerful and flexible means of defect engineering, it is not without drawbacks. The process inevitably creates additional, unwanted defects, introduces strain into the crystal, and offers only stochastic or random control over the final positions of individual emitters [195]. Although post-implantation annealing can mitigate the first two issues, deterministic placement of single-photon sources remains challenging due to the inherently probabilistic nature of the process; it has been estimated, for example, that creating a perfect array of ten single emitters by implantation alone could require more than 2×10^4 attempts [198].

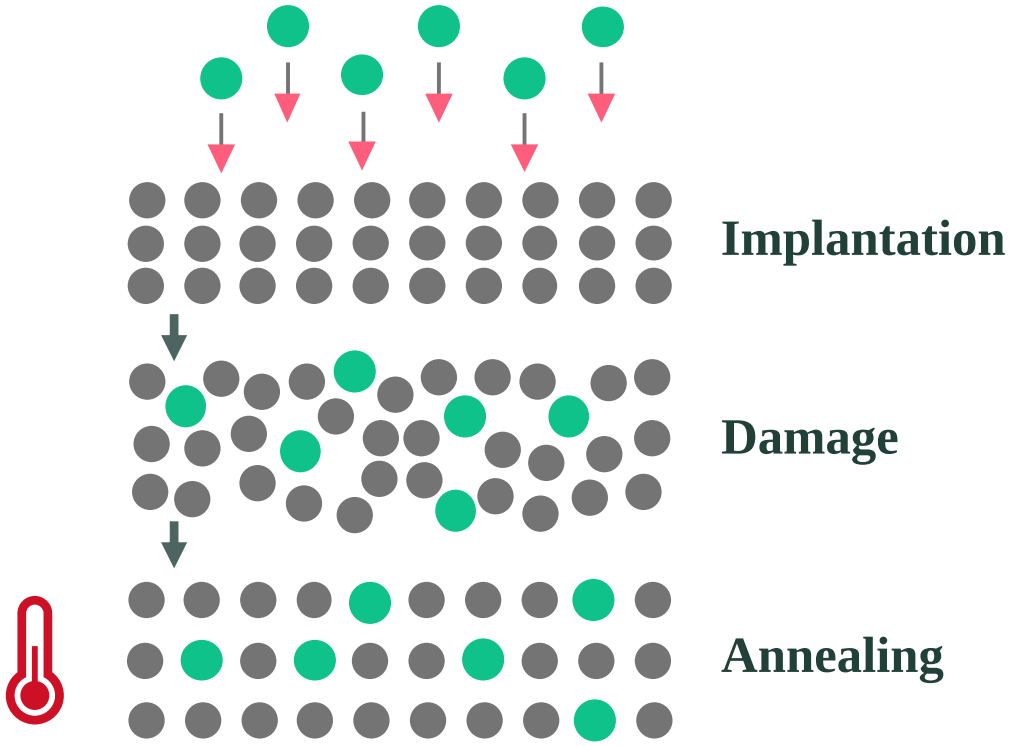

Figure 3.3 Diagram of the steps of ion implantation with an atomic graphic shown. First, ions are accelerated towards the pristine diamond surface. The ions collide with the carbon atoms and displace them, creating vacancies, and other strain and defects. Then, high temperature annealing and sometimes pressure is added to rearrange the atoms back to a energetically favorable positions. Importantly, this diagram should include vacancy defects, as it stands it only shows substitutional defects.

3.3.1.1 Implantation Damage and Annealing

The lattice damage produced during ion implantation can significantly degrade the optical and spin properties of the defects of interest. In particular, implantation-induced strain can shift the zero-phonon lines of color centers and lead to substantial inhomogeneous broadening of their optical transitions [199]. In addition, implantation creates interstitial carbon atoms and vacancy complexes (including single vacancies, divacancies, and larger vacancy chains), which can act as charge traps and contribute to charge-state instability [200]. To repair this damage, post-implantation annealing is routinely employed. Single vacancies become mobile at temperatures around 900°C, while divacancies typically require temperatures near 1100°C [201]. Annealing is usually performed in vacuum or in an inert gas atmosphere, such as argon, to prevent oxidation of the diamond surface [202]. Higher-order vacancy complexes are less well understood but are known to be removable using high-temperature, high-pressure annealing treatments. In practice, such annealing steps substantially improve the optical linewidths and spectral stability of implanted defects and are therefore essential when using ion implantation for quantum emitter fabrication. Additional damage can also manifest as surface graphitization, in which broken sp^3 bonds are converted into sp^2-bonded carbon [136]. This graphitic layer can typically be removed using appropriate acid cleaning procedures.

For the specific case of NiV formation, both a nickel atom and a nearby lattice vacancy must come together to form the desired split-vacancy complex. Annealing therefore plays a dual role: it not only heals implantation-induced damage but also activates the NiV centers by enabling the migration and pairing of nickel atoms and vacancies into their thermodynamically stable configuration, as predicted by first-principles calculations.

3.3.1.2 Alternative Approaches

Alternatives to ion implantation for the creation of defects for use in quantum information processing exist. Ion implantation is useful because the silicon electronics industry heavily developed it for doping purposes, but as stated above it can introduce damage and strain to the sample. The first main alternative is chemical vapor deposition (CVD). The growth process involves a diamond seed crystal being exposed to hydrogen and a carbon containing gas, for example methane, in a chamber at temperatures from 900 to 1200 ° C. Then, a microwave is applied to the gas, which breaks the gas molecules down and causes the carbon atoms to diffuse toward the diamond seed [203] and the diamond grows from there. This method is a nice alternative as, unlike high pressure high temperature recipes, which mimic the extreme conditions of the earth, such high temperatures (1600-2000° C) and high pressures are not required. Impurities can be incorporated during growth by introducing additional dopant gases to the chamber [204]. The natural incorporation during

growth minimizes the creation of strain and produces no damage associated with bombarding the surface like ion implantation. However, it is not without its downsides. In particular, control over the density of incorporated defects is difficult and achieving low concentrations is also challenging. Furthermore, there is no control over where the defects will be located as it is related to a plasma which usually engulfs the entire sample. Moreover, the plasma created by the heating of the gas can even etch away parts of a diamond growth reactor and cause incorporation from the resulting material etched away. For example, creation of SiV defects from quartz windows or domes.

A second approach is laser writing of individual defects using short, high energy laser pulses. This fabrication method has emerged in recent years as a serious competitor to ion implantation as it offers much higher spatial resolution and thus more spatial control for the creation of single emitters [67]. In this approach, tightly focused femtosecond laser pulses are used to locally generate vacancies within the crystal, and subsequent annealing (which can be done locally with more laser pulses or conventional oven annealing) activates color centers at the written locations. Owing to the nonlinear nature of femtosecond laser–matter interactions [205] and the use of aberration correction techniques [206], vacancies can be created with sub-diffraction-limited spatial resolution at arbitrary depths within the diamond, without damaging the material. Because any damage created is localized to the defect creation site, it can usually be healed far easier than ion implantation. Furthermore, one large disadvantage of ion implantation is the creation of large vacancy complexes. Laser writing; however, does not suffer from this because it creates individual vacancies and then converts them to defects. Indeed, this method has been used to generate NV^- centers with near-unity yield [207] and to create single color centers in silicon carbide [208]. Additionally, defects created with this method have been shown to possess lifetime limited linewidths necessary for most complex quantum information processing tasks [209]. This technique also enables the creation of defects within existing nanophotonic structures and even diamond membrane devices [210]. Importantly, however, this technique requires that the material already contain the impurity of interest.

3.3.2 Nanopillar Sample

This is the only sample in this thesis in which nanopillars were etched, hence, the name. Prior to nanopillar fabrication, we performed cryogenic magneto-optical spectroscopy and Debye-Waller factor measurements (see Chapter 4). After characterizing it as a bulk substrate, we decided to etch nanopillars into it in order to improve the light collection efficiency of the NiV emitters and for charge state reasons. First, I will discuss the original bulk substrate and implantation recipe. Then I will motivate why we etched nanopillars, followed by the nanopillar recipe and clean room tips and tricks used to pull it off.

Figure 3.4 Camera photo of the two NDT IIa and IIb HPHT samples. We only used the IIa sample in this thesis. The numbers in the different regions on the sample indicate the order of magnitude for ion implantation dose used in that region, e.g. 15 corresponds to 10^{15} ions/cm^2.

3.3.2.1 Sample Description

3.3.2.1.1 Starting Material The starting material was a ($\langle 111 \rangle$)-oriented, type IIa high-pressure high-temperature (HPHT) grown single crystal diamond substrate with 35(5) ppb of uncompensated substitutional nitrogen as measured by EPR. The sample was implanted with ^{58}Ni ions at an energy of 1 MeV using four different fluences: 10^{11}, 10^{12}, 10^{13}, and 10^{15} ions/cm^2, as indicated in Fig. 3.4. The implantation was performed at RUBION (Ruhr University Bochum, Germany). Following implantation, high-pressure high-temperature annealing was carried out for two hours at 2000°C and 8 GPa at Element Six in order to repair lattice damage and activate nickel-related defect complexes.

3.3.2.1.2 Post-Implantation Observations As can be seen in Fig. 3.4, the region implanted at the highest dose (10^{15} ions/cm^2) exhibits a markedly different appearance compared to the lower-dose regions, which remain relatively transparent. We attribute this change in appearance to severe implantation-induced damage, potentially including partial graphitization. After acid cleaning, this region appears greenish under illumination, a coloration that is commonly associated with nickel-containing materials and/or a high density of vacancies. Regardless of the precise microscopic origin, this high-dose region serves primarily as a convenient alignment and landmark area due to its high fluorescence count rate. For quantitative optical and spin measurements, however, we focus on the lower-dose regions, where lattice damage, strain, and inhomogeneous broadening are expected to be significantly reduced.

3.3.2.1.3 Diamond Types A brief discussion of diamond types is useful for context. Type IIa diamond is the purest class of diamond, characterized by the absence of measurable nitrogen and boron impurities, and is therefore particularly attractive for quantum applications. Type IIb diamonds are similarly low in nitrogen content but contain higher concentrations of boron. In nature, type IIa diamonds are rare, comprising less than approximately 2% of gem-quality diamonds, and are correspondingly valuable. In contrast, chemical vapor deposition (CVD) diamonds can be grown in the laboratory with extremely high purity and at much lower cost. The electronic-grade CVD diamonds used elsewhere in this thesis were purchased from Element Six, a leading supplier of high-quality synthetic diamond. These electronic-grade substrates typically contain less than 5 ppb of substitutional nitrogen and less than 1 ppb boron, making them the preferred choice for demanding quantum optical and spin experiments.

3.3.2.2 Why Nanopillars?

A central challenge for diamond-based quantum emitters is efficient photon extraction. Although diamond is an excellent host for optical interfaces due to its wide bandgap and high optical

transparency, its large refractive index ($n \approx 2.4$) severely limits the fraction of fluorescence that can escape a planar diamond-air interface. This limitation arises primarily from total internal reflection (TIR), which confines most of the emitted light to guided modes within the diamond. This is useful for making waveguides, but in terms of getting light out of bulk diamond, it makes it challenging [28].

For a simple illustration, consider a point emitter located near a flat diamond-air interface. For a simple estimate, we assume isotropic emission within diamond (optimistic approximation which useful here; real emitters radiate with a dipole pattern and experience depth-dependent near-field effects). Light incident on the interface at an internal angle θ_1 refracts according to Snell's law,

$$n_1 \sin(\theta_1) = n_2 \sin(\theta_2), \tag{3.6}$$

where $n_1 \approx 2.4$ (diamond) and $n_2 \approx 1$ (air). Total internal reflection occurs for $\theta_1 > \theta_c$, where the critical angle is

$$\theta_c = \sin^{-1}\left(\frac{n_2}{n_1}\right) \approx 24.6^\circ. \tag{3.7}$$

Thus, even before considering the collection optics, only light emitted within this small escape cone can actually leave the diamond.

In practice, the collection objective imposes an additional constraint. An objective with numerical aperture NA in air collects angles up to $\theta_{\text{air}} = \sin^{-1}(\text{NA})$. The corresponding maximum internal angle in diamond that can be collected is

$$\theta_{\max} = \sin^{-1}\left(\frac{n_2}{n_1} \sin\theta_{\text{air}}\right) = \sin^{-1}\left(\frac{\text{NA}}{n_1}\right). \tag{3.8}$$

For our cryogenic objective (NA = 0.82), this gives $\theta_{\max} \approx \sin^{-1}(0.82/2.4) \approx 20^\circ$, which is slightly smaller than the critical angle and therefore is the dominant limitation.

Using the isotropic-emission approximation, a geometric upper bound on the collected fraction is given by the collected solid angle divided by 4π:

$$\eta_{\text{bulk}} \approx \frac{\Omega_{\text{col}}}{4\pi} = \frac{2\pi\,(1 - \cos\theta_{\max})}{4\pi} = \frac{1 - \cos\theta_{\max}}{2}. \tag{3.9}$$

With $\theta_{\max} \approx 20^\circ$, this yields $\eta_{\text{bulk}} \approx 3\%$. This estimate neglects Fresnel reflection at the interface and dipole-radiation effects, so it should be regarded as an optimistic geometric bound; in practice, the collected fraction can be lower and depends on emitter depth and dipole orientation [194].

Nanopillars address this extraction bottleneck by modifying the optical environment around the emitter. Instead of emitting into bulk diamond bounded by a planar interface, the emitter can couple to guided or quasi-guided modes of the pillar, which direct a larger fraction of the light upward into

modes that better overlap with the collection cone of the objective. At the same time, the pillar geometry suppresses emission into high-angle trajectories that would otherwise be trapped by total internal reflection at a flat diamond surface. In this way, the nanopillar acts both as a local photonic structure and as a waveguide, improving the probability that emitted photons leave the diamond and are collected. Achieving strong enhancement requires the pillar dimensions to be chosen so that the supported optical modes are well matched to the collection optics. These considerations motivate the nanopillar geometry and fabrication approach described in the following section. In practice, collection-efficiency improvements by a factor of roughly 5 to 10 are commonly achieved [211].

3.3.2.3 Fabrication Recipe

Nanopillars were fabricated in-house at the Keck Microfabrication Facility (KMF) in the Biomedical Physical Sciences building at Michigan State University. I still remember my first day getting trained in there, learning that some purple liquid had been mistakenly poured in the waste bin when it should not have. Back to the recipe. The process consists of (i) electron-beam lithography (EBL) to define an etch mask, (ii) metal deposition and liftoff to form a robust hard mask, (iii) inductively coupled plasma reactive-ion etching (ICP-RIE) to transfer the pattern into diamond, and (iv) mask removal. The full recipe diagram can be seen in Figure 3.5

Sample mounting for spin coating Diamond chips are typically smaller than the spin coater chuck and may not seal reliably to the vacuum hold-down. To ensure uniform resist coating and reliable chucking, each diamond sample was attached to a larger Si carrier wafer using a small amount of silver paint. The paint was hardened on a 30°C hot plate for 2-3 minutes. Mounting on a carrier wafer also reduces edge-beading and helps produce a more uniform resist thickness across the patterned area.

Bilayer resist stack and baking A bilayer resist stack was used to enable reliable liftoff of the aluminum hard mask. First, MMA(8.5)/MAA EL9 (9% poly(methyl methacrylate/methacrylic acid) in ethyl lactate) was spin-coated at 4000 rpm for 50 s, followed by a 180°C hot-plate bake for 2 minutes. Next, PMMA C2 (2% poly(methyl methacrylate) in chlorobenzene) was spin-coated at 4000 rpm for 50 s and baked at 180°C for 2 minutes. This bilayer process creates an undercut profile after development (the bottom layer develops faster), which reduces sidewall metal deposition and significantly improves liftoff yield compared to a single-layer resist, particularly for metals with larger grain size such as aluminum.

Electron-beam exposure and pattern design Pillar patterns were defined using a CAD software which could be loaded onto the by EBL (Hitachi SU5000 FESEM at KMF). The design consisted of repeated 10×10 arrays of circular features, where each column corresponded to a different nominal

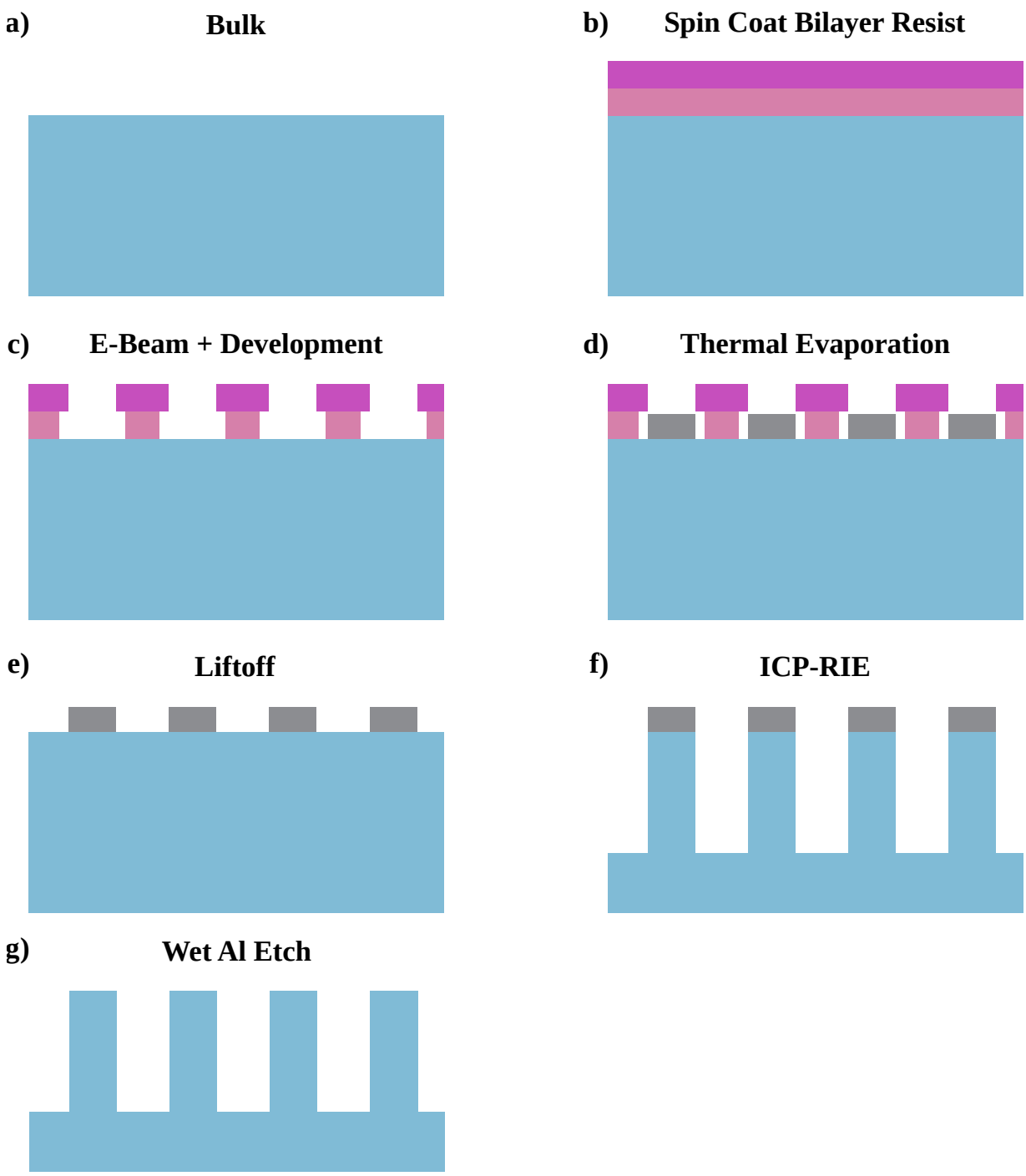

Figure 3.5 **(a)-(g)** Diagram of steps taken to fabricate diamond nanopillars. Full description for each step can be found in the main text.

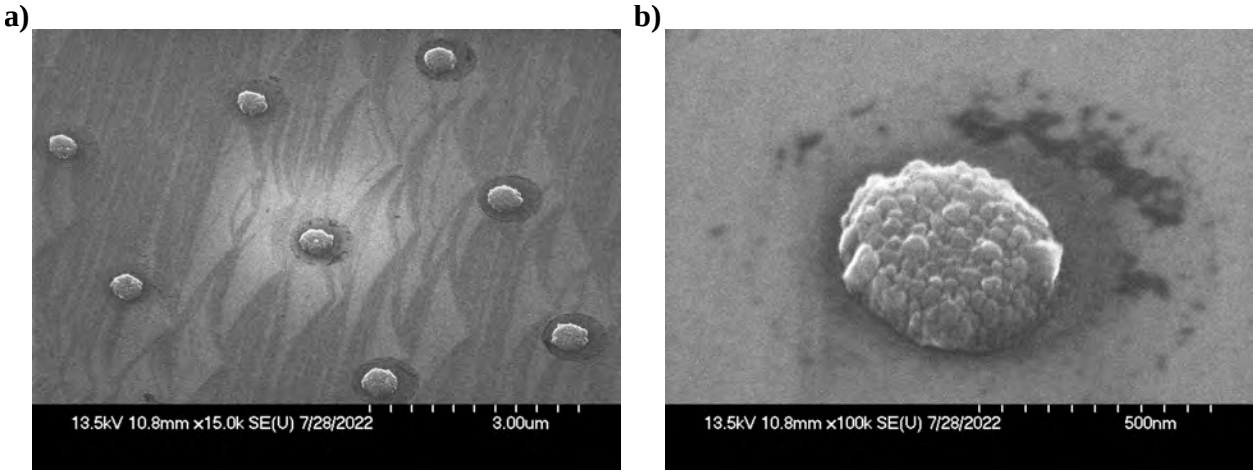

Figure 3.6 SEM images of aluminum masks on diamond after performing liftoff.

pillar diameter. This allowed rapid exploration of pillar geometries and objective coupling. The diameters ranged from 200 to 400 nm in 20 nm increments (200, 220, 240, 260, 280, 300, 320, 340, 360, 380, 400 nm).

Development After exposure, the resist was developed in a 1:3 mixture of MIBK:IPA for approximately 55 s, followed by an IPA rinse for 15–20 s and a nitrogen dry. This development condition was chosen to balance feature fidelity and resolution.

Aluminum hard-mask deposition Following development, an aluminum hard mask was deposited by thermal evaporation. The chamber was pumped to a base pressure of approximately 2.5×10^{-6} Torr before deposition. A nominal aluminum thickness of 100 nm was used, monitored by a quartz crystal microbalance. In practice, mask integrity during liftoff was strongly influenced by the deposited film morphology; slower evaporation rates tended to improve liftoff yield by reducing effective grain size and minimizing resist sidewall bridging.

Liftoff Liftoff was performed by soaking the sample in acetone for 1 hour, followed by brief ultrasonication. To minimize redeposition of dissolved resist and metal flakes, the sample was transferred to a fresh acetone bath for ultrasonication. During transfer, the sample was kept continuously wet with acetone to prevent drying artifacts that can compromise mask adhesion. Ultrasonication was kept short (~3–5 s) to avoid dislodging the aluminum masks. Mask quality was first assessed using an optical microscope and, when necessary, confirmed by SEM (see Fig. 3.6).

ICP-RIE etching of diamond Nanopillars were etched using an inductively coupled plasma reactive-ion etcher (Trion Technology Phantom III ICP-RIE). Prior to etching, an O_2 plasma chamber clean was performed (30 sccm O_2, 250 mTorr, 100 W RIE power, 100 W ICP power, 300 s). The

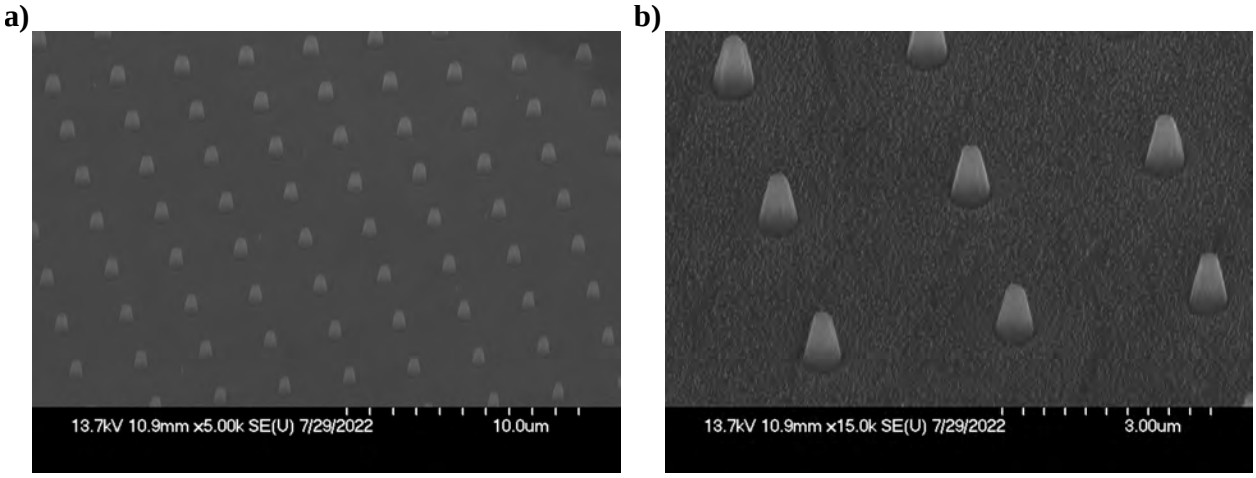

Figure 3.7 SEM images of diamond nanopillars containing NiV centers fabricated in this Thesis. a) shows a 5000x magnification image with scale bar in bottom right, while b) shows a more zoomed in 15000x magnification image of the pillars. Full description of their properties and fabrication recipe can be found in the text. The sample used for this was the NDT IIa HPHT sample and these are pillars in the $10^{13}13$ ions/cm^2 region.

chamber was then conditioned using the intended etch recipe before loading the sample.

The diamond etch was performed using an Ar/O_2 chemistry (30 sccm O_2, 10 sccm Ar) at 15 mTorr for 3 minutes with 400 W ICP power and 300 W RIE power. In this process, the ICP source primarily controls plasma density (and thus the concentration of reactive species for chemical etching), while the RF bias (RIE power) controls the ion energy and directionality, which is critical for anisotropic etching and vertical sidewalls. Aluminum exhibits a substantially lower etch rate than diamond under these conditions, enabling it to serve as an effective hard mask for the durations used here.

If only a portion of the sample was to be etched (e.g., leaving an unetched ensemble region), a thin glass coverslip was used as a physical shadow mask to block the plasma over selected areas. During operation, occasional plasma instabilities were mitigated by minor tuning adjustments (e.g., matching network capacitance), as needed.

Mask removal and post-processing After etching, the aluminum masks were removed using a commercial aluminum etchant (acid mixture), with a typical etch time of 3-4 minutes (or until bubbling ceased), followed by a 5-minute DI water soak and nitrogen drying. During wet processing, the sample was handled carefully to prevent flipping or strong fluid agitation, which can mechanically damage high-aspect-ratio pillars. After mask removal, the sample was rinsed and dried, completing the nanopillar fabrication process.

Notes on micromasking In some etched regions, a grass-like background was observed surrounding

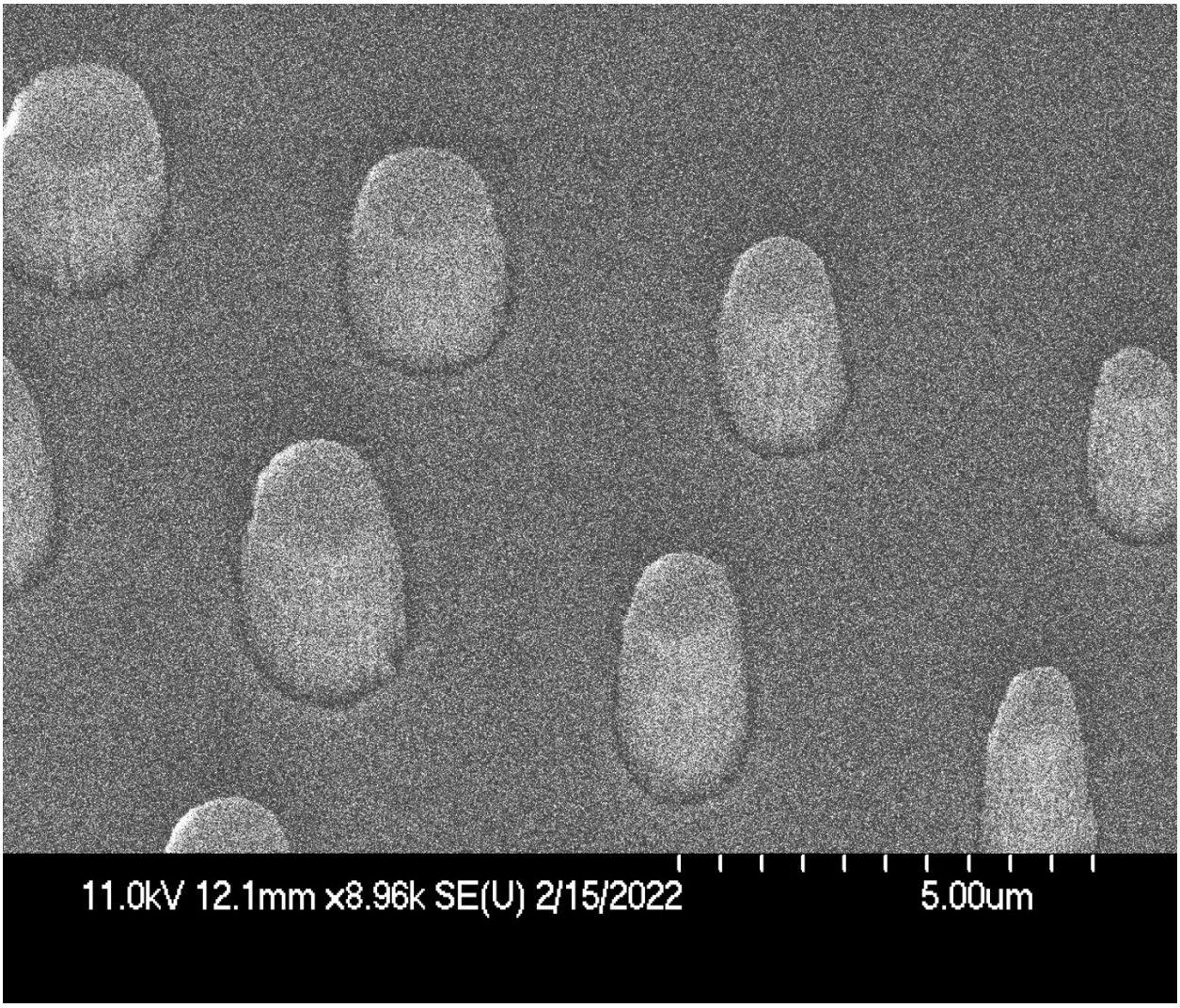

Figure 3.8 SEM image of diamond nanopillars showing different radius size for pillars as well as at an angle of 40 degrees with respect to the sample. From the right at the bottom of the image are the: electron beam energy, working distance, magnification, type of electron being detected, date, and scale bar.

the pillars, consistent with micromasking. This effect can occur when redeposited material or residual particulate contaminants act as local masks during etching. It was particularly common in HPHT substrates, which can contain residual metallic inclusions and other implantation- or growth-related contaminants.

3.3.3 p-i-p Sample

The p-i-p sample refers to a device in which two p-type doped regions are separated by a thin intrinsic (i) region. The starting substrate was a (100)-oriented, CVD-grown electronic-grade diamond from Element Six. A widefield microscope image of the fabricated device is shown in Fig. 3.9. The detailed motivation for this device architecture is discussed in Chapter 5; briefly, applying a bias voltage across the junction allows the Fermi level in the diamond to be tuned locally. This enables controlled stabilization of different defect charge states, in particular the negatively charged NiV^- center studied in this work. In the following, we summarize the fabrication process.

3.3.3.1 Fabrication Recipe

The device used in this work was a p-i-p junction fabricated on a (100)-oriented, chemical-vapor-deposition-grown electronic-grade diamond substrate obtained from Element Six, with a substitutional nitrogen concentration below 5 ppb. The p-type regions were created by boron ion implantation through a bow-tie-shaped Ti/Au mask defined by electron-beam lithography.

To form the p-type regions, boron was implanted at two energies, 40 keV and 15 keV, in order to produce an approximately uniform acceptor concentration over a depth exceeding 50 nm. This implantation profile was designed to leave a thin, highly damaged near-surface layer, less than 40 nm thick. The sample was then annealed in vacuum at 900°C for 1 h, followed by a second anneal at 1600°C for 3 h, in order to electrically activate the boron acceptors. During this process, the heavily damaged near-surface region, where the vacancy density exceeded $10^{22}\,\mathrm{cm}^{-3}$, was converted to graphite. This graphitized layer was subsequently removed by cleaning the sample for 4 h in a boiling mixture of nitric, sulfuric, and perchloric acids, leaving behind a highly p-doped diamond surface layer.

After formation of the p-type regions, nickel was implanted into the intrinsic region of the device in order to create Ni-related defects. The implantation was performed at an energy of 70 keV using four different fluences, 3×10^9, 1×10^{10}, 3×10^{10}, and $1 \times 10^{12}\,\mathrm{cm}^{-2}$, so that the effect of applied bias could be compared for both dilute and dense defect ensembles. A rectangular aperture of dimensions $15 \times 35\,\mu\mathrm{m}^2$ was used to spatially confine the implantation to the central intrinsic region of the p-i-p junction. Following nickel implantation, the sample was annealed again at 1600°C in vacuum and then subjected to a gentle oxygen plasma clean.

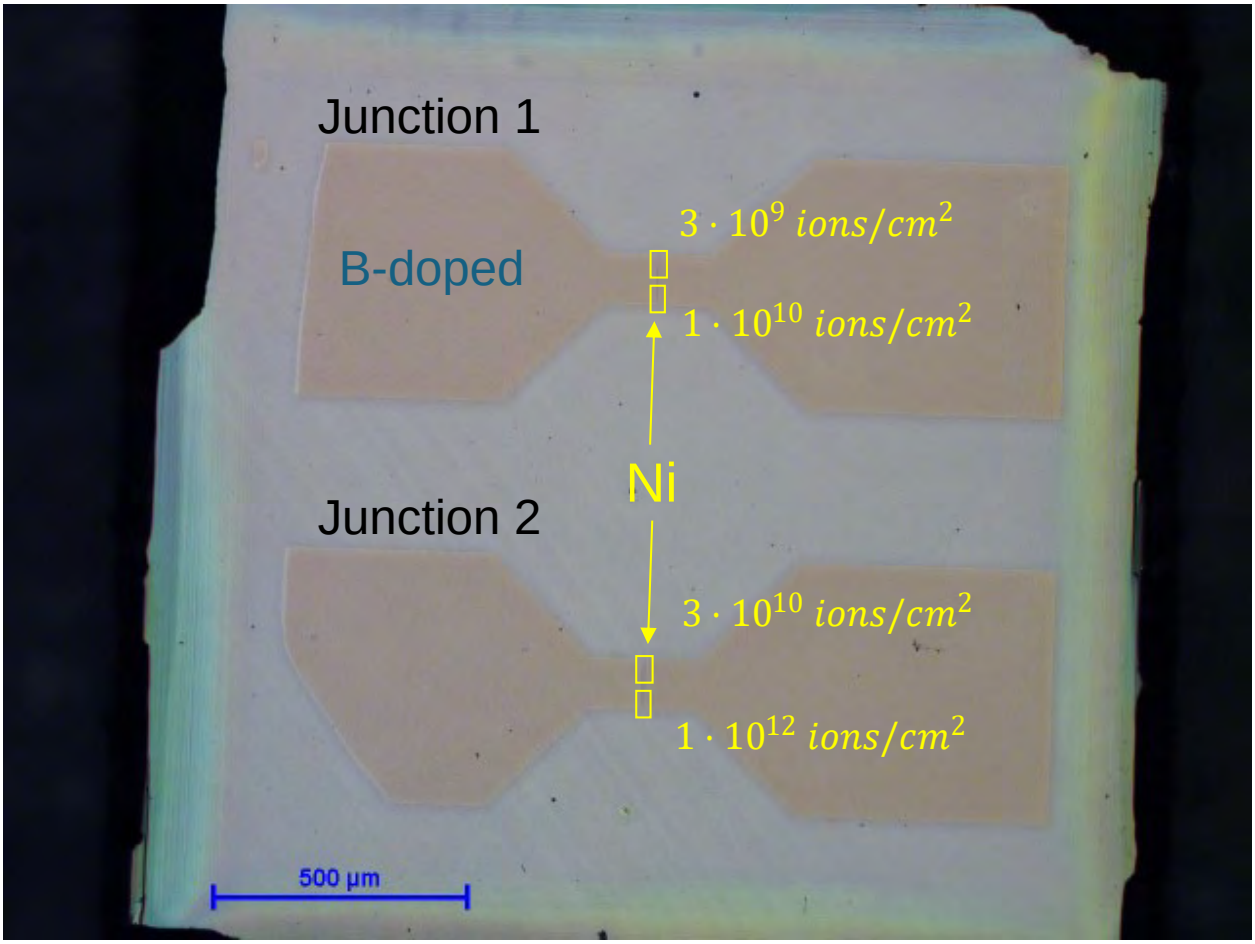

Figure 3.9 Widefield transmission microscope image of the p-i-p sample along with labels indicating implantation doses and corresponding implantation regions. Full description of the fabrication can be found in the main text.

Unlike the NDT IIa sample discussed previously, this p-i-p device was not subjected to a high-pressure high-temperature (HPHT) anneal. This decision was made because of concern that the implanted junction structure, particularly the near-surface doped regions, might not survive such extreme processing conditions and could be degraded or removed. As a result, we anticipated that the optical linewidths in this sample might be broader than those observed in the HPHT-annealed NDT IIa sample.

3.3.3.2 Electrical Characterization

The p-i-p device was electrically contacted using silver conductive paint and 38-gauge copper wires. Current–voltage (I–V) characteristics were measured with a Keithley 2400 source meter. All I–V measurements were first performed at room temperature to verify the Schottky-like behavior of the junctions (see Chapter 5), before cooling the sample to 1.6K for optical experiments.

3.3.4 Other Samples Used

This subsection describes additional samples that were studied in this thesis but played a more limited role in the main results and did not appear in the primary publications. They are included here for completeness.

3.3.4.1 Sandia 8-Implantation-Dose Sample

This sample is a ($\langle 111 \rangle$)-oriented HPHT Type IIa diamond implanted with eight different ^{58}Ni fluences: 10^9, 5×10^9, 10^{10}, 5×10^{10}, 10^{11}, 5×10^{11}, 10^{12}, and 5×10^{12} ions/cm^2. A high-temperature anneal high pressure anneal was performed to partially heal lattice damage induced by implantation and to activate the defects. The sample and the individual implantation regions are shown in Figure 3.10. The implantation was carried out at Sandia National Laboratories.

3.3.4.2 Low-Density Electronic-Grade Samples

Two additional low-dose implantation samples were studied. Both were electronic-grade CVD diamonds from Element Six, implanted with ^{58}Ni at fluences of 1×10^9 ions/cm^2 and 1×10^{10} ions/cm^2, respectively. Post-implantation annealing was performed to reduce residual lattice damage and activate the implanted defects.

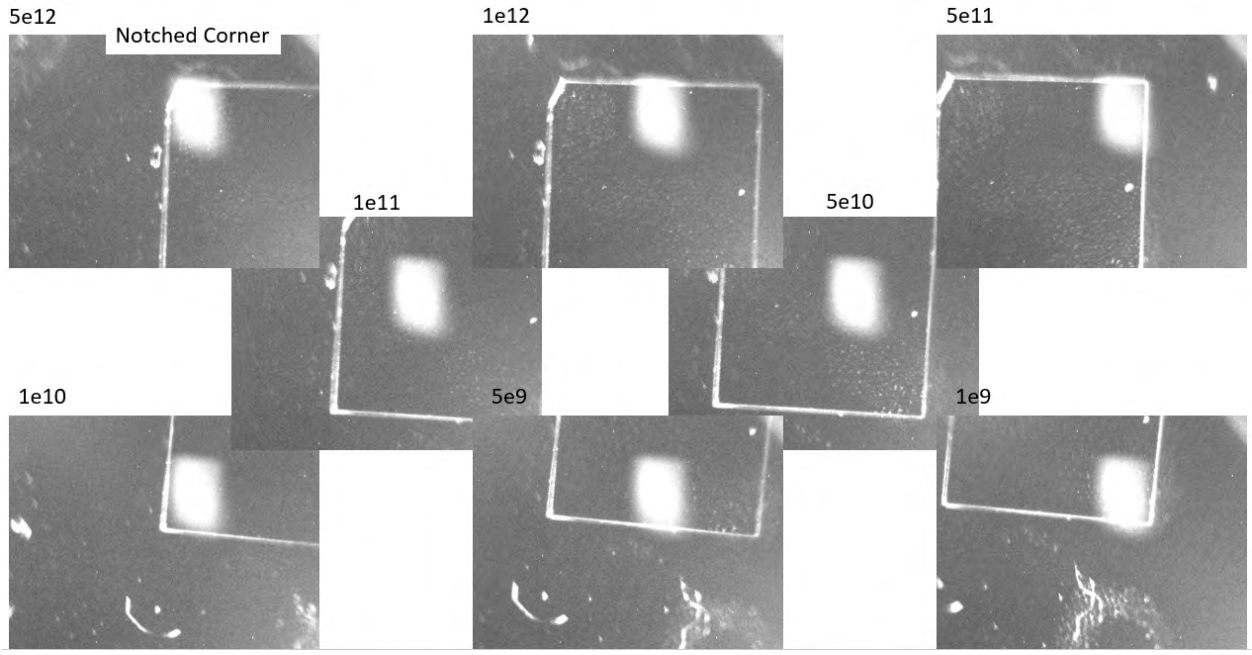

Figure 3.10 Widefield transmission microscope images of the multi-dose implantation sample fabricated at Sandia National Laboratories. Each image corresponds to a different implantation dose, with the bright region indicating the ion beam spot and the associated dose labeled in each panel.

3.4 Summary

This chapter reviewed the experimental methods and samples used in this thesis. First the basic operating principles of confocal microscopy are explained along with widefield microscopy and the resolution benefits gained from adding spatial filters to reject out of focus light. Then, the experimental setup is described in terms of excitation lasers, coupling optics, cryostat, and various detection systems. These include a spectrometer, single photon detectors and a Hanbury Brown-Twiss setup. Control electronics are then described including bias voltage control for the p-i-p sample and the electronics necessary for coherent control. Then, various defect creation strategies are described including ion implantation, laser writing and CVD incorporation along with their respective disadvantages. Then the samples used in this thesis are described in terms of starting material and fabrication method including the nanopillar sample, p-i-p sample, and other ion implanted samples in HPHT and CVD grown material.

Chapter 4

Electronic structure and optical properties of the NiV

In this chapter, we introduce a group theoretical model for the NiV^- and use it to predict how the energy levels split under a magnetic field. We then perform magneto-optical spectroscopy at cryogenic temperatures to compare to the theory, finding close agreement. This allows us to confirm the electronic and geometric structure of the NiV^-. Afterwards, we assess the optical properties of ensembles of NiV^- under off-resonant excitation, finding spectrometer limited linewidths of tens of GHz. We also measure the Debye-Waller factor, finding a value of 0.62. Moreover, we examine the temperature dependence of the NiV^- PL and linewidth, finding a factor of 2 increase in PL intensities at 1.6K compared to room temperature, potentially indicative of stronger non-radiative transition rates at higher temperatures. Additionally, we perform resonant excitation, achieving lifetime-limited linewidths with the aid of 532 nm light to revive the NiV^- charge state. Lastly, we perform autocorrelation measurements to determine if the emitters are single centers, finding that we can isolate individual emitters separated in frequency.

4.1 Group Theory for NiV

Before experimentally assessing whether the NiV center can serve as a spin qubit, we must first understand its electronic structure. In particular, the orbital level structure determines which optical transitions are allowed and whether the defect can support spin initialization, readout, and coherent control. Group theory provides a powerful way to infer much of this structure directly from symmetry, without requiring a full solution of the underlying many-electron quantum mechanical problem. In practice, this allows one to identify the symmetry of the allowed orbitals, their degeneracies, and which couplings or perturbations are permitted by symmetry. Once these orbitals have been identified, they can be filled with the appropriate valence electrons to determine the resulting spin configurations for the ground and excited states. In this section, we introduce the group-theoretical

concepts needed for the NiV center and use them to construct the relevant symmetry-adapted orbitals. For a more complete treatment, especially for the closely related SiV center, we refer the reader to Ref. [194].

4.1.1 NiV Point Group and Representations

To use group theory for a defect, one must first identify the symmetry of the defect itself. If the defect structure is not already well-known, this requires making an assumption about its structure. Once a certain structure has been chosen, then one needs to identify which point group the defect belongs to. A point group is the set of symmetry operations that leave the defect structure unchanged while keeping at least one point fixed in space. These operations can include rotations, reflections, inversion, and improper rotations, where an improper rotation means a rotation followed by a reflection. The point group therefore describes the local geometric symmetry of the defect. This should be distinguished from a space group, which describes the symmetry of an entire crystal lattice. In addition to point-symmetry operations, a space group also includes translations, meaning shifts by whole lattice vectors that map one unit cell of the crystal onto another. A point group does not include such translations, because it is concerned only with the symmetry of the localized defect rather than the periodic symmetry of the full crystal.

To proceed, we must now assume a specific atomic structure for the NiV defect, since the point group is determined by the geometry of the defect. This assumption about structure can later be tested by comparing the predicted level structure with experimental magneto-optical measurements. When nickel is incorporated into diamond, for example through ion implantation, several defect configurations are possible in principle. First-principles calculations identified both substitutional nickel and nickel-divacancy complexes as energetically favorable, with their relative stability depending on the Fermi level of the diamond [212]. However, as discussed in Chapter 1, more recent density functional theory (DFT) calculations by Thiering and Gali found the near-infrared 1.4 eV emitter to be most consistently explained by a split-vacancy nickel-divacancy complex, NiV^-, in which the nickel atom relaxes to the midpoint between two adjacent vacancies along the $\langle 111 \rangle$ axis [171]. Hence, we adopt this split-vacancy configuration as the starting point for the present group-theory analysis.

This structure belongs to the D_{3d} point group, which is the same symmetry class as the SiV center and the heavier group-IV vacancy centers [136, 213]. In particular, this point group possesses inversion symmetry as well as a threefold rotational axis. Following the standard treatment of the SiV center, we model the localized defect complex as consisting of the nickel atom, the two vacancies, and the six nearest-neighbor carbon atoms [136]. Because NiV and SiV share the same D_{3d} symmetry, the general symmetry analysis of their defect orbitals follows the same overall

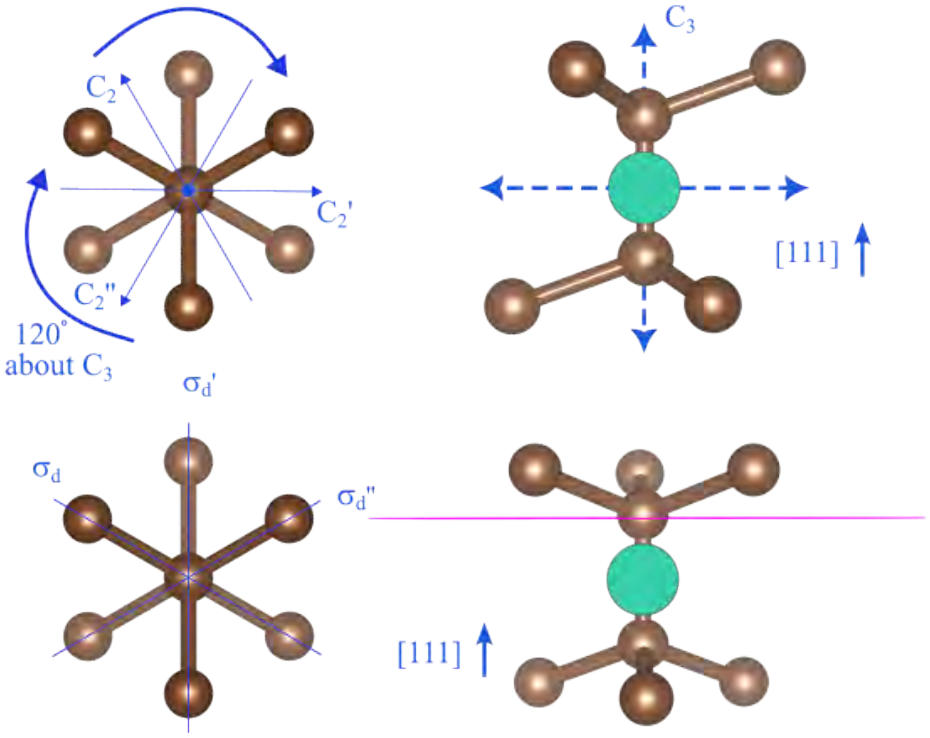

Figure 4.1 Diagram of diamond defect structure with different orientations labeled and symmetry axes shown.

structure. The main difference; however, lies in the impurity orbitals: whereas the SiV electronic structure is dominated primarily by combinations of the neighboring carbon dangling-bond orbitals; in NiV, the nickel $3d$ orbitals play an important role and hybridize differently with the surrounding lattice [171]. As a result, the detailed orbital composition differs from that of SiV even though the overall symmetry framework remains the same.

Having made our assumption about the NiV defect's point group, the next step is to determine what this symmetry implies for its electronic states. The point group consists of all symmetry operations that leave the defect geometry unchanged. Since these operations do not alter the physical structure of the defect, they also do not alter its energy, and so the Hamiltonian must remain unchanged under them. Mathematically, this means the Hamiltonian is invariant under the select symmetry operations, or put another way, the Hamiltonian commutes with these operations. We can therefore choose the eigenstates of the Hamiltonian to also transform in well-defined ways under the symmetry operations of the D_{3d} point group. The task of group theory is then to classify the defect orbitals according to these transformation properties.

This is done using representations of the group. A representation assigns a matrix to each

symmetry operation, describing how a chosen set of basis functions changes when that operation is applied. For example, one could choose the x,y,z basis and write matrices which perform certain symmetry operations on that basis. One can then expand this by considering a set of local atomic orbitals and asking the question of how these orbitals are changed or mixed for each symmetry operation of the defect. Furthermore, because the choice of basis is arbitrary, these representations are not in general unambiguous identifiers ofcertain symmetry operations. Indeed, in many cases their description is actually larger than necessary / contains redundancy and can be decomposed into smaller subsets that do not mix with one another under the symmetry operations. Such a description is called a reducible representation, and the smallest independent components which come out after decomposing are referred to as the irreducible representations, or irreps. These irreps are the fundamental symmetry labels of a point group and they tell us which orbitals share the same symmetry, which states are degenerate and which orbitals can hybridize.

The irreducible representations of the D_{3d} point group are summarized in the character table shown in Table 4.1, which provides the symmetry labels needed to construct the defect orbitals. In this table, the columns correspond to classes of symmetry operations and the rows correspond to the irreducible representations of the group. The entries, called characters, describe how basis functions belonging to a given irreducible representation transform under each class of operations, while the basis functions listed in the rightmost columns show how familiar quantities such as coordinates, rotations, and atomic orbitals transform under D_{3d}. The symmetry operations appearing in the table have the following meanings. The symbol E denotes the identity operation, which leaves the system unchanged. The $2C_3$ operations correspond to rotations by $\pm 120^\circ$ about the principal symmetry axis, while the $3C_2$ operations correspond to π rotations about the three twofold axes perpendicular to that axis. The operation i denotes inversion through the center of symmetry. The $2S_6$ operations are improper rotations consisting of a C_3 rotation followed by inversion, and the $3\sigma_d$ operations correspond to the three dihedral mirror planes containing the principal symmetry axis. The labels of the irreducible representations also encode important information. The letters A and E denote non-degenerate and doubly degenerate irreducible representations, respectively. The subscripts g and u indicate even (gerade) and odd (ungerade) parity under inversion, specifying whether the wavefunction is symmetric or antisymmetric under the transformation $\mathbf{r} \to -\mathbf{r}$. More generally, in other point groups one may also encounter T representations, which are triply degenerate, although these do not occur in D_{3d}. For one-dimensional A-type representations, a character of $+1$ means that the basis function is unchanged by the operation, while a character of -1 means that it changes sign. For the two-dimensional E-type representations, the character is the trace of the corresponding 2×2 transformation matrix. A value of 2 means that both components are unchanged, -2 means that both change sign, and 0 indicates that the operation mixes the two components in such a way that the trace vanishes. These properties make the character table a compact summary of how

orbitals and many-electron states transform under the full symmetry group, and therefore provide the foundation for classifying the electronic structure of the defect.

This table is extremely useful as it provides a link between the abstract symmetry of the point group and the physical orbitals of the defect. Starting from a set of local atomic or dangling-bond orbitals, one can determine how they transform under the symmetry operations of the defect and decompose them into irreducible representations. One then forms linear combinations of these orbitals that transform according to definite irreps of the point group. These are called symmetry-adapted orbitals. Because each symmetry-adapted orbital belongs to a specific irrep, its degeneracy and its allowed couplings to other orbitals are determined by symmetry alone. This makes the symmetry-adapted basis a natural starting point for constructing the defect Hamiltonian and for deriving optical selection rules that can be compared directly with experiment.

Table 4.1 Character table of the D_{3d} point group.

D_{3d}	E	$2C_3$	$3C_2$	i	$2S_6$	$3\sigma_d$	Linear, rotations	Quadratic
A_{1g}	1	1	1	1	1	1		$x^2+y^2,\ z^2$
A_{2g}	1	1	−1	1	1	−1	R_z	
E_g	2	−1	0	2	−1	0	(R_x, R_y)	$(x^2-y^2, xy),\ (xz, yz)$
A_{1u}	1	1	1	−1	−1	−1		
A_{2u}	1	1	−1	−1	−1	1	z	
E_u	2	−1	0	−2	1	0	(x, y)	

4.1.2 NiV Symmetry Adapted Orbitals

Now, once the relevant local orbitals have been classified by symmetry, the next step is to construct symmetry-adapted linear combinations (SALCs). These are linear combinations of atomic or dangling-bond orbitals chosen so that they transform according to definite irreducible representations of the point group. This is useful because the symmetry label of an orbital immediately tells us two important things: its degeneracy, and which other orbitals it is allowed to hybridize with. Orbitals belonging to different irreducible representations cannot mix, whereas orbitals transforming according to the same irreducible representation can.

We now analyze the actual orbitals. For the divacancy part of the defect, we follow the same symmetry analysis used for the SiV center. The six dangling-bond orbitals associated with the two adjacent vacancies combine into symmetry-adapted orbitals transforming as

$$a_{1g} \oplus a_{2u} \oplus e_g \oplus e_u. \tag{4.1}$$

For explicit analysis of this, we refer the reader to [194]. The nickel impurity contributes valence orbitals of predominantly $3d$ character. For an isolated Ni atom, there are ten valence electrons which

can be described by a $4s^2 3d^8$ configuration. The five d orbitals are the familiar real combinations

$$xy, \quad xz, \quad yz, \quad z^2, \quad x^2 - y^2,$$

which originate from the $\ell = 2$ spherical harmonics written in Cartesian form. Because the character table of the D_{3d} point group lists how these basis functions transform, it tells us directly how the fivefold degenerate atomic d manifold splits in a D_{3d} crystal field. In particular, the Ni-derived d-orbitals transform as

$$a_{1g} \oplus e_g \oplus e_g, \tag{4.2}$$

that is, as one non-degenerate orbital and two doubly degenerate manifolds.

With this, we can compare orbital symmetries in the divacancy and the ones which match are able to hybridize. As such, it is immediately clear that the Ni-derived e_g orbitals can mix with the divacancy-derived e_g orbitals, forming bonding and antibonding combinations. This hybridization is the main qualitative distinction between NiV and SiV. In SiV, the low-energy electronic structure is dominated primarily by combinations of the carbon dangling-bond orbitals, whereas in NiV the impurity $3d$ orbitals of the nickel atom also play a role [171].

4.1.3 Electron counting and single-electron orbital picture for neutral NiV^0

Now that we have the symmetry-adapted orbitals, we can start filling these single electron orbitals, with each orbital accommodating two electrons of opposite spin in accordance with the Pauli exclusion principle. These many-electron states may then be classified by combining the symmetries of the single-particle orbitals using standard group-theoretical product rules.

We begin with the divacancy. In diamond, each carbon atom is tetrahedrally coordinated and forms four covalent bonds with its neighbors. Removing two adjacent carbon atoms therefore breaks the bonds associated with those lattice sites. Because the two missing atoms originally shared one bond with each other, the divacancy produces six, rather than eight, dangling bonds in total. Each dangling bond contributes one electron, so the divacancy contributes six orbitals and six associated electrons. The nickel impurity contributes additional valence electrons. To a good approximation, neutral nickel has a $3d^8 4s^2$ valence configuration, giving ten valence electrons. The neutral NiV^0 defect therefore contains sixteen electrons in total.

Now, group theory alone does not give the absolute energies of these symmetry adapted levels. Group theory only reveals which orbitals are allowed and which states may hybridize. For this, we utilize the DFT results from Ref. [171]. These calculations indicate that the divacancy-derived levels are occupied in the sequence

$$(a_{1g}^2 a_{2u}^2 e_g^4 e_u^2), \tag{4.3}$$

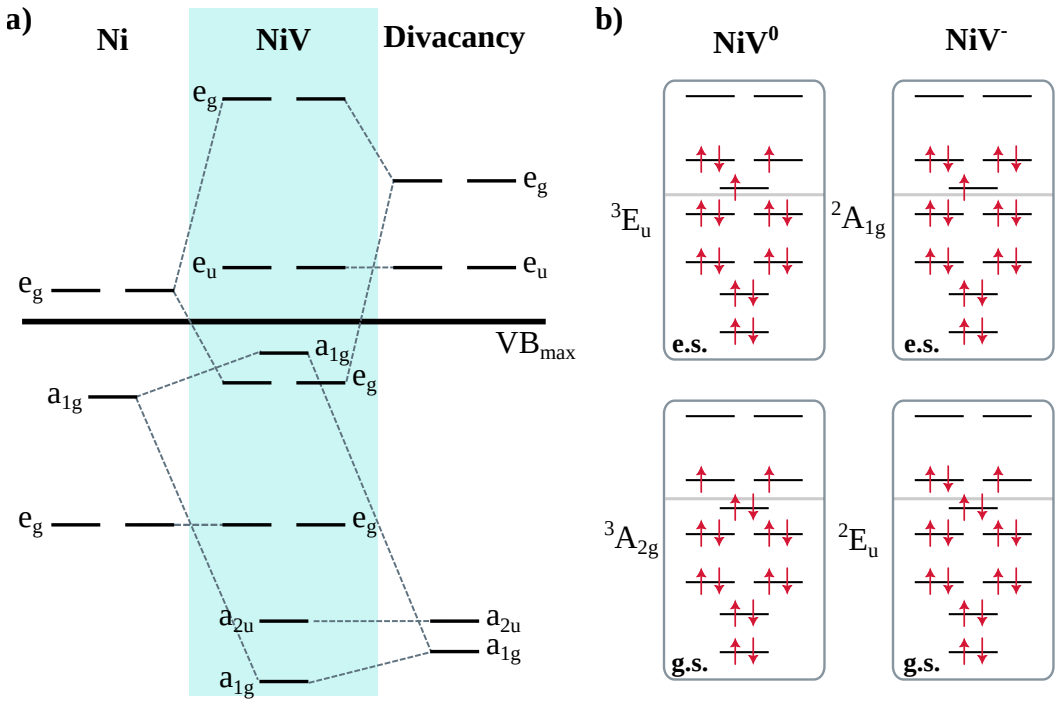

Figure 4.2 **(a)** Linear combination of atomic orbitals for a Ni atom in D3d point group symmetry along with a carbon divacancy in D3d. **(b)** Single electron orbitals with filled orbitals shown represented by the spin up and down arrows. e.s. and g.s. stand for excited state and ground state respectively. Multielectron irreducible representation is shown to the left of each of the configurations.

with the lower-lying a_{1g}, a_{2u}, and e_g orbitals forming closed shells. The Ni-divacancy hybridization pushes the bonding e_g combinations deep into the valence band, while the antibonding e_g combinations lie much higher in energy, near the conduction band minimum [171]. Within this picture, the neutral NiV center has two electrons occupying the e_u manifold. This gives a spin-triplet ground-state configuration with total spin $S = 1$ and overall symmetry ${}^3A_{2g}$. The same DFT calculations further indicate that the experimentally observed optical transition near 883–885 nm may be understood as a hole excitation from the e_u manifold to an a_{1g} level [171].

This orbital picture provides the basis for the effective Hamiltonian developed in the following section. Once the symmetry and orbital content of the defect have been identified, additional interactions such as spin–orbit coupling, Jahn–Teller coupling, strain, and Zeeman terms can be introduced systematically and compared directly with magneto-optical spectroscopy.

4.1.4 NiV$^-$ ground and excited states

The single-particle orbital picture developed above provides the starting point for understanding the experimentally relevant charge state of the defect, NiV$^-$. Although the preceding discussion focused

on the symmetry and ordering of the single-particle defect orbitals, the states probed experimentally are many-electron states obtained by filling these orbitals with the appropriate number of electrons. For NiV^-, this configuration differs from the neutral defect by the addition of one extra electron captured from the surrounding diamond, which occupies the lowest available defect orbital. Once the orbitals are filled according to the ordering established by the LCAO picture and supported by DFT calculations, the symmetry of the resulting many-electron states is determined by taking direct products of the irreducible representations associated with the occupied orbitals, thereby specifying how the total electronic wavefunction transforms under the symmetry operations of D_{3d}.

Carrying out this construction yields a NiV^- ground-state manifold transforming as ${}^2E_u$ and an excited-state manifold transforming as ${}^2A_{1g}$. Here the superscript $2S+1$ denotes the spin multiplicity, with S the total electronic spin; in both cases there is a single unpaired electron, so $S = \frac{1}{2}$ and the states are spin doublets. In the presence of an external magnetic field, this spin degeneracy is lifted by the Zeeman interaction, splitting each manifold into the two spin projections $m_s = \pm\frac{1}{2}$. These ground- and excited-state manifolds form the basis for the magneto-optical spectroscopy discussed in the following sections.

The ${}^2E_u$ ground state is orbitally degenerate, meaning that in addition to the spin degree of freedom there is also a twofold orbital degree of freedom associated with the E irrep. When this orbital doublet is combined with the spin-$\frac{1}{2}$ degree of freedom of the unpaired electron, the result is a four-dimensional ground-state manifold. A convenient basis for this manifold is

$$\mathcal{B}_{\text{gnd}} = \left\{ |e_{u,x}\uparrow\rangle, |e_{u,x}\downarrow\rangle, |e_{u,y}\uparrow\rangle, |e_{u,y}\downarrow\rangle \right\}, \tag{4.4}$$

which we also write more compactly as

$$\{|e_x\uparrow\rangle, |e_x\downarrow\rangle, |e_y\uparrow\rangle, |e_y\downarrow\rangle\}.$$

This structure is closely analogous to that of the negatively charged group-IV vacancy centers, such as SiV^-, GeV^-, SnV^-, and PbV^-, where an orbital doublet combined with spin-1/2 likewise produces a four-state ground manifold. Because the ground state is orbitally degenerate, it is sensitive to interactions that act on the orbital degree of freedom. In particular, spin-orbit coupling, Jahn-Teller interactions, and static strain can all mix or split the orbital components even at zero magnetic field. In addition, an orbital Zeeman interaction can produce further magnetic-field-dependent splittings. By contrast, the excited ${}^2A_{1g}$ state is an orbital singlet. In other words, it has no residual orbital degeneracy within this low-energy description. Its manifold is therefore spanned only by the spin degree of freedom,

$$\mathcal{B}_{\text{exc}} = \left\{ |a_{1g}\uparrow\rangle, |a_{1g}\downarrow\rangle \right\}, \tag{4.5}$$

so to first order it does not couple to orbital-dependent interactions such as the Jahn-Teller effect, and the dominant magnetic response is the ordinary spin Zeeman splitting. The explicit definitions of the $\{e_x, e_y, a_{1g}\}$ orbitals may be found in Table 2.7 of Ref. [**Hepp_2014**].

4.1.5 Interaction Terms

The ground and excited state multi-electron orbitals have now been described along with the basis in which they are written. The interactions that lift the degeneracies of these states will now be described. All interaction terms included in the model are constrained by the D_{3d} symmetry of the NiV^- center. The spin quantization axis is chosen along the high-symmetry $\langle 111 \rangle$ axis of the defect, which we define as the z-axis, with x and y orthogonal to it. The resulting effective Hamiltonian is expressed in the ground-state basis $\mathcal{B}_{\text{gnd}} = \{|e_x \uparrow\rangle, |e_x \downarrow\rangle, |e_y \uparrow\rangle, |e_y \downarrow\rangle\}$ introduced previously, and its eigenvalues and eigenvectors are obtained numerically using MATLAB.

The dominant symmetry-allowed contributions included in the Hamiltonian are spin–orbit coupling, Jahn–Teller interactions (including strain-induced orbital splitting), and magnetic-field interactions. Each of these terms is described below.

4.1.5.1 Spin-Orbit Coupling

The spin orbit interaction is a relativistic effect which originates from the fact that a charged particle, electron usually, is orbiting around a positively charged nucleus. In the electron's frame of reference, the positively charged nucleus is moving around at fast speeds, and as such creates a magnetic field which can couple to the electron's intrinsic magnetic moment of spin. As such, the spin couples to the orbit, hence spin-orbit interaction. It is usually written as

$$H_{SO} = \lambda \mathbf{L} \cdot \mathbf{S} \tag{4.6}$$

where $\mathbf{L}$ is the orbital angular momentum, $\mathbf{S}$ is the spin of the electron, and λ is the spin orbit coupling strength. As such, for any electronic structures which feature both non-zero spin quantum number and orbital angular momentum, spin orbit interaction will exist.

For the NiV^-, this manifests in the ${}^2E_u$ ground-state, which features both a spin doublet, $S = 1/2$, and orbital doublet, $l = 1$. In contrast, the excited state features an orbital singlet, $l = 0$, and so there is no spin-orbit interaction. For the ground state, the spin-orbit interaction splits the two orbital branches into two Kramers doublets. Because the states are not pure spin states nor pure orbital eigenstates, they are instead a mixture of spin and orbit and that is why they are referred to as Kramers doublets. Ab initio calculations indicate that these states can be labeled by effective total angular momentum projections $J_z = \pm 3/2$ and $J_z = \pm 1/2$, separated by an intrinsic splitting

D_g [214]. The dominant SOC originates from the Ni ion and is on the order of meV. Because the ^2E_u state also experiences strong vibronic coupling through the Jahn-Teller effect, the observable spin–orbit splitting is reduced by the Ham vibronic reduction factor f. For NiV^- we take $f = 0.124$. In the effective operator representation used in the simulations, the SOC Hamiltonian is written as

$$H_{\mathrm{SO}} = D_g \, L_y \otimes S_z, \tag{4.7}$$

where L_y acts in the orbital subspace and S_z acts in the spin subspace. This form is symmetry-allowed in D_{3d} and is equivalent, up to basis conventions, to the $L_z \otimes S_z$ representation commonly used for group-IV vacancy centers.

In the explicit ground-state basis $\mathcal{B}_{\mathrm{gnd}}$, the SOC term takes the matrix form [215]

$$H_{SO} = \frac{\lambda}{2} \begin{pmatrix} 0 & 0 & -i & 0 \\ 0 & 0 & 0 & i \\ i & 0 & 0 & 0 \\ 0 & -i & 0 & 0 \end{pmatrix}, \tag{4.8}$$

where λ is the effective (vibronically reduced) spin–orbit coupling constant.

4.1.5.2 Jahn-Teller Interaction and Other Orbital Splitting

The Jahn-Teller theorem states that any non-linear molecules with a spatially degenerate electronic state will experience a geometric distortion that removes that degeneracy. Hence, it will affect the ground state orbital doublet, but not the excited state orbital singlet. In particular, the Jahn-Teller interaction couples the ground state orbital doublet to vibrational modes of E_g symmetry and acts purely within the orbital sector, mixing the $|e_x\rangle$ and $|e_y\rangle$ components. This interaction can be written as

$$H_{\mathrm{JT}} = Q_{g,x} \, L_z + Q_{g,y} \, L_x, \tag{4.9}$$

where $Q_{g,x}$ and $Q_{g,y}$ parameterize the strength of the static Jahn-Teller distortion or strain-induced splitting along the two components of the E_g vibrational mode.

In the explicit basis $\mathcal{B}_{\mathrm{gnd}}$, this contribution takes the matrix form

$$H_{JT} = \begin{pmatrix} \xi_x & 0 & \xi_y & 0 \\ 0 & \xi_x & 0 & \xi_y \\ \xi_y & 0 & -\xi_x & 0 \\ 0 & \xi_y & 0 & -\xi_x \end{pmatrix}, \tag{4.10}$$

with $\xi_x \propto Q_{g,x}$ and $\xi_y \propto Q_{g,y}$.

Together, spin-orbit and Jahn-Teller interactions lift the orbital degeneracy even at zero magnetic field, producing a ground-state splitting

$$\Delta_{\mathrm{gnd}} = \sqrt{\lambda^2 + 4\xi^2}, \qquad \xi = \sqrt{\xi_x^2 + \xi_y^2}. \tag{4.11}$$

In addition to this first-order Jahn-Teller interaction, higher-order vibronic processes produce a small correction to the magnetic response of the system. Following Ref. [214], this second-order Jahn–Teller contribution can be written as

$$H_{\mathrm{JT}}^{(2)} = 2\,\delta_P\, g_L\, \mu_B\, S_z\, B_z, \tag{4.12}$$

where $\delta_P = 0.0839$ is the second-order parameter and $g_L = 0.7821$ is the Stevens reduction factor.

4.1.5.3 Zeeman Interaction

The Zeeman interaction contains both spin and orbital contributions. The spin Zeeman term is

$$H_{Z,S} = \mu_B g_S\, \mathbf{B} \cdot \mathbf{S}, \tag{4.13}$$

with $g_S = 2.002319$ and μ_B the Bohr magneton. In the ground-state basis, this interaction takes the matrix form

$$H_{Z,S} = \mu_B g_S \begin{pmatrix} B_z & B_x - iB_y & 0 & 0 \\ B_x + iB_y & -B_z & 0 & 0 \\ 0 & 0 & B_z & B_x - iB_y \\ 0 & 0 & B_x + iB_y & -B_z \end{pmatrix}. \tag{4.14}$$

The orbital Zeeman interaction is symmetry-allowed for the E_u manifold but is strongly quenched by vibronic dynamics associated with the Jahn–Teller effect. Retaining the leading contribution used in the simulations yields

$$H_{Z,L} = \mu_B\, f\, g_L\, B_z\, L_y, \tag{4.15}$$

where $g_L = 0.7821$ is the effective orbital g-factor and $f = 0.124$ is the Ham vibronic reduction factor. In matrix form,

$$H_{Z,L} = \mu_B f g_L \begin{pmatrix} 0 & 0 & iB_z & 0 \\ 0 & 0 & 0 & iB_z \\ -iB_z & 0 & 0 & 0 \\ 0 & -iB_z & 0 & 0 \end{pmatrix}. \tag{4.16}$$

Because spin-orbit coupling and the Zeeman interaction define competing quantization axes, a magnetic field that is misaligned from the defect symmetry axis leads to spin-orbital mixing. This mixing plays an important role in understanding weakly allowed or nominally spin-forbidden optical transitions observed in magneto-optical spectroscopy.

4.1.6 Full Hamiltonian

Collecting all symmetry-allowed contributions within the ground-state manifold, the effective ground-state Hamiltonian used in the simulations is

$$H_{\text{gnd}} = H_{SO} + H_{JT} + H_{Z,L} + H_{Z,S} + H_{\text{JT}}^{(2)}. \tag{4.17}$$

In the basis $\mathcal{B}_{\text{gnd}}$, this is a 4×4 matrix that is diagonalized numerically for each magnetic-field configuration to obtain field-dependent eigenenergies and eigenvectors.

For the excited state, the orbital singlet nature of ${}^2A_{1g}$ implies that orbital-dependent SOC and JT terms vanish to first order. We therefore take the excited-state Hamiltonian to be purely spin Zeeman:

$$H_{\text{exc}} = \mu_B g_S \, \mathbf{B} \cdot \mathbf{S}, \tag{4.18}$$

represented in the basis $\mathcal{B}_{\text{exc}}$. Optical transition frequencies are then computed as differences between the excited- and ground-state eigenvalues, forming the basis for the magneto-optical simulations. We use this Hamiltonian to model the full dynamics of the NiV and the experimental results are compared against it below.

4.2 Cryogenic Magneto-Optical Spectroscopy

Having built up and described the theoretical model for the NiV^- electronic structure, we now test its predictions. We accomplish this with magneto-optical spectroscopy, in which we record optical spectra of the defect's fluorescence while applying external magnetic fields of varying magnitude. The applied magnetic field lifts the degeneracy of the defect spin states via the Zeeman interaction, leading to characteristic field-dependent splittings in the optical transitions. We performed these measurements in the nanopillar sample; however, they were taken prior to etching. Hence, this data was performed on flat, bulk diamond in the region, which had an ion implantation dose of 1×10^{12} ions/cm^2. In order to model use the group theoretical model to predict how the level structure splits under a magnetic field, we need both the strength of the applied magnetic field and the angle with which it is applied with respect to the NiV high symmetry axis. The magnet is a superconducting solenoid wrapped around the sample position. As such, the magnetic field is

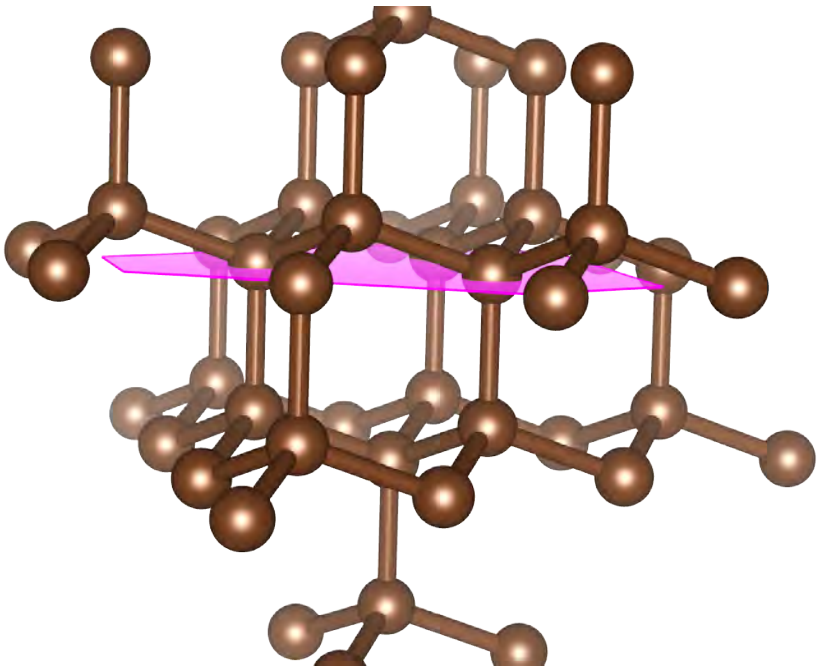

Figure 4.3 VESTA image of diamond crystal with the⟨111⟩ surface highlighted as the pink plane. The 4 different crystallographic orientations can be seen.

oriented perpendicular to the sample surface or parallel to the optical axis. This is also referred to as the Faraday configuration, where as a magnetic field perpendicular to the optical axis (or in-plane in our situation) would be referred to as the Voigt configuration. Knowing this, we simply need the orientation of the emitter within the sample to identify the relative angle between the two. Because diamond is tetrahedrally bonded, a split-vacancy defect can occur in four possible crystallographic orientations. These orientations align along the ⟨111⟩ axes (all equivalent directions). A sample that has a ⟨111⟩ orientation refers to the fact that the surface is perpendicular to the ⟨111⟩ axis. Hence, one class of defects within a ⟨111⟩ oriented diamond sample is parallel to the ⟨111⟩ direction and thus vertical in the sample. The other three orientations are tilted by 109.5° with respect to the axis perpendicular to the surface, pointing in a trigonal pattern. This can be seen in Hence, for the nanopillar sample, which has a ⟨111⟩ surface, we take the relative angle between the applied magnetic field and the high symmetry axis of the NiV (⟨111⟩ direction) to be 109.5°. In theory, there is a distribution of defects with different orientations which depends on the growth settings and the defect formation kinetics, however, we take the distribution to be random which could be measured by performing polarization dependent In addition to these ideal crystallographic angles, there is typically a small but nonzero sample off-cut on the order of 1-3°, which slightly modifies the true angle between a given NiV center and the applied magnetic field.

Figure 4.5 shows both the experimentally measured magneto optical spectrum of the NiV^- as well as the theoretical prediction from group theory. We performed this sweep at 1.7K in order to

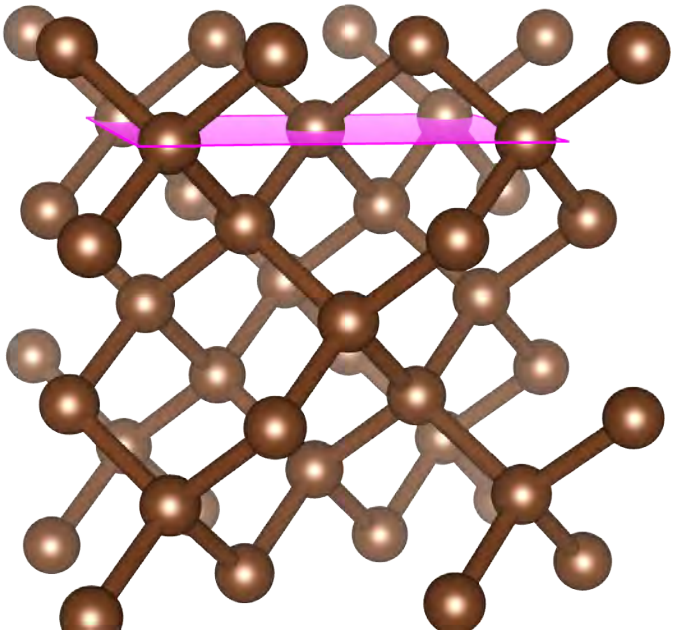

Figure 4.4 VESTA image of diamond crystal with the ⟨100⟩ surface highlighted as the pink plane. The 4 different crystallographic orientations can be seen and the fact that they all share the same angle with respect to the normal vector to the pink plane can also be seen.

be able to resolve the spectral lines. We did this at low temperature as, at room temperature, the phonon induced linewidth broadening would make this challenging. At a field of 9T, we observe eight distinct splittings, consistent with the level structure described in the previous section. The next figure shows the theoretical model's predicted transition frequencies for this field orientation superimposed on the experimental data, using a ground-state spin-orbit splitting of D_g = 670GHz extracted from the spectroscopy data. The simulated transitions are seen to be in good agreement with the observed spectral lines. Moreover, from the group theory simulation, we identify spin-orbit coupling as the dominant interaction responsible for splitting the ground-state manifold, in agreement with density functional theory predictions [171]. We also find that there is a very weak Jahn-Teller component of 8 GHz and we find little to no strain. This is consistent with the use of HPHT annealing for the sample, which is known to remove most strain introduced from ion implantation. The cryogenic magneto-optical spectroscopy therefore provides strong experimental support for our effective Hamiltonian model and confirms the assignment of NiV^- as an inversion-symmetric defect with D_{3d} symmetry. Furthermore, it confirms the advantageous orbital-singlet nature of the excited state, which is expected to facilitate efficient spin pumping and to allow relatively small magnetic fields to activate otherwise spin-forbidden transitions. Being able to operate at modest magnetic fields is particularly beneficial because it allows for the use of fast magnetic-field switching techniques to alternate between off-axis fields for optical spin pumping and near-axis fields for

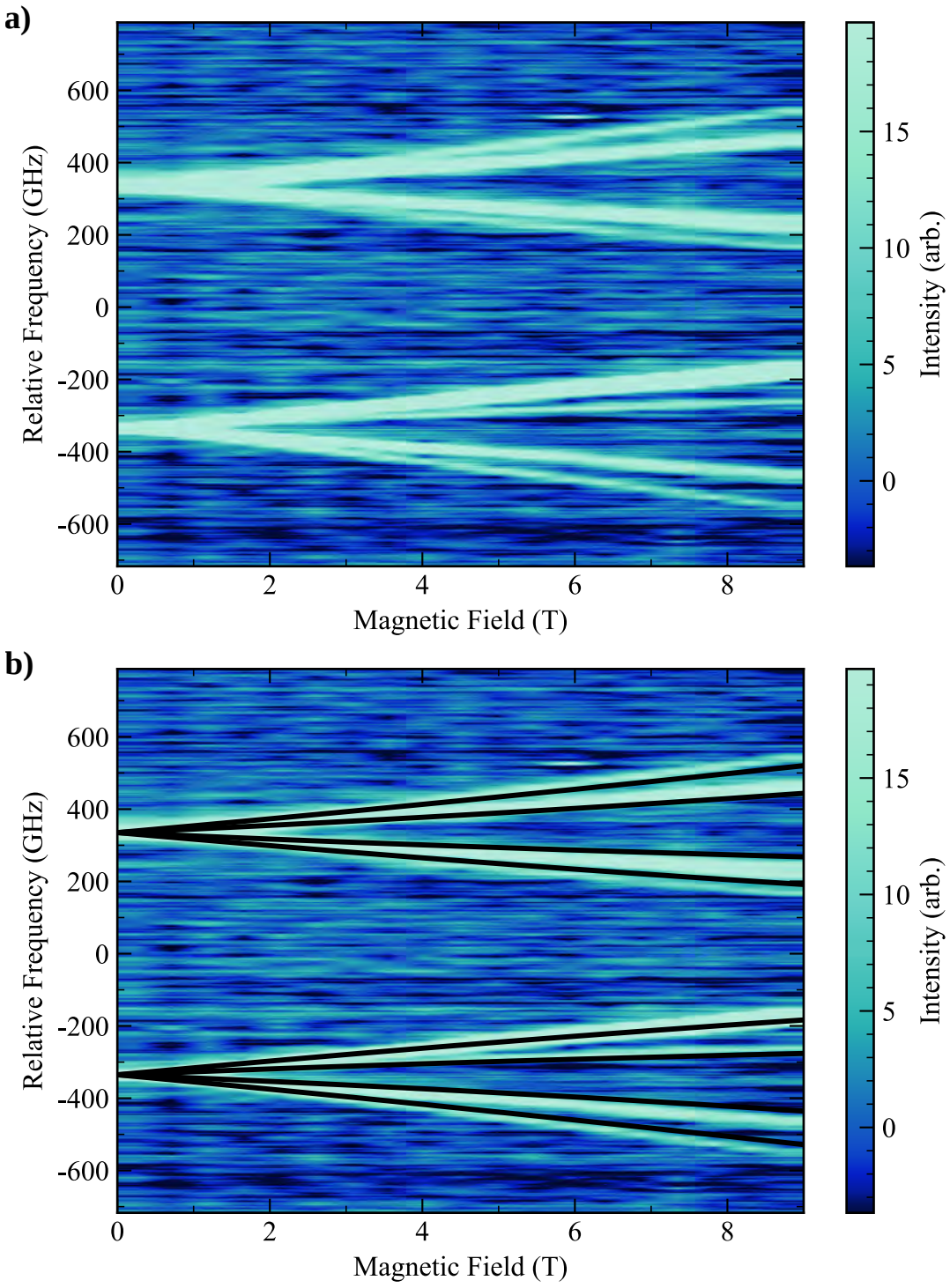

Figure 4.5 **(a)** Experimental magneto-optical spectrum of NiV^- at 1.6 K. We used off-resonant excitation at 740 nm at a power of 7 mW before the objective lens. We integrated for 30 s, repeated six times and then averaged with the magnetic field ramped up in 0.5 T steps. We used the highest grating at 1800 g/mm to achieve maximum resolution. **(b)** Group theoretical simulation of the magneto optical spectrum overlayed as solid black lines on top of the experimental data. The model parameters used 670 GHz for D_g, 8 GHz for Q_{gx} and 0 GHz for Q_{gy} and $\theta = 109.5°$.

single-shot spin readout on the cycling transition.

4.3 NiV^- Optical Properties

Having confirmed the electronic and geometric structure of the NiV^-, we now assess its optical properties experimentally. In particular, as the introduction motivated, we are interested in learning what fraction of light the defect emits into the zero phonon line and what fraction goes to the phonon sideband. Further, we want to determine whether we can achieve lifetime-limited linewidths in the center, as those are necessary for indistinguishable photons. These properties are central to evaluating the suitability of NiV^- as a quantum network node and for other quantum information processing applications.

4.3.1 Debye-Waller Factor & Phonon Sideband

We begin by characterizing the optical emission of NiV^- under off-resonant excitation by determining its Debye-Waller (DW) factor. As discussed in Chapter 1, the DW factor is a critical figure of merit for solid-state quantum emitters, as it quantifies the fraction of emission that occurs into the coherent and potentially indistinguishable zero-phonon line (ZPL), as opposed to the broadband and incoherent phonon sideband. A large DW factor thus implies that a significant portion of the emitted photons can, in principle, be used for interference-based quantum protocols.

To measure the DW factor, we record fluorescence spectra of NiV^- in the 1×10^{12} ions/cm^2 implantation dose region at 1.7K and observe two sharp emission peaks accompanied by a relatively weak phonon sideband, as shown in Fig. 4.6. From this spectrum, the DW factor is obtained by integrating over the ZPL portion of the spectrum and dividing that by the total emission, which includes both ZPL and phonon sideband. After doing this, we find a DW factor of approximately 62%, demonstrating that the NiV^- exhibits strong emission into the zero-phonon line, comparable to other group-IV vacancy centers such as SnV^- and SiV^-, making it a strong candidate for quantum networking applications. From this measurement, we can also extract the Huang-Rhys factor $S = -\ln(w_{\mathrm{ZPL}})$, where w_{ZPL} is the DW factor [216]. The Huang-Rhys factor provides a quantitative measure of the strength of electron-phonon coupling and corresponds physically to the average number of phonons emitted per optical excitation cycle. For NiV^-, we obtain $S = 0.51$, indicating relatively weak coupling to lattice vibrations, consistent with the observed strong ZPL emission. Interestingly, one primary reason for a high DW factor is how different the ground state spatial wavefunction is from the excited state. If the charge distribution is very different going from ground to excited state, then after a transition, there are more opportunities to interact with the lattice and emit a phonon before radiatively decaying back to the ground state. This is one of the main reasons

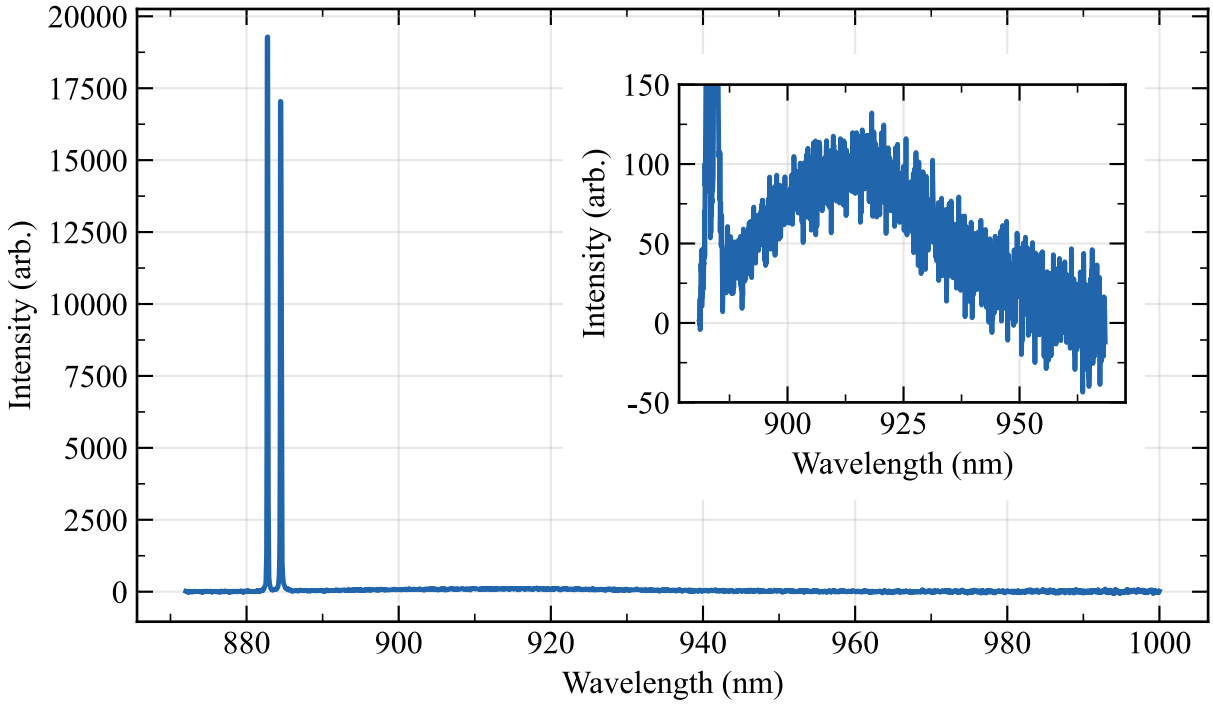

Figure 4.6 Typical fluorescence spectrum for NiV^- at 1.6 K in the bulk of the $10^{12}12$ ions/cm^2 region in the NDT HPHT sample. Inset shows a zoomed-in view of the phonon sideband. We used 740 nm excitation and 7 mW of power before objective. The Debye Waller factor of 0.62 was determined by dividing the intensity of the ZPL, from 882 to 886 nm by the intensity of the full spectrum from 882 to 1100 nm. The spectrum was obtained by averaging over four 20s long exposures using 600 grooves/mm grating on our spectrometer. The data were background subtracted and corrected for the spectral response of the spectrometer and camera by normalizing to the manufacturer provided wavelength-dependent quantum efficiencies. This is necessary because the spectrum we observe is a convolution of the camera response and the true spectrum, $E = R \times S$

why the NV^- has such a large phonon sideband, there is a big difference in spatial wavefunctions between ground and excited state.

Beyond the DW factor, the shape of the phonon sideband itself provides insight into the nature of the electron-phonon coupling. Comparing our measured spectrum to the density functional theory simulations presented in Figure 3 of Reference [171], we find the best agreement with the model that includes coupling only to A_{1g} vibrational modes. This conclusion is further supported by the fact that the Huang-Rhys factor extracted in that work for the A_{1g}-only model is closer to our experimentally measured value than the alternative model that includes coupling to both A_{1g} and E_g modes, which predicts a larger Huang–Rhys factor.

4.3.2 Low Temperature Ensemble Spectra

Having measured the DW factor, we now turn to the linewidths and lineshapes of ensembles of NiV^-. Ensembles, in contrast to single centers, are large groups of emitters. We investigate how the optical linewidth is affected by implantation dose. Indeed, we are primarily interested in the degree of inhomogeneous broadening introduced by implantation induced damage and residual strain not healed by the annealing process. Inhomogeneous broadening occurs when there is some distribution of emitters, in this case NiV^-, which all possess different transition frequencies due to inhomogeneities within the sample such as strain or other location dependent differences. This is in contrast to homogeneous broadening which is something experienced by all emitters, such as the excited state lifetime of the emitter. The extent of the ion implanted damage depends on several factors, including the implantation energy, the implantation dose, and the size of the implanted ion. For example, Orwa et al. showed that high-pressure, high-temperature (HPHT) annealing is particularly effective at healing implantation-induced damage in Ni-implanted diamond and yields the narrowest ensemble linewidths [217]. We can understand this by comparing it to nitrogen vacancy centers. For NV's, the smaller atomic size of nitrogen means that implantation leads to less lattice distortion, and so high-quality NV centers can be obtained even after relatively modest annealing treatments around 800°C. By contrast, the larger size of the nickel atom favors the split-vacancy configuration and makes more aggressive annealing necessary to relieve strain and restore crystalline order. This is also why for the nitrogen vacancy, the nitrogen atom relaxes back into the carbon substitutional site because its size is closer to carbon. Nickel on the other hand is larger and so energy is likely released in the form of the lattice not being strained if it sits in the middle between the two vacancies as opposed to in a substitutional site.

Figure 4.7 presents high-resolution spectral data for four different implantation dose regions of the pillar sample, measured prior to nanopillar fabrication, i.e., in the bulk crystal. These measurements were performed using off-resonant excitation at 690 nm. In the lowest-dose region, the observed linewidth is close to the limit of the spectrometer's resolution, while in the higher-dose regions the linewidths remain on the order of tens of GHz. This behavior indicates that the implantation and HPHT annealing procedure is effective at suppressing inhomogeneous broadening, even at relatively high defect densities, and is consistent with the earlier observations of Orwa et al. [217]. Furthermore, we consistently observe a larger linewidth in the higher orbital branch transition at 885 nm. This is likely due to there being a potential to relax into the lower orbital branch (particularly at cryogenic temperatures where phonon populations are lower and so repopulating the higher orbital is less likely), thereby shortening the effective lifetime of that transition and thus increasing the linewidth due to the time-energy uncertainty principle.

The narrow linewidths extracted are promising as they indicate relatively low amounts of inhomogeneous broadening even in relatively dense ensembles. This is encouraging going forward

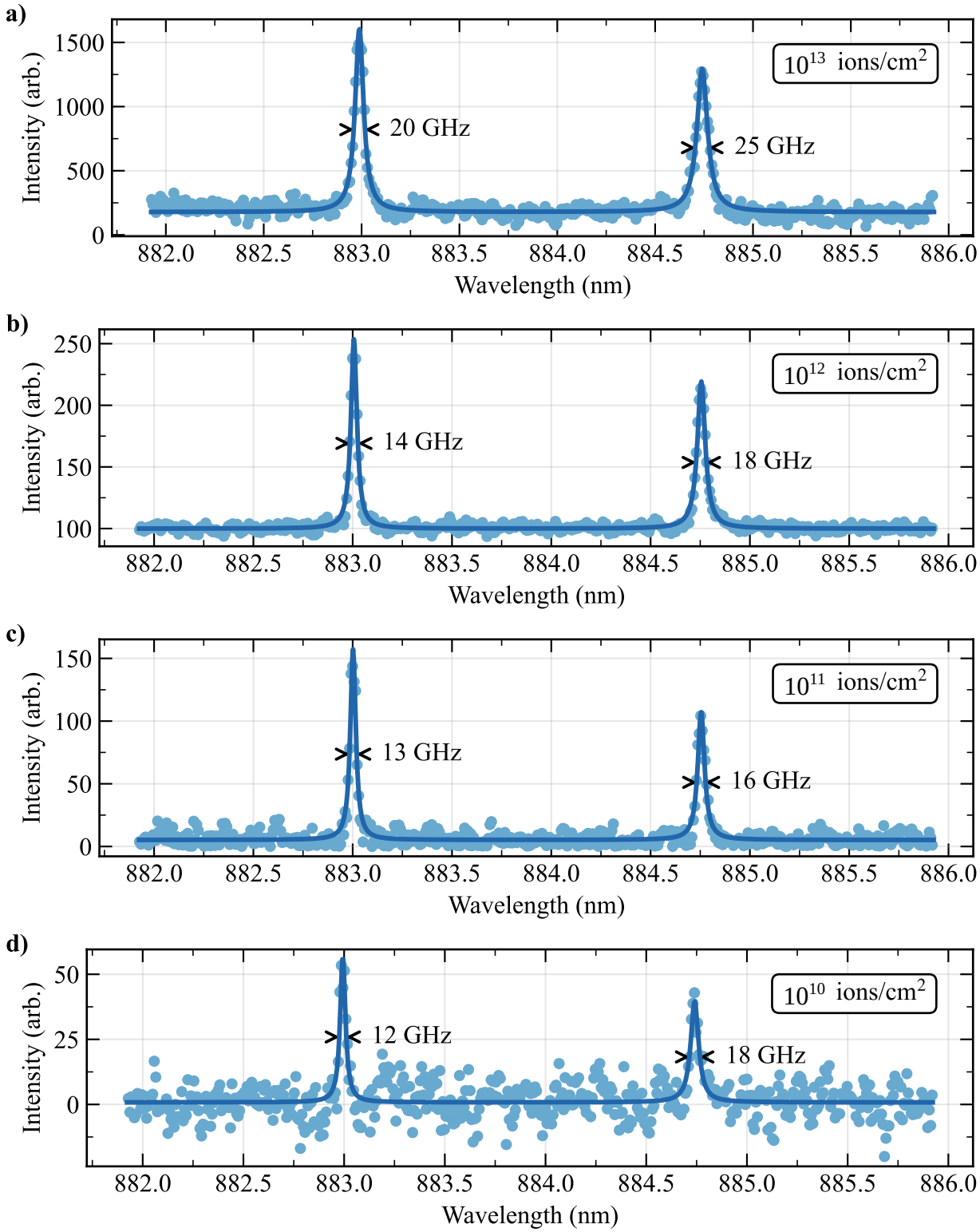

Figure 4.7 **(a)-(d)** Spectroscopic measurements of four different implantation doses. **(d)** was taken in the electronic grade CVD grown sample while the other three measurements were performed in the ⟨111⟩ NDT HPHT sample. This data was taken at 1.6K using 5mW of 690nm excitation. The measurements were taken using the highest resolution spectrometer grating at 1800g/mm.

both for the prospect of generating indistinguishable photons with single centers but also because it means NiV ensembles might have applications in ensemble-based quantum memories. In these schemes, an incoming photon carrying quantum information is coherently mapped onto a collective excitation shared across many defects. The probability of absorption is set largely by the density of emitters which possess a wavelength that enables them to strongly interact with the light, and so the larger the number of resonant emitters, the more efficiently the photon can be captured. After absorption, the photonic state is stored as a phase-coherent superposition over the ensemble, and is later retrieved by converting this collective excitation back into an emitted photon. For this process to function well, however, the ensemble must provide both strong absorption and minimal dephasing. High defect density improves the optical depth and therefore the storage efficiency, while a narrow homogeneous linewidth suppresses decoherence and helps preserve the phase information [145, 218, 219]. The ability to increase the emitter density without introducing substantial additional broadening is therefore especially promising, because it enables simultaneously strong light-matter coupling and long coherence times, leading to a large time-bandwidth product. Dense NiV^- ensembles are therefore attractive candidates for solid-state quantum memories.

4.3.3 Temperature Dependence

In addition to the base-temperature spectroscopy at 1.6 K discussed above, we also performed spectral measurements over a range of temperatures in the 1×10^{12} ions/cm^2 implantation-dose region. As before, these measurements were carried out prior to etching, so the defect was studied in bulk diamond. Figure 4.8 shows the NiV^- spectrum at several temperatures, revealing two clear trends as the sample is cooled: the linewidth narrows and the fluorescence intensity increases.

Both trends can be understood within the same general framework of electron-phonon coupling. As the temperature rises, the thermal occupation of phonon modes increases, strengthening the interaction between the defect electronic states and lattice vibrations. This has two important consequences. First, phonon-assisted non-radiative relaxation channels become more accessible, so a larger fraction of the excited NiV^- decays without producing a photon, thereby reducing the observed fluorescence intensity. Second, thermally populated phonons produce fluctuations in the transition energy and enable additional phonon-assisted broadening processes, which increase the optical linewidth. Upon cooling, the phonon population is suppressed, making non-radiative decay less likely and reducing phonon-induced dephasing, so the fluorescence increases while the transition narrows. The thermal phonon occupation is given by

$$n(\omega, T) = \frac{1}{e^{\hbar\omega/k_B T} - 1}, \tag{4.19}$$

which decreases monotonically with temperature. As T decreases, both phonon-assisted transitions

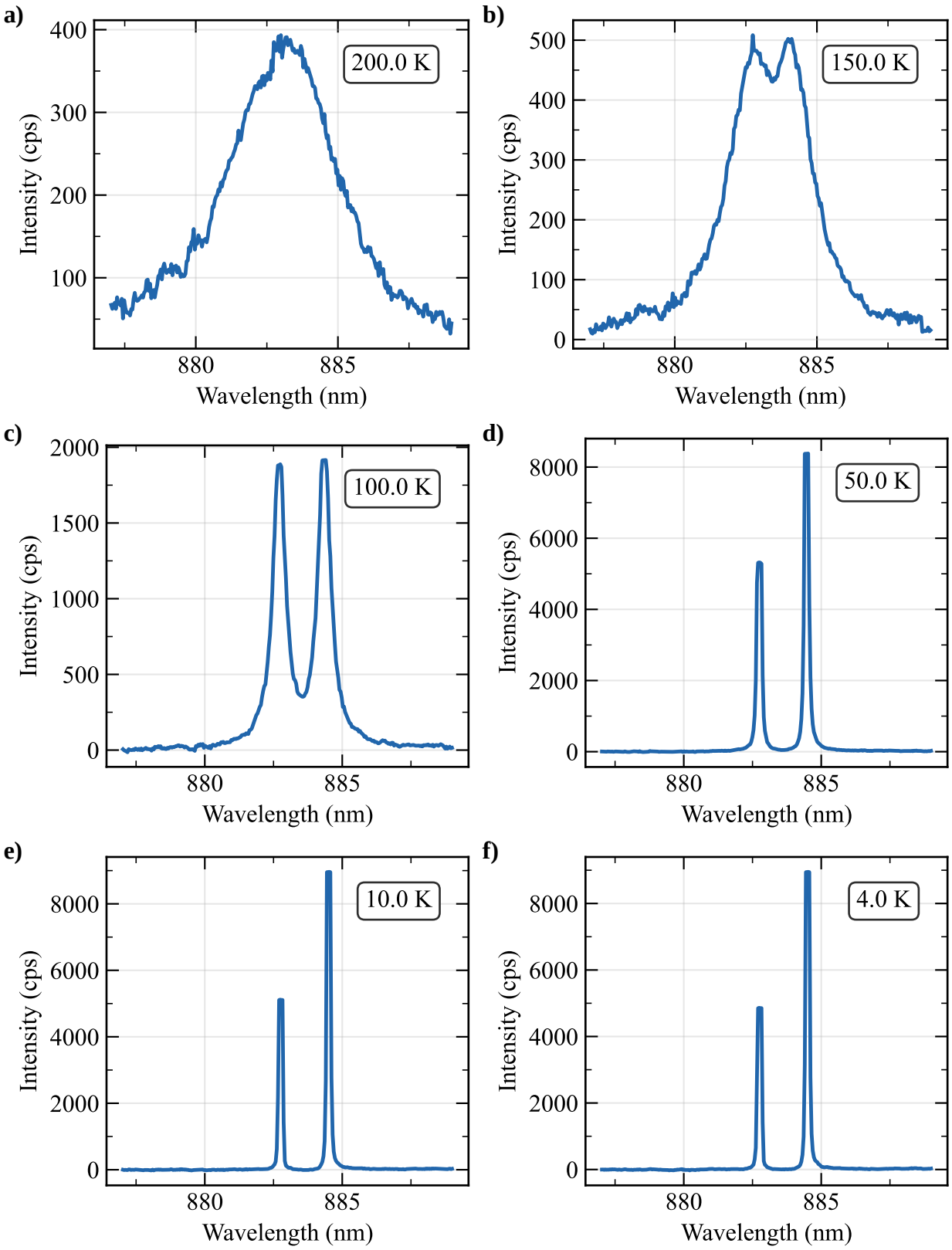

Figure 4.8 **(a)-(f)** Temperature dependent spectra of the NiV^- taken in the $10^{12}12$ ions/cm^2 region of the bulk NDT IIa sample prior to nanopillar etching. The sample was excited with 1mW of 690nm light. The 600 g/mm spectrometer grating was used.

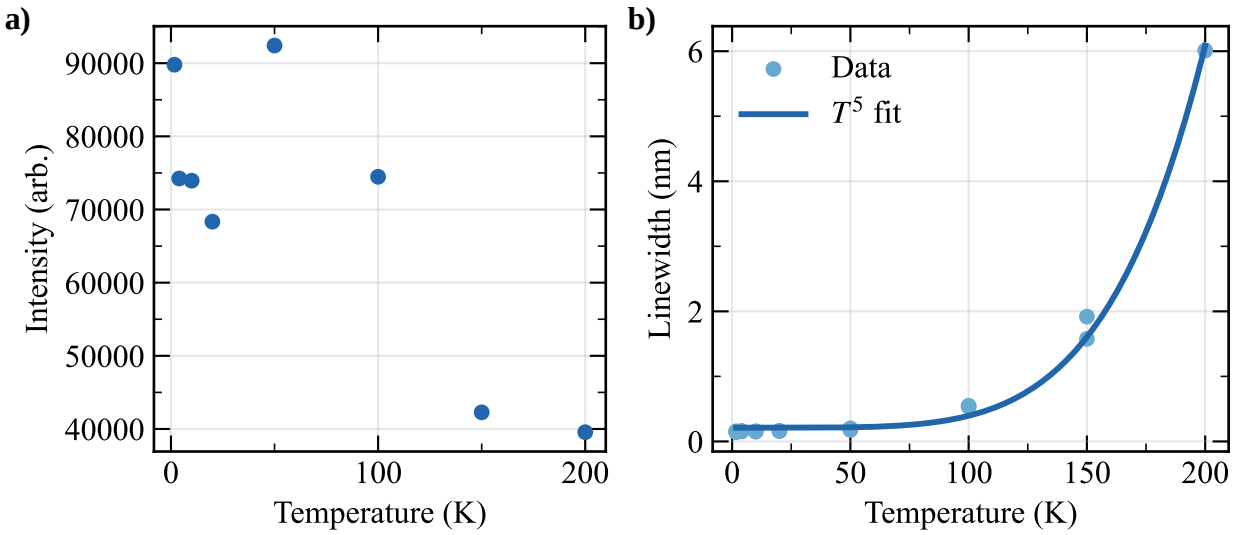

Figure 4.9 NiV fluorescence intensity and linewidth dependence on temperature from the $10^{12}12$ region of the bulk NDT IIa sample prior to nanopillar etching. **(a)** Integrated intensities over the spectral range 880 nm to 886 nm as a function of temperature. **(b)** Linewidths extracted from fitting the temperature dependent spectra to two, or in the case of 200K, one Lorentzian.

and phonon-induced energy fluctuations are therefore suppressed, allowing the intrinsic optical coherence of the center to emerge more clearly.

This behavior is broadly consistent with what has been observed for other diamond color centers. For group-IV vacancy centers such as SiV and GeV, the optical linewidth typically decreases strongly at low temperature because phonon-driven orbital relaxation and dephasing are frozen out [140, 220, 221]. Similar trends are also seen more generally across solid-state emitters, where the zero-phonon line sharpens as thermal lattice motion is reduced. In many diamond defects, the homogeneous linewidth follows a cryogenic power-law temperature dependence, often written as T^5 or T^7, reflecting the details of the electron-phonon coupling mechanism and the symmetry of the electronic states [90]. Although we do not attempt a detailed temperature-scaling analysis here, the observed increase in fluorescence together with linewidth narrowing is fully consistent with this established physical picture. More detailed modeling of the temperature dependence would certainly be possible, but it was not the focus of this thesis, whose primary aim is to assess the NiV center as a quantum networking node rather than as a temperature sensor.

The NiV center has nevertheless also been proposed as a candidate for temperature sensing because its optical transition frequencies shift appreciably with temperature and can be modeled using established solid-state mechanisms [222]. In addition, its zero-phonon line lies within a wavelength window that may be favorable for certain biological imaging applications, in contrast to emitters such as NV and SnV. In our measurements, we observed systematic spectral shifts during temperature sweeps. Although these data are not shown here, we also observed resolvable

resonance shifts in resonant PLE measurements over a narrow temperature interval from 1.61 K to 1.65 K, suggesting that NiV may provide high sensitivity as a low-temperature sensor. This form of thermometry is classical in the sense that it relies on tracking the resonance position, but its simplicity could make it attractive in nanodiamond environments or when integrated into nanophotonic structures, as suggested in Ref. [222].

4.3.4 Resonant Excitation

Now that we've confirmed both the advantageous electronic structure and the off-resonant optical properties of the NiV^- center, we now turn to resonant excitation of individual optical transitions. Being able to perform resonant excitation is crucial for two major reasons. First, it allows us to selectively address individual spin transitions. For example, if we want to use the two lowest spin sublevels of the lower orbital branch as our qubit, we would need to be able to initialize coherently transfer population between those states. We can do this by applying an off-axis magnetic field, which in addition to lifting the degeneracy of those spin sublevels, will also tilt the quantization axis of the excited state, giving a now non-zero spin overlap between previously spin forbidden transitions. This means that if we were to resonantly drive one of the spin sublevels, the spin population would get pumped out of that state into the other spin state in a stochastic or random fashion. This is how we can perform initialization of our qubit state, via optical spin pumping. If we tried this with off-resonant excitation, it would not be selective of the frequency and would drive both spin transitions simultaneously, resulting in spin pumping in both directions, thus preventing effective initialization or polarization of the states. This is in contrast to the NV center, which can be spin-polarized using off-resonant 532 nm excitation owing to its spin-1 ground state and the presence of spin-selective intersystem crossing pathways. For NiV^-, with its spin-$\frac{1}{2}$ ground state, resonant excitation of specific transitions is therefore essential for implementing optical spin pumping and spin initialization. The second main reason as to why resonant excitation is important, is it allows us to probe the intrinsic homogeneous linewidth of the optical transitions, rather than the broader features obtained under off-resonant excitation.

For these measurements, we again use the nanopillar sample prior to etching. To perform resonant excitation, we first estimate the relevant transition frequency by recording an off-resonant spectrum using the highest-resolution grating of the spectrometer. We then determine the calibration offset between the spectrometer wavelength and the laser wavemeter. This is done by removing the long-pass filter which normally blocks the laser from the output fiber, and heavily attenuating the laser with neutral-density filters. We can then send it into the spectrometer without fear of damaging the spectrometer camera. The laser wavelength measured on the spectrometer is then compared with the wavemeter reading, and the resulting difference is used as a correction to the wavemeter

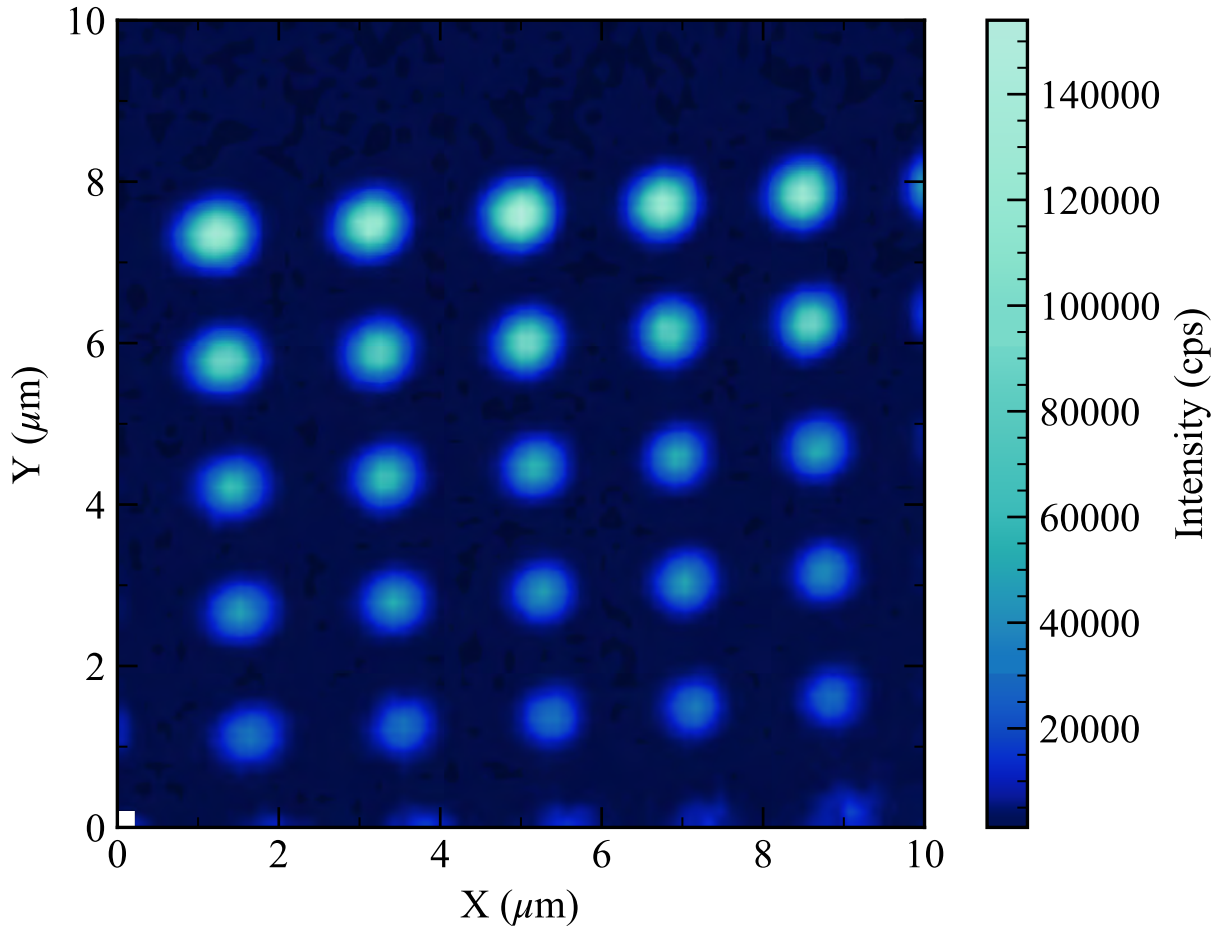

Figure 4.10 Confocal scan of nanopillar array in the 10^{13}13 implantation dose region using 690nm excitation light.

value. Applying this correction places the laser much closer to the expected transition frequency before scanning, which significantly reduces the time required to locate the resonance. Being off by even 1 GHz can substantially prolong the search.

A second experimental challenge is how to resonantly excite the defect while simultaneously collecting its fluorescence. Direct detection at the excitation wavelength is not practical, because any unfiltered resonant laser light reaching the single-photon detectors will likely destroy them. Instead, we detect fluorescence on the phonon sideband. For example, when the laser is scanned resonantly across the transition near 883 nm, excitation of the defect also produces red-shifted emission into the phonon sideband. This emission is spectrally distinct from the laser and can therefore be isolated with optical filters. In our case, we use 925 ± 25 nm bandpass filters, which collect a large fraction of the phonon sideband while rejecting the resonant laser light at 883nm. We are thus able to scan a narrow-linewidth Ti:sapphire laser across the NiV^- zero-phonon-line transition near 883 nm while detecting fluorescence in the phonon sideband. The detected signal arises from resonant excitation of the NiV^- center: when the laser is tuned into resonance, population is transferred to the excited state and subsequently relaxes, producing phonon-sideband emission that we collect. In this sense, photoluminescence excitation (PLE) spectroscopy is closely analogous to an absorption measurement. As the laser frequency is scanned across the optical transition, the excitation probability follows the absorption profile of the defect, so the detected phonon-sideband fluorescence is proportional to the excited-state population. As described in Chapter 2, for resonant excitation of a two-level system this excited-state population follows a Lorentzian lineshape. Also, for these resonant measurements, we focus on the lower-energy ground-state transition near 883 nm, since the higher-energy ground-state branch is only weakly thermally populated at 1.6 K.

4.3.4.1 Fluorescence Extinction and Revival

In our first attempt at resonant excitation, we observed little to no fluorescence. This absence of signal was not due to simple misalignment-a common concern of ours when working at 883 nm, which lies in the infrared and is not visible to the eye-as we carefully verified alignment, stability and scanned the laser over a wide frequency range, as illustrated in Fig. 4.11. Despite this, no clear resonances were observed. However, upon adding a small amount of off-resonant 532 nm excitation light, typically on the level of a few microwatts, a dense set of NiV^- resonances immediately became visible. This "green revival" effect is well known from resonant spectroscopy of other diamond color centers, including NV, SiV, GeV, and SnV centers [143, 223]. The prevailing interpretation is that resonant excitation alone tends to pump the defect into some dark state, either by ionizing the defect, transferring it to a different charge state, or populating a nearby charge trap that effectively removes the electron from the optically active NiV^- configuration. As a result, the resonant transition becomes optically inactive and fluorescence disappears. The addition of weak green light therefore

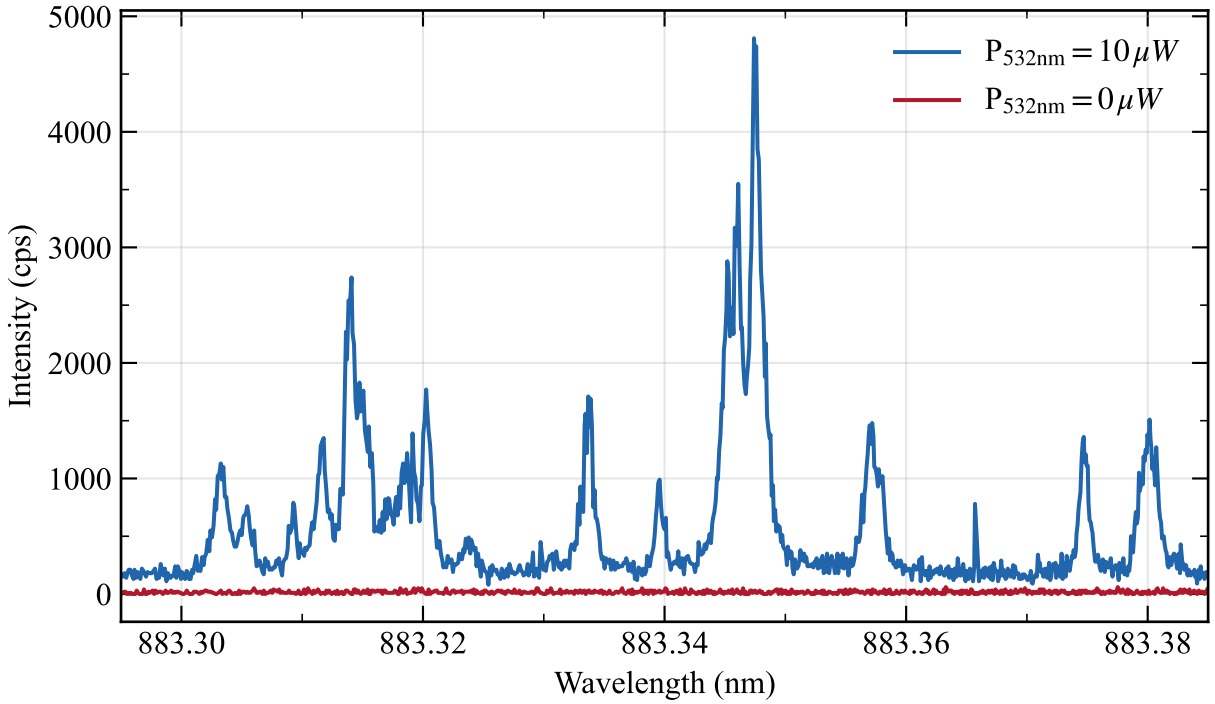

Figure 4.11 Resonant excitation of a nanopillar containing NiV's. 20 μW's of resonant light were used for both scans with the only difference being the addition of 532 nm light in addition.

provides a repumping mechanism: although it is far off-resonant from the NiV^- ZPL, it efficiently drives charge cycling in the surrounding excitation volume, resetting the charge-state dynamics and repopulating the optically active NiV^- state. In the steady state then, the resonant laser can then excite the NiV^- while simultaneously tending to pump it dark, and the green light continuously restores the bright charge state. This dynamic equilibrium enables stable observation of resonant fluorescence and makes resonant PLE spectroscopy possible.

4.3.4.2 PLE Nanopillar Sample

At this point, we decided to create nanopillars in an attempt to both improve the light collection efficiency and also to separate NiV's spatially. Our goal of separating them with nanopillars was an attempt to improve the charge state stability, as nearby NiV's could be the dark state that the electron gets pumped to. A confocal microscope scan of a nanopillar array containing NiV's is shown in figure 4.10. We then used the piezoelectric stages to move the objective lens over a variety of nanopillars and looked at each resonantly.

So, with the discovery that weak amounts of 532 nm light can serve as an effective repump, we could then begin to characterize the transition linewidths as a function of power. In particular, we were interested in what the narrowest achievable optical linewidth was and how close this was

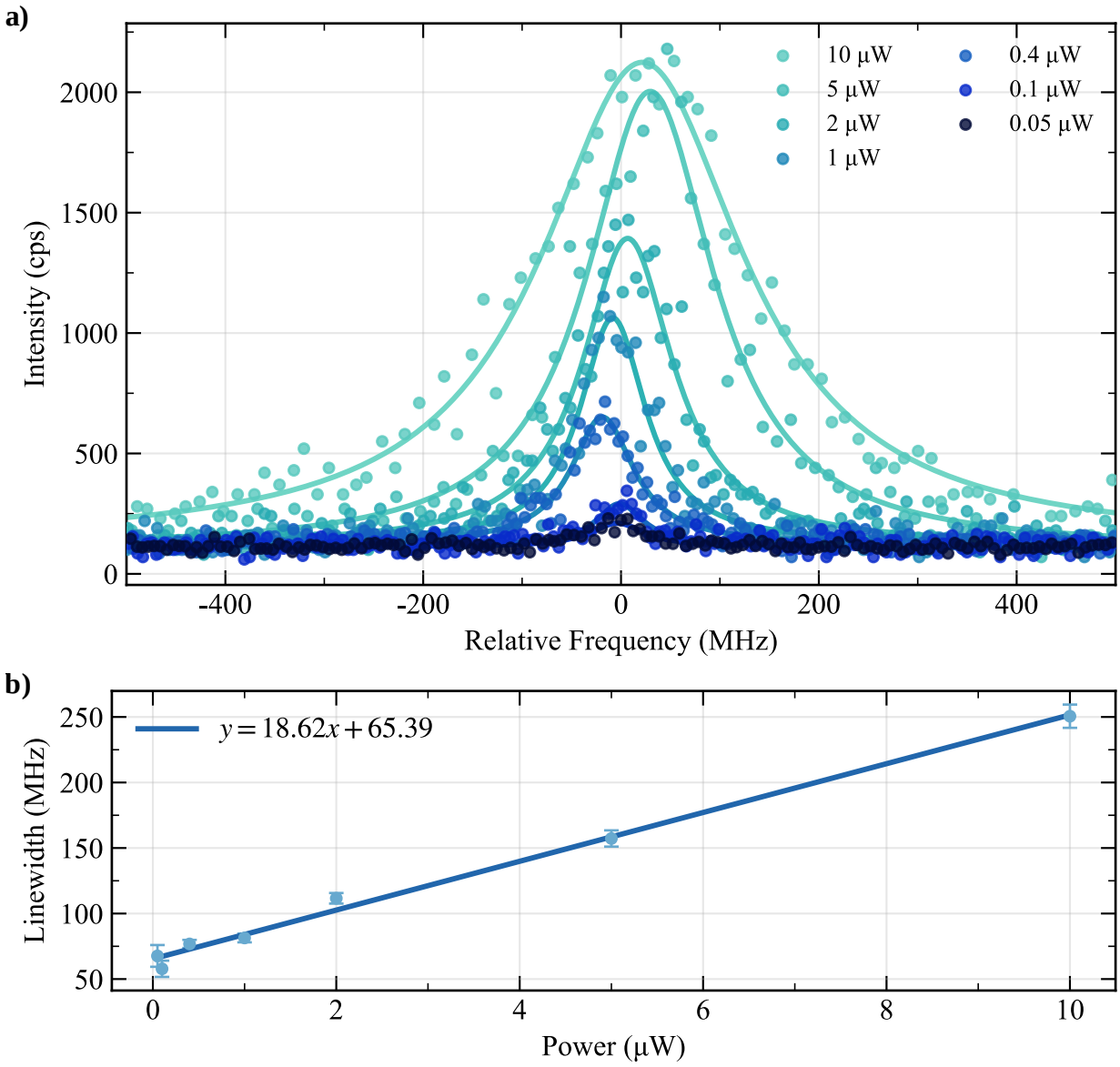

Figure 4.12 **(a)** Resonant excitation at various resonant powers of a single resonance within a nanopillar in the⟨111⟩ HPHT sample. These measurements were perfomed at 1.6 K. A continuous beam of 532 nm light at a constant 10 μW was used in conjunction with the resonant light. The data set was fit to Lorentzians and the linewidths were extracted and plotted in **(b)**. We then fit these to a line finding a linewidth of 65.39 MHz at zero power.

to the lifetime-limited regime. This is important because as stated before, such lifetime-limited photons are necessary for two-photon interference, which is a prerequisite to many complex quantum networking and computing protocols [92]. To characterize the optical linewidth under resonant excitation, we measured multiple individual resonances across a variety of different nanopillars. Figure 4.12(a) shows a representative resonance recorded at several resonant laser powers. As expected, the transition narrows as the resonant power is reduced. This behavior is known as *power broadening* and arises from the saturation physics of a coherently driven two-level system: as the drive strength increases, the optical coherence decays faster in the rotating frame and the steady-state absorption/emission spectrum broadens.

In Fig. 4.12(a), each spectrum is fit to a Lorentzian to extract an experimental linewidth, and these linewidths are plotted as a function of resonant power in Fig. 4.12(b). The observed trend is consistent with power broadening: the linewidth decreases as the drive power is reduced, and the extracted linewidth increases with increasing power. Extrapolating to zero resonant power yields a linewidth of $\Delta\nu_0 \approx 65\,\mathrm{MHz}$.

To compare these values to the natural linewidth, we first need a measure of the excited state lifetime, as it is this time which is the fundamental limit to how narrow a linewidth can be. We previously measured the excited-state lifetime to be $\tau = 10.5\,\mathrm{ns}$, in close agreement with the value $\tau \approx 11\,\mathrm{ns}$ reported by Orwa *et al.* [224]. For a purely radiative two-level transition with no additional dephasing, the lifetime-limited (Fourier-transform-limited) full-width at half-maximum (FWHM) linewidth is

$$\Delta\nu_{\mathrm{TL}} = \frac{1}{2\pi\tau} = 15.4\mathrm{MHz}. \tag{4.20}$$

The measured linewidth is significantly broader than the lifetime-limited linewidth expected from the bulk excited-state lifetime, by roughly a factor of 4-5. There are two main possible explanations for this discrepancy. The first is that the optical transition is broadened by mechanisms beyond the intrinsic radiative decay of the excited state. For example, fluctuations in the local electrostatic environment can cause the transition frequency to wander in time, a process known as spectral diffusion. In nanopillars, such fluctuations can be enhanced by proximity to surfaces, fabrication-induced defects, residual strain, or charge noise. These effects would increase the zero-power linewidth above the ideal lifetime limit. In the present measurements, however, the transition frequencies remained relatively stable even over long timescales, suggesting that strong slow spectral diffusion is unlikely to be the dominant cause of the observed broadening.

A second possibility is that the linewidth is broadened because the excited-state lifetime is in fact shorter in the nanopillar than in bulk. The natural linewidth of an optical transition is inversely related to the excited-state lifetime, so any lifetime shortening leads directly to a broader lifetime-limited linewidth. One mechanism that can produce this is Purcell enhancement, in which the nanophotonic environment modifies the local optical density of states and increases the radiative

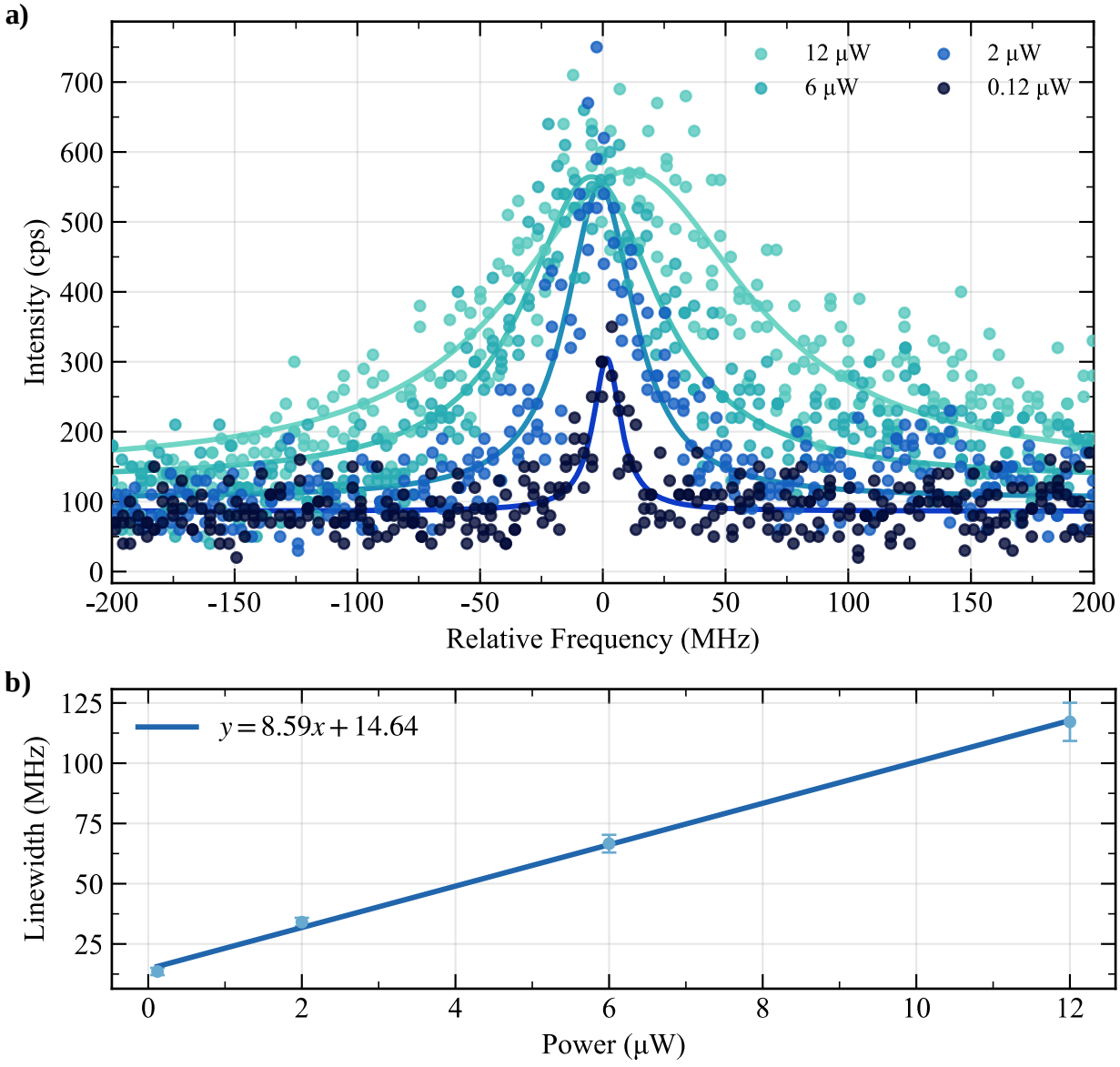

Figure 4.13 **(a)** Resonant excitation at various resonant powers demonstrating how the linewidth is power broadened. These measurements were perfomed at 1.6 K. A continuous beam of 532 nm light at a constant 10 μW was used in conjunction with the resonant light. The data set was fit to Lorentzians and the linewidths were extracted and plotted in **(b)**. We then fit these to a line finding a linewidth of 14.64 MHz at zero power, consistent with the lifetime limit.

emission rate. Because the lifetime measured previously was obtained from a bulk sample, it would not capture any such nanopillar-induced shortening of the excited-state lifetime. To compare, we then performed similar measurements on an unstructured sample in order to test whether a bulk-like environment yields closer to lifetime-limited linewidths.

4.3.4.3 PLE Bulk 1×10^{10} ions/cm^2 Sample

Given the comparatively large zero-power linewidths observed in the nanopillar sample, we next investigated an unstructured sample implanted at a significantly lower dose of 1×10^{10} ions/cm^2 as compared to the 1×10^{13} ions/cm^2 region which the nanopillars were created in. This sample was a CVD-grown, electronic-grade diamond with ultra-high purity and was also subjected to HPHT annealing, which is known to be particularly effective at healing implantation-induced lattice damage and minimizing strain. As such, this sample is expected to exhibit narrower optical linewidths that more closely reflect the intrinsic optical coherence properties of the NiV$^-$ center.

As in the nanopillar measurements, we observed that under purely resonant excitation at 1.6 K the NiV$^-$ fluorescence was completely quenched, and that the addition of weak 532 nm illumination was required to repump the defect and recover stable resonant fluorescence. Figure 4.13 shows a representative resonance measured in this sample, using the same resonant photoluminescence excitation (PLE) protocol as for the nanopillars. We again recorded spectra at several resonant powers, fit each resonance to a Lorentzian lineshape, extracted the full width at half maximum (FWHM), and plotted the linewidth as a function of power. This can be seen in figure 4.13. As before, we observe a linear increase of the linewidth with increasing resonant power, consistent with power broadening of a driven two-level system. Extrapolating to zero resonant power yields a linewidth of $\Delta\nu_0 = 14.64$ MHz, which is in excellent agreement with the lifetime-limited linewidth inferred from the previously measured excited-state lifetime. This result indicates that, in this unstructured and low-dose sample, the NiV$^-$ optical transition is squarely within the transform-limited regime.

4.3.4.4 Distribution of Resonances

Having shown that we can achieve lifetime-limited optical linewidths for NiV$^-$ centers, the natural next step is to investigate the distribution of transition frequencies across many emitters. While the linewidth characterizes the coherence of a single optical transition, the distribution of resonance frequencies across a sample reflects the degree of inhomogeneity introduced by residual strain, local electric fields, implantation damage, and other static or slowly varying perturbations of the crystal environment.

To quantify this distribution, we performed resonant photoluminescence excitation (PLE) measurements on emitters from several different samples, including the nanopillar sample, the

1×10^{10} ions/cm^2 sample, and the p-i-p sample. By compiling the extracted resonance frequencies into a histogram, we obtained a statistical measure of the spread of transition frequencies. From this analysis, we found a standard deviation of approximately 15.5 GHz around a central transition frequency. This inhomogeneous distribution is a key parameter for quantum networking applications. In protocols that rely on two-photon interference or remote entanglement generation, photons emitted by spatially separated emitters must be indistinguishable in frequency to within their homogeneous linewidths. In an idealized scenario, all emitters would share exactly the same optical transition frequency. In practice, however, some amount of spectral dispersion is unavoidable, and it is therefore essential to know both the typical spread and the available tuning range required to bring different emitters into mutual resonance.

4.3.5 Single NiV Centers

Having identified narrow resonances under resonant excitation, the next step is to determine whether these features arise from individual NiV^- centers or from multiple nearby emitters whose spectra overlap. This distinction is important because several emitters within the same nanopillar can, under some conditions, produce a single broadened or partially unresolved spectral feature. One common indication of this is that a line appearing isolated at high power may split into multiple peaks as the excitation power is reduced. For resonances that remain spectrally isolated and show no evidence of such splitting, a more direct test is to measure the photon statistics of the emitted light.

To do this, we measured the second-order correlation function, $g^{(2)}(\tau)$, using a Hanbury Brown and Twiss (HBT) interferometer, as described in Chapter 2 and 3. In this measurement, the emitted photons are divided by a 50:50 beam splitter and sent to two single-photon detectors. By recording the arrival times of photons at the two detectors and building a histogram of their time delay τ, one obtains the autocorrelation function $g^{(2)}(\tau)$. For an ideal single-photon emitter, two photons cannot be emitted simultaneously, so coincidences at zero delay are suppressed, producing an antibunching dip at $\tau = 0$. In practice, background fluorescence, detector dark counts, and imperfect isolation of a single emitter can prevent the dip from reaching zero. For this reason, a value of $g^{(2)}(0) < 0.5$ is generally accepted as strong evidence that the detected emission is dominated by a single emitter.

We first performed these measurements at room temperature on two different nanopillars, as shown in Fig. 4.14. These data were taken under off-resonant excitation using 840 nm light together with a weak 532 nm repump. In neither case does the measured autocorrelation fall below the $g^{(2)}(0) = 0.5$ threshold required to clearly identify single-photon emission. This is not surprising, since off-resonant excitation does not selectively address a single optical transition. Instead, it can excite all NiV centers within the nanopillar that are coupled to the pump, so emission from multiple defects contributes simultaneously to the detected signal. As a result, the measured $g^{(2)}(0)$ remains

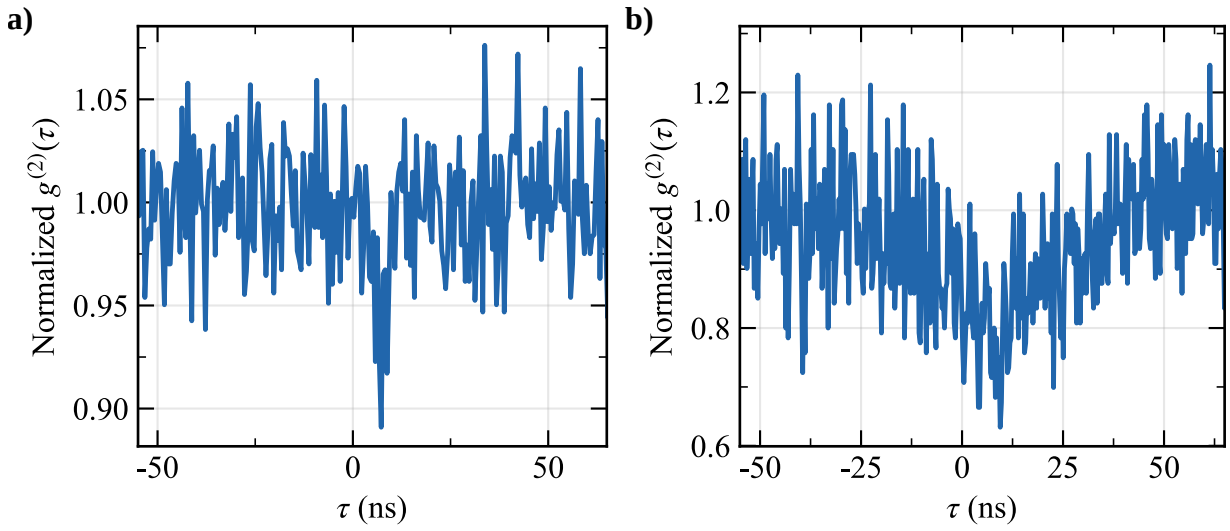

Figure 4.14 **(a),(b)** Both graphs show normalized data of second-order correlation function $g^{(2)}(\tau)$ on two different NiV nanopillars. The lower the $g^{(2)}(0)$ value, the lower the number of NiV emitters within a nanopillar. These measurements were carried out at room temperature with 0.6mW of 840 nm light and 10 μW of 532 nm light.

above zero and, in these cases, above the single-emitter threshold.

To more selectively address individual emitters, we next performed autocorrelation measurements at low temperature using resonant excitation. Under these conditions, the laser can be tuned to a specific optical transition, greatly reducing the likelihood of exciting multiple centers at once. Representative measurements at several excitation powers are shown in Fig. 4.16. In this case, we observe a strongly suppressed zero-delay correlation, with $g^{(2)}(0) = 0.1$, providing clear evidence that the resonance originates from a single NiV^- center.

In addition to antibunching, the low-temperature resonant measurements also show oscillations in $g^{(2)}(\tau)$. These arise from coherent optical driving of the two-level system and are the time-domain signature of optical Rabi oscillations between the ground and excited states. Such behavior has been observed previously in other solid-state emitters [192] as well as in diamond defects [225]. The measured correlation function can be fit using

$$g^{(2)}(\tau) = 1 - e^{-\eta|\tau|}\left[\cos(\mu|\tau|) + \frac{\eta}{\mu}\sin(\mu|\tau|)\right], \tag{4.21}$$

where $\eta = \left(\frac{1}{T_1} + \frac{1}{T_2}\right)/2$ and $\mu = \sqrt{\Omega^2 + \left(\frac{1}{T_1} - \frac{1}{T_2}\right)^2}$. Here, T_1 is the excited-state lifetime, T_2 is the optical coherence time, and Ω is the optical Rabi frequency. Fitting the data gives $1/\eta = 10$ ns, consistent with the independently measured lifetime and indicating that the optical coherence is primarily limited by excited-state decay.

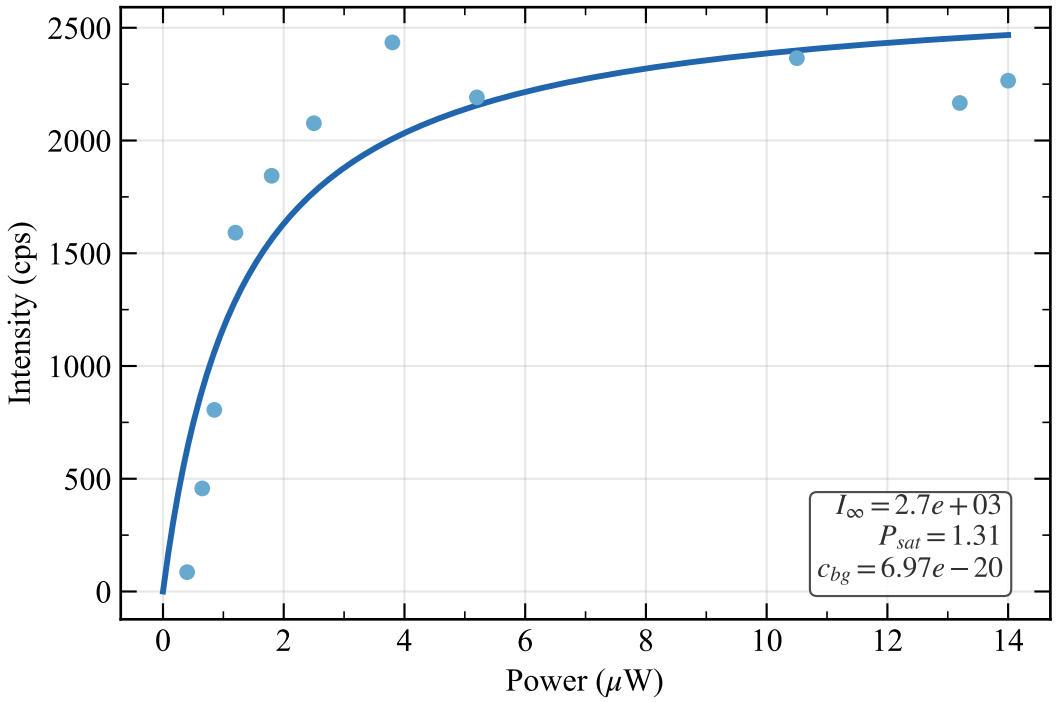

Figure 4.15 Saturation curve for a nanopillar in the $10^{13}13$ ions/cm^2 fit to a typical saturation curve model with extracted parameters in the bottom right.

The $g^{(2)}(\tau)$ measurements were corrected for background using saturation measurements, with $P_{\text{sat}} = 300$ nW and an estimated background contribution of 2%. After this correction, a small residual nonzero value of $g^{(2)}(0)$ remains, which we attribute to sample drift and laser drift not fully captured by the background calibration. Taken together, these measurements show that while room-temperature off-resonant excitation probes multiple emitters within a nanopillar, low-temperature resonant excitation can isolate individual NiV^- centers and reveal both their single-photon character and their coherent optical dynamics.

Experimentally, we also include a small temporal offset τ_0 to account for a path distance between the two detection channels of the Hanbury Brown and Twiss setup. The measured correlation function is then written as

$$g^{(2)}(\tau) = 1 - e^{-\eta|\tau-\tau_0|}\left[\cos(\mu|\tau-\tau_0|) + \frac{\eta}{\mu}\sin(\mu|\tau-\tau_0|)\right]. \tag{4.22}$$

This is the form used when fitting to the data presented in Chapter 4.

Importantly, there is no applied magnetic field for this data, so the two level system we are driving is simply the orbital state and the excited state, which is why the exponential decay we observe in the Rabi oscillation is on the order of 10 ns, which is consistent with the T_1related spontaneous decay time corresponding to the excited state lifetime of the emitter. This is not to be confused with the

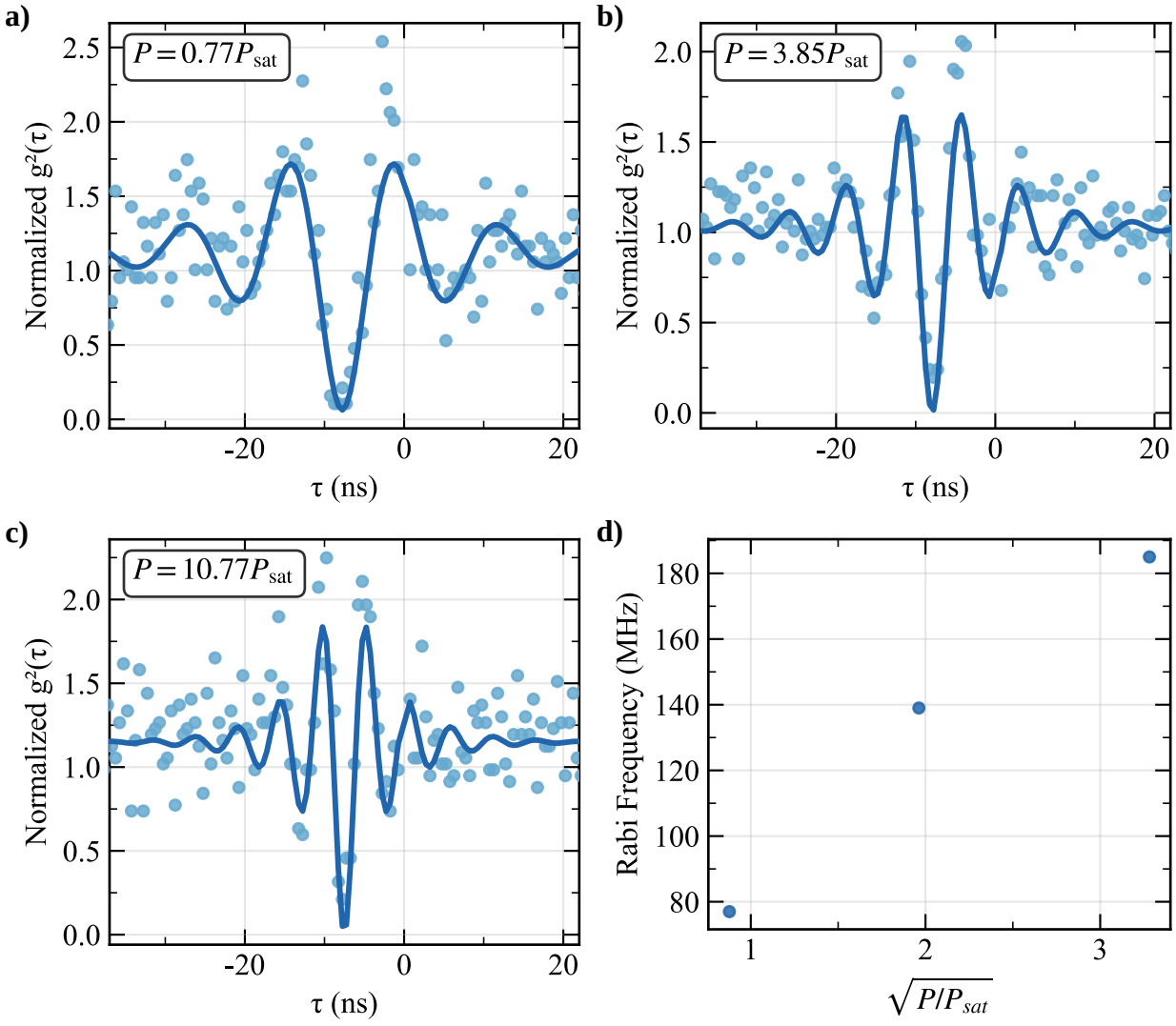

Figure 4.16 **(a)-(c)** Data of second-order correlation function $g^{(2)}(\tau)$ on an NiV in a nanopillar at 1.6K using an $NA = 0.7$. **(b)** Rabi frequency extracted from the coherent g2 model plotted as a function of the $\sqrt{(P)}$ dependence, which produces the expected linear behavior as described (insert where).

coherence time for example of the spin sublevel ground state, which has ms T_1times.

4.3.6 Polarization Properties

Having now confirmed that individual resonances are indeed individual NiV emitters, we now turn to another key aspect of the optical response of NiV^-: the polarization properties of their emission. Polarization-resolved spectroscopy provides complementary information about the orientation of the optical dipole moments, and the geometric alignment of individual defects within the crystal or nanostructure. These measurements were performed on the nanopillar sample and, in particular on individual optical resonances under resonant excitation. Experimentally, polarization analysis was implemented by placing a polarizing beam splitter (PBS) in the detection arm of the confocal microscope, which serves as a polarization filter. A half-wave plate (HWP) was inserted before the PBS, allowing the detected polarization to be rotated continuously. By rotating the HWP and recording the detected intensity, we obtain the polarization dependence of the emission.

In addition to resonant measurements on individual ZPL transitions, we also investigated the polarization properties under off-resonant excitation by placing the half-wave plate in the excitation path and analyzing both the zero-phonon line (ZPL) and the phonon sideband (PSB). For the pillar sample, these measurements were performed on individual emitters confined to single nanopillars. We find that the polarization dependence of the PSB emission is identical to that of the ZPL, indicating that the dominant emission dipole orientation is the same for both the coherent ZPL and the phonon-assisted transitions.

Representative polarization data are shown in Fig. 4.17. Two distinct behaviors are observed. Some emitters exhibit polarization-independent emission, which is well described as circularly polarized. In this case, rotating the analysis polarization does not change the detected intensity, consistent with an emitter whose optical dipole lies in the plane perpendicular to the pillar axis. Other emitters show a clear sinusoidal modulation of the detected intensity as the analyzer is rotated, characteristic of elliptical polarized emission in which intensity does not go fully to zero but is reduced. These emitters are associated with NiV centers oriented at approximately 109.5° (up to a small off-cut) with respect to the pillar axis.

Quantitatively, the linearly polarized data are well described by Malus' law,

$$I(\theta) = I_0 \cos^2(\theta) + I_{\mathrm{bg}}, \tag{4.23}$$

where I_0 is the modulation amplitude, θ is the angle of the half-wave plate (or, equivalently, the analyzer angle), and I_{bg} accounts for background or unpolarized contributions. In contrast, circularly

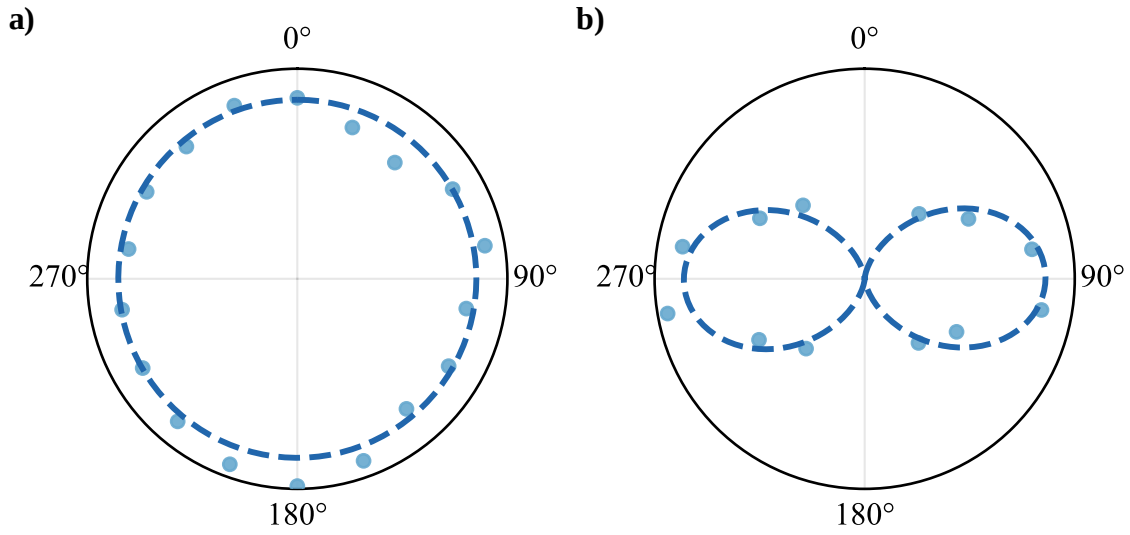

Figure 4.17 **(a)** Circularly polarized emission data from an NiV in a pillar. **(a)** Polarization data taken from a linearly polarized emitter at a 109.5 and some offcut angle. Data was taken by placing a half waveplate and a polarizing beam splitter before the detection arm of the confocal. As such, this data represents polarization properties of the phonon sideband, which we have found to be identical to that of the ZPL.

polarized emission is described by a constant intensity,

$$I(\theta) \approx \text{const.}, \tag{4.24}$$

corresponding to a circle in a polar plot representation.

From a symmetry perspective, these observations are consistent with the selection rules of the NiV^- center in D_{3d} symmetry. The excited state transforms as a_{1g}, the ground state as e_u, and the electric dipole operator transforms as (e_u, e_u, a_{2u}). The relevant triple products for optical transitions are therefore $a_{1g} \otimes e_u \otimes e_u$ for the x and y components and $a_{1g} \otimes a_{2u} \otimes e_u$ for the z component. In D_{3d}, the x and y dipoles are symmetry-allowed, while the z dipole is forbidden. This implies that the dominant emission dipole lies in the plane perpendicular to the high-symmetry axis, leading naturally to circularly polarized emission for centers aligned along the pillar axis and linearly polarized emission for centers tilted with respect to it.

We did not perform analogous polarization measurements on the planar (p-i-p) sample, as its $\langle 100 \rangle$ surface orientation implies that all four possible NiV orientations project to the same linear polarization in the detection plane, with an angle of approximately 54.5° to the surface normal. In that geometry, the different crystallographic orientations cannot be distinguished by simple polarization analysis. Overall, these polarization-resolved measurements further support the symmetry-based picture of the NiV^- optical transitions and provide a direct, experimentally

accessible signature of the defect orientation within individual nanopillars.

Chapter 5

Charge State Stability and Photophysics of the NiV

In this chapter, we explore the various charge state dynamics within the NiV^-. We begin with a theoretical review of defect charge states in semiconductors and common charge traps in diamond. We then review the different charge states for NiV^-. We then go into the different mechanisms which have been utilized to charge stabilize different defect states. From there, we describe the experiments performed to probe the charge state stability of the NiV^-. We begin with the excitation wavelength dependence of NiV^- photoluminescence (PL) as well as the extinction of PL observed under resonance excitation. We continue with an analysis of photon bunching observed, which is indicative of a dark shelving state and also show evidence for blinking in low density defect regions for certain samples. Then, we go into work done using a p-i-p doped sample as a means to stabilize the NiV^- charge state. This covers the revival of NiV^- PL at resonant excitation with bias voltage as well as second order Stark shifts under higher bias voltages confirming the inversion symmetric nature of the NiV. Then, we demonstrate lifetime-limited linewidths using bias voltage as well as time correlated single photon counting to measure the excited state lifetime. We conclude with a proposed charge state model of the NiV^- and compare it to other defects in diamond, ultimately determining that the NiV^{2-} is likely the dark shelving state.

5.1 Theoretical Review

For many point defects in semiconductors, charge state stability is a major concern that can ultimately be a primary limiting factor for their usefulness in quantum information applications. There are many sources of charge state instability ranging from other impurities in the crystal to internal charge states to surface effects and more. These sources can drive unwanted charge state transitions, which can quench fluorescence, cause spectral diffusion, and limit coherence time. In this section, we review the various physical origins of charge state instability in diamond and discuss the implications

for the NiV^-. Finally, we outline how optical excitation induced processes can further influence charge state dynamics.

5.1.1 Charge States and Fermi Level

Defects in semiconductors are not always electrically neutral. Depending on the surrounding electronic environment, a defect can capture an electron and become negatively charged, or lose an electron and become positively charged. These different possibilities are referred to as the defect's charge states [226]. Determining which charge state is most stable is important because the optical and spin properties of a defect often depend strongly on its charge configuration. Indeed, while certain charge states may feature favorable spin properties, others may not, and so stabilizing the desired charge state is crucial [227].

To understand what makes a charge state stable, it is useful to introduce the Fermi level. The Fermi level determines how energetically favorable it is for electrons to occupy available states. In a semiconductor, the Fermi level lies within the band gap and is influenced by the concentration of donors, acceptors, and other charged impurities in the material. For an intrinsic semiconductor it typically lies near mid-gap, whereas doping or unintentional impurities can shift it upward or downward [227]. A defect embedded in this electronic environment introduces localized energy levels within the band gap. Because the defect can exchange electrons with the surrounding crystal, it may change charge state depending on the position of the Fermi level. The relevant quantities are the charge transition levels, which are the values of the Fermi level at which two different charge states of the defect have equal formation energy [128]. Put differently, these levels mark the points at which it becomes energetically favorable for the defect to gain or lose an electron. As the Fermi level moves through the band gap, different defect charge states therefore become thermodynamically stable. These transition levels can now be calculated with reasonably good accuracy, often to within about 0.1 eV, using modern density functional theory approaches such as hybrid functionals [213, 228]. This picture can also be understood in terms of electron occupation. In thermal equilibrium, the probability that an electronic state of energy E is occupied is given by the Fermi-Dirac distribution,

$$f(E) = \frac{1}{1 + e^{(E-E_F)/kT}}, \tag{5.1}$$

where E_F is the Fermi level, k is the Boltzmann constant, and T is the temperature. A higher Fermi level corresponds to an environment that is more electron-rich, making electron occupation of defect-related states more likely, while a lower Fermi level favors less occupied configurations. In this way, the Fermi level sets the tendency of a defect to adopt one charge state rather than another.

For the nickel-vacancy center, the negatively charged state NiV^- corresponds to the defect having captured an additional electron from a nearby defect or from the host crystal itself. Whether

this charge state is stable therefore depends on the local electronic environment and on where the Fermi level lies relative to the relevant charge transition levels. In diamond, this issue is especially important because the effective Fermi level experienced by a defect is not determined only by the average bulk purity. It has been shown, for example, that nearby donors, acceptors, and other charged defects can strongly modify the local electrostatic environment, leading to substantial spatial variation in charge stability even within otherwise high-purity material [229]. As a result, controlling the concentration and distribution of donors and acceptors, reducing unwanted charge noise, or deliberately engineering the local electronic environment is often essential for stabilizing the desired defect charge state in diamond-based quantum devices. We now review the most common charge traps that can exist within diamond.

5.1.2 Common Charge Traps in Diamond

In diamond, the most common and influential impurity is substitutional nitrogen (N_s), which acts as a donor and tends to raise the Fermi level, thereby favoring more negative charge states of nearby defects [230]. Substitutional boron (B_s) is another common and important impurity, which acts as an acceptor and shifts the Fermi level down towards the valence band, but in most high-purity CVD-grown samples, nitrogen is typically the dominant residual impurity.

Beyond intentional or unintentional dopants, lattice damage introduced during defect creation—particularly via ion implantation—provides another major source of charge traps. High-energy implantation can produce a variety of vacancy-related complexes, including monovacancies (V), divacancies (V_2), and potentially higher-order vacancy clusters [231]. Both V and V_2 act as acceptors [232–234], tending to lower the Fermi level and destabilize negative charge states of optically active defects. While monovacancies and divacancies are generally expected to anneal out at temperatures of approximately 900°C and 1100°C, respectively, less is known about the formation and removal of higher-order vacancy complexes, which may persist even after high-temperature annealing.

Finally, the defect of interest itself can introduce additional complexity. Many defects in diamond can form multiple different defect complexes (e.g. substitutional, interstitial, vacancy) with different charge state and electronic properties. If the desired defect configuration is not the one with the lowest formation energy, competing complexes may form and act as unintended donors or acceptors, further contributing to local charge state instability.

5.1.3 Charge States of the NiV Center

Having discussed charge states and common charge traps in diamond, we now review the internal charge states for the NiV center. Hybrid functional DFT calculations predict three relevant charge

states: NiV^0, NiV^-, and NiV^{2-} [214]. We are interested in the negatively charge state NiV^- for quantum applications, and so stabilizing this charge state is our primary goal. The calculated charge transition levels can be found in [214] are shown in Figure 5.1. In intrinsic diamond, the Fermi level should theoretically lie near the mid gap, and so the DFT calculations would suggest that NiV^{2-} would be the thermodynamically favored charge state. Similar behavior has been predicted and observed for other group-IV vacancy centers such as the SiV. Furthermore, it would suggest that to achieve a truly stable NiV^-, we would need to bring the Fermi level down.

In addition to the internal charge states for the ideal NiV configuration, other nickel-related defect complexes can form during implantation or growth. These include nickel–nitrogen complexes [236, 237], substitutional nickel [161, 165], and other nickel–vacancy-related defects. Although the NiV center is predicted to have a lower formation energy and thus be thermodynamically favored, this argument applies strictly to the final equilibrium state. In practice, kinetic barriers and the details of defect migration and recombination during annealing can strongly influence which complexes actually form. This is particularly relevant when comparing relatively simple complexes such as NiV and Ni_s to more complex nickel–nitrogen defects.

5.1.4 Optically Induced Charge State Transitions

The Fermi level sets the probability for electron occupation of states in equilibrium, but when laser light is shone onto the sample, it is put into a non-equilibrium state. In particular, optical excitation can actively drive charge state transitions. Thiering and Gali showed that excitation at 1.22 eV can induce a transition from NiV^0 to NiV^-, while excitation at 1.92 eV can drive a transition from NiV^- to NiV^{2-}, both via bound-exciton processes [214]. Higher-energy excitation at 3.42 eV leads to ionization and can convert NiV^{2-} back to NiV^-.

This set of processes suggests the possibility of optically driven cycling between NiV^- and NiV^{2-} under sufficiently energetic excitation. Importantly, the zero-phonon line of NiV^- lies at 1.4 eV, below the 1.92 eV threshold for promoting the $NiV^- \rightarrow NiV^{2-}$ transition. As a result, resonant or near-resonant optical control of NiV^- should not directly drive the system into the doubly negative charge state. At the same time, any population in NiV^0 can be funneled into NiV^- via the 1.22 eV excitation pathway. From this perspective, the NiV^- state is expected to be relatively stable under typical resonant optical excitation conditions, even in the presence of multiple accessible charge states.

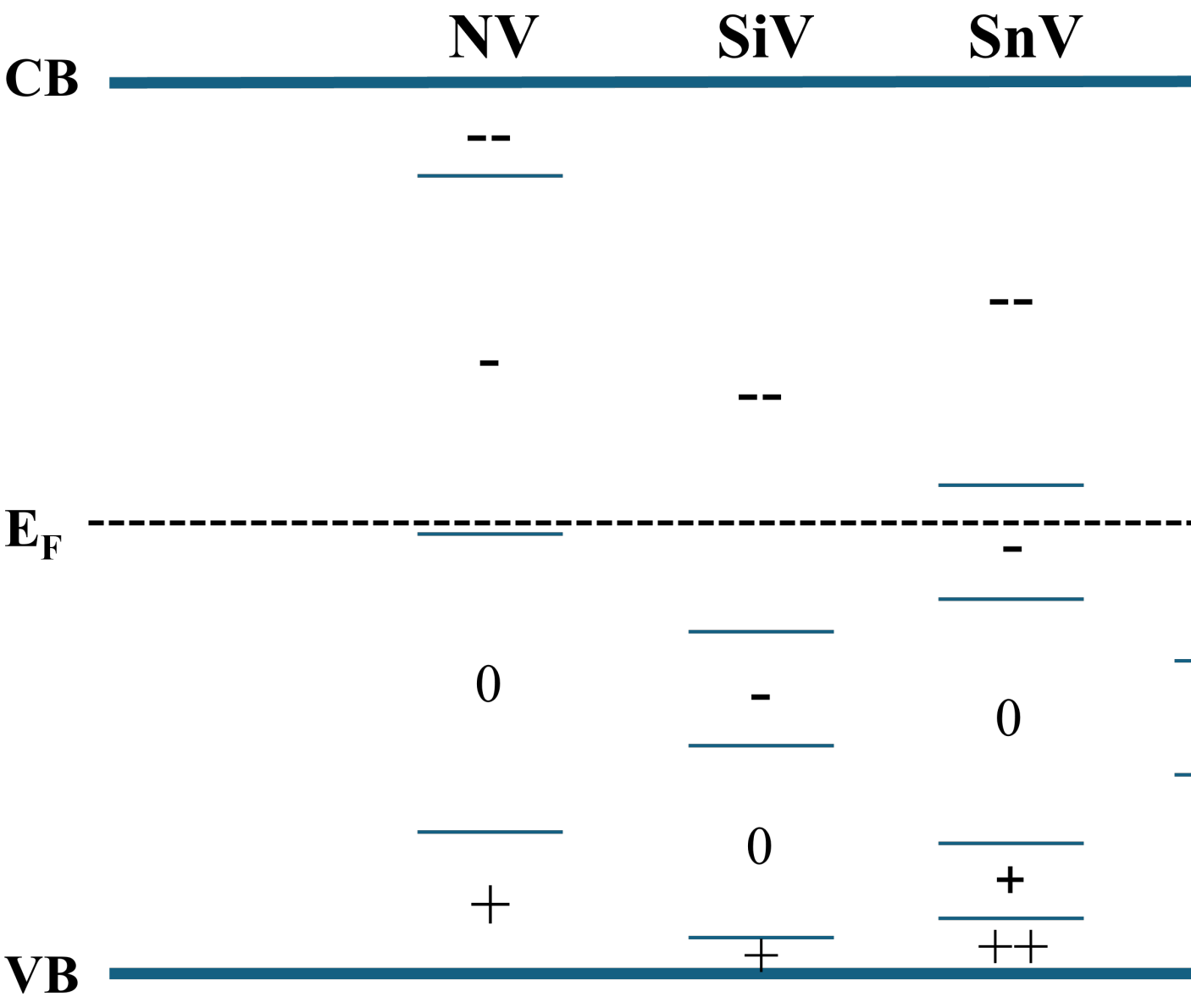

Figure 5.1 Graph showing charge state transition levels with different charge configurations indicated based on Fermi level position within diamond. Values are to scale and were extracted from [235] for NV, [213] for SiV and SnV, and [171] for NiV.

5.2 Evidence for Charge State Instability

In this section, we present several experimental signatures that point toward the NiV^- center experiencing charge state instability. In particular, we examine (i) the strong dependence of the NiV^- fluorescence on the excitation wavelength, (ii) photon bunching behavior that suggests the involvement of additional non-radiative or dark states beyond a simple two-level system, and (iii) intermittent blinking observed in some emitters, indicative of switching into and out of optically inactive states. Together, these observations are consistent with a picture in which the NiV^- center can be pumped into one or more dark states, compromising its stability.

5.2.1 Excitation Wavelength Dependence

5.2.1.1 PL Decline at 700nm

We first noticed a strong wavelength dependence of the NiV^- fluorescence while surveying the sample that would later be fabricated into nanopillars. In the bulk 1×10^{12} ions/cm^2 region of this sample, prior to etching, switching the excitation wavelength from 740 nm to 690 nm produced a noticeable increase in fluorescence. Motivated by this, and by the earlier finding that NiV^- fluorescence is quenched under purely resonant excitation, we performed a systematic measurement of the fluorescence as a function of excitation wavelength. In this experiment, the laser wavelength was scanned over a broad range, while the excitation power was kept fixed and the confocal focus was re-optimized at each wavelength. The emitted fluorescence was then recorded on the avalanche photodiodes. To determine whether the effect was specific to one sample, we repeated the same measurement in two different structures: first in the bulk region of the future nanopillar sample, and then in the p-i-p sample in the 1×10^{10} ions/cm^2 region.

In both samples, we observed the same qualitative behavior. As the excitation wavelength was increased from 690 nm toward 710 nm, the detected fluorescence dropped sharply, with the transition occurring near 700 nm. In the future nanopillar sample, the counts fell to roughly 30% of their initial value, while in the p-i-p sample they fell to roughly 20%. The fact that this behavior appears reproducibly in two distinct samples indicates that it is unlikely to arise from a device-specific artifact, and instead points to an intrinsic threshold-like excitation or charge-conversion process. Indeed, we considered two main explanations for this behavior.

The first possibility is that the effect is related to the neutral charge state, NiV^0. The predicted zero-phonon line of NiV^0 lies in this spectral region, near 1.66 eV [214, 238, 239]. This raises the possibility of a charge-state cycle in which excitation at wavelengths shorter than about 700 nm drives NiV^0 into an excited state that can subsequently relax into NiV^-, thereby replenishing the negatively charged, optically bright configuration. Once the excitation wavelength is increased beyond this

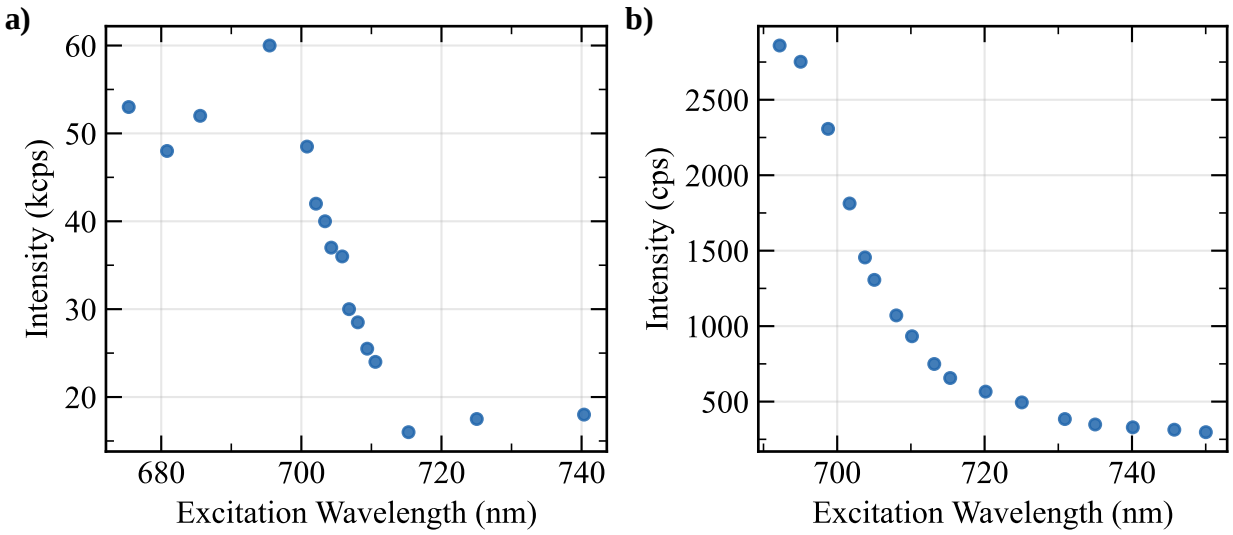

Figure 5.2 NiV^- intensity as a function of excitation wavelength. The power was kept constant across each wavelength used and the focus of the confocal was adjusted as the wavelength shifted. **(a)** was taken in the HPHT IIa sample, $1{\cdot}10^{12}$ ions/cm^2 region, at a power of 1 mW. **(b)** was taken in the $3{\cdot}10^{10}$ ions/cm^2 region of the p-i-p sample at a power of 0.6 mW.

threshold, that repumping pathway would no longer be available, and the NiV^- population could gradually be depleted into NiV^0 or another darker charge state. This interpretation is qualitatively similar to the well-known charge cycling between NV^0 and NV^- in diamond [223].

The second possibility we considered is that the relevant process involves the doubly negative charge state, NiV^{2-}. Theory predicts a charge transition from NiV^- to NiV^{2-} near 1.92 eV, and the lowest excited state of NiV^{2-} is expected to be an A_{1g} bound exciton state [174, 214]. This state may decay non-radiatively into the 1.4 eV excited state of NiV^-, providing an indirect route for populating the bright NiV^- manifold [214]. Since intrinsic diamond is expected to favor NiV^{2-} as the equilibrium charge state, excitation below the threshold could enhance fluorescence by driving this $NiV^{2-} \rightarrow NiV^-$ conversion pathway. When the excitation wavelength becomes too long to access that transition efficiently, the conversion rate would fall, and the observed fluorescence would drop. This interpretation is further supported by earlier absorption measurements from Lawson *et al.*, which show a localized absorption band in approximately the same spectral region [239].

From the data, we conclude that the sharp fluorescence decrease near 700 nm most likely reflects the onset or cutoff of a charge-related excitation pathway, although the wavelength data alone was not enough to unambiguously distinguish whether the dominant mechanism was an internal charge state of the NiV or another defect complex nearby or a combination of both.

5.2.1.2 PL Termination at 840nm

A second, and perhaps even more striking, manifestation of this wavelength dependence is observed when exciting with 840 nm light. As shown in Fig. 5.3, when using only 840 nm excitation without any green light, the detected count rate is extremely low, on the order of 250 cps. However, upon adding a small amount of 532 nm light, the fluorescence increases dramatically to approximately 30,000 cps. This measurement was performed in the sample which has 8 different implantation doses. Furthermore, spectroscopy data was taken using only 840 nm excitation, and the resulting spectrum was featureless, devoid of the characteristic NiV^- emission or phonon sideband. Only when 532 nm light was added in addition to the infrared beam did the familiar NiV^- spectrum reappear. This suggests that not just resonant but also near resonant and potentially even any wavelength longer than 700 nm, pumps the NiV^- center into a dark state from which it does not readily return without assistance from higher-energy light such as 532 nm light.

One possible explanation for this near-resonant quenching, which has also been discussed for group-IV vacancy centers, is that near-resonant excitation promotes an electron and under continuous illumination, a second electron from the valence band can be promoted to fill the resulting hole in the ground state. This would then convert the original NiV^- into the optically dark NiV^{2-} charge state. In the absence of higher-energy light (e.g. 532 nm), the system may remain trapped in this dark state for long periods of time. More generally, the dark state could correspond to NiV^0, NiV^{2-}, or a nearby charge trap or donor that effectively removes or adds an electron from the optically active configuration.

We also measure saturation curves with different excitation wavelengths, as shown in Fig. 5.4. For excitation at 694 nm, 710 nm, and 840 nm without green light, the detected signal is dominated by background contributions, and the NiV^- fluorescence is strongly suppressed. In particular, the total count rates under 710 nm and 840 nm excitation are nearly an order of magnitude lower than those obtained under 694 nm excitation. Strikingly, though, when we add a weak 532 nm repump beam to the 840 nm excitation, clear saturation behavior is recovered. In this configuration, the green light serves primarily to stabilize the charge state rather than to directly excite background fluorescence, while the 840 nm light is too long in wavelength to efficiently excite most other defects, thus suppressing the overall background counts. As a result, the recovered signal is dominated by NiV^- emission, yielding a favorable signal-to-background ratio. Indeed, the restored count rates are nearly comparable to those obtained under 694 nm excitation, but with substantially reduced background contributions. These measurements were performed in a nanopillar and goes to show that these observations with near resonant light and the addition of green are not limited to a single sample. This further reinforces the conclusion that optical excitation can drive the system into long-lived dark states unless an active repumping pathway is provided.

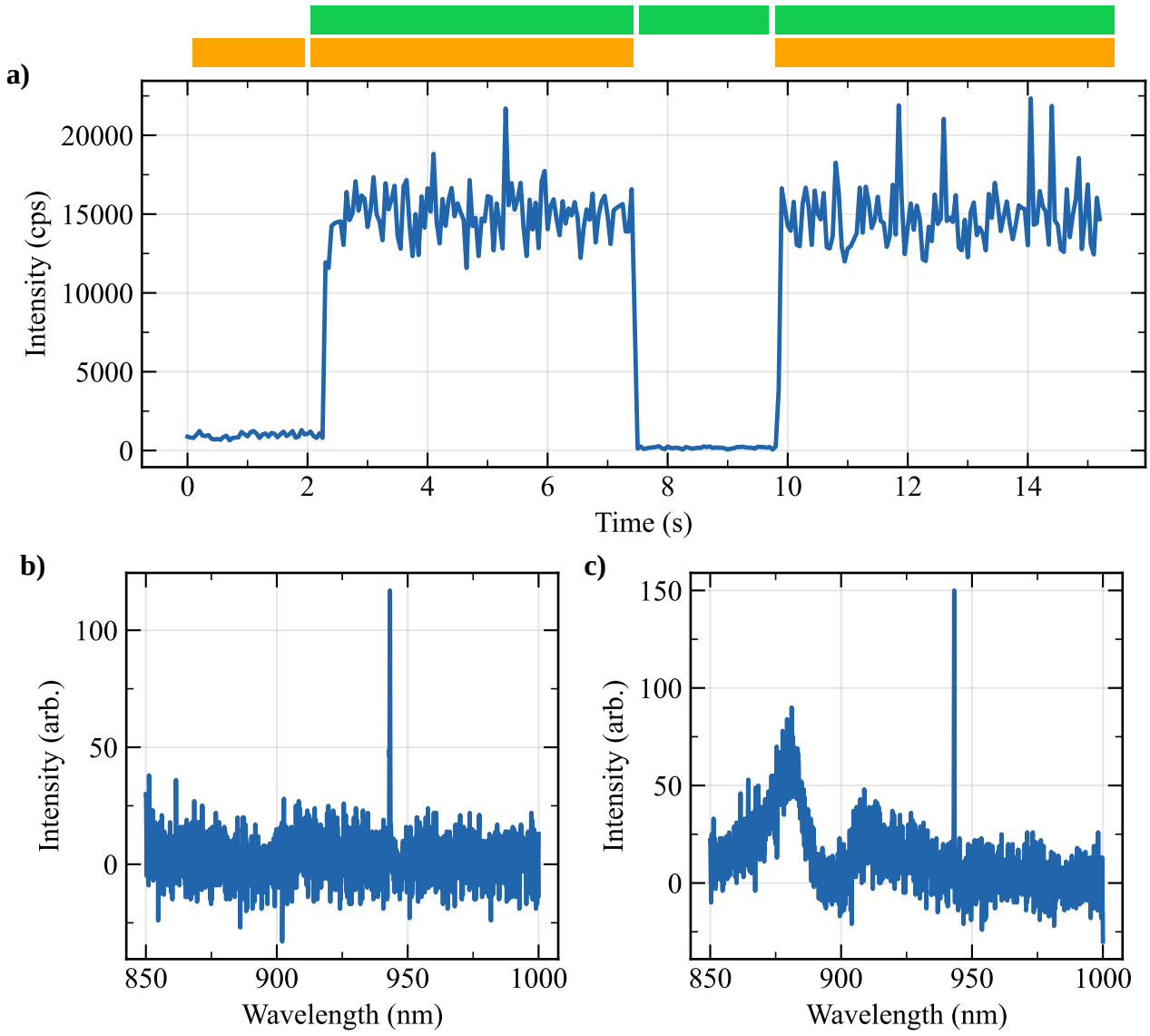

Figure 5.3 **(a)** Spectrum when exciting a nanopillar containing NiV^- using no green light and 0.6 mW of 840 nm light. **(b)** Spectrum when exciting with 10 μW of green light in addition to 0.6 mW of 840nm light. **(b)** Time trace of fluorescence from the nanopillar using NiV^- PL bandpass filters. The orange and green color bars at the top indicate when the 840/532 nm light was on.

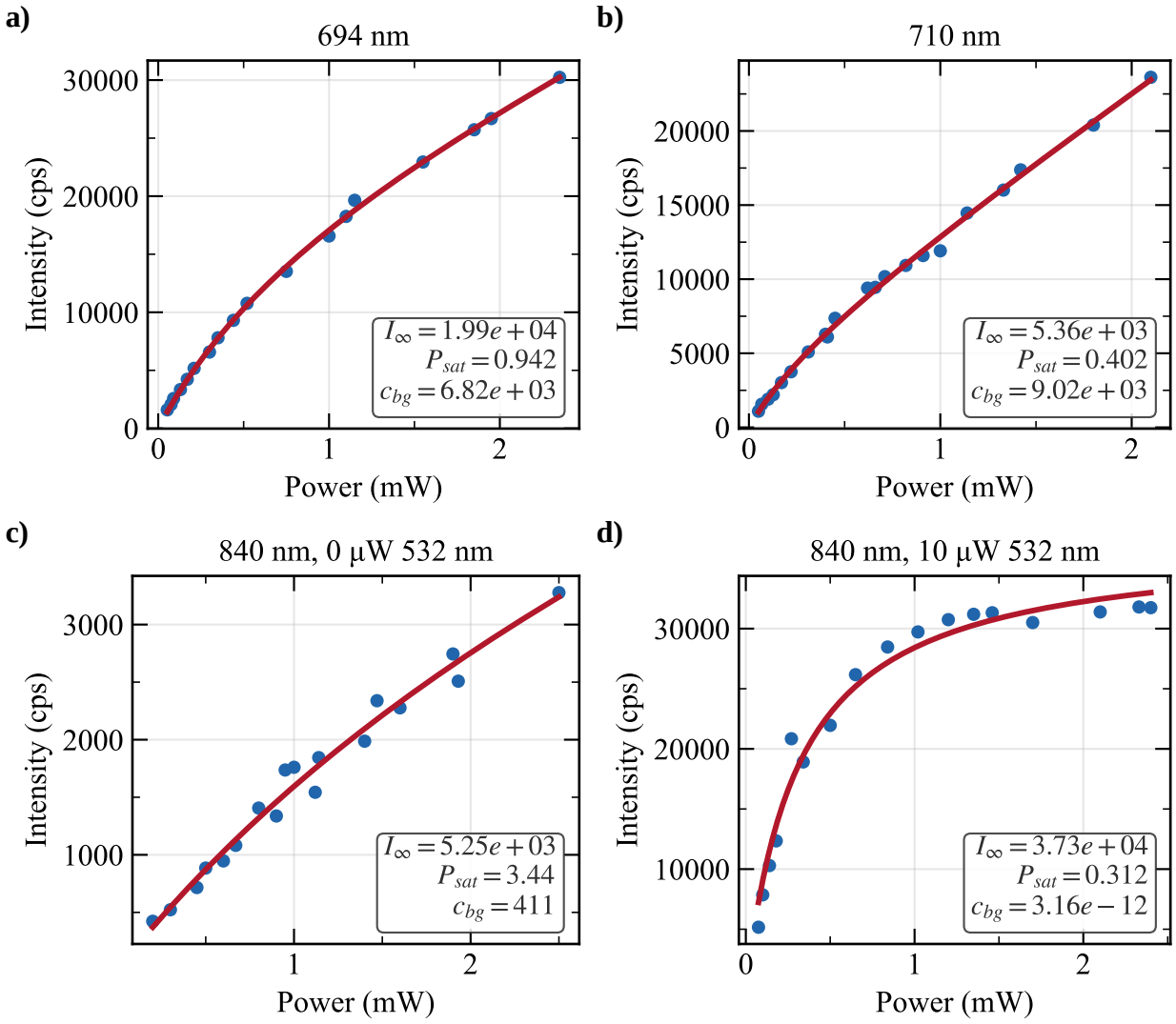

Figure 5.4 Comparison of excitation wavelength on saturation curve for a 10^{13}13 nanopillar. **(a)** uses 692nm excitation, **(b)** uses 710nm excitation, **(c)** uses 840 nm excitation, and **(d)** uses 840nm along with a constant green power of 5 μW. In all the graphs, the fit represents a fit to the typical saturation curve model featuring both a plateauing signal and linear background term as described in the text.

5.2.1.3 Resonant PL Termination

Finally, we return to the fluorescence quenching observed under resonant excitation, first introduced earlier in Chapter 4. In light of the strong excitation-wavelength dependence and the repump behavior discussed above, this effect can now be understood as a further and internally consistent signature of charge-state instability in the NiV system. The fact that even off-resonant excitation at 840nm strongly suppresses NiV^- fluorescence in the absence of green light already suggests that long-wavelength excitation can drive the defect out of its optically bright configuration. It is then perhaps not surprising that purely resonant excitation near the zero-phonon line leads to a complete termination of the photoluminescence as well. In this regime, the excitation appears to pump the defect efficiently into a long-lived dark state from which it does not spontaneously recover on experimental timescales.

This interpretation is consistent with recent studies of the SnV [143] and SiV [240] centers, where resonant fluorescence loss has been attributed to optically driven charge conversion. In those systems, the dominant process is thought to be the capture of an electron from the valence band by the negatively charged defect while it is in its optically excited state. This fills the unoccupied ground-state orbital and converts the center into the doubly negative charge state. Restoring fluorescence then requires ionization, either through the conduction band or through a nearby defect such as the divacancy (V_2) [143], in order to remove the additional electron. Because the relevant defect levels in SnV and SiV lie close to the valence-band edge, resonant photons are sufficient to initiate this process. A similar mechanism is plausible for NiV^-, which is also predicted to lie within approximately 1eV of the valence-band edge [214]. Resonant excitation at 1.4eV would therefore be energetically capable of driving the same kind of valence-band-assisted conversion to NiV^{2-}. By contrast, recovery through ionization into the conduction band is less likely under resonant excitation, since that would require a process involving more than three photons. Thiering et al further predict that NiV^{2-} can be excited by UV light and emit at 2.96eV (419nm), and suggest that UV excitation may drive charge conversion in both directions: from NiV^{2-} to NiV^- by ionizing an electron, and from NiV^- to NiV^{2-} by exciting an electron from the valence band, thereby establishing a dynamic equilibrium between the two charge states [214].

5.2.2 Photon Bunching

Moving on from fluorescence measurements, a second signature consistent with charge-state instability is the observation of photon bunching in the measured intensity autocorrelation functions $g^{(2)}(\tau)$. While antibunching at short times is the hallmark of single-photon emission, bunching at longer times ($g^{(2)}(\tau) > 1$ for intermediate τ) indicates that the emitter intermittently enters a long-lived non-emissive state. Physically, this behavior is naturally captured by extending the ideal

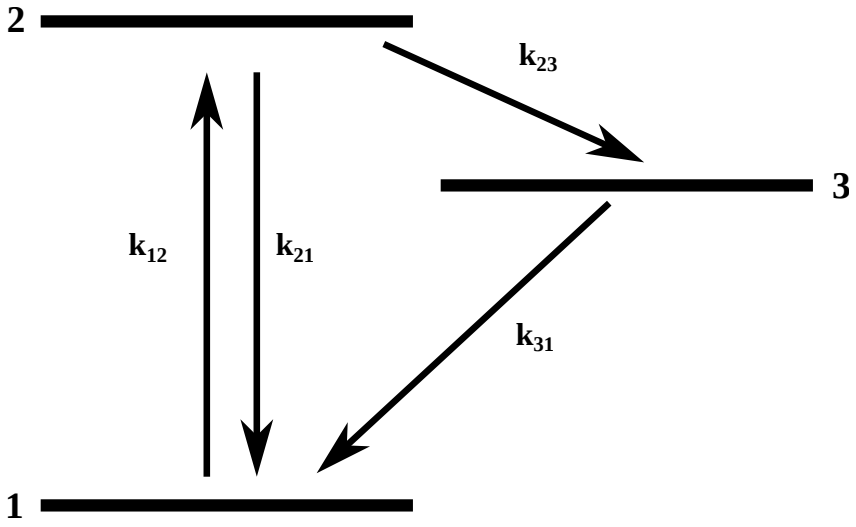

Figure 5.5 Diagram of 3-level shelving model in which there is excitation and decay between ground and excited states along with a pathway to a metastable shelving state.

two-level model to a three-level system that includes a metastable *shelving* (dark) state.

The three-level model, illustrated in Figure 5.5 consists of a ground state (level 1), an optically excited state (level 2), and a shelving state (level 3). Optical pumping drives population from level 1 to level 2 at rate k_{12}. The excited state decays radiatively back to the ground state at rate k_{21}, producing the detected fluorescence. In addition, population can be transferred from the excited state into the shelving state at rate k_{23}, with subsequent relaxation back to the ground state at rate k_{31}. While the system resides in the shelving state, emission on the $2 \rightarrow 1$ transition is suppressed, producing 'dark' intervals in the photon stream. This framework has been widely used to describe photon bunching in diamond color centers (e.g. SiV) and molecular emitters with metastable states [241, 242].

The population dynamics are described by the rate equations

$$\frac{dN_1}{dt} = -k_{12}N_1 + k_{21}N_2 + k_{31}N_3, \tag{5.2}$$

$$\frac{dN_2}{dt} = k_{12}N_1 - (k_{21} + k_{23})N_2, \tag{5.3}$$

$$\frac{dN_3}{dt} = k_{23}N_2 - k_{31}N_3, \tag{5.4}$$

with normalization $N_1 + N_2 + N_3 = 1$. In an HBT measurement under continuous-wave excitation, a photon detection at $t = 0$ projects the system into the ground state, so we take $N_1(0) = 1$ and $N_2(0) = N_3(0) = 0$. Following Ref. [243], the second-order correlation function is then proportional

to the conditional excited-state population, and can be written as

$$g^{(2)}(\tau) = \frac{N_2(\tau)}{N_2(\tau \to \infty)}. \tag{5.5}$$

Solving the coupled rate equations yields the standard three-level form [244]

$$g^{(2)}(\tau) = 1 - (1 + a)e^{-|\tau|/\tau_1} + a\, e^{-|\tau|/\tau_2}, \tag{5.6}$$

where the characteristic timescales are

$$\tau_{1,2} = \frac{2}{A \mp \sqrt{A^2 - 4B}}, \tag{5.7}$$

$$A = k_{12} + k_{21} + k_{23} + k_{31}, \tag{5.8}$$

$$B = k_{12}k_{23} + k_{12}k_{31} + k_{21}k_{31} + k_{23}k_{31}, \tag{5.9}$$

and the bunching amplitude is

$$a = \frac{1 - \tau_2 k_{31}}{k_{31}(\tau_2 - \tau_1)}. \tag{5.10}$$

In this parameterization, τ_1 governs the short-time antibunching recovery (set primarily by excitation and radiative decay), whereas τ_2 captures the longer-time dynamics associated with the shelving process (set primarily by the residence time in the dark state). The amplitude a determines how pronounced the bunching is, and thus how strongly the shelving pathway influences the photon statistics.

Figure 5.6 shows representative $g^{(2)}(\tau)$ measurements taken on the same region under the same optical power but at two different off-resonant excitation wavelengths. In both cases, we observe clear bunching on microsecond timescales, indicating that the emitter is being intermittently pumped into a long-lived dark state. Notably, the extracted bunching timescale depends strongly on the excitation wavelength: using 690 nm excitation yields a decay constant of $\tau = 1.37$ μs, whereas 740 nm excitation yields $\tau = 3.18$ μs. This wavelength dependence supports the interpretation that optical excitation drives charge-state dynamics and/or trap-mediated processes that modulate the bright-state population of NiV^-.Further, the fact that the time scale is less for 690nm is potentially indicative of faster pumping out of the dark state consistent with the higher count rates.

5.2.3 Blinking

The final signature of charge state instability we present is blinking of emitters. Here, blinking refers to an emitter switching between a bright state and a dark state on timescales ranging from milliseconds to seconds or longer. Such behavior is widely observed in solid-state quantum emitters

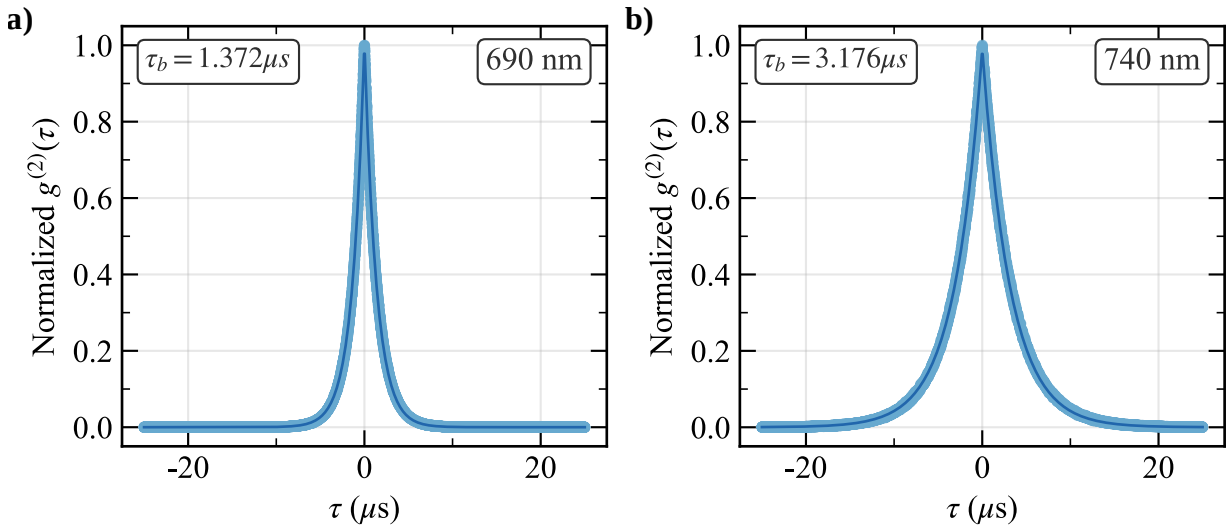

Figure 5.6 **(a)** $g^{(2)}(\tau)$ autocorrelation measured in the 10^{13} ions/cm^2 ensemble region of the ⟨111⟩ NDT sample under 3 mW of 690 nm excitation. A bunching decay constant of τ = 1.37 μs was extracted from the fit. **(b)** Same measurement at the same location under 3 mW of 740 nm excitation, yielding τ = 3.18 μs.

and is commonly attributed to optically driven transitions between different charge states or to trapping and de-trapping of charges in the local environment.

Figure **??** shows representative time traces of NiV$^-$ fluorescence recorded at different spatial locations. Each trace was obtained by positioning the confocal spot on a localized emitter and recording the detected count rate as a function of time. In some cases, the signal initially appears bright and then decays in discrete steps; in others, the fluorescence switches repeatedly between high and low levels before eventually turning off and remaining dark. These intermittent on/off dynamics are a hallmark of blinking behavior. The confocal scan shown in Fig. **??**(d) shows a variety of bright spots in the 10^9 ions/cm^2 region of the Sandia multi-dose sample. Time traces were recorded at several of these localized spots, where blinking was first observed. Taken together, the observation of blinking provides further support for the presence of charge-state dynamics in the NiV system. Along with the excitation-wavelength dependence and the photon bunching behavior discussed above, these results point to a picture in which optical excitation can drive the emitter into long-lived dark states, compromising the stability of the NiV$^-$ fluorescence in the absence of an active repumping mechanism. Notably, these measurements were performed without the use of green repump illumination. In this regime, once the emitter is optically pumped into a dark state—whether this corresponds to a different charge state (e.g. NiV^0 or NiV^{2-}) or to a nearby charge trap—it is not efficiently returned to the optically active NiV$^-$ configuration. As a result, the fluorescence can abruptly drop to zero and remain quenched for extended periods. Occasional spontaneous recovery events, or brief returns to the bright state, are consistent with stochastic charge

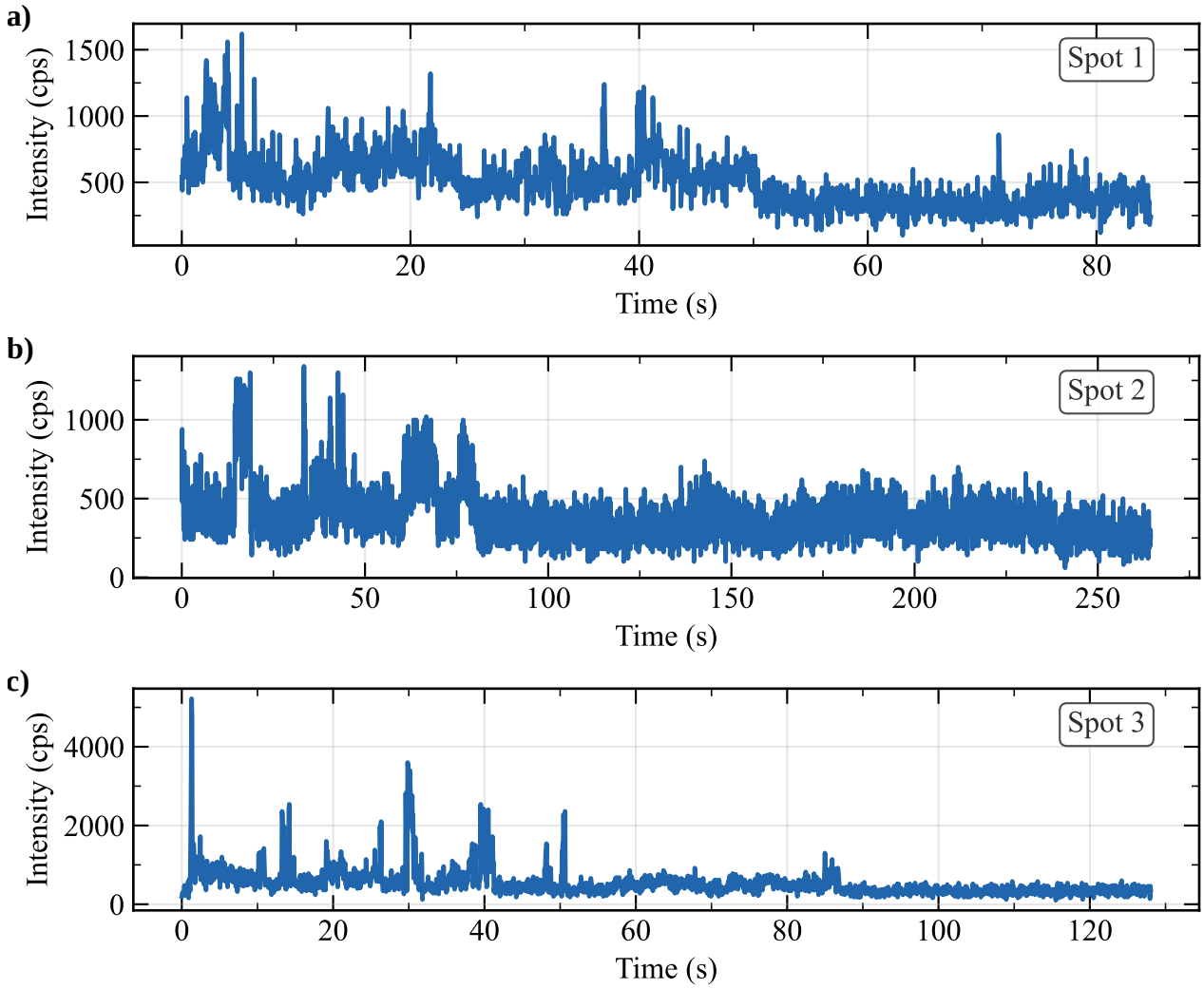

Figure 5.7 **(a)-(c)** Time traces of NiV^- fluorescence at different spots on the Sandia 8 implantation dose sample. **(d)** Confocal microscope scan of the 10^9 ions/cm^2 implantation dose region in the Sandia many implantation dose sample. Different spots were chosen from this scan and time traces of the NiV^- PL intensity were recorded. This is where blinking was first observed.

rearrangements in the local environment.

5.3 Charge State Stabilization

Having observed various signatures associated with charge state instability, we now turn to approaches which seek to mitigate it. Numerous approaches have been explored, but we can group them into roughly three categories: (i) optical repumping to dynamically restore the desired charge state, (ii) chemical control via co-doping, and (iii) Fermi level engineering using electrostatic control or device structures. We will explore each below.

5.3.1 Optical Repumping

The most widely used and experimentally straightforward method is optical repumping with a high-energy laser. High energy is relative and the exact value depends on the host material, the defect of interest and the charge traps which could cause it to go dark, but it should be sufficiently high so that it can drive a charge conversion process. This could be for example optically cycling nearby charge traps, or internal charge state conversions within the defect itself. The net effect of this is to establish a dynamic steady state in which electrons removed from the optically active defect can be replenished, thereby restoring photoluminescence. For diamond defects, 532 nm light is often used for this, however, this is largely because it is a very technologically accessible wavelength and not because it is the best. Although, 532 nm light can efficiently excite nitrogen-vacancy related defects, which often play a role in the local charge state dynamics. The primary downside of optical repumping is that it achieves a dynamic equilibrium, which is just that, dynamic. By cycling nearby charge traps and impurities, it can generate fluctuating local electric fields, which in turn may lead to undesirable effects such as spectral diffusion or charge state switching. Spectral diffusion makes photons distinguishable and can make coherent control challenging as it changes the frequencies which are needed to perform spin selective excitation. Such effects have been observed for several diamond color centers, including NV, SiV, SnV, and GeV [245–249]. Charge state switching, even if it ultimately returns to the desired charge state, can serve as an effective T_1 limit because, even if it returns to the right charge state, when it returns, it will be random which spin state it possesses.

To reduce these undesirable effects, many experiments use pulsed repumping: a short pulse first initializes the defect into the desired charge state, followed by whatever coherent control needs to be performed. In some systems, the defect may remain in its desired charge state for seconds or even minutes after the charge state initialization pulse. However, the charge state initialization is often times not deterministic, and so the pulse is sent out, and it may or may not initialize the correct charge state. For example, getting an NV neutral charge state for some pulse sequence runs as

opposed to the desired NV^-. As such, even if such pulsing can work, it is ultimately not a permanent solution for charge state stabilization. Furthermore, in our samples, the NiV^- fluorescence quenches almost immediately once the green light is removed, making pulsed repumping impractical and requiring continuous repump illumination instead.

5.3.2 Co-Doping

A second strategy is to modify the charge environment by introducing donor or acceptor impurities into the diamond. This process, usually referred to as co-doping, changes the position of the Fermi level and as such can stabilize charge states directly without the need for an additional optical repump beam [250]. The challenge comes in how much doping is necessary to achieve a specific Fermi level within the material. This is complicated by the fact that certain charge states may have very narrow windows of stability for which the Fermi level must lie. An additional consideration is that when optical excitation is performed to do for example coherent control, the local charge environment is also dynamically changed, and so the co-doping may need to account for this as well. Another challenge is diamond is particularly challenging to n-type dope with donors in a controlled and spatially homogeneous way [251]. This means that if one needed the Fermi level to go up to create a more electron rich regime, this might be non trivial to perform. Furthermore, high dopant concentrations can also introduce additional optical absorption which can reduce fluorescence and electron and nuclear spin magnetic noise, which can limit coherence times.

5.3.3 Fermi Level Engineering

Fermi level engineering generally refers to any attempt at engineering the local electric potential so that one can tune the Fermi level to a desired level. This is desirable over co-doping because it provides a range of Fermi levels in one device while co-doping only provides a set Fermi level. One route to achieve this is with surface chemistry and in particular, modifying the surface termination of the material. Different terminations, such as hydrogen or oxygen, modify the surface electronic structure and can therefore shift the near-surface band bending and local Fermi level [125]. This has been used, for example, to help stabilize near-surface NV centers in sensing applications. A second route, and the one pursued in this work, is to fabricate an electrically contacted diamond device that allows the local electronic environment to be tuned with an applied voltage.

Specifically, we use all-diamond p-i-p junctions consisting of two boron-doped p-type regions separated by an intrinsic region containing the NiV centers. Here, “intrinsic” means nominally undoped, so that the charge state of the embedded defects can be influenced by the surrounding electrostatic potential rather than being fixed entirely by heavy local doping. By applying a voltage across the junction, we control the local electrochemical potential in the intrinsic region. Under bias,

one often speaks more precisely of a quasi-Fermi level, which is an effective Fermi level describing the electron or hole population when the system is driven out of thermal equilibrium. In practice, the applied bias shifts the local energetic balance and can therefore tune how stable different defect charge states are. Compared with optical repumping, this approach is attractive because it aims to stabilize the defect charge state through the underlying electronics of the device rather than through continuous optical cycling of the surrounding charge environment. As a result, it offers a more deterministic and potentially scalable route to charge-state control in diamond quantum devices, particularly for photonic architectures in which additional repump beams would add complexity. The central idea is to use controlled doping and electrostatic band bending to shift the local Fermi level at the defect site such that the NiV^- charge state is energetically favored. Similar device-based Fermi level control has previously been demonstrated for NV^- and SnV^- centers [127, 252]. where the electrostatic potential can be tuned by the applied bias and by the built-in fields arising from the doped regions.

In thermal equilibrium, the difference in doping between the p-type regions and the intrinsic region leads to band bending: the conduction and valence bands bend in energy so that the Fermi level remains constant throughout the structure. This creates an internal electrostatic potential that shifts the local position of the Fermi level relative to the defect's charge transition levels. If the Fermi level lies above (below) a given charge transition level, the corresponding negative (positive) charge state of the defect is energetically favored. In this way, the p-i-p structure provides a means of stabilizing the NiV^- charge state by design, rather than relying solely on optical or surface-based techniques. When an external bias voltage is applied across the device, the band bending can be further modified. A forward or reverse bias changes the electrostatic potential in the intrinsic region, thereby shifting the local Fermi level at the position of the NiV center. This provides an additional experimental "knob" to tune the charge-state stability of the defect in situ.

5.4 p-i-p Device

Here we present various measurements performed on our so-called p-i-p device. A widefield microscope image of the device is shown in Chapter 2. Figure 5.8 shows a schematic of the p-i-p structure together with a simulated band diagram.

5.4.1 Electrical Characterization

To verify that the fabricated structures behave as intended, we first measured current-voltage (IV) curves of the junctions. In particular, we wanted to confirm that the boron-doped pads are electrically conductive and that the device exhibits Schottky-like behavior. A Schottky barrier arises whenever

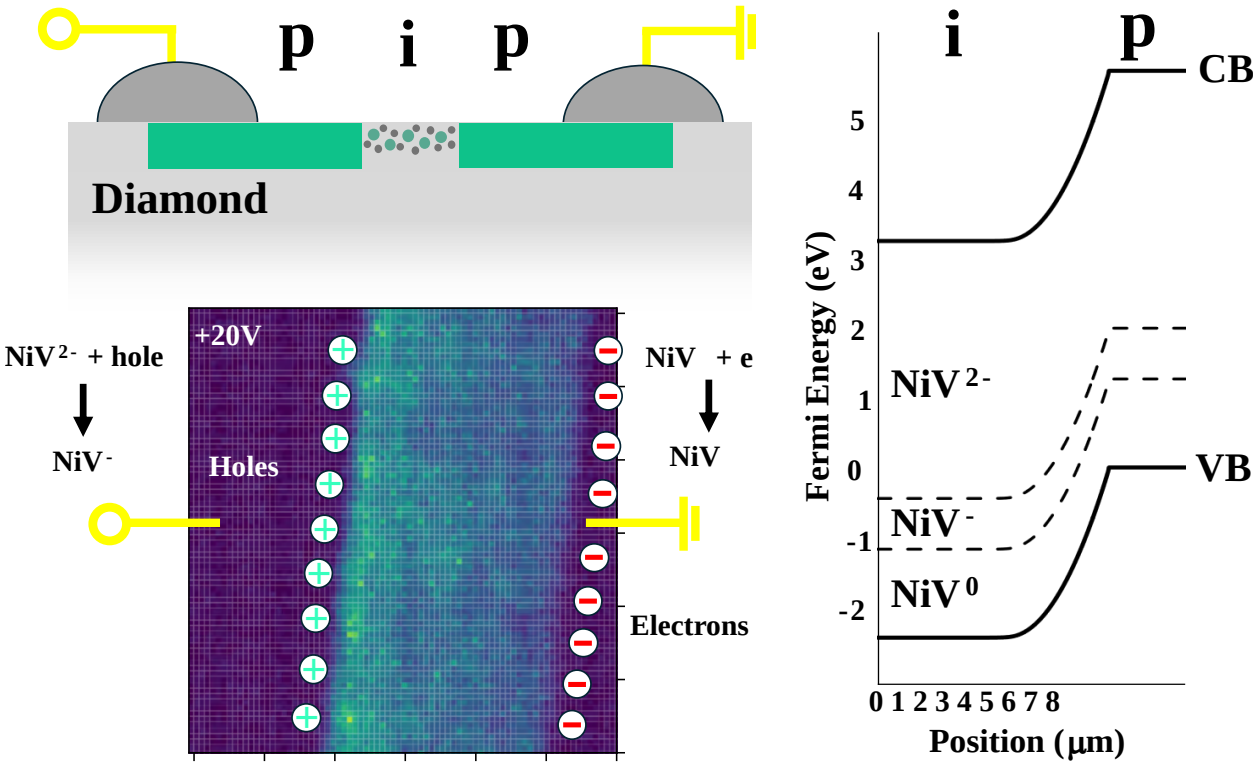

Figure 5.8 On the left is a visual diagram of the p-i-p junction with boron doped pads in the p-region and the Ni atoms implanted in the center or intrinsic region. On the right, shows band bending which occurs as a result of the p-type doping and the charge state transitions of NiV^- are shown as well, extracted from [171, 252]. In the bottom left is a confocal scan at a bias voltage with the positive potential and ground labeled indicating the direction of current and the electric field.

a conductive material meets an insulating one or more generally at any interface in which the Fermi levels are different [227]. Because these Fermi levels must be continuous and align at thermal equilibrium, the formation of a potential barrier, which carriers must overcome in order to pass through shows up. In our case, although the structure is entirely diamond, the p-type doped regions and the intrinsic region form effective barriers to carrier transport [123]. The intrinsic diamond acts as a wide-bandgap, low-carrier-density region, so carriers injected from the p-type regions must overcome an electrostatic potential barrier to traverse the junction. As a result, we expect strongly nonlinear IV characteristics: very little current at low bias voltage, followed by a rapid increase in current once the applied voltage is sufficient to lower the barrier and let the carriers through.

To perform the measurement, we electrically contacted the junctions using silver conductive paint and 38-gauge copper wires. IV curves were measured using a Keithley 2400 source meter. All measurements were first performed at room temperature to confirm the Schottky-like nature of the junctions before cooling the sample to 1.6 K. The initial room temperature measurements can be seen in Figure 5.9, which features IV curves for both junctions. The current compliance limit was set to ± 50 μA, resulting in the observed current plateaus. This was done to ensure the junctions did not breakdown electrically and potentially form a graphitic line across them, as this would act as a short circuit, and prevent any band bending or charge buildup. In both junctions, the current remains strongly suppressed at low bias and then increases sharply beyond a threshold voltage. This is consistent with electronic transport limited by a potential barrier across the intrinsic region. The threshold voltage differs between the two junctions, which we attribute primarily to the different junction widths: junction 1 has a width of approximately 3.5 μm, while junction 2 has a width of approximately 5 μm.

We also measured IV curves as a function of temperature while cooling the sample to 1.6 K, as shown in Fig. 5.10. The overall Schottky-like behavior persists at low temperatures; however, the magnitude of the current decreases as the temperature is reduced. This is consistent with a reduction in thermally activated carrier density in the boron-doped regions and a decreased probability for carriers to surmount the barrier in the intrinsic region. These measurements confirm that the devices behave as expected, validating their use as electrostatic structures for tuning the local Fermi level and, consequently, the NiV charge state.

5.4.2 Voltage Dependent Confocal Scans

Having cooled the sample and confirmed the Schottky-like nature of the p-i-p device, we then took confocal microscope scans using off-resonant excitation. First, though, we had to find the narrow junctions. Thankfully, the boron doped pads appear dark when compared to intrinsic diamond when it comes to the diamond Raman line. This could be because the high boron concentration modifies

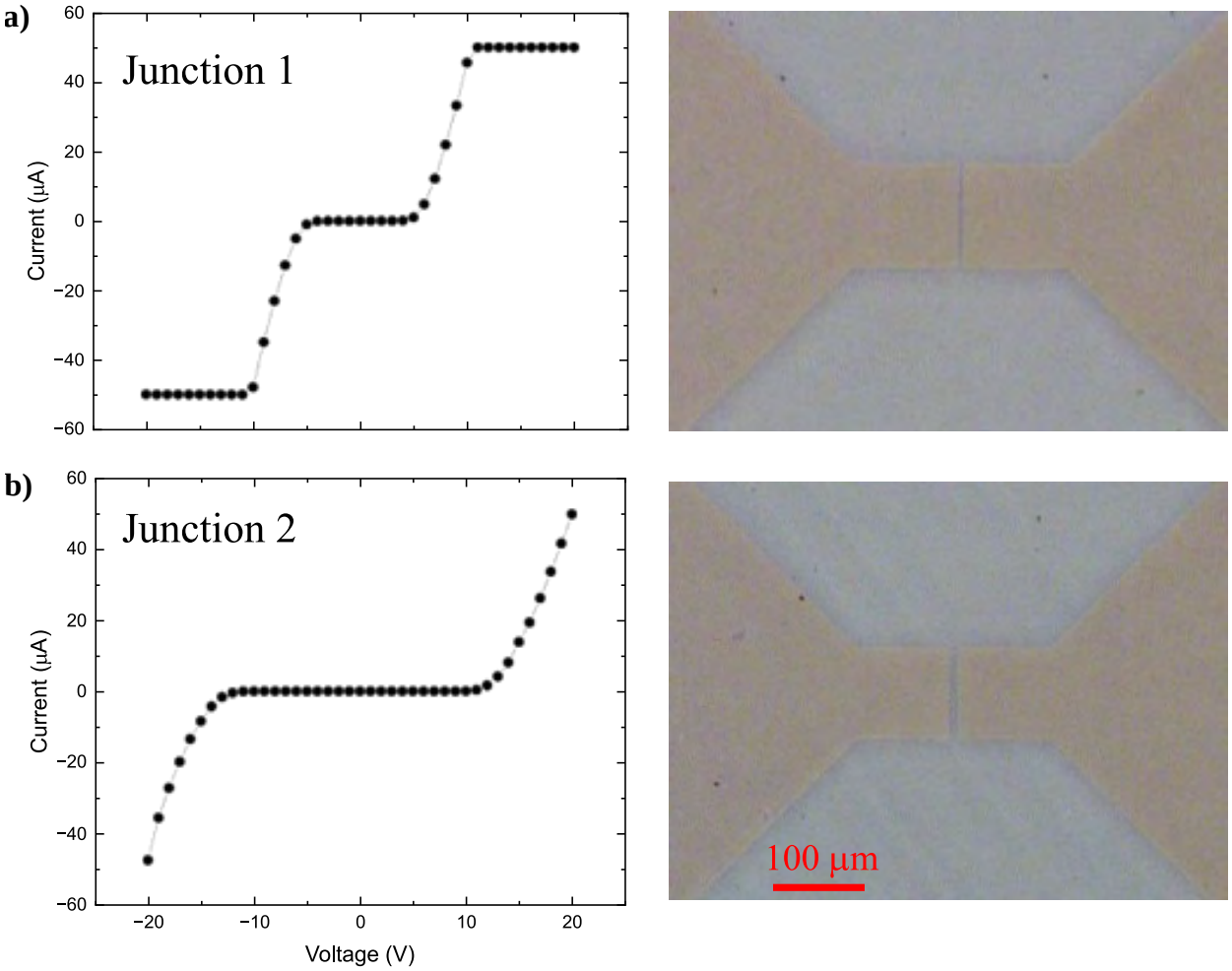

Figure 5.9 (a) Current-Voltage (IV) curves at room temperature on left and widefield image of junction 1 on right (junction width is 3.5 μm). Voltage axis and scale bar from (b) are applied here. **(b)** Same format but for junction 2 (junction width is 5 μm).

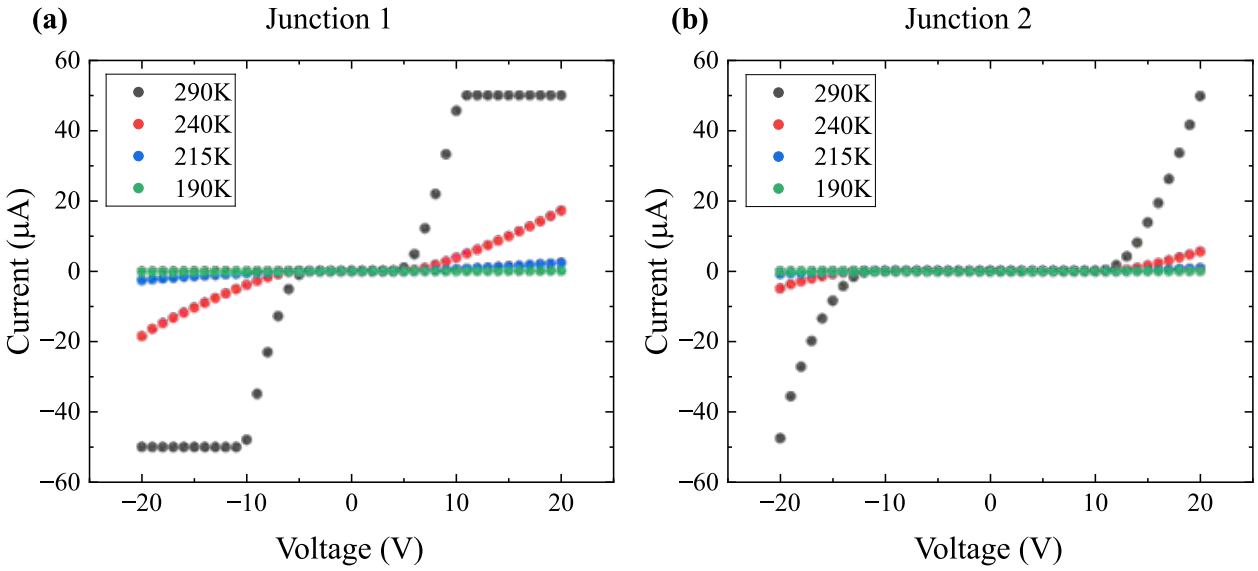

Figure 5.10 (a) IV curves at varying temperatures for junction 1. **(b)** IV curves at varying temperatures for junction 2.

the diamond structure to an extent that it either absorbs or scatters light or because it changes the vibrational modes. Either way, when observed with a Raman selective filter, the dark pads provide a very convenient way to find the junctions. Once we identified the junctions, we then performed off-resonant scans at $\tilde{6}$90nm at various bias voltages as shown in Figure 5.11. These scans are of the $3{\cdot}10^{10}$ ions/cm^2 region. When the bias is applied, a clear increase of fluorescence along one edge and quenching along the opposite edge of the junction is observed, with the sides switching depending on the sign of the applied voltage. This has been observed for a similar p-i-p device used for NV and SnV centers [127, 252, 253] and is with the fact that the electric field from the built up charges will be strongest nearest to the edge of the junction. As such, for resonant excitation, we chose emitters along the edge of the junction, as the tuning range is likely the greatest here and as such, chances for charge state revival are the greatest. Furthermore, for resonant excitation, we restricted our search to the most dilute implantation dose of $3{\cdot}10^{9}$ ions/cm^2.

In addition to collecting NiV fluorescence as a function of bias voltage, we also conducted cross-correlation measurements by using two different filter windows for two APDs to check for the correlated revival/quenching of other defects when the NiV$^-$ fluorescence changes. In particular, we investigated the 700 nm wavelength window. We tried this with both 690 nm excitation (filters: 700-40nm band pass and 700nm long pass) and 532 nm excitation (700-40nm band pass); however, we did not observe any cross-correlation nor spectral signal for the NiV^0, which is predicted to have a zero phonon line in that wavelength regime.

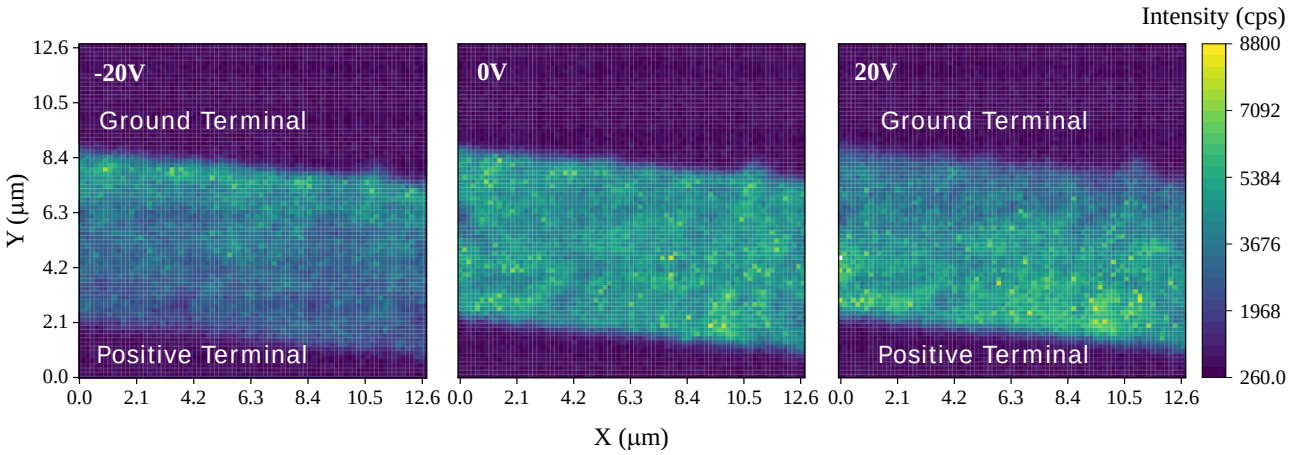

Figure 5.11 Left to right, confocal microscope images of the $3{\cdot}10^{10}$ ions/cm^2 region in junction 2 under different bias voltages. We used an an 850nm long pass and 880nm band pass as detection filters and 690nm excitation wavelength.

5.4.3 Resonant Excitation

Having identified the junctions and observed an NiV^- fluorescence response from bias voltage, we then performed resonant excitation. To do this, we increased our laser power before the objective to about 1mW, and set it to a resonant wavelength around 883nm. We used a high power so that when we performed a confocal scan, any resonances which did revive would be power broadened enough so that we could observe them. Normally, we would apply 532 nm laser light in conjunction with this resonant light, and we would observe emitters revived by this optical repump. This time, we used no 532 nm light and only applied a bias voltage of -20V across the junction. This value was chosen primarily because previous works had identified some charge state switching at higher voltages [123]. With the bias voltage set, we observed various bright NiV^- emitters throughout the junction, revived solely by bias voltage without the need for an optical repump. We found that most of them had a side dependence, which determined whether positive or negative bias voltage would revive them.

Having identified resonances which were revived under applied bias voltage, we wanted to see what varying the bias voltage would do. In Figure 5.13, we see that the resonance shifts as a function of applied bias voltage. This is due to the well known DC Stark effect in which an applied static electric field modifies the transition energy. We will discuss this below in more detail. Second, we also noticed that many of the emitters have a threshold voltage below which, they do not revive, and we observe no fluorescence. This tended to be around ± 5V. For a semiconductor, the Fermi level is located close to mid-gap, making the NiV^{2-} the favored charge state according to ab initio calculations in [214]. By applying a bias voltage to the p-i-p junction, the Fermi level is pushed down, entering the NiV^- charge state regime around -5 V. This can be seen in Figure

5.14 where frequency scans were taken at various bias voltages, revealing both a threshold voltage upon which fluorescence is revived and also the parabolic and thus second order nature of the Stark shift. Interestingly, although the p-i-p junctions are symmetric, we do not see revival of the NiV^- when using positive voltages (reversed field direction). This in combination with the fact that the threshold voltage for NiV^- revival coincides with the voltage at which current begins to pass through the junction (see Figure 5.9) indicates that electron injection in addition to band bending may be involved.

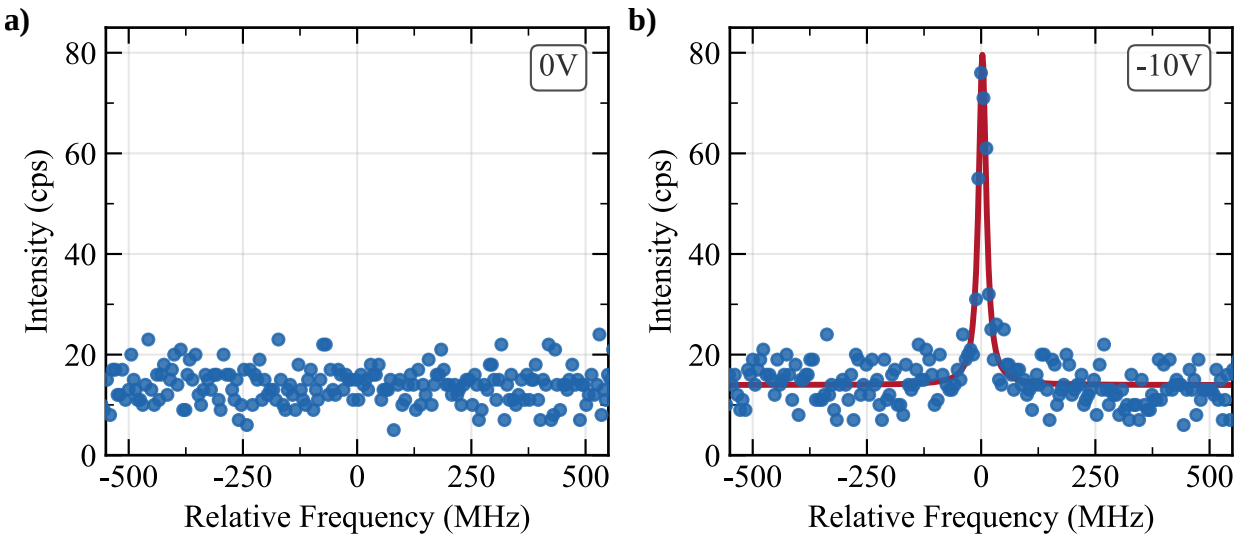

Figure 5.12 Resonant excitation of a single emitter with and without bias voltage at -10V applied. A power of 1000 nW of resonant light was used when scanning the laser across the transition.

Now, not all the emitters we looked at were revived by bias voltage. We also observed emitters which still required 532 nm light to repump. It should be noted that we were still able to observe a DC Stark shift on these emitters, interestingly, suggesting that the NiV still experienced an electric field, but that it wasn't strong enough to revive fluorescence. We think this is likely dependent on emitter location relative to the boron doped pads, which are thin and the for which the electric field may not be homogeneous. For these emitters which require green light, we probe the relative stability with and without bias voltage. In particular, we measure the charge state lifetime by resonantly exciting the NiV^-, while applying 40 μs pulses of green (532 nm) light to initialize the NiV^- charge state. After each pulse of green, we measure the decay of intensity as shown in Figure 5.14(d). When there is no bias voltage applied, we find both a fast decay time constant of 1.6 μs as well as a longer decay time constant of 42 μs. When we do apply a bias voltage, in this case -15 V, we observe a slower decay. In fact, the intensity remains stable for about 15 μs after the green pulse ends, followed by a slow exponential decay with a time constant of 170 μs, indicating substantially improved charge state stability. Note that this decay occurs under continuous illumination of resonant light. As such,

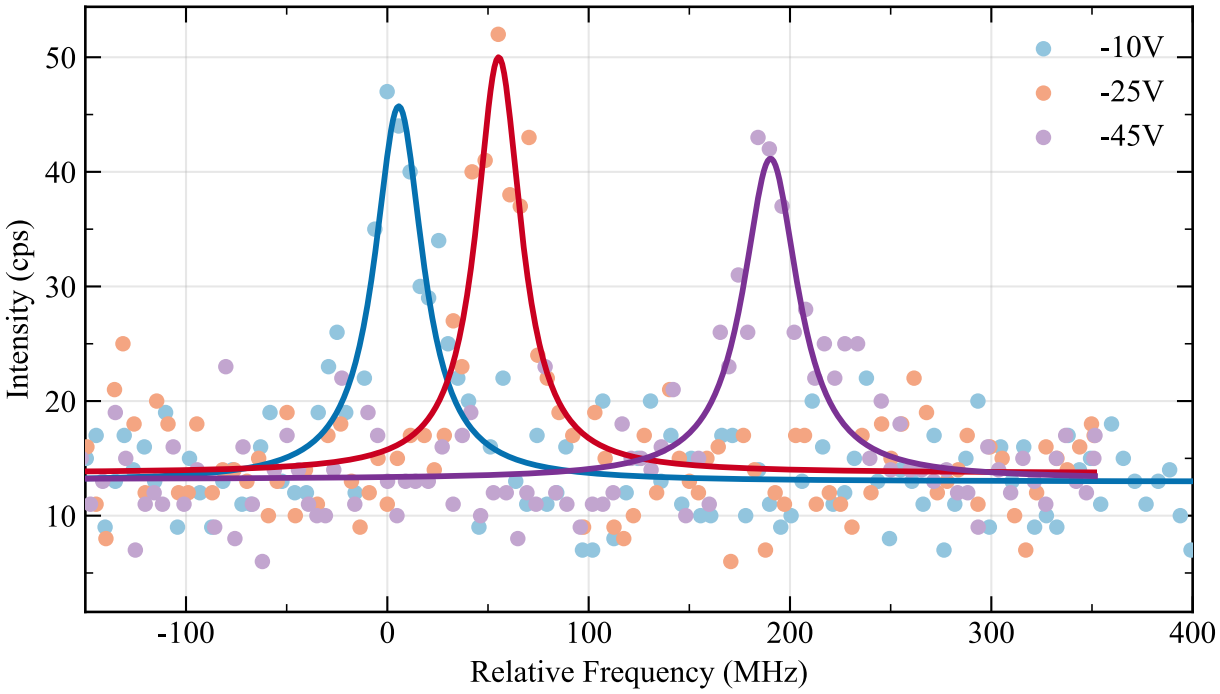

Figure 5.13 Resonant excitation of a single emitter with a different bias voltages shown in the legend. The shift observed displays a parabolic nature.

the short optical pulses of ns to low μs length, as used for all-optical spin control [139], are unlikely to induce charge transitions in biased centers.

5.4.4 Time Constants for Voltage Revival

Another figure of merit for bias voltage revived emitters is the duration over which they remain bright for. To test this, we performed resonant scans over time under an applied bias voltage. We did this also to see if there was any spectral diffusion as a function of time and or if the emitter would blink on or off during this time. We observed no blinking, and the shift in transition frequency was within the specification of our wavemeter, so it was minimal to the point that our measurement was limited by the wavemeter. From this, we conclude that long term stability can be achieved with an applied bias voltage. Further, when we have used these emitters for coherent control measurements, we have used the same emitter under bias voltage for weeks without observing blinking behavior or spectral diffusion. As such, it seems an effective method for stabilizing the charge state of color centers.

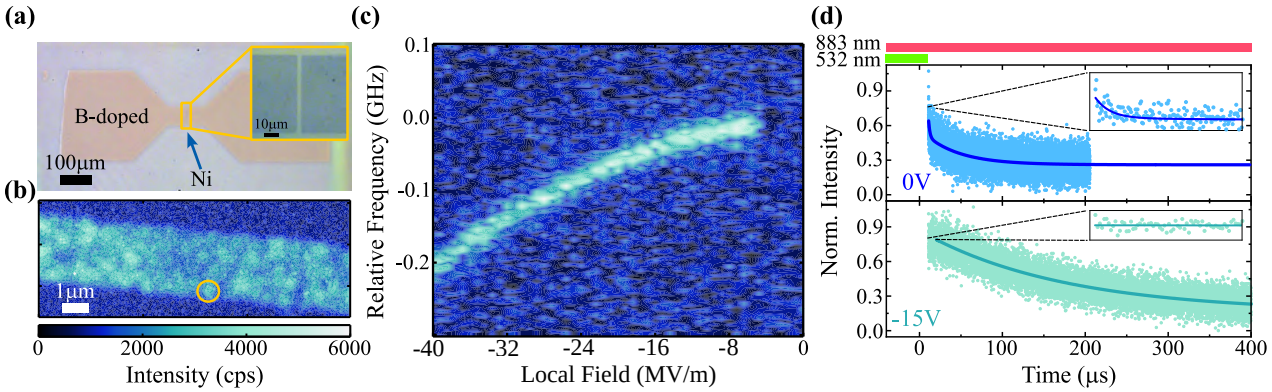

Figure 5.14 **(a)** Widefield microscope image of junction 1 with boron doped pads and nickel implantation region labeled. Top right insert shows zoom-in of junction. **(b)** Confocal microscope scan of junction at 1.6 K with 692 nm excitation at 1 mW. Note that, a switch from 740 nm to 692 nm off-resonant excitation was performed compared to previous figures, as we observe higher count rates under these conditions. Orange circle represents the location at which data was taken. **(c)** Revival of the NiV^- fluorescence signal under resonant excitation by application of bias voltage across the p-i-p junction. The map displays many photoluminescence excitation (PLE) scans at different bias voltages. The x axis is the local field created from an applied bias voltage calculated using the Lorentz local field approximation described in the text. The NiV^- signal revives at $\sim$ -5 V. **(d)** Comparison of charge state lifetime by measuring the decay time of the NiV^- signal after a 532 nm initialization pulse at 100 μW for 40 μs with constant resonant light being applied also at 100 μW. The top graph has no bias voltage applied while the bottom graph has -15V applied. Insets show the first two microseconds after the green pulse has finished. Intensity is normalized to the value when the 532 nm pulse is off, as compared with the background response from the detector (instrument response function) when it is just resonant light.

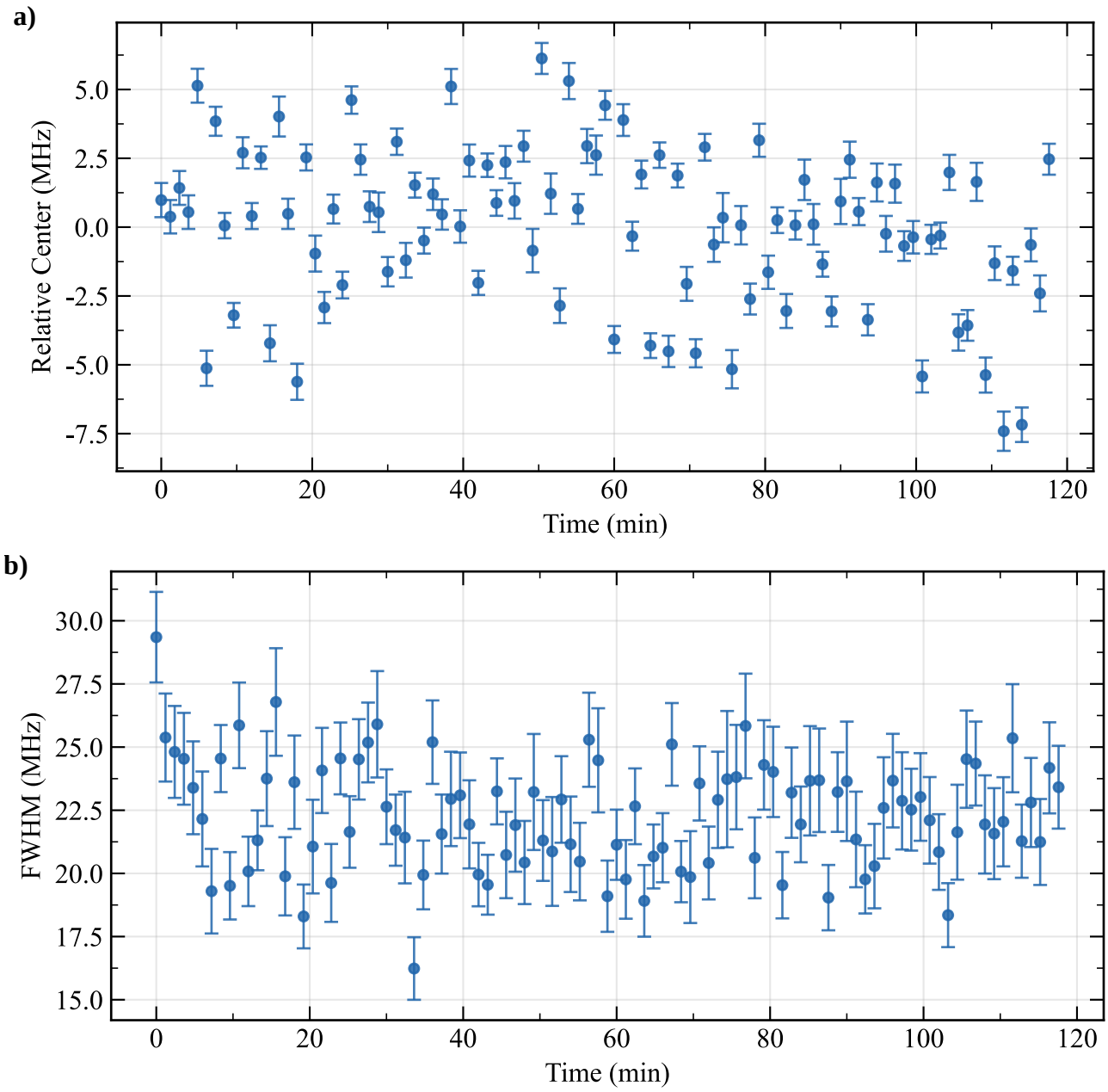

Figure 5.15 **(a)** Relative frequency shift of a resonance revived using a bias voltage of -10V. This data was taken by scanning across the resonance and extracting the center frequency and linewidth (as shown in **(b)** as FWHM) along with the respective errors for both.

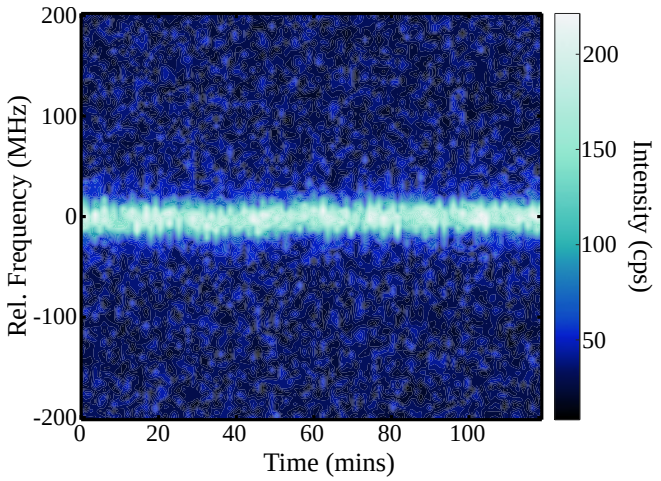

Figure 5.16 PLE map of a resonance over time using an applied bias voltage of -10V and an optical power before objective of 1 μW were used. This was taken by scanning across the resonance repeatedly over time.

5.4.5 Stark Shifts and Tunability

We now discuss the DC Stark effect and what it can tell us about the NiV^-. To start, the DC Stark effect is what is observed when a static electric field changes the energy of an atom-like transition. Here, we mainly explore the first and second order shifts to determine the dipole moment and polarizability of the defect, but others have looked as high as third and fourth order. These higher orders of course require higher electric fields to be probed. The DC Stark perturbation to the Hamiltonian takes the form $\hat{H}_{\text{Stark}} = -\vec{\boldsymbol{\mu}} \cdot \boldsymbol{F}$, where $\vec{\boldsymbol{\mu}}$ is the electric dipole operator and $\boldsymbol{F}$ is the local electric field. The effect of this perturbation is an energy shift of the transition which depends on the difference $\Delta\mu$ between the excited and ground state dipole moments, and which can be expanded as a power series in the electric field $\boldsymbol{F}$ [254]. Similar investigation has been done for SnV in [253]. As we are only concerned with shifts up to the second order in F, the expected energy shift of the transition is

$$\Delta E = -\Delta\mu_{ind} F = \Delta\mu F - \frac{1}{2}\Delta\alpha F^2, \tag{5.11}$$

with change in transition energy ΔE, electric field F, and differences in ground and excited orbital state permanent dipole moment $\Delta\mu$ and polarizability $\Delta\alpha$, respectively [255]. Using the Lorentz local field approximation $F = F_{ext}(\epsilon + 2)/3$ and diamond dielectric constant $\epsilon = 5.7$ [256] we convert between internal (F) and external (F_{ext}) electric fields. We calculate the latter with $F_{ext} = V_{bias}/d$ in which d is the thickness of the junction which we find to be $\sim 3.5\mu m$. With this, we can extract $\Delta\mu$ and $\Delta\alpha$ by fitting this model to the frequency-voltage map seen in Figure 5.14. Additionally, we fit this model to data from 16 emitters and find an average $\Delta\mu = 6.9 \pm 4.7 \cdot 10^{-4}$ GHz/MV/m which corresponds to $1.4 \pm 0.9 \cdot 10^{-4}$ Debye and $\Delta\alpha = -2.1 \pm 0.16 \cdot 10^{-4}$ GHz/$(MV/m)^2$ which

corresponds to 2.47 ± 0.1^3. This indicates that second-order effects dominate, as expected for an inversion symmetric defect with a vanishing permanent dipole moment. The values obtained are comparable to the SnV^- [253], and the permanent electric dipole moment is more than three-orders of magnitude less than that of the NV^- [257, 258]. Along with the magneto-optical data, this provides further confirmation of the defect's assumed structure. Lastly, we find that the linewidths are relatively unchanged even with increasing bias, suggesting the use of electric fields for tuning the transitions over hundreds of MHz to enable overlapping of transitions for QIP applications.

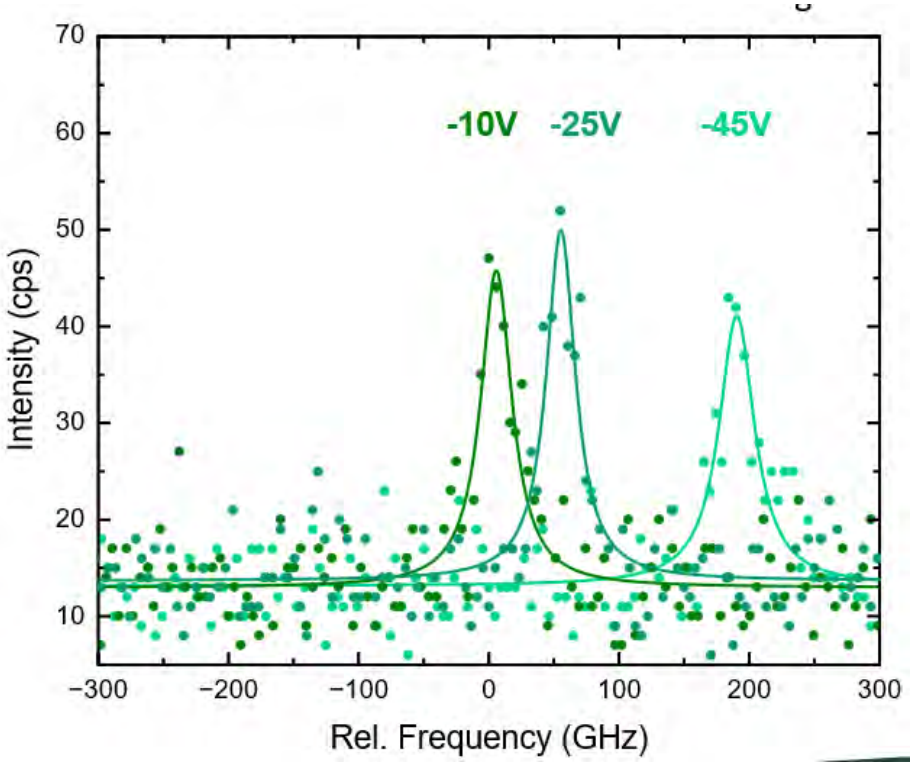

Figure 5.17 Resonant excitation at different bias voltages, showing three different bias voltages and the corresponding transition shifting.

5.4.6 TCSPC and lifetime-limited Linewidths

Next, we try and see what the narrowest linewidth we can achieve is while using the p-i-p device. We do this because as stated previously lifetime-limited indistinguishable photons are a prerequisite for many photonic quantum networking and computing applications [92, 259]. To characterize the transition linewidths, we use the usual PLE spectroscopy. Across 12 emitters, we observe lifetime-limited linewidths for 8 of them, with the remaining 4 showing slightly broader linewidths of 24, 28, 19 and 18 MHz, likely due to residual implantation damage. Figure 5.19 displays one such characteristic measurement. We measure the lifetime of the defect to be $\tau = 10.43 \pm 1.6$ ns

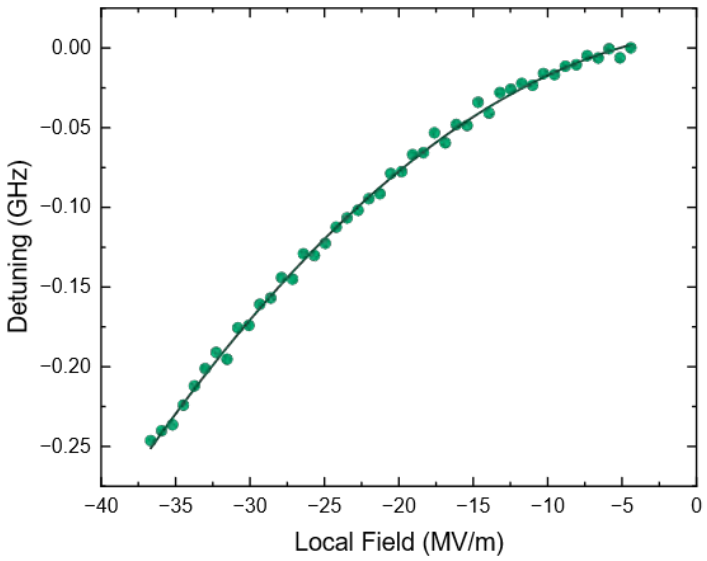

Figure 5.18 Frequency center's and the corresponding shift from center as a function of bias voltage. These were extracted from Lorentzian fits of the resonant transitions at each bias voltage.

(Fig. 5.19(b)) using time-correlated single photon counting (TCSPC), in close agreement with a previous measurement of $\tau = 11$ ns from [224]. This corresponds to a lifetime-limited linewidth of $\Delta\nu_{lim} = (2\pi\tau)^{-1} = 15.3 \pm 2.1$ MHz. Thus across multiple emitters we observe linewidths consistent with the lifetime limit. From these emitters we estimate the width of the inhomogeneous distribution to be approximately 50 GHz, with multiple emitters being within mutual Stark shift tuning range. Note that the NiV^- is known to show improved spectral properties after HPHT treatment [224] which has not been performed after Ni implantation in this study to avoid potential damage to the p-i-p junctions. Further, with bias voltage applied, we find long term stability of these resonances (Fig. 5.20) with an RMS shift of the transition peak of 3 MHz, likely limited by the long-term frequency resolution of our setup.

5.4.7 Statistics on Linewidths and Stark Shifts

In Figure 5.20, we show a large number of emitters under various Stark shifts. This ensures that the emitter we primarily studied was not an outlier and builds statistics for the variations across emitters in terms of differences in dipole moment and polarizability.

We also perform low power PLE scans on a variety of emitters to gauge what the distribution of linewidths we could achieve were. The results are discussed above with only 4 having slightly larger than lifetime-limited linewidths. Furthermore, the fact that this material did not undergo HPHT

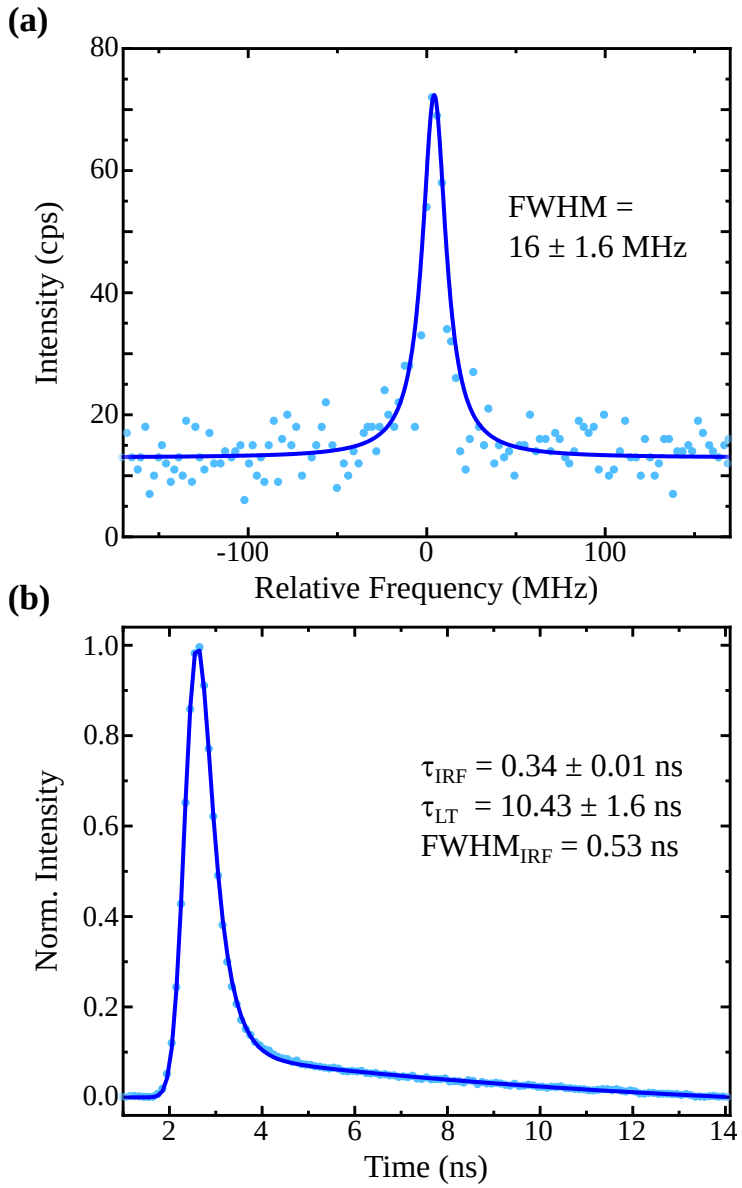

Figure 5.19 **(a)** Resonant (883 nm) PLE scan across an NiV^- optical transition at 0 T and 1.6 K with an applied bias voltage of -10 V. The measured linewidth is 16 MHz, which is consistent with being lifetime limited. Power before objective lens was measured at 30 nW. **(b)** Time correlated single photon counting measurement to determine the excited state lifetime. Sample was excited using 698 nm light at a power of 0.55 mW through an NA=0.82 objective lens. We find an instrument response function (IRF) with a gaussian width of 0.53 ns. To fit this, we used a convolution of a gaussian and two exponential decays. Two decays because the IRF has a fast exponential decay tail and the second for the slower, excited state lifetime. After deconvolution of the fast 0.34 ± 0.01 ns IRF, the excited state lifetime was found to be τ_{LT} =10.43 ± 1.6 ns.

annealing and just did a 1600° C anneal is encouraging as it means that such a rigorous process is potentially not critical to obtain narrow linewidths. The inhomogeneous distribution was 50 GHz; however, so perhaps this could be what is improved.

5.4.8 Attempts at Observing NiV^0

In addition to observing the NiV^-, we were also curious if we might be able to observe any signature of the NiV^0 because we have p-type diamond. As such, because there is some creep / diffusion of implanted centers, it wouldn't be impossible for there to be a regime where the NiV^0 is charge stable. In addition, there is the possibility of applying bias voltages to achieve NiV^0 charge stability. We explored many different bias voltages and different filter windows, but we couldn't observe any

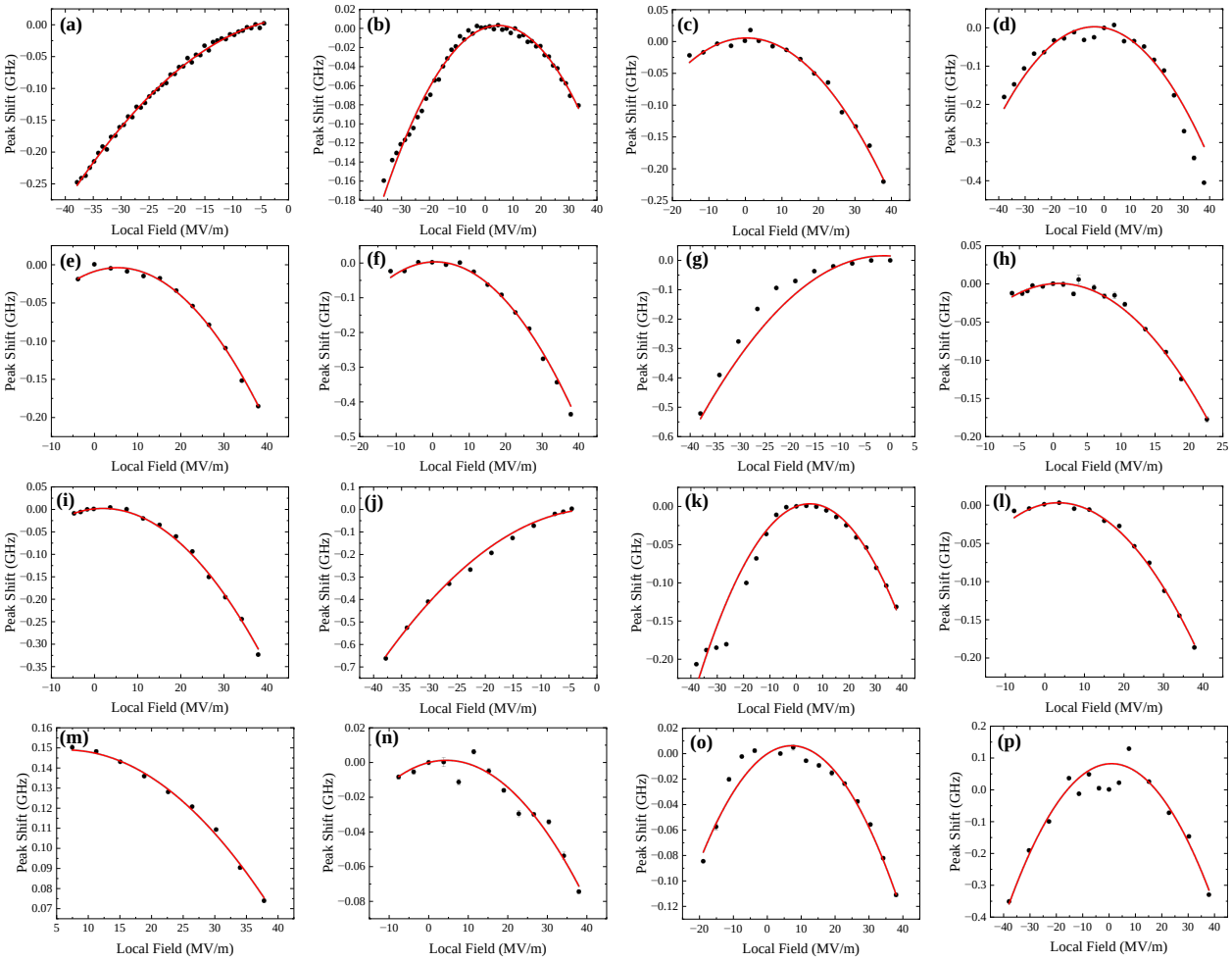

Figure 5.20 **(a-p)** Stark shift of transition under resonant excitation as a function of the local field. (a) and and (j) were taken using solely resonant light, while the rest were taken using a green laser in conjunction with resonant light. Each graph was taken at a different spot in the $3{\cdot}10^9$ implantation dose region of the sample.

Table 5.1 Extracted Stark-shift values for $\Delta\mu$ and $\Delta\alpha$, together with their uncertainties and the R^2 value for each fit. The letter in the first column corresponds to the labeled graph in Fig. 5.20.

Label	$\Delta\mu$ (10^{-3} D)	Error (10^{-3} D)	$\Delta\alpha$ (Å^3)	Error (Å^3)	R^2
a	−0.187 56	0.054 02	1.885 42	0.040 48	0.996 96
b	−0.197 17	0.012 51	1.258 93	0.017 79	0.979 90
c	−0.026 23	0.034 97	1.881 85	0.034 84	0.995 02
d	0.262 26	0.038 09	2.173 65	0.078 79	0.942 44
e	−0.365 58	0.041 70	2.043 83	0.040 63	0.995 29
f	−0.097 55	0.111 48	3.594 57	0.152 22	0.968 41
g	0.199 68	0.400 71	4.926 14	0.390 39	0.955 73
h	−0.130 08	0.065 92	4.442 59	0.137 27	0.988 57
i	−0.187 77	0.034 59	2.889 47	0.042 38	0.996 80
j	−0.327 83	0.327 83	5.005 95	0.239 43	0.997 94
k	−0.270 21	0.024 46	1.469 75	0.033 91	0.971 89
l	−0.220 54	0.040 93	1.869 94	0.039 97	0.995 40
m	−0.038 56	0.063 58	0.709 15	0.044 88	0.992 21
n	−0.121 26	0.053 64	0.773 58	0.050 80	0.950 17
o	−0.359 62	0.037 83	1.531 68	0.053 51	0.945 07
p	−0.114 34	0.117 14	3.488 56	0.157 28	0.918 23

clear cross correlations. However, more work needs to be done. one spectroscopic we did observe however at low temperature, which did not show up at room temperature is shown in the Figure below along with absorption spectral data taken by [155]. The shapes kind of match, but not exactly. Magneto-optical spectroscopy would need to be carried out to determine if it was indeed the spin-1 ground state of the NiV^0. Additionally, it was observed using green light instead of 690nm light. UV excitation could also be attempted to see if that improves the excitation. UV excitation might also shed light on if there's any substitutional Ni or NiV^{2-} that is visible.

5.5 Charge State Model

Having conducted a variety of measurements with the p-i-p sample, we now return to a charge-state model for the NiV center that is consistent with these results. In particular, we focus on the physical origin of the photoluminescence (PL) quenching observed under resonant excitation. Similar behavior has been reported for NV^- [223], SiV^- [260, 261], GeV^- [249], and SnV^- centers [143], and is generally attributed to optically induced charge state instability. In all of these systems, resonant excitation can drive the defect into a different, optically dark charge state, thereby terminating fluorescence. Several microscopic mechanisms could, in principle, be responsible for this behavior in NiV. One possibility is charge transfer involving implantation-induced vacancy

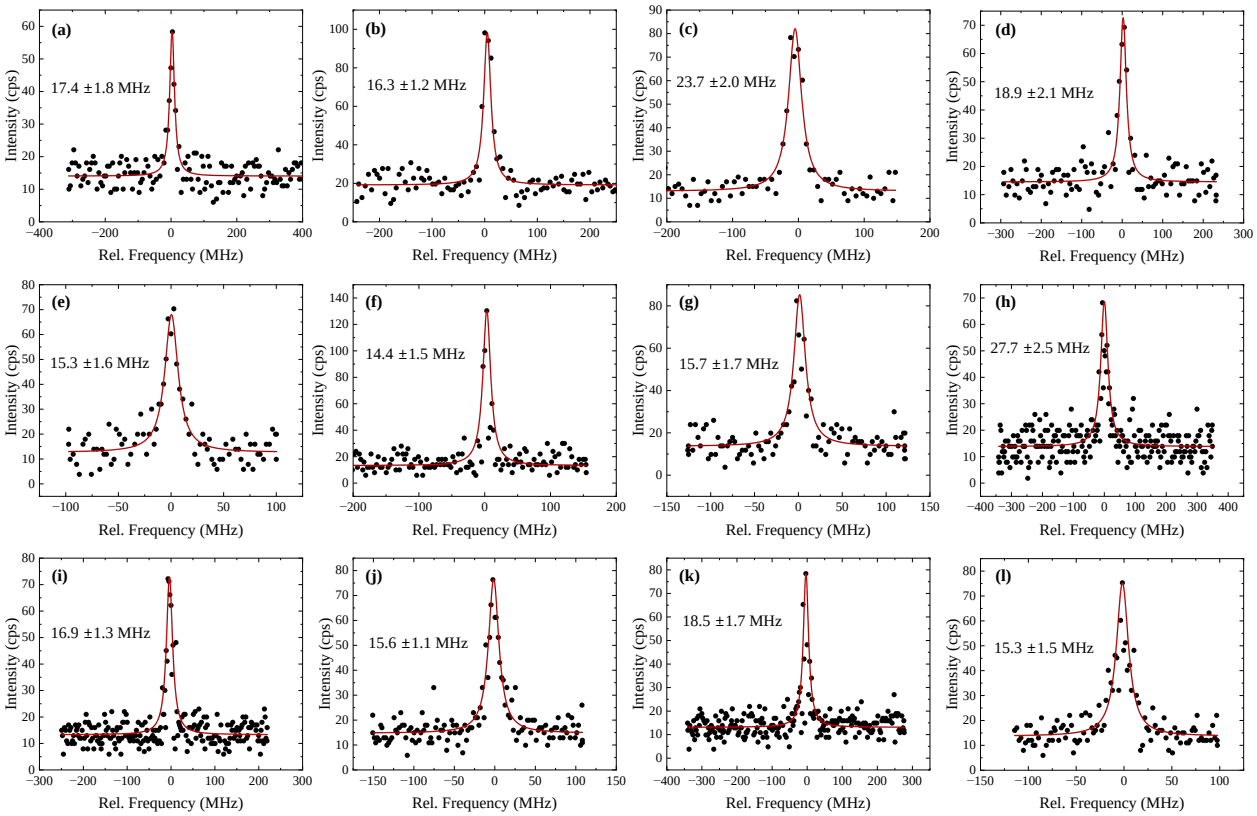

Figure 5.21 **(a-l)** PLE scans across the optical transition at a variety of applied voltages for the spots measured, with the letter corresponding to the same spot at which the Stark shift graph data was taken in Fig. 5.20. The FWHM of the fitted Lorenztian is the number displayed within the graph.

complexes, such as divacancies. However, in our case the Ni implantation energy of 70keV produces approximately 410 vacancies per ion according to SRIM simulations, which is more than an order of magnitude fewer than for typical MeV-scale implantations. Together with the high-temperature annealing and the ultrapure nature of the starting material, this makes it unlikely that divacancies dominate the observed charge dynamics. We also tried revival with UV laser light at 405 nm, however, we did not observe nearly the improvement that has been observed with SnV when compared to 532 nm light [143]. Similarly, while substitutional nitrogen is a common charge trap in diamond, its low concentration in our material suggests that nitrogen-related processes are not the primary cause. A more plausible alternative is the involvement of other nickel-related defects, such as substitutional nickel, which is known to introduce a low-lying acceptor level in diamond [233], and could act as a local charge reservoir.

In addition to charge state conversion only involving NiV, it is also possible for auxiliary defects to contribute to the charge state switching process. Here, we focus mainly on defects arising from the sample fabrication process itself as the electronic grade substrate only contains very low levels of impurities. In particular, we consider divacancies created during ion implantation as discussed by

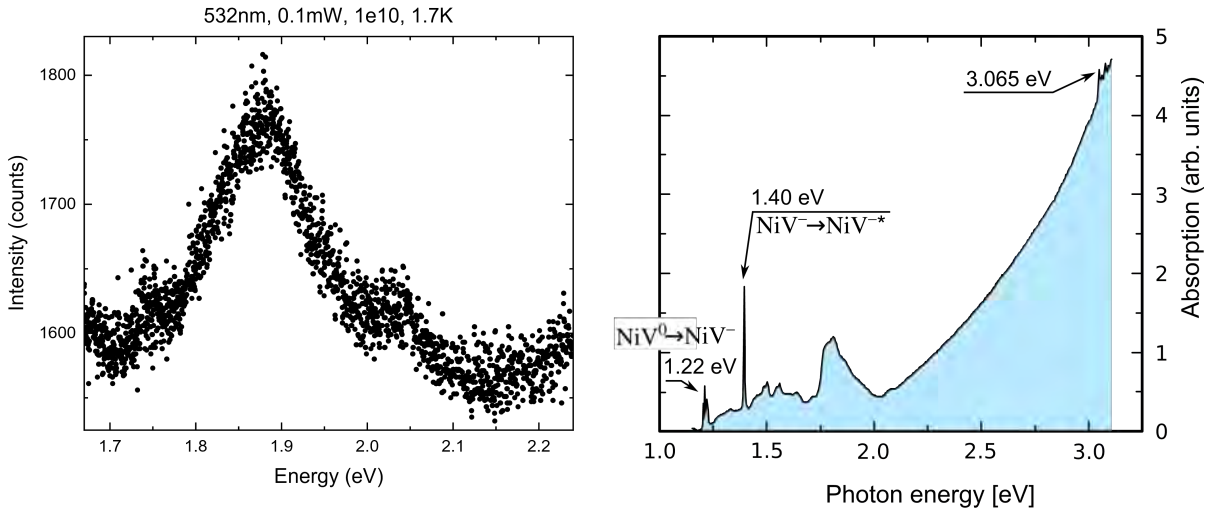

Figure 5.22 The graph on the left is a spectroscopic measurement taken with a 600 g/mm grating with 532 nm excitation at 1.7K. The graph on the right is an absorption measurement of a Ni sample reprinted from [239]

[143] as well as other nickel-related defects such as the nickel substitutional which will not anneal out even at high temperatures.[262]. Using SRIM simulations [263], we find 410 vacancies per Nickel ion are formed for 70 keV implantation energy. Compared to what was found in [143], this is nearly an order of magnitude less. However, we did not perform an HPHT treatment on the p-i-p sample which tends to reduce the concentration of residual concentration of vacancies and vacancy complexes. Thus, divacancies may still play a role in the re-ionization process of NiV^{2-} and we tentatively attribute repumping using green light to a process like this.

Beyond these extrinsic mechanisms, a particularly compelling explanation is that the charge conversion occurs intrinsically at the NiV center itself, in close analogy to recently proposed mechanisms for SiV^- [240] and SnV^- [143]. In these systems, optical excitation of the negatively charged defect promotes it to an excited state, after which absorption of an additional photon can lift an electron from the valence band into the defect's unoccupied Kohn-Sham orbital. This process effectively converts the center into the doubly negative charge state, which is optically dark under resonant excitation. Ab-initio calculations by Thiering et al. [214] indicate that an analogous process is energetically allowed for the NiV center. In this picture, resonant excitation of NiV^- is followed by a second optical absorption event that transfers an electron from the valence band into the defect, filling the previously unoccupied ground-state orbital and producing NiV^{2-}. Once in this charge state, the center becomes dark to resonant excitation, leading to the observed quenching of PL.

This interpretation is consistent with our experimental observations where recovery of NiV^- fluorescence is observed under applied electrical bias. In particular, by analyzing which polarity

of the p-i-p junction enhances the NiV^- signal, we can infer the nature of the dark state. If the enhancement occurs when the device is biased such that holes are injected into the intrinsic region, this implies that the dark state is NiV^{2-}: the increased hole density facilitates recombination with the excess electron, converting NiV^{2-} back to the optically active NiV^- state. Conversely, if the signal increases under electron injection, this would indicate that the dark state is NiV^0 and that electrons are required to repopulate NiV^-. Our observations favor the former scenario, supporting a model in which resonant excitation optically pumps NiV^- into the doubly negative, optically dark NiV^{2-} state. This provides a natural explanation for the rapid quenching of PL under resonant drive and highlights the central role of intrinsic, optically assisted charge conversion in the charge state instability of the NiV center.

For band bending calculations of qualitatively identical p-i-p junctions we refer the reader to [252]. As can be seen from the charge transition levels calculated in [214], the NiV^{2-} is the dominant charge state for intrinsic diamond with the Fermi level at mid-gap. As bias voltage is applied to the junctions, the Fermi level is pushed down towards the NiV^- regime. We also observe a sharp decline in fluorescence when varying the excitation light from 690 nm to around 710 nm as shown in Fig. 5.2. Absorption data from [239] shows a localized absorption band in this region, similar to the ramp-up point in Fig. 5.2. Given that we expect the equilibrium charge state to be NiV^{2-} (see above), we attribute this sharp change in excitation efficiency to the onset of the A_{1g} bound exciton level which may non-resonantly decay into the 1.4 eV excited state as predicted by Thiering et al [214]. Moreover, we tentatively attribute the local maximum around 820 nm to excitation into a second excited state, similar to what was observed for SiV^- [264].

Secondly, termination of PL under resonant excitation can be compared to recent studies for the SnV [143] and SiV [240] defects, suggesting the dominant charge conversion process is the capture of an optically excited electron from the valence band by the negatively charged defect in its excited state, filling the unoccupied ground state orbital and resulting in the 2- charge state. Ionization e.g. via the conduction band or a nearby defect such as the divacancy (V_2) [143] is required to remove an electron to restore fluorescence. For both of these defects, their proximity to the valence band makes resonant photons sufficient to trigger this process. Similarly, the NiV^- is also expected to be within 1 eV of the valence band edge [214] and thus resonant light at 1.4 eV would suffice to drive this process, too. In contrast, recovery via ionization to the conduction band is unlikely as it would require a >3 photon process under resonant excitation. The NiV^{2-} is predicted to be excited by UV light and to emit at 2.96 eV (419 nm). Thiering et al. suggest that UV excitation can cause a charge transition from NiV^{2-} to NiV^- by ionizing an electron while also cause NiV^- to NiV^{2-} charge conversion by exciting an electron from the valence band, resulting in a dynamic equilibrium of both NiV^- and NiV^{2-} charge states [214].

In the p-i-p junction, we observe NiV^- revival at around 5 V. This voltage closely corresponds

to the threshold voltage at which current starts to flow through the junction as seen from the IV curves, leading to electron (hole) injection in the inversion (depletion) regions along the edges of the junction. In combination with the fact that we see NiV^- revival only on the hole injection side of the junction, this suggests that the injection of holes is an important part of reviving the NiV^- in addition to band bending. Similar effects were seen recently with SiV in [240] in which SiV^- PL was directly correlated with current flow. However, we note that we do not see such a direct correlation of PL intensity and current, potentially due to a saturation of intensity as we are dealing with a far less dense implantation of emitters. We also still observe a DC Stark shift suggesting that a combination of both current injection and applied electric field play a role.

Finally, we would like to note that the zero-phonon line of the neutral charge state, NiV^0 has been theoretically predicted to be around 700 nm [214]. While being inconsistent with the expected charge state equilibrium and our observations in the pi-p junction, hypothetically, the sharp change in NiV^- fluorescence with varying excitation wavelength around 700 nm, could also be explained by a bi-directional charge transfer process involving NiV^0, whereby, at excitation below 700 nm, it is excited to its ^3E_u excited state from which it may decay into the NiV^- excited or ground state (state assignments taken from [214]). The inverse process could also occur whereby the NiV^- $^2A_{1g}$ excited state decays into the excited state of the NiV^0. In contrast, at excitation wavelengths longer than the NiV^0 ZPL, only a unidirectional transfer from NiV^- to NiV^0 can occur, without subsequent repopulation of NiV^-, somewhat similar to NV charge dynamics [223, 265] (see Figure 3b from [223]). A competing process of NiV^0 to NiV^- charge conversion at 1.22 eV (1016 nm) by addition of an electron from the valence band is predicted by Thiering et al. [174, 214]. In theory, at all wavelengths appropriate for NiV^- excitation, this process occurs continuously, depleting NiV^0, further reducing the likelihood of NiV^0 involvement in the observed dynamics.

Chapter 6

Spin Coherence Properties of the NiV

In this chapter, we perform all-optical control of the NiV^- ground state electron spin states. To do this, we first identify the $A1$ and $A2$ optical transitions required for spin-selective initialization and readout via optical pumping. Using these transitions, we then perform coherent population trapping (CPT) measurements to establish a lower bound on the ground state spin coherence. We then demonstrate Raman-based spin control using two-photon Raman transitions, enabling the observation of Rabi oscillations and Ramsey fringes and allowing us to extract a $T_2^* = 286$ ns from a Ramsey measurement. Using this technique, we achieve multi-axis control of the spin qubit in under 60 ns, enabling rapid preparation of arbitrary superposition states. Finally, we perform a Hahn-echo sequence, measuring a $T_2^{\text{echo}} = 126\mu s$. The refocusing pulse suppresses dephasing from the nearby ^{13}C nuclear spin bath, and demonstrates that at 1.65 K the spin coherence is not limited by the phonon bath.

6.0.1 Identifying the NiV^- Lambda Scheme

To use an NiV^- center as a spin qubit, we can use the two spin states in the lower orbital branch of the ground state, $|1\rangle$ and $|2\rangle$, together with the lower excited state spin branch, $|A\rangle$, which together form a three-level Λ system. In the absence of a magnetic field, the two ground state spin levels are degenerate. This degeneracy can be lifted with the Zeeman interaction by applying a magnetic field and the orientation of the field determines whether spin pumping is possible. If the applied field is parallel to the NiV high symmetry axis, then it will align with the spin-orbit interaction and the spin quantization axes between the ground and excited state will remain the same, as in the unperturbed case. As such, when the field is aligned, the optical transitions remain largely spin conserving: $|1\rangle$ couples strongly to $|A\rangle$, while $|2\rangle$ remains largely spin forbidden. When the field is not aligned or off-axis, the ground state spin quantization axis will remain largely pinned by the strong spin orbit interaction (670 GHz $\approx$ 24 T for g=2), but the excited state spin quantization axis will align to the magnetic field completely. This relaxes the spin selection rules and gives both $|1\rangle \leftrightarrow |A\rangle$ and $|2\rangle \leftrightarrow |A\rangle$ nonzero transition strength. As a result, driving one optical transition can transfer

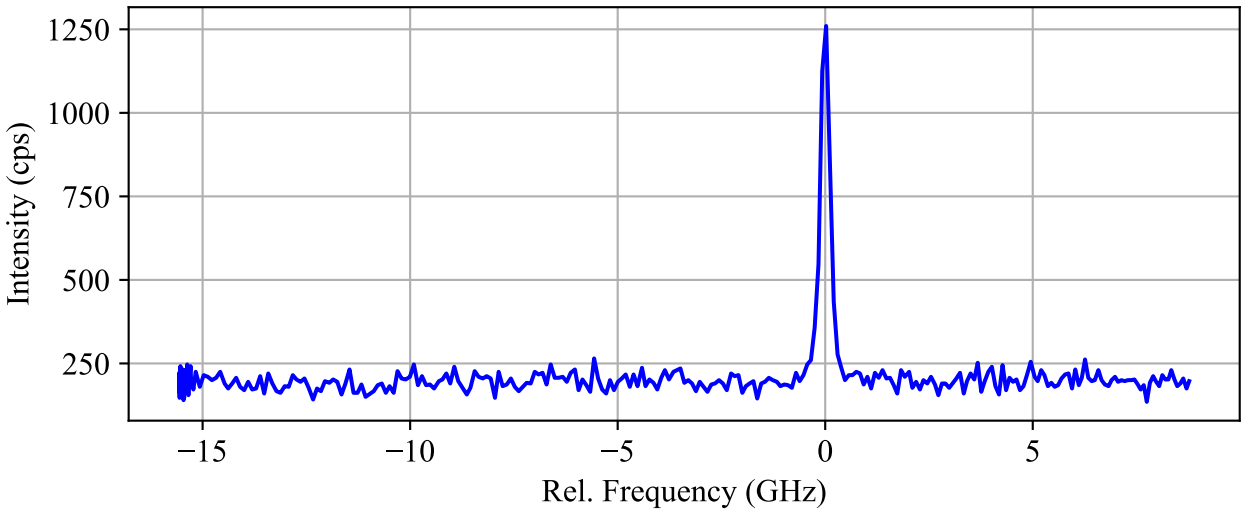

Figure 6.1 Resonant PLE spectrum of an NiV emitter in a nanopillar. We used a power of 2 μW of 883 nm light and 1 μW of 532 nm light.

population through spontaneous emission into the other ground-state spin sublevel, enabling optical spin pumping. This Λ configuration opens the door for coherent population trapping, which can also be used to achieve all-optical control via two-photon Raman transitions. This can be seen in Figure 6.3.

A key figure of merit for quantum systems is how quickly the state of a system can be read out. For many systems, this must happen over many attempts because the interaction probability is low. However, this can limit the efficiency of many quantum protocols. Hence, performing these read out steps in a single step is desirable. Indeed, high fidelity single shot readout can be achieved within the Λ configuration without destroying the coherent superposition state by removing the off-axis component of the magnetic field. This results in cycling transitions, which can provide a fluorescence response and indicate which spin state the system is in without optically pumping. High fidelity single-shot readout has been achieved with SiV [145] and this is because .

ld which still be achieved with the A1 transition as long as any transverse or off-axis magnetic field is turned off or made very weak.

Before CPT could be performed, the A1 and A2 transitions needed to be identified. The lower orbital branch states were chosen because at cryogenic temperatures, the population thermally relaxes into these states. Resonant PLE at 1.65K was performed to identify the two transitions. Cryogenic temperatures are necessary to resolve the magnetic field split transitions and the lifetime limited linewidths, which are broadened significantly at room temperature due to electron-phonon coupling. First, a spectrally isolated resonance was identified as shown in Figure 6.1. The nanopillar sample was probed first by slowly ramping the magnetic field and scanning a large frequency range

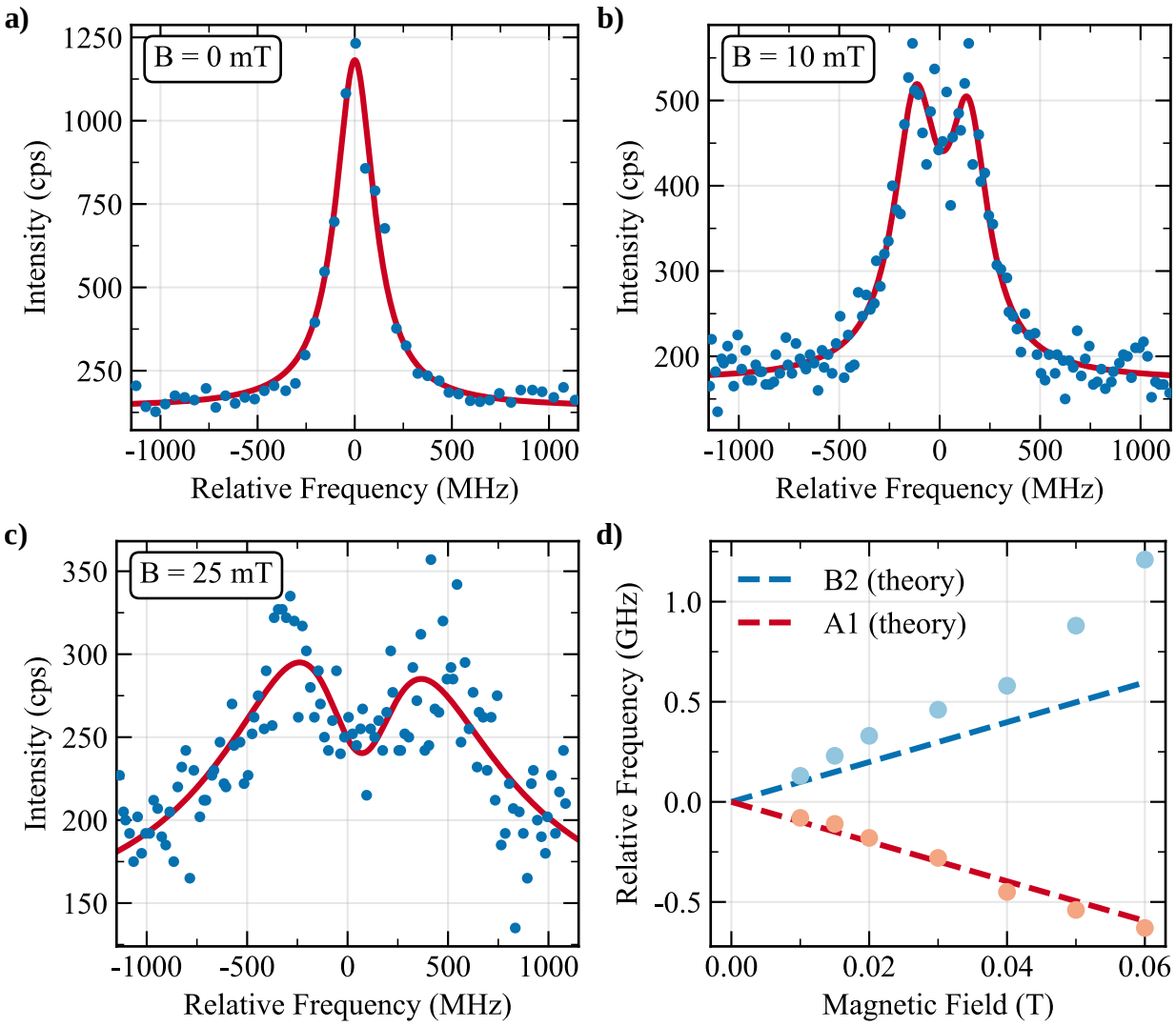

Figure 6.2 **a)-c)** Resonant PLE spectrum of an NiV^- within a nanopillar at various magnetic fields. 1.2 μW of resonant along with 1μW of 532 nm light was used to excite the emitter. **d)** Extracted center frequencies of the two peaks, A1, and B2 at various magnetic fields are shown as dots while the group theoretical model assuming no strain and a 71.5° angle between emitter and magnetic field is shown as the dotted lines.

centered at the zero field resonance frequency. Even at low fields of 50 mT, little to no fluorescence was observed due mostly because of optical spin pumping, which occurred as the laser became resonant with one of the spin transitions. The population was then rapidly pumped into a different state on a timescale too fast to observe when scanning (on the order of 100s of ns as confirmed by later time-resolved optical spin-pumping experiments). Because the spin relaxation time, T_1, at this temperature is on the order of milliseconds (based on previous defects [139, 145, 225], there was no efficient mechanism to repopulate the initial state during the scan. As a result, the emitter quickly became dark and the PLE signal vanished. To overcome this, even lower magnetic

fields between 5-20 mT were employed, in which the spin splitting remained small enough so that high power excitation would sufficiently power-broaden the transition, such that both transitions were partially addressed simultaneously. This provided an effective repumping mechanism, which enabled observation of the two cycling transitions, A1 and B2. Figure 6.2 shows that even at relatively small magnetic fields, the fluorescence drops substantially as the two cycling transitions, A1 and B2, split, both because the linewidth is distributed over a wider frequency range and because repumping becomes less efficient. The nominally spin forbidden transitions, A2 and B1, were too weak to identify directly in PLE and were instead most readily identified through CPT measurements. The group theoretical model was overlaid on top of the experimentally determined A1 and B2 transitions to compare theory with experiment. The theory qualitatively agrees and requires no strain contribution from the Hamiltonian.

6.0.2 Coherent Population Trapping

With one half of the transitions identified, CPT was used to identify the other. As described in Chapter 2, when both legs of the Λ system are driven simultaneously and the two-photon detuning δ is zero, the system can be optically pumped into a coherent dark state $|D\rangle$. This dark state corresponds to a superposition state between the two ground state spin levels. Once population is accumulated in $|D\rangle$, the system is no longer coupled to the excited state, resulting in a reduction in fluorescence and producing the characteristic CPT dip in PLE. To achieve this, the laser was positioned such that it was resonant with the $A1$ transition. Then, an electro-optic modulator was used to generate frequency shifted sidebands via serrodyne (sawtooth) modulation from an arbitrary waveform generator (AWG, Tektronix 70000A1). By sweeping the microwave modulation frequency from the AWG, the sideband could scan for the $A2$ resonance. This enabled efficient searches for A2 because once the sideband approached the A2 transition, optical spin pumping could occur in both directions, leading to a continuous fluorescence response. Moreover, when both transitions were resonant, a CPT dip was observed, indicative of formation of a coherent dark state. Representative CPT measurements are shown in Figure 6.3 for the nanopillar sample and Figure 6.4 for the p-i-p sample. For the p-i-p sample, only emitters which were revived by bias voltage alone without the need for additional green light were used. The theory overlaid on top is based on the three-level model developed in Chapter 2, in which the system is described by a three-level Hamiltonian and a Lindblad master equation that includes population decay between the levels and pure dephasing between the two ground states.

Despite observing a dip, confirmation that this came from CPT and not some optical artifact from e.g. the measurement equipment was needed. This confirmation was done in two ways. First, the single photon detuning was shifted by scanning the carrier frequency over different parts of the

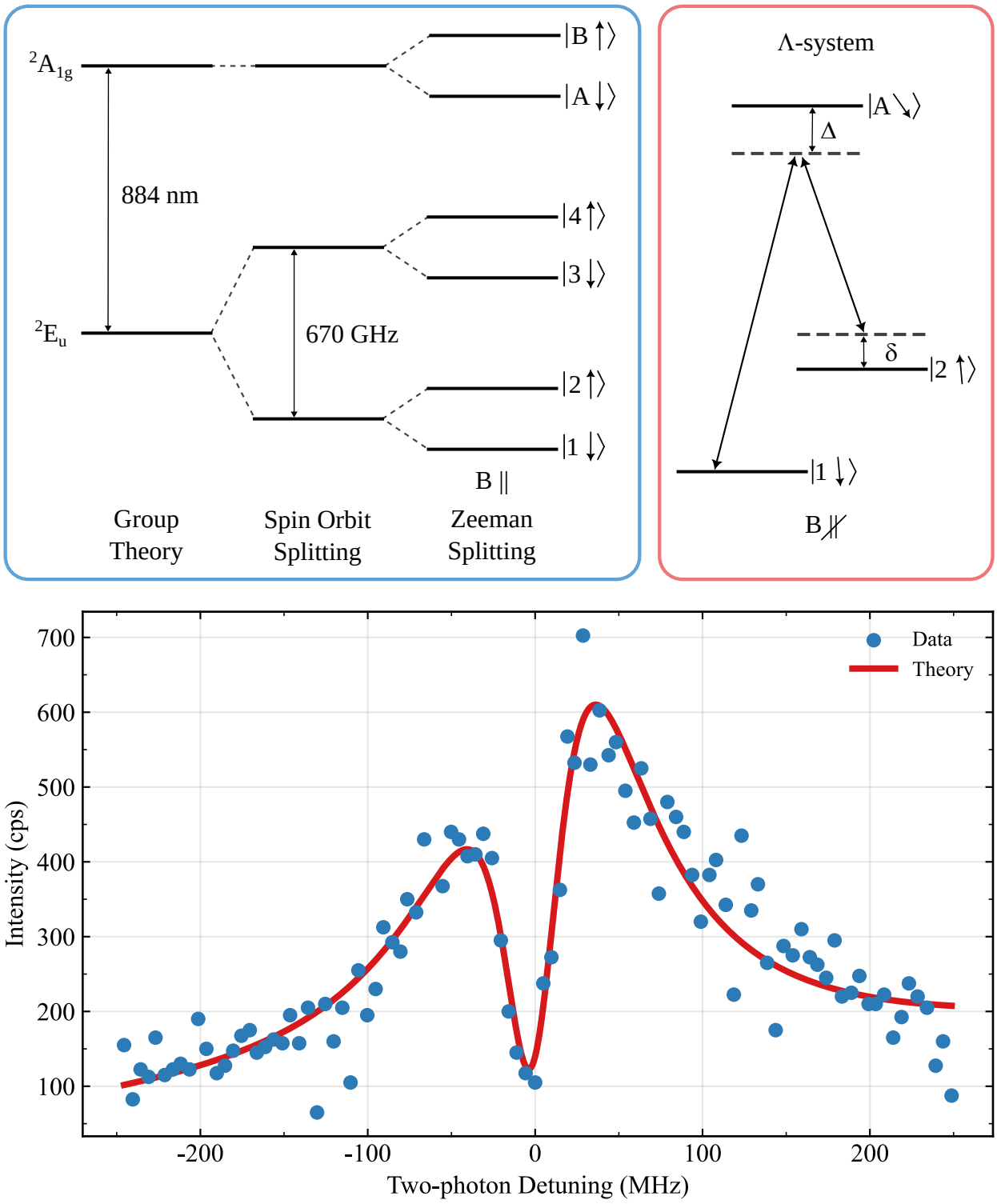

Figure 6.3 Top left shows the electronic structure of the NiV^- under various different perturbations. Top right shows the Λ-system for the NiV^- under an off axis magnetic field. Bottom graph shows a typical CPT measurement in the nanopillar sample. This measurement was taken at 180 mT, with 55 nW of resonant light and 9 muW of 532 nm light. The red line is the theoretical model.

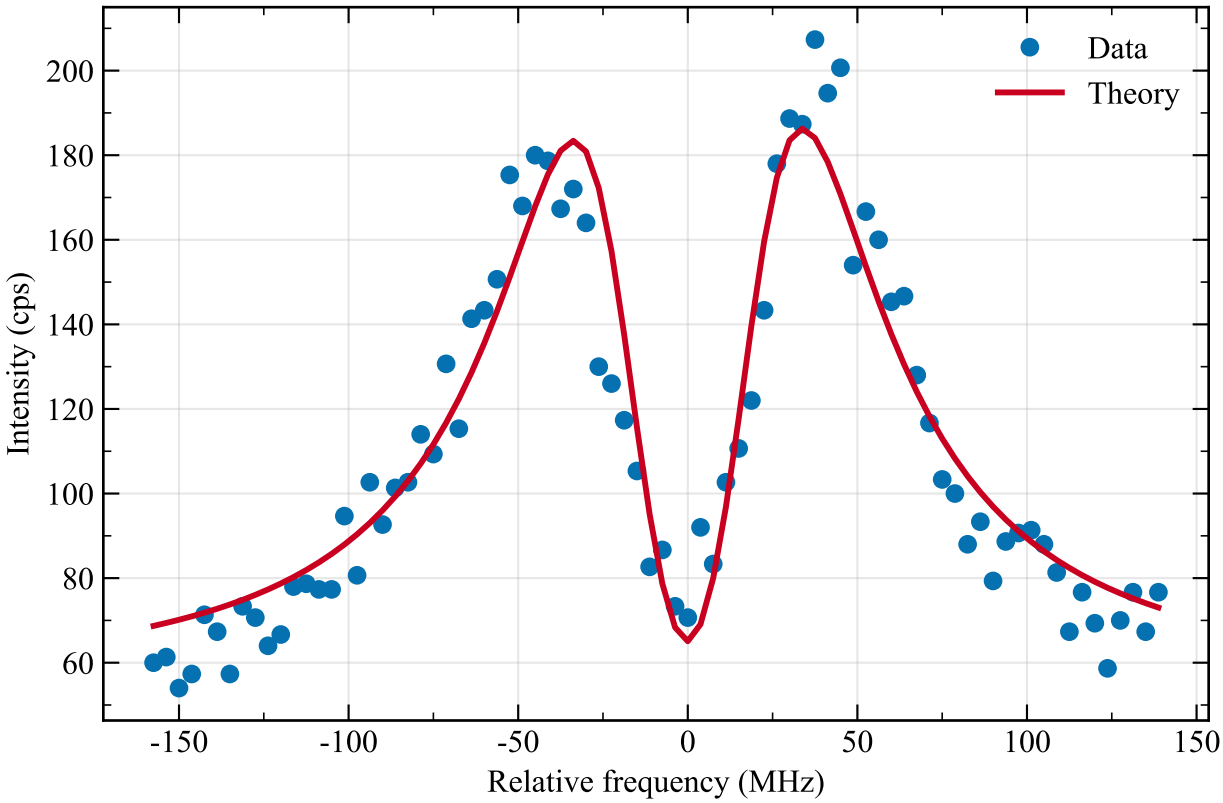

Figure 6.4 Representative CPT scan for the p-i-p sample. The power was set to 27 μW before the objective and 20V of applied bias voltage were used. Furthermore, the magnetic field was set to 150 mT.

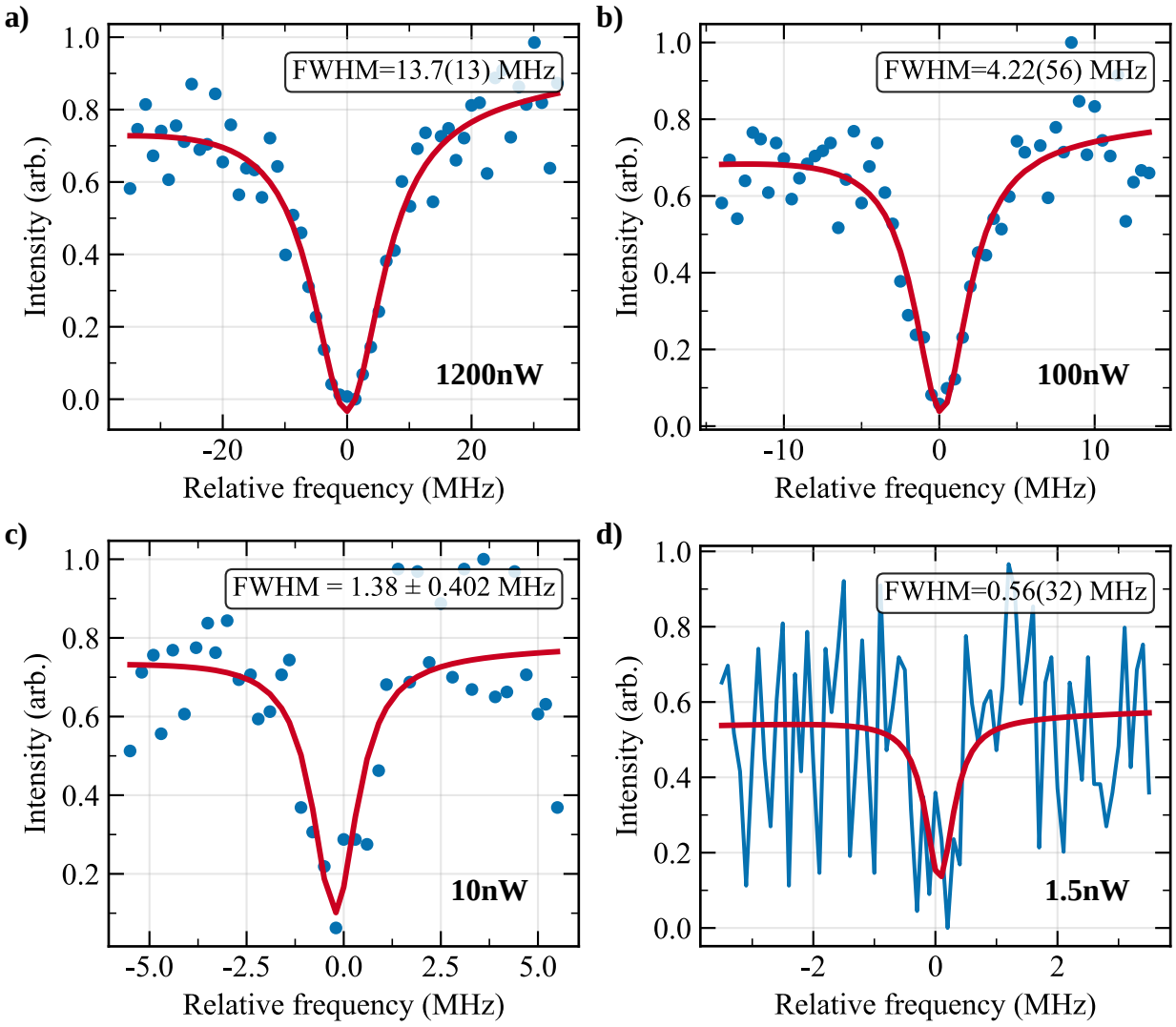

Figure 6.5 **a)-d)** Coherent population trapping measurements in a nanopillar at 1.6 K at 100 mT. 2 muW of 532 nm light was used and the power of the resonant beam is labeled in each respective plot, along with the full-width-half-maximum of each of the Lorentzian functions fit to the data.

A1 transition. This produced a shift of the dip as observed when the A2 transition was scanned over and as described in Chapter 2. Second, the width of the dip can be described by a Lorentzian lineshape if it is homogeneously broadened. One broadening mechanism is power induced. Thus, the linewidth of the dip was measured as a function of power. This can be seen in Figure 6.5 along with a narrowing of the linewidth as the power is reduced. At 1.5 nW of resonant light, a full-width at half-maximum of 570 kHz was measured. This is significantly narrower than the roughly 15 MHz lifetime limited linewidth associated with decay out of the excited state and thus provides a strong confirmation of CPT. In the nanopillar sample in which continuous 532 nm was necessary to revive the NiV^- charge state and for emitters in the p-i-p sample which were excited using 532 nm light instead of bias voltage, shifting the single photon detuning and observing a corresponding shift of the CPT dip proved challenging. This is because while the dip would shift, the resonance would as well, making it challenging to identify the dip as actual CPT. This could arise from spectral diffusion from exciting A1 at a different frequency and because the green light causes a permanent cycling of nearby charge traps and states. Importantly, this was not observed in the emitters revived with bias voltage alone in the p-i-p sample in which it was trivial to observe a shifting of the dip with the single photon detuning. Indeed, Figure 6.6 shows this in one such bias voltage revived p-i-p emitter.

With the CPT nature of the dip confirmed, the linewidth of the dip also reveals information about ground state spin coherence time. The longer the ground state superposition state can be maintained, the less probable it is for it to interact with the field and hence the narrower the linewidth. This is for example an intuitive reason why driving the system with a higher power increases the linewidth because it increases the probability for interaction. As such, the linewidth of 570 kHz can be used to roughly predict a lower bound for the ground state spin coherence time. This can be calculated with $T_2^* = 1/(\pi\Delta\nu) = 550$ ns where $\Delta\nu$, is the linewidth measured. This time is similar in order of magnitude to what has been observed with SnV centers in diamond [139, 143] and longer than the SiV times at 1.65K. This is encouraging considering the measurement was performed on an NiV embedded within a nanopillar and under continuous application of green light, suggesting that the NiV can maintain appreciable coherence times even while integrated within nanophotonic structures. This timescale also provided a rough idea for how long initial Rabi measurements could be performed before expecting to see oscillations decay.

In the p-i-p sample, once CPT had been observed, power dependent measurements were also taken, typically finding a roughly 1 MHz FWHM of the CPT dip at low powers ($\leq$50nW). While slightly broader than the linewidth observed in the nanopillar sample, this was still far narrower than the lifetime limit on the optical transition and a sufficiently long baseline ground state coherence time of $T_2^* = 150$ns. One challenge with the p-i-p sample is there is no photonic structure to enhance coupling or collection efficiency, so low power CPT measurements are close to dark count levels on the APDs. This makes measurements time consuming requiring sufficient averaging of runs to

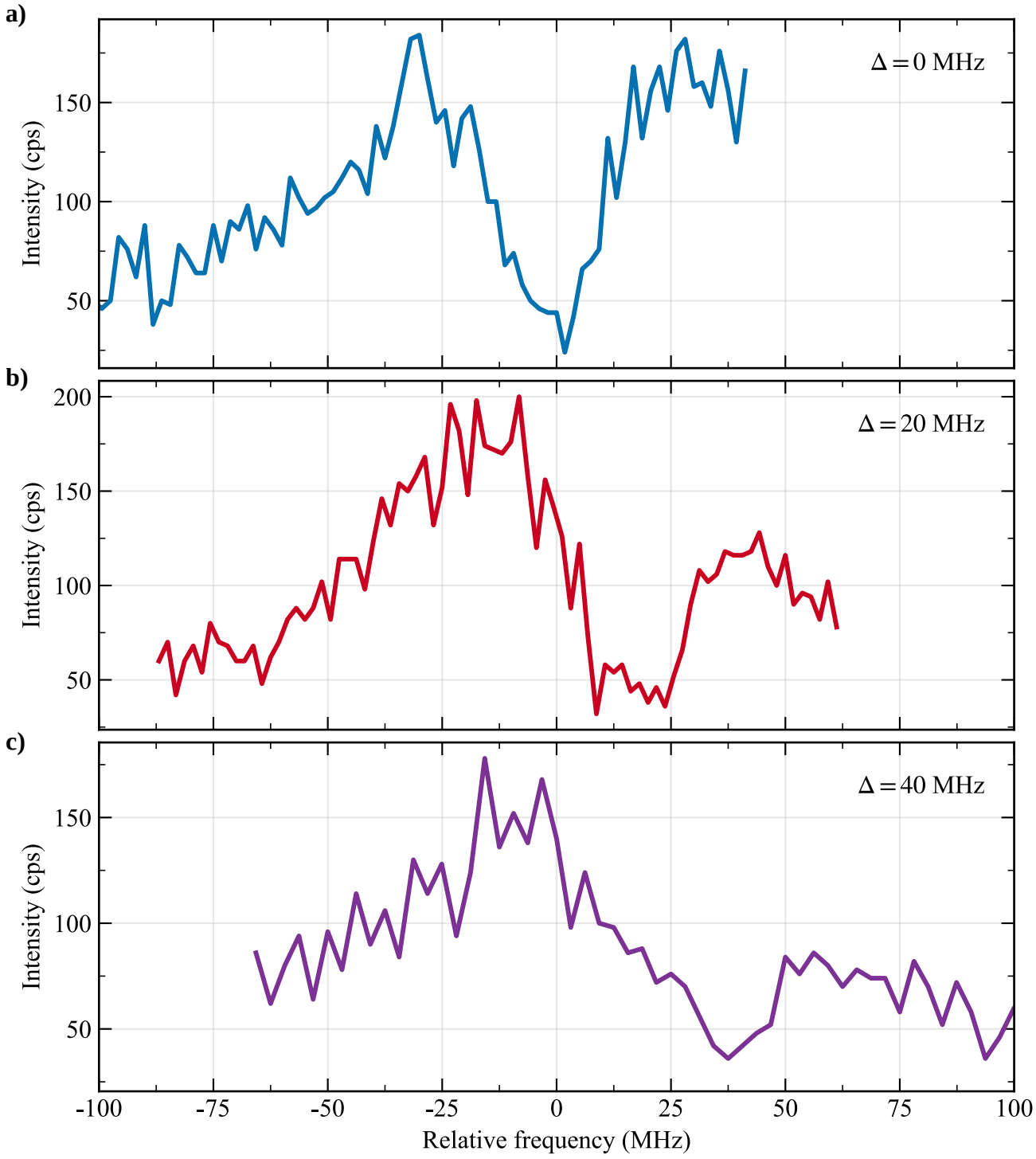

Figure 6.6 **a)-c)** Coherent population trapping as a function of the single photon detuning as measured by the different relative frequencies for the carrier on A1.

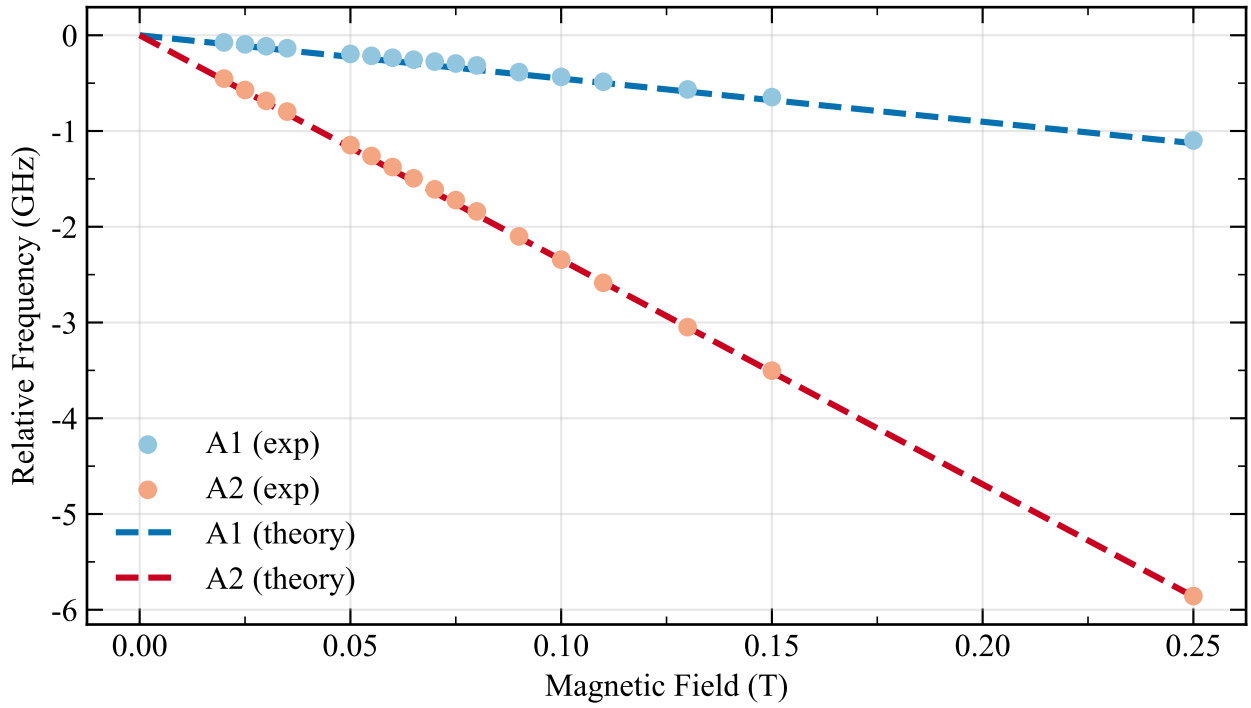

Figure 6.7 A1 and A2 transition energies at various magnetic fields relative to the zero field transition. These transition values were extracted from fits of CPT data where the laser was resonant with A1 and the EOM sideband scanned over A2. The dotted lines are the group theory prediction using parameters of 670 GHz for D_g, 170 GHz for Q_{gx} and 0 GHz for Q_{gy} and $\theta = 54.7°$.

observe. Further, because the wavemeter stability is specified to ±15MHz, temperature related shifts could cause frequencies to drift, making the dip appear wider than it actually is. Hence, instead of performing long measurements of this, achieving Rabi oscillations with two-photon transitions was prioritized.

Before moving to Rabi oscillations, a magnetic field map of the A1 and A2 transitions was taken in the p-i-p sample. This can be seen in Figure 6.7. The values were taken relative to the zero field resonance frequency and obtained by centering the CPT dip and then extracting the carrier frequency for the A1 transition and the CPT center frequency (as extracted by fitting to a Lorentzian) for the A2 transition. By comparing this data to the group-theoretical model, residual strain in the emitter can be identified. The p-i-p sample is a ⟨100⟩ sample, so all NiV's are at an angle of 54.7° angle plus or minus some offset angle with respect to the vertical magnetic field. As such, the splittings are different than the⟨111⟩ sample, which can host emitters at angles of 0 and 71.5 ° up to some offset angle with respect to the magnetic field. As shown in Figure 6.7, the group theoretical model matches quite well with the data, however to achieve this, a large strain value of 170 GHz was used. This large strain value is not a pre-requisite to achieving Rabi, Ramsey, Hahn-Echo, and CPMG data because the change in branching ratio with the strain compared to an unstrained emitter

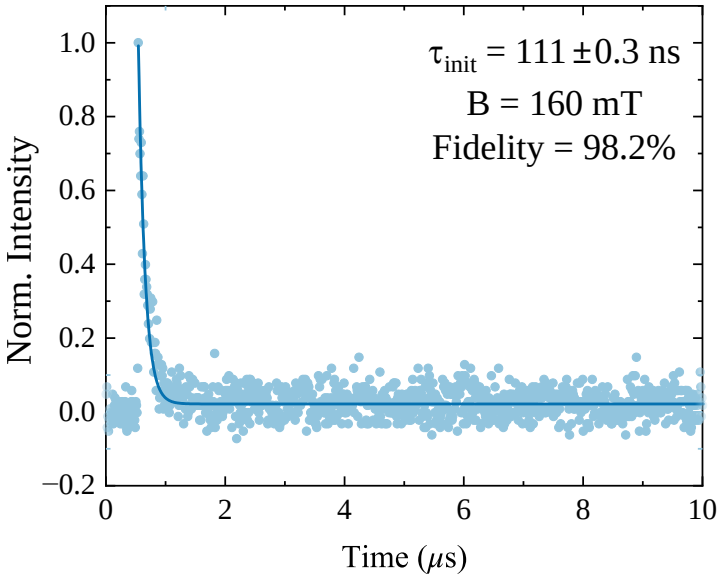

Figure 6.8 Spin pumping measurement performed with 1000 nW of resonant light on the A1 transition. The decay time constants are in the upper right for each graph. The magnetic field was 160 mT and the green power was 2 μW. The pulses were carried out using an AOM.

is 0.2 and hence not significant enough to change the coupling efficiency to the transition. The large strain value may be because high pressure high temperature annealing was not performed. In the future, unstrained emitters should be identified and tested because although the η value should be low regardless of strain, it is necessary to confirm it. The map also provides a convenient look-up table in the event of needing to access larger ground state spin splittings between A1 and A2. Such higher splittings would enable larger Raman detunings which would not normally be as accessible owing to the possibility for cross excitation of A2 or another state by the carrier frequency.

6.0.3 Optical Spin Pumping Time

With both the A1 and A2 spin transitions identified, a more quantitative examination of the optical spin pumping time was necessary. Optical spin pumping is how the spin qubit can be initialized and how population can be readout, so it is important for it to be well-characterized. This was achieved by analyzing the time-resolved fluorescence from the spin transitions in response to short resonant optical pulses carried out by sending in short microwave pulses to the EOM and creating pulses of the sideband frequencies. It was also done using the more traditional AOM approach in which the carrier frequency was simply gated on and off using a delay generator and digital modulation of the AOM. The measurement was performed as follows: first, a pulse resonant with the A2 transition and only the A2 transition (generated via a sideband from serrodyne modulation of the EOM) was sent for 50 μs; then, the pulse was turned off and a second pulse resonant only with the A1 transition was

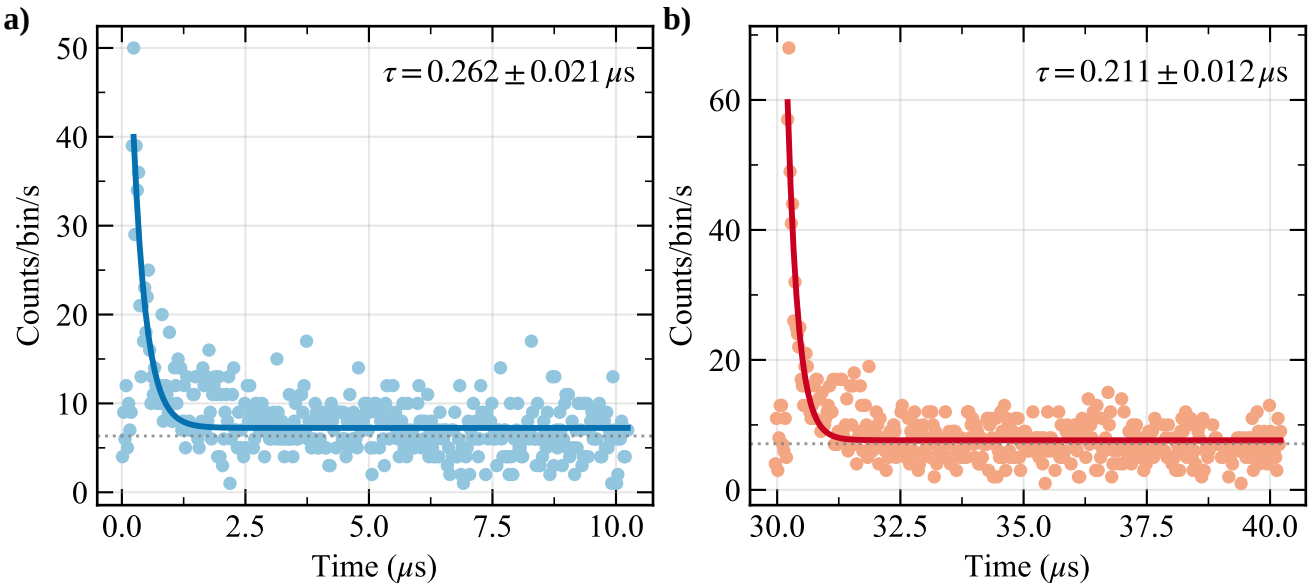

Figure 6.9 **a)** and **b)** showcase spin pumping measurements performed with 150 nW of resonant light on the A1 and A2 transition respectively. The decay time constants are in the upper right for each graph. The magnetic field was 100 mT and the green power was 2 μW. The pulses were carried out using an EOM.

sent out. This pulse sequence was repeated many times to build up statistics on the pump dynamics. The fluorescence and corresponding decay observed as a result of these two pulses provides an indicator for the populations of the two states being driven, being excited and decaying back to their original state. The decay occurs because each time the state is excited there is a probability determined by η of the state decaying into the other, un-driven state and eventually fluorescence will drop the zero in which all population has been pumped out. Thus, these decays can be fit to exponential functions and the corresponding time constant is representative of the time scale which it takes to pump population from one spin state to the other. In doing this, a decay constant of τ = 112 ns is extracted for pumping from the A1 to the A2 state as can be seen in Figure 6.8. The short time enables fast initialization times suitable for quantum networking and computation applications. The reason pulses of both frequencies were used is because without a reset pulse, the system will stay in a dark state because the rate at which population is naturally repumped depends on the T_1 time which is ms at these temperatures for diamond, hence population could be pumped quickly and then decay slowly back, making any measurement take much longer than needed.

Because the spin pumping time is related to the branching ratio, it can also be extracted from such measurements. To do this however, the spin pumping time must be recorded as a function of power on the transition. This dependence can be described by the equation $\frac{\Gamma}{2}\frac{p/p_{\text{sat}}}{1+p/p_{\text{sat}}}\frac{1}{\eta}$ [139, 184] where $\Gamma/2\pi$ = 15 MHz is the excited state decay rate. The fit provides both the branching ratio η and the saturation power p_{sat}. One of these measurements is shown for the nanopillar sample at 150

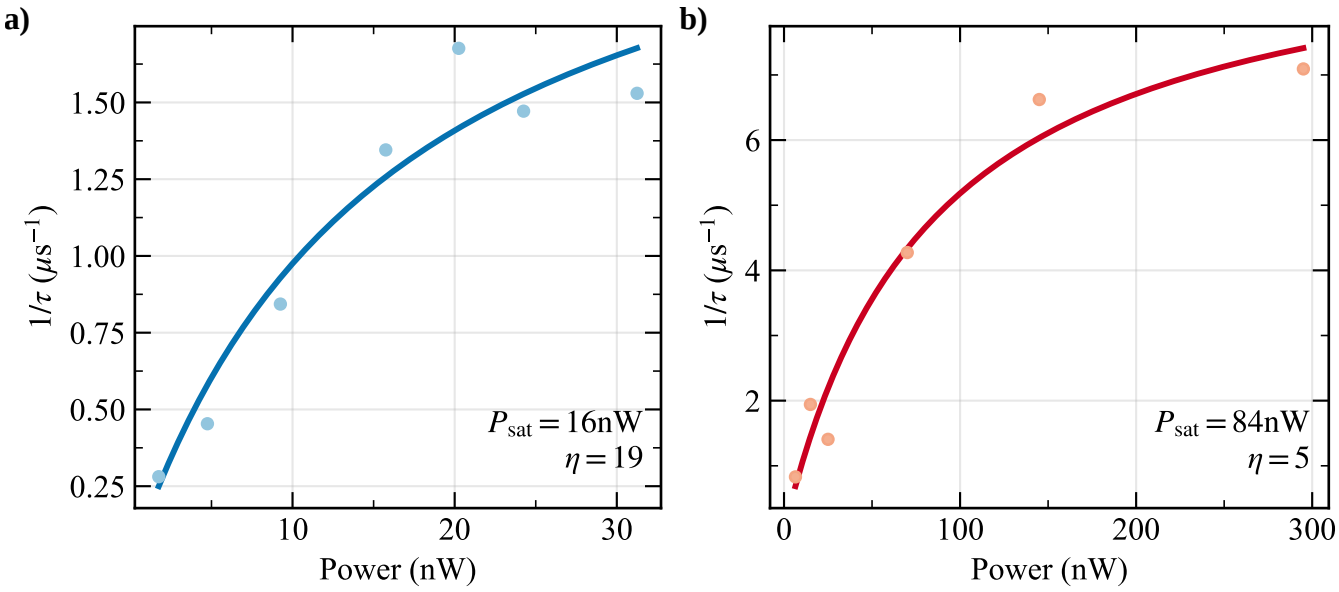

Figure 6.10 **a)** and **b)** show fits of the spin pumping time plotted as a function of power. **a)** is on a nanopillar using 2 μW of green light at a field of 120 mT while **b)** is on an emitter in the p-i-p sample at a field of 150 mT with no green light only 20V bias voltage.

nW in Figure 6.9 in which it takes about 25% longer to pump out the A1 transition than the A2 transition. This is because the A1 has a stronger transition overlap and so it is more likely to decay back to the original state and hence continue to show fluorescence compared to when A2 is being pumped.

The power dependence of this spin pumping time also reveals how efficiently the system can be driven when it comes to optical powers needed. A lower p_{sat} means lower power is needed to achieve similar Rabi frequencies when compared to a system with higher saturation power. A lower η value also means this as was described in Chapter 2. For the nanopillar sample, p_{sat} = 16nW and η = 16 were extracted as can be seen in a of Figure 6.10. For the bulk p-i-p sample, a larger p_{sat} = 84nW and η = 5 were extracted as shown in b of Figure 6.10. The difference in saturation power can be attributed to the coupling enhancement due to the nanopillar structures compared to bulk diamond. The measured η values are different but this may be due to the off-resonant green light used to excite the pillar sample. Additionally, both values are close to what group theoretical model would predict which is 3.5 for their respective field angles and magnetic field strengths of 150 mT and 120 mT respectively (also using the different field angles for the different samples).

To determine the fidelity of these pulses or the degree to which population is pumped out and into the other state, the ratio of the fluorescence at the first time bin is compared to the fluorescence in the steady state in which population has decayed to a point that the fluorescence response is largely flat. Any background count contributions are also subtracted from this measurement. In

doing so, an initialization fidelity of 98.2% can be extracted in the nanopillar sample at 160 mT as seen in Figure 6.8. This could be limited by off-resonant cross-excitation of one of the other spin states or another NiV in the viscinity (spectrally) either by a higher order sideband or the carrier frequency as both of these mechanisms could prevent the steady state counts from reaching zero.

6.0.4 T_1 Time

Another question to answer before attempting coherent control is the spin relaxation time or T_1 of the emitter. Fundamentally, the intrinsic coherence time is limited to $T_2 = 2T_1$ when no dephasing mechanism exists, so it provides an upper bound on the coherences times that can be expected. In the nanopillar sample, T_1 times were measured for two single emitters in different nanopillars. These measurements can be seen in Figure 6.11 with measured times of $\sim$ 800 μs and $\sim$ 1ms respectively. While these times provide a long runway for coherence times, they are shorter compared to what has been observed in other diamond defects [139, 145, 225]. Because many of these other works use only pulsed green light, it was possible that the continuous application was potentially artificially shortening the T_1 time in the nanopillars. Such an off-resonant beam constantly applied continuously cycles both spin states; however, given the low power and far off-resonant nature of the beam, it was more likely that charge state switching as opposed to optical driving is what limits the time. To measure this, the power of the 532 nm beam was varied to see the degree to which it could shorten the T_1 time. From this, a substantial power dependence of the T_1 time was observed. In particular, tens of μW seemed to shorten the T_1 time dramatically to tens of μs while the long times mentioned above were achieved using low green power ($1 - 2$ μW). Nevertheless, pulsing the green on and off would likely be necessary if it were to be used in any advanced scheme which required much longer times as is necessary for long-distance quantum networking applications.

In the p-i-p sample, no green light was used, only bias voltage and initially, very short T_1 times on the order of tens of μs were measured. These measurements were carried out with the EOM; however, and the carrier was left on during the delay times. As such, this was cross-exciting slowly and artificially shortening the T_1 time as confirmed later by gating the carrier on and off with an AOM. Once this change was made, spin relaxation could not be observed even after 5 ms. This is more consistent with previous measurements for defects in diamond especially given the operating temperature of 1.65K. In order to measure the T_1 time accurately however, would require long waiting times and as such a more efficient way to achieve this would be to heat the sample to 2 or 4K and measure the temperature shortened T_1 times. Then the lower temperature value could be extrapolated accurately from that. However, given that the ^{13}C nuclear spin noise limit to coherence time is on the order of 1 μs, these T_1times are sufficiently long to observe Rabi oscillations with frequencies of MHz before spin relaxation occurs.

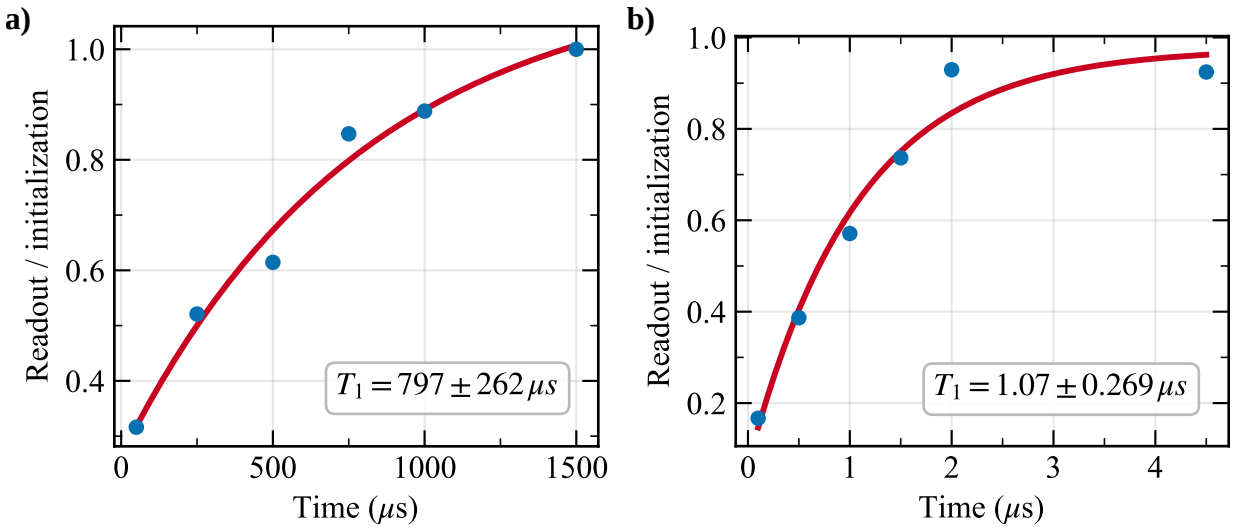

Figure 6.11 Both are are graphs of T_1 measurements taken at 120 mT in two different nanopillars with 500 nW of resonant light and 1 μW of 532 nm light.

6.0.5 Rabi Oscillations

Having confirmed coherent access to the ground state spin as well as sufficiently long T_1 times, an attempt to observe Rabi oscillations between these two spin states was made. These utilized two-photon Raman transitions as described in Chapter 2 to coherently transfer population between the two ground states. As mentioned above, CPT linewidths provide a lower bound for the coherence time of the system. The reason it is a lower bound is because in addition to many sources of experimental noise, it involves direct scattering off the excited state because the single photon detuning is equal to zero or close to it. This optical scattering induces spin flips and scattering induced dephasing. As such, for the Raman-Rabi oscillations, a single photon detuning of $\Delta = 250$ MHz is utilized to operate in the far-detuned regime and thus minimize optical scattering related decoherence processes. This limit is determined by degree to which $\Delta >> \sqrt{s}\Gamma$ is true. In this limit, the scattering rate is dependent on the single photon detuning and can be written as $\Gamma_{os} = \left(\frac{p}{p_{sat}}\right)\left(\frac{\Gamma^3}{8\Delta^2}\right)$. Each time an excitation to the excited state occurs, there is a chance for the spin to flip and thus it limits the T_1 spin relaxation time to $T_{1,os} = \frac{\eta}{\Gamma_{os}}$ and also limits the spin coherence time to $T_{2,os} = \Gamma_{os}$ [139, 184]. As such, a large single photon detuning can mitigate these challenges however, it will also reduce the Rabi frequency, so both must be balanced to enable high fidelity Rabi oscillations.

To realize this, the following pulse sequence was employed: first, a reset pulse resonant with A2; second, an initialization pulse resonant with A1; then a Raman pulse which consisted of a sin-modulated wave from the AWG equal to the two-photon transition frequency using the two first order sidebands to drive two photon transition; lastly, a readout pulse resonant with A1 was performed. This is similar to what has been done with the SnV [139]. The reset pulse was done to

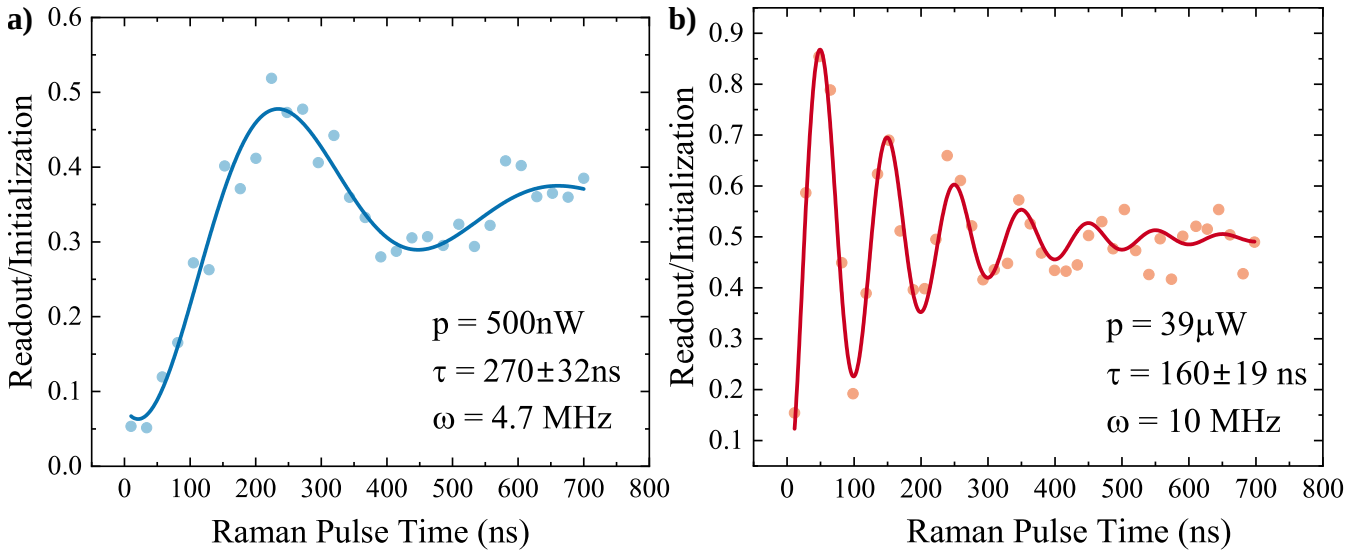

Figure 6.12 **a)** shows Rabi oscillations with specifications listed in the nanopillar sample, while **b)** shows Rabi oscillations in an emitter within the p-i-p sample.

ensure that 100% of the population started in the A1 state after each sequence. The initialization pulse ensured that the $|1\rangle$ spin down state was fully depleted. Then the Raman pulse would cause the spin state to oscillate at a Rabi frequency. The two photon transition frequency used for the Raman pulse was extracted by comparing the carrier frequency to the center of the CPT dip. Importantly, the Raman pulse is detuned off the excited state by $\Delta = 250$MHz and this is achieved by offsetting the carrier frequency from the center between A1 and A2 by Δ. The readout pulse was then used to determine how much population had been transferred. The fluorescence peaks for both the readout and initialization were integrated over, background subtracted and the ratio between them provided a measure for the amount of population in that spin state. This is precisely why the reset pulses are necessary as they ensure that the fluorescence from the initialization pulses are consistent across different runs. Additionally, because the initialization pulse drives all the population to the $|2\rangle$ state, the Raman drive coherently transfers from that state into $|1\rangle$, so the Rabi curves should start low and go high as the length of the Raman pulse gets longer. The initialization, reset, and readout pulses are all achieved with serrodyned pulses using the stronger of the two first-order sidebands.

Rabi oscillations between the two spin states were observed when the spin population was measured as a function of Raman drive time. This was observed in both the nanopillar and p-i-p sample as seen in Figure 6.12. For unpolarized light, the Rabi frequency at which the spin oscillates is $\Omega = \frac{1}{\sqrt{\eta}}\left(\frac{p}{p_{\text{sat}}}\right)\left(\frac{\Gamma^2}{4\Delta}\right)$ [184], where p is the power in each of the optical fields driving $A1$ and $A2$, p_{sat} is the measured saturation power for our emitter, $\Gamma/2\pi = 15$ MHz is the spontaneous decay rate from the excited state to the ground state, and η is the branching ratio, which is defined as the ratio of the transition probability between the two ground states and the excited state. For most

measurements in the p-i-p sample, a $p/p_{\text{sat}} = s \sim 80$ and $\Delta/2\pi = 250$ MHz were used primarily. The observed Rabi frequencies are on the order of MHz faster than the expected T_2^* decay due to the ^{13}C nuclear spin bath. In particular, the one shown in b of Figure 6.12 features $\Omega/2\pi = 10$ MHz. The Rabi measurements also provide a way to extract the π and $\pi/2$ pulse times necessary for Ramsey, Hahn-Echo, and CPMG pulse sequences.

Being able to demonstrate coherent control of NiVs in both nanophotonic structures and via the use of Fermi-level engineered devices goes a long way toward proving that this defect is a strong contender for quantum applications. In particular, it demonstrates that coherent control can be achieved in nanophotonic structures such as nanopillars and means NiV integration into such structures can be achieved without compromising coherence. This serves as a proof of principle. However, it should be noted that despite these observing oscillations, there were many attempts, even with seemingly similar parameters, where coherent oscillations were not observed for the nanopillar sample. At the time, this was attributed to charge state instability from the use of continuous green light; however, upon reflection, there were a plethora of technical challenges which had not been figured out yet, so revisiting that sample may prove fruitful. In particular, the T_1 time may have been artificially shortened as there was no AOM at the time to gate the carrier frequency on and off. As such, the carrier may have slowly excited the A2 state during delay times. Another possibility is an incorrect choice of two-photon transition. Having overcome many of these challenges, returning to that sample may yield more success. Nevertheless, the requirement for continuous application of green light during CPT and coherent control may have delterious effects as well, including charge state switching and spectral diffusion. Hence, the remaining measurements were carried out using the p-i-p sample exclusively, where bias voltage alone can be used for stabilization. In particular, this applies to the Ramsey, Hahn-Echo, and CPMG sequences.

6.0.5.1 Technical Challenges

Below are some of the challenges that needed to be overcome to achieve consistent Rabi oscillations. Reaching this point required extensive debugging and resolving several technical issues. These included stabilizing the applied optical power, which fluctuated because of improper polarization coupling and components that were inherently polarization- and temperature-dependent, such as beam samplers, as well as mitigating large temperature fluctuations. The temperature fluctuations were especially problematic because the setup is not enclosed within an actively temperature-stabilized optical table. Ultimately, fully polarization-maintaining fibers were implemented, along with the waveplates needed to align the polarization state for the fiber. In addition, a PID loop based on feedback from a photodiode measuring the power before the objective was implemented. A d-shaped mirror was used to cut off the back-reflected beam from the beam sampler, and the photodiode signal was routed to a USB DAQ to adjust the analog modulation of the AOM and

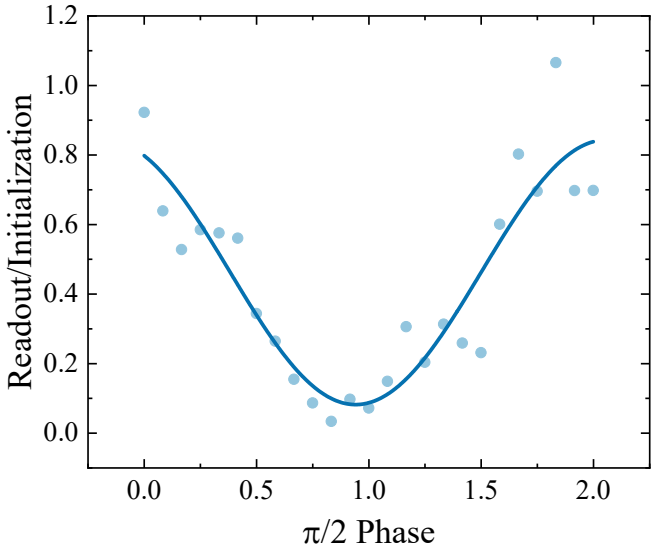

Figure 6.13 A sweep over the phase of the second $\pi/2$ pulse for a Ramsey measurement. The measurement was taken at 150 mT, with a power before the objective lens of 16 μW at a single photon detuning $\Delta/2\pi$ = 250 MHz. The fit is that of a sine function shifted by π.

consequently stabilize the power before the objective. Additional issues involved ensuring that the two-photon resonance frequency was correct and that the frequencies output by the AWG were as expected. Care was also taken to minimize cross-excitation from higher-order sidebands as well as from the carrier frequency, which could produce incoherent drives and shorten the T_1 time. These challenges help explain why, despite observing coherent Rabi oscillations, achieving them consistently remained difficult for a period of time. Another important lesson was the sensitivity of the EOM modulation efficiency to polarization modes. Once a polarization maintaining fiber was implemented, EOM sideband efficiency increased dramatically.

6.0.6 Ramsey Interferometry

While far-detuned Raman control can mitigate optical scattering, further separation can be achieved with Ramsey interferometry as described in Chapter 2. In a typical Ramsey sequence, an initial Raman $\pi/2$ pulse is sent to create a superposition state and then the system is allowed to freely precess before receiving another Raman $\pi/2$ pulse which transfers phase to population and enables one to determine the degree to which the system decohered over that free precession time. By varying the free precession time, a measure for the T_2^* time can be acquired. This is because while Ramsey can more effectively mitigate optical scattering compared to Rabi, it still cannot correct for the inhomogeneities or magnetic noise sources which cause decoherence for single spins. Before

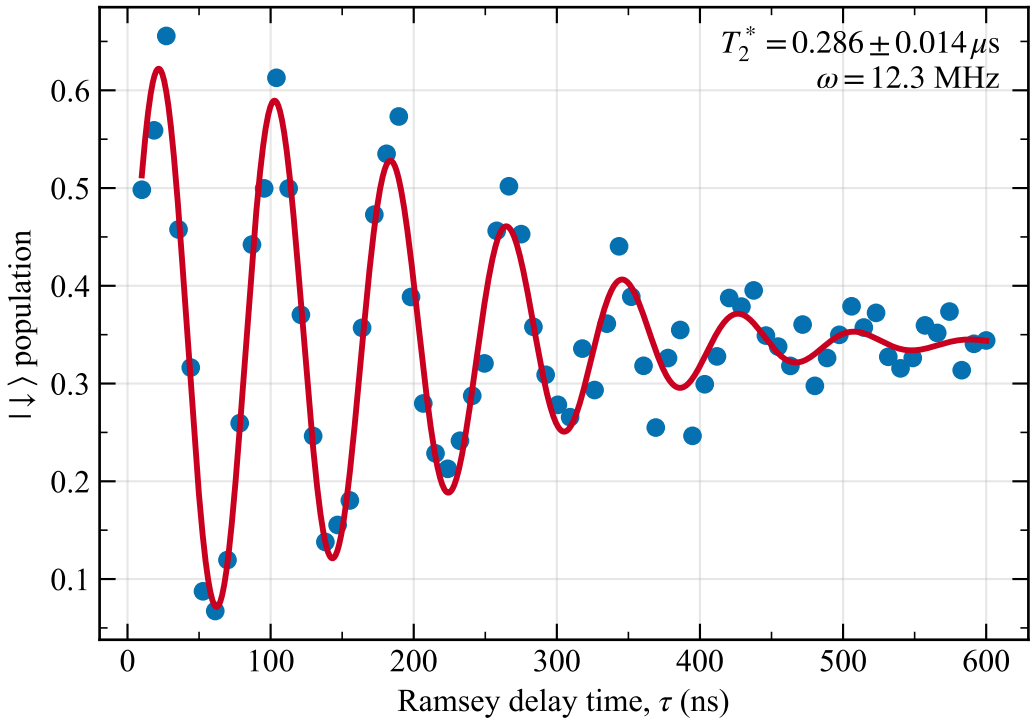

Figure 6.14 This is a Ramsey measurement in which ω = 10 MHz, the power is set to 14 μW and the magnetic field is at 150 mT with a detuning of 250 MHz.

attempting Ramsey measurements with different delay times, a sweep over the phase of the second $\pi/2$ pulse at 0 time delay between pulses was performed. This can be seen in Figure 6.13, which clearly shows the expected cosine behavior featuring maxima near 0 and 2π and minima at π. This demonstrates coherent control over the defect and confirms that pulses with relative phase stability between them can be created.

The free precession time was then varied and the phase of the second $\pi/2$ pulse was evolved according to $\phi = \omega_s \tau$ where $\omega_s/2\pi = 5$ MHz for example and τ is the free precession time. From Chapter 2, the probability of measuring the $|1\rangle$ state is then dependent on the artificially introduced phase factor

$$P_\downarrow = \frac{1}{2}[1 + \cos(\omega_s \tau)]. \tag{6.1}$$

True to form, Ramsey fringes are observed, as shown in Figure X, for the case $\omega_s/2\pi = 5$. This data was fit to a damped sine wave of the form

$$a \exp\left[-\left(\tau/T_2^*\right)^2\right] \sin\left(\omega_{\text{Ramsey}}\tau + \alpha\right). \tag{6.2}$$

This captures both the oscillatory behavior and the decay envelope. As discussed in Chapter 2, this decay arises from fluctuations in the ground-state splitting, which can come fro magnetic

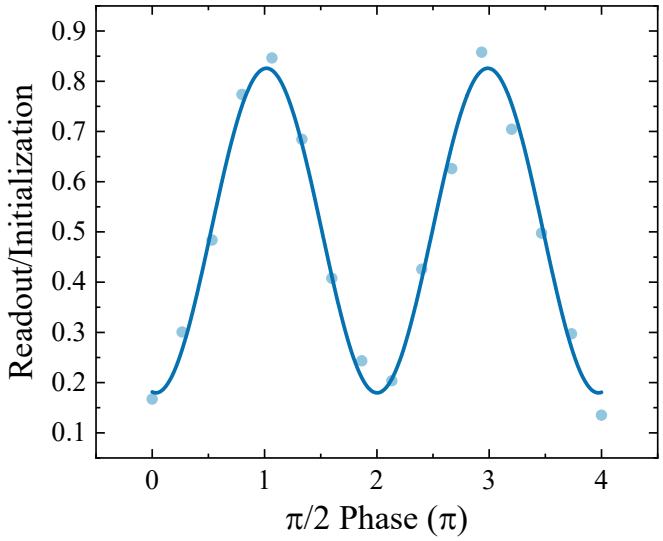

Figure 6.15 This is phase sweep for a Hahn-Echo sequence over the second $\pi/2$ pulse phase (units of π in rads) at a field of 150 mT and 250 MHz detuning. The resonant power before the objective was 14 μW. The fit overlaid is a sine function.

field variations, and other sources of spin noise that lead to different phase accumulations between measurements. When averaged over many repetitions, these noise sources can wash out the oscillations, causing the Ramsey contrast to decrease with increasing free-precession time. For the Ramsey fringe measurement shown in Figure 6.14, the extracted ground-state coherence time is $T_2^* = 286$ ns. This value is consistent with dephasing limited by ^{13}C nuclear spins in natural-abundance diamond. Both the nanopillar sample and the p-i-p sample studied here contain 1.1% naturally abundant ^{13}C nuclear spins, and the extracted coherence time is consistent with the expected T_2^* limit of approximately 300 ns to 1 μs set by the surrounding nuclear spin bath. Indeed, T_2^* values in this range are similar to those reported for SiV^-, SnV^-, and NV^- centers, where coherence is likewise limited by the ^{13}C nuclear spin bath [107, 139, 145].

6.0.7 Hahn-Echo

Having measured T_2^* using Ramsey interferometry, a Hahn-echo rephasing measurement was then carried out. The Hahn-echo sequence extends the Ramsey sequence by inserting a refocusing π pulse midway through the free-precession interval. This pulse reverses the phase accumulation caused by quasi-static or slowly varying fluctuations in the spin splitting, thereby suppressing dephasing from magnetic field noise. As in the Ramsey measurement, a phase sweep of the final $\pi/2$ pulse was first performed at zero delay time in order to verify the phase dependence of the readout. The result is

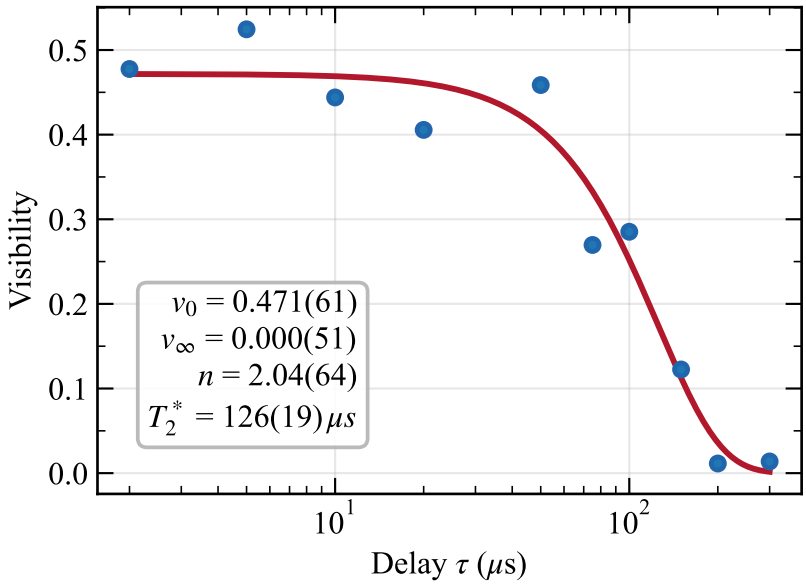

Figure 6.16 This Hahn-Echo dataset showcases visibilities extracted from performing Hahn-Echo measurements at two different phase values and using that to extract the visibility by subtracting each other then dividing by the sum. The dataset was taken at 150 mT, with a sin frequency of 1.4187 GHz, and a power before the objective lens of 14 μW of resonant light at a single photon detuning $\Delta/2\pi = 250$ MHz.

shown in Figure 6.15, where sinusoidal behavior is observed. This oscillation is shifted by π in phase relative to the Ramsey phase sweep because the intermediate π pulse is applied about the X axis, which inverts the state relative to the Ramsey measurement, as described in Chapter 2. A second measurement was then performed in which the free-precession delay was varied while the readout was recorded at phase values of 0 and π, corresponding to the minimum and maximum signal, respectively, in order to extract the visibility as a function of delay time.

The observed decay time is much longer than the Ramsey T_2^*, providing strong evidence that the dominant dephasing mechanism for the NiV^- center at 1.65 K is not phonon-induced decoherence, but rather slowly varying magnetic field noise, most likely arising from the ^{13}C nuclear spin bath. Because such noise evolves slowly compared to the pulse sequence, it can be effectively refocused by the Hahn-echo π pulse. The Hahn-echo data was fit to the function

$$v(\tau) = v_0 \exp\left[-\left(\frac{\tau}{T_2}\right)^n\right] + v_\infty,$$

with the extracted fit parameters given in the figure. From this fit, a coherence time of $T_2^{\text{echo}} = 126\,\mu$s was obtained. The decay envelope was also found to be best described by $n = 2$, rather than $n = 1$. This Gaussian-like decay is consistent with non-Markovian, slowly varying noise, as expected for a

quasi-static nuclear spin environment, and is not characteristic of fast, Markovian phonon-induced decoherence. Thus, both the long Hahn-echo coherence time and the extracted value $n = 2$ support the conclusion that at 1.65 K, coherence is primarily limited by the surrounding ^{13}C nuclear spin bath rather than by phonon-driven processes.

We then attempted a Carr-Purcell-Meiboom-Gill dynamical decoupling sequence comprised of two π pulses; however, we are still working through technical challenges with this one.

6.0.8 Estimating NiV Coherence Time

To get an initial estimate for the coherence time associated with the NiV, there are a few theoretical predictions for what it should be. But we can also use a model which has been used for the group-IV vacancy centers, which is to predominantly focus on the phonon induced decoherence [48]. This makes up an upper bound for the coherence time These phonon absorption events, like the one shown by the upward arrow in Figure 2.4, ultimately either decohere the qubit (if the population returns to the initial spin state, T2 time) or destroy the qubit state (if the population relaxes to the opposite spin state, T_1time) [266]. The phonon absorption rate (+) and phonon emission rate (-) can be expressed as [109].

$$\gamma_+(\Delta, T) = 2\pi\chi\rho\Delta^3 n_{th}(\Delta, T) \tag{6.3}$$

and

$$\gamma_-(\Delta, T) = 2\pi\chi\rho\Delta^3 (n_{th}(\Delta, T) + 1), \tag{6.4}$$

where χ and ρ are proportionality constants related to the electron phonon interaction rate and the phonon density of states, respectively. Δ is the resonant frequency of the phonon mediated transition, in this case, the orbital doublet ground state splitting. $n_{th}(\Delta, T)$ is the population at temperature T of phonons of frequency Δ. Phonon populations obey the Bose-Einstein distribution, so

$$n_{th}(\Delta, T) = \frac{1}{e^{\frac{h\Delta}{k_B T}} - 1}, \tag{6.5}$$

where h is Planck's constant and k_B is Boltzmann's constant. For the NiV, the ground state splitting is the resonant phonon mediated transition frequency, and if we are interested in using the lower orbital branch for our spin qubit, then we can focus on the phonon absorption rate. A coherence time of T2 = 250 ns has been achieved by straining a SiV center at 4 K [267]. While straining is a useful tool to have for both wavelength tuning [268, 269] and manipulating color center coherence, it is preferable to find a color center that naturally possesses long coherence times at temperatures above 1 K. Now, for the NiV$^-$, if we approximate the coherence time as $\tau_{spin} = 1/\gamma_+$ where γ_+ is the acoustic phonon absorption rate we just found, we find $\tau_{spin} = 12$ms at 1.65K and using the

ground state splitting of the NiV and the parameters for group-IV vacancies from [141, 214].

6.1 Summary

In conclusion, we have performed all-optical coherent control of the NiV. We observed coherent population trapping, Rabi oscillations, and Ramsey fringes using two-photon Raman transitions. Further, we were able to successfully extend the coherence time with the aid of a Hahn-Echo sequence indicating that at 1.65K, we are no longer limited by phonon induced processes. Taken together, these results make the NiV^- an attractive candidate for quantum memory and quantum networking applications.

Chapter 7

Novel Defects for Fundamental Symmetry Tests

Detecting a non-zero electric dipole moment (EDM) in a particle would unambiguously signify physics beyond the Standard Model. A potential pathway towards this is the detection of a nuclear Schiff moment, the magnitude of which is enhanced by the presence of nuclear octupole deformation. However, due to the low production rate of isotopes featuring such "pear-shaped" nuclei, capturing, detecting, and manipulating them efficiently is a crucial prerequisite. Incorporating them into synthetic diamond optical crystals can produce defects with defined, molecule-like structures and isolated electronic states within the diamond band gap, increasing capture efficiency, enabling repeated probing of even a single atom, and producing narrow optical linewidths. In this study, we used density functional theory (DFT) to investigate the formation, structure, and electronic properties of crystal defects in diamond containing ^{229}Pa, a rare isotope that is predicted to have an exceptionally strong nuclear octupole deformation. In addition, we identified and studied stable lanthanide-containing defects with similar electronic structures as non-radioactive proxies to aid in experimental methods. Our findings hold promise for the existence of such defects and can contribute to the development of a quantum information processing-inspired toolbox of techniques for studying rare isotopes.

7.1 Introduction

Outside of using defects in diamond for quantum bits in a quantum computer or quantum network, there are also alternate applications as quantum sensors. In particular, there is a large body of research focused on making sensors which reach quantum noise limits. These have been looked into as sensors for gravitational waves, electric dipole moments, and in magnetic resonance imaging. Here, we will explore a project which focused on using a diamond defect as a sensor to measure fundamental physical constants. In particular, I will describe a computational density functional

theory study done for protactinium defects in diamond, which might be useful for the measurement of electric dipole moments of electrons thanks to the octupole deformation within ^{229}Pa.

The story begins with one of modern day Physics' biggest questions: why is there more matter than anti-matter in our universe? This question is known as the baryon asymmetry problem. Baryons are protons and neutrons and there are correspondingly antibaryons which make up antimatter. The observed asymmetry is something the standard model cannot account for, so researchers have been looking for ways to prove physics beyond it. In particular, one method is to look for violations of charge-conjugation parity (*CP*-violations) [270]. These were first observed with in Kaons in 1964 [271]. However, current observations of *CP* violations are not significant enough to account for such phenomena. Recently, the measurement of a non-zero permanent electric dipole moment (EDM) within atomic nuclei induced by the nuclear Schiff moment has garnered considerable attention as a potential solution. The existence of a permanent EDM requires breaking of both time-reversal symmetry (T) and parity symmetry (P), which, by the CPT theorem, implies that it breaks *CP* symmetry as well [272]. Therefore, the study of permanent EDMs in atomic nuclei provides an exciting avenue for detecting *CP*-violating phenomena and addressing some of the most pressing questions in physics today.

Measuring a permanent EDM poses a significant challenge due to its extremely weak signature. However, certain pear-shaped (octupole-deformed) nuclei, such as ^{223}Fr, ^{225}Ra, and ^{229}Pa, have shown to be particularly sensitive to EDM measurements, making them ideal candidates for further study [273, 274]. In particular, ^{229}Pa is predicted to provide over six orders of magnitude more sensitivity than the current experimental limit on EDM measurements taken with ^{199}Hg [275, 276]. Despite its potential, the limited global production of ^{229}Pa has hindered its experimental study. However, the newly-opened Facility for Rare Isotope Beams (FRIB) at Michigan State University is expected to produce a significant amount of ^{229}Pa within the decade [277]. This will provide a host of opportunities to study ^{229}Pa. One such opportunity that has been proposed is to implant ^{229}Pa nuclei within an optical crystal, thereby enhancing the signal for EDM measurements. This approach provides numerous advantages, such as high number densities, efficient optical probing, and large internal electric fields for oriented non-inversion symmetric crystal defects in optical crystals. However, one other factor that has limited the study of ^{229}Pa is its extreme toxicity and radioactivity. As such, stable nuclear surrogates are necessary for the development of experimental and testing schemes prior to use of ^{229}Pa. ^{141}Pr is an excellent candidate for this as it is expected to be isoelectronic with ^{229}Pa and has the same nuclear spin $I = \frac{5}{2}$. Moreover, ^{141}Pr is not as toxic and not radioactive. Thus, ^{141}Pr can serve as a stable nuclear surrogate to ^{229}Pa, allowing for method development and testing. This approach can pave the way for future experiments in detecting EDMs in atoms and addressing some of the most profound questions in modern physics.

Diamond is a highly suitable host material for EDM-sensitive isotopes such as ^{229}Pa. It possesses

exceptional radiation hardness, making it more resistant to damage from implantation and the decay of incorporated radioactive species than most other host materials [278, 279]. Additionally, its wide band gap (5.5 eV) increases the probability of defect formation within the gap, as demonstrated by the existence of thousands of optically active crystal defects in diamond [157]. Furthermore, synthetic diamond can be made nuclear spin-free using ^{12}C enriched precursors in chemical vapor deposition (CVD) growth, eliminating a significant source of spin decoherence and effectively creating an almost perfect spin environment [280, 281]. The extensively studied nitrogen vacancy center in diamond can also be utilized as a highly sensitive quantum magnetometer and can be used for in-situ co-magnetometry [282]. Overall, these properties make diamond a highly attractive material for hosting isotopes such as ^{229}Pa.

This paper presents a study on the geometric structure, thermodynamic stability, and electronic properties of ^{229}Pa and ^{141}Pr defects in diamond using density functional theory (DFT). Specifically, we investigate a variety of different defect configurations, including substitutional defects as well as defects with one to four vacancies introduced nearby. The paper is organized as follows: Section II outlines the computational details and methods involved in the DFT calculations; Section III presents results of these calculations, including geometric structure, formation energy, charge transition levels, electronic structure and EDM sensitivity along with potential measurement schemes. Finally, in Section IV, we draw conclusions based on our findings.

7.2 Computational Methods

Spin-polarized DFT was employed using the projector augmented wave method [283, 284] as implemented in VASP 6.2.1 [285] to characterize isotopic ^{229}Pa and ^{141}Pr defects in diamond. The exchange and correlation behavior of the valence electrons ($2s^2 2p^2$, $6d^2 7s^2 5f^1$, and $4f^3 6s^2$ electrons for C, Pa and Pr, respectively) during structure optimization was described using the Perdew-Burke-Ernzerhof (PBE) generalized gradient approximation (GGA) [286]. To account for the strongly correlated behavior of the f-electrons in actinides and lanthanides, a Hubbard-U-type correction (DFT+U) was included for Pa and Pr f-electrons in all PBE-level calculations. The implementation suggested by Leichtenstein et al. [287] was used with an on-site Coulomb parameter U = 7 eV and on-site exchange parameter J = 1 eV for Pa and Pr, as has been used by others to study lanthanide defects in diamond [288–291]. Additionally, the Heyd-Scuseria-Ernzerhof (HSE06) hybrid functional [292, 293] was used for the calculation of highly accurate electronic structures. This range-separated hybrid functional can accurately reproduce experimental band gaps and charge transition levels in diamond and other group-IV semiconductors to within 0.1 eV [294, 295] and has successfully described a variety of defects in diamond [295–301].

A variety of defect configurations were studied, including defect ions placed in the substitutional

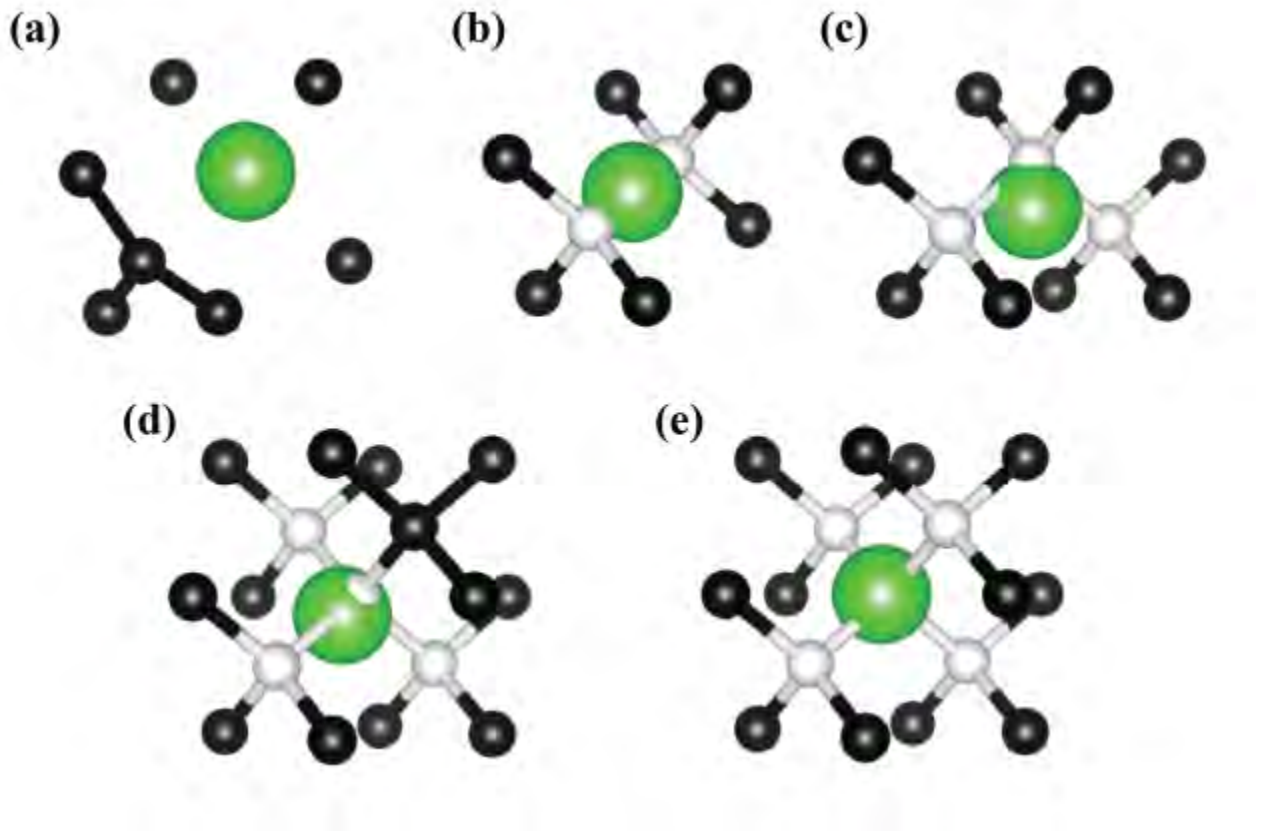

Figure 7.1 Relaxed defect structures of **(a)** $^{229}Pa_{sub}$, **(b)** ^{229}PaV, **(c)** $^{229}PaV_2$, **(d)** $^{229}PaV_3$, and **(e)** $^{229}PaV_4$. For clarity, only the defect ion and the nearest neighbor carbon atoms are displayed. The larger green atom is the ^{229}Pa ion. The black atoms represent carbon, while the white atoms represent vacancies. For $^{229}PaV_2$, $^{229}PaV_3$, and $^{229}PaV_4$ the "extra" white vacancy ball that can be seen through the ^{229}Pa is the initial position of the ^{229}Pa at a lattice site.

lattice site as well as in substitutional lattice site positions with one to four vacant sites adjacent to them. Calculations were performed on a 3x3x3 diamond supercell containing 216 atoms, and the Brillouin zone was sampled at the Γ point. The excited states were calculated using the constrained-occupation DFT method (Δ-SCF) [295] with zero phonon lines (ZPL) calculated by taking the energy difference between ground and excited states. The initial geometries of the models are depicted in Figure 7.1. The supercell defects were allowed to relax with a constant volume using a conjugate gradient method to ensure that the defect formation energies are comparable. The plane-wave energy cutoff was set to 370 eV. Ionic optimization was performed until forces were less than 10^2 eV/Å, and the break condition for the electronic self-consistent loop was set to 10^{-6} eV for the ZPL, hyperfine, and electric field calculations. To account for the isotopic nature of ^{229}Pa and ^{141}Pr, the mass value in the POTCAR file was changed accordingly.

The PBE functional was chosen for geometry relaxation due to its lower computational cost and its ability to predict the structures of a variety of defects in diamond with sufficient accuracy [302–305]. Furthermore, using a smaller 2x2x2 supercell of 64 atoms, we relaxed the geometry using both PBE+U and HSE06 functionals and found that the difference in atomic positions between the two relaxed structures was less than 10^{-5} Å on average, demonstrating that the accuracy of PBE+U is comparable to that of HSE06 for geometry relaxation.

To assess which defect configuration was most stable, formation and cohesive energies were calculated for each defect studied. The formation energy for a defect X with charge state q can be calculated according to:

$$E^{\mathrm{f}}[X^q] = E_{\mathrm{tot}}[X^q] - E_{\mathrm{tot}}[\mathrm{bulk}] - \sum_{i=1}^{k} n_i \mu_i + q(\epsilon_{\mathrm{VBM}} + E_{\mathrm{F}}) + E_{\mathrm{corr}}, \tag{7.1}$$

where $E_{\mathrm{tot}}[X^q]$ and $E_{\mathrm{tot}}[\mathrm{bulk}]$ are the total energies of the bulk material with and without the defect, respectively; n_i is the number of atoms of species i that have been added to or removed from the supercell (for example, $^{229}\mathrm{Pa}_{\mathrm{sub}}$ removed 1 C and added 1 ^{229}Pa); μ_i is the chemical potential corresponding to atomic species i; ϵ_{VBM} is the valence band maximum of the bulk material; E_{F} is the Fermi level, which can have values within the material's band gap; and E_{corr} is the finite-size electrostatic correction [306]. E_{corr} was obtained using the scheme proposed by Freysoldt, Neugebauer and Van de Walle (FNV) [307] as implemented in the Spinney code package [308]. The chemical potential for C was obtained by dividing the total energy of the pristine diamond supercell by the number of atoms. The chemical potential of Pa was calculated as the total energy of metallic Pa (with a bcc tetragonal structure, I4/mmm, no. 139) divided by the number of Pa atoms. Similarly, the chemical potential of Pr was calculated using the total energy of metallic Pr (with a hexagonal structure, P63/mmc, no. 194) divided by the number of Pr atoms. For the chemical potential, the k-point sampling was increased to 9x9x9 due to the small crystal structure.

Cohesive energies were calculated according to:

$$E_{\mathrm{c}} = \frac{1}{n}\left(\sum_{i=1}^{k} n_i E_{\mathrm{atom},i} - E_{\mathrm{tot}}\right), \tag{7.2}$$

where n is the total number of atoms, E_{tot} is the total energy of the defect system, n_i is the number of atoms of species i, and $E_{\mathrm{atom},i}$ is the energy per atom for species i [309]. In order to evaluate the cohesive energies of the structures, it was necessary to calculate the total energies of the corresponding isolated atoms in the structures (using the same exchange functionals and calculation quality settings). For the calculation of the C atom, a 10x10x10 Å cube with a single C atom in the center was used, giving enough space around the atom for it to be considered as an isolated atom. For the Pa and Pr atoms, a slightly larger cube of 15x15x15 Å was used to ensure isolation of the atoms.

To determine the most stable charge state for a given defect, its charge transition levels (CTLs) are calculated. The CTL is the Fermi level at which a transition between two charge states becomes energetically favorable [310]. It is calculated using the formula:

$$\epsilon(q_1/q_2) = \frac{E_{q_1}^{\mathrm{tot}} + E_{q_1}^{\mathrm{corr}} - E_{q_2}^{\mathrm{tot}} - E_{q_2}^{\mathrm{corr}}}{q_2 - q_1} \tag{7.3}$$

where E_q^{tot} is the total energy of the supercell calculation in charge state q and E_q^{corr} is the corresponding charge correction that accounts for the periodic interaction of charges between neighboring supercells [307, 311, 312].

The formation and cohesive energies were evaluated for the neutral charge states of the different defect configurations to determine which configuration is most stable. From there, we limited our analysis to the most stable structure and plotted the formation energies for different charge states as a function of Fermi level to determine which charge state is most stable (determined by which charge state has the lowest formation energy for any given Fermi level). The crossing points of these formation energy lines represent charge transition levels, where one charge state becomes more favorable than another.

Zero-field splitting (ZFS), magnetic hyperfine, and electric field gradient tensors were all calculated within VASP. For the ZFS tensor in particular, we use the method by [313] with the PBE functional, which has been demonstrated to be sufficiently accurate [303]. For all of these calculations, a higher cut-off energy of 700 eV was used. VESTA [314] was used to visualize the defect structures in addition to the wave functions, whose plane wave coefficients we extracted using the Python class PyVaspwfc [315]. Similarly, transition dipole moments were also calculated using PyVaspwfc.

7.3 Results and Discussion

7.3.1 Structure and Stability

First, the structure of each of the defect configurations was studied to determine which is thermodynamically most likely to form during ion implantation and subsequent annealing. All defect ions were initially placed at a substitutional lattice site with nearest neighbor C atoms removed to create vacancies. The final relaxed structures for each defect configuration are shown in Figure 7.1. Interestingly, we find that ^{229}Pa and ^{141}Pr defects form qualitatively identical structures for all defect models considered. As such, the following descriptions and images for each defect configuration apply to both.

For the substitutional defect with no vacancies, the defect ion did not move, but the nearest neighbor carbon atoms were displaced outwards. For the single vacancy, the ion moved into the split vacancy configuration, while for the higher-order vacancy complexes, it moved into a position that filled the void created by the removed carbons. It is worth noting that while the split vacancy is inversion symmetric, the higher-order vacancy complexes are not, resulting in a permanent electric dipole moment and thus static internal electric field. While this is usually avoided for quantum information processing applications as it makes defects susceptible to environmental field fluctuations, it is in fact desirable for EDM experiments, as it increases the sensitivity of EDM measurements [276].

The calculated formation and cohesive energies shed light on which configuration is most energetically favorable to form. Our analysis reveals that, for both ^{229}Pa and ^{141}Pr, the substitutional model is less favorable than those containing vacancies, as it generally has a higher formation energy despite having a marginally higher cohesive energy in certain cases. This is in agreement with other first principles studies of defects in diamond that feature large ions, which can introduce significant strain [289, 291, 305, 316]. The introduction of vacancies helps to offset this by creating additional room for the dopant atom. Among the defects with vacancies, the double and triple vacancies are the most energetically favorable in terms of formation energy and have comparable or larger cohesive energy values compared to the single and quadruple vacancy defects. Between the double and triple vacancy, however, we find that the double vacancy is the most stable, as there is diminishing gains by adding yet another vacancy [288]. Moreover, higher-order vacancy complexes are kinetically less likely to form due to the low mobility of substitutional defects in diamond at typical processing temperatures [317]. Additionally, a similar ab-initio study was done on Ce defects in diamond, and CeV_2 was found to be most stable [289, 318]. Therefore, we conclude that the most stable structure for both ^{229}Pa and ^{141}Pr defects in diamond is a defect ion accompanied by two vacancies.

To further assess the probability of these defects forming, we compare our calculated results with values calculated for other defects in diamond. A combined experimental and theoretical

study done on Er^{3+} ions implanted in diamond calculated similar cohesive and formation energies. Importantly, they also experimentally observed the characteristic telecom band emission from the Erbium ions after implantation and annealing [305]. Additionally, formation energies calculated for nickel complexes in diamond are also comparable to our values and these nickel defects are known to form in diamond [319]. Lastly, we compare the formation energies of the various charge states with the common NV center (see Figure 7.3) and they are the same order of magnitude. These examples demonstrate the feasibility of lanthanides and actinides forming luminescent centers in diamond.

Notably, non-inversion-symmetric defect configurations are preferred. As noted above, while typically not ideal for quantum information processing applications, [181], the opposite is true for EDM measurements [320, 321]. As was stated above, this results in a permanent electric dipole moment which can lead to linear Stark shifts. This results in symmetric doublet splittings in optical transitions when two states with oppositely-oriented dipole moments are degenerate in a non-inversion symmetric site. This makes it possible to specifically address ions that have a specific direction of electric polarization. Going back to the initial statement of inversion-breaking defects being preferred, this means that for any given sample, the majority of defects formed will not be inversion-symmetric and will thus retain the advantages of enhanced EDM measurement sensitivity. Based on these findings, we focused subsequent calculations on ^{229}Pa and ^{141}Pr defects with two vacancies.

7.3.2 Charge State Formation Energies

Since $^{229}PaV_2$ and $^{141}PrV_2$ appear to be the most thermodynamically favorable defects, which also feature promising geometries for EDM measurements, we will focus on these configurations from here on out. We start by determining their potential charge states and charge transition levels. Our findings indicate that both defects can potentially take on charge states ranging from -3 to +1. The formation energy as a function of Fermi level is displayed in Figure 7.3. As mentioned above, the calculated formation energy values are comparable to those of other defects in diamond that contain large defect ions [288, 305], indicating that, at least thermodynamically, defect formation is possible. Additionally, for the purposes of NV co-magnetometry, the -1, -2, and -3 charge states for both defects all land squarely within the Fermi levels where negatively charged NV centers are likely to form. Furthermore, since NV co-magnetometry requires a relatively high donor concentration, the negative charge states are preferred. In terms of which charge state is most likely to form in diamond without the need for careful doping, the -1 charge state is nearest the Fermi level for un-doped diamond [322].

Charge transition levels (CTLs) were calculated using the information shown in the formation energy diagram (Figure 7.3). Calculating the CTLs for different doping levels allowed us to

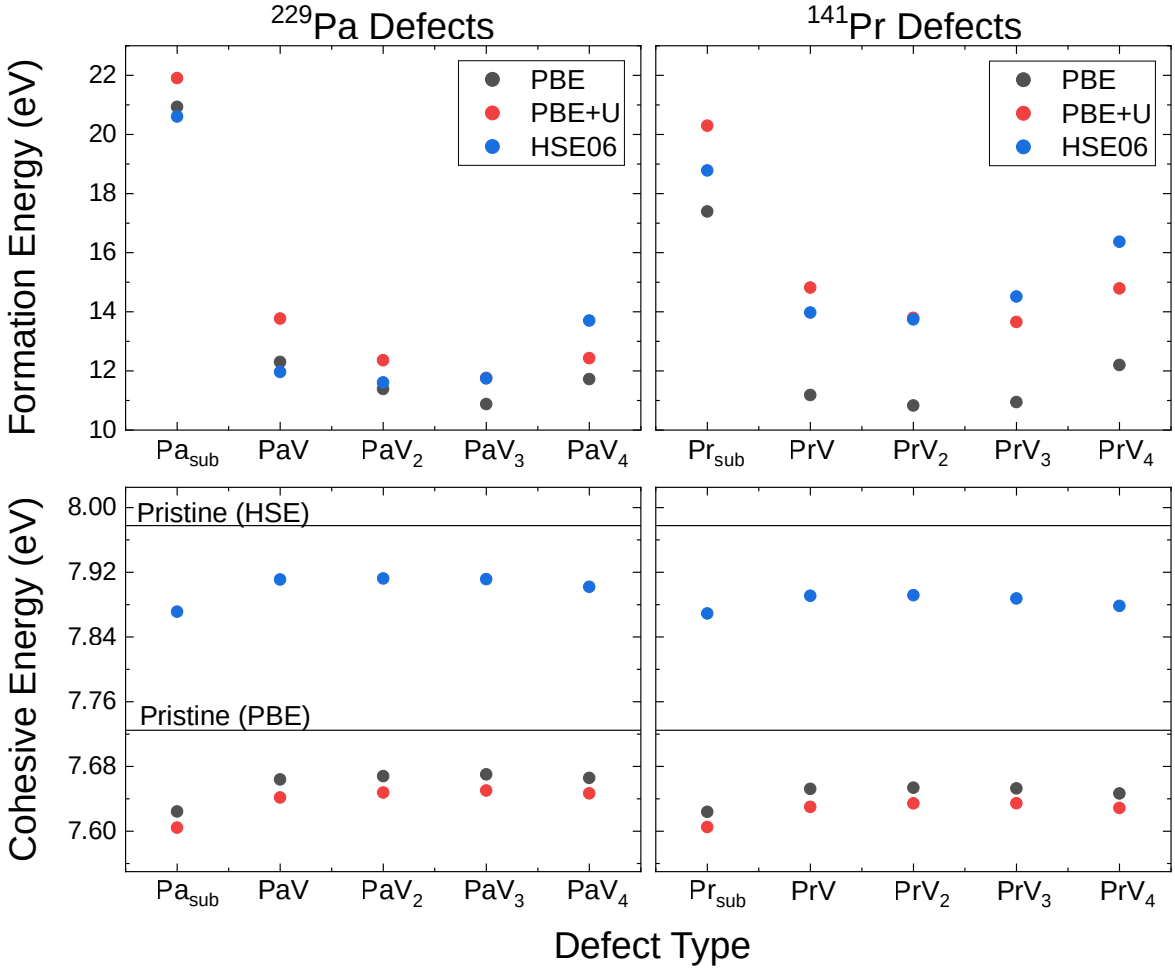

Figure 7.2 Top two panels are formation energies for different defect configurations using different functionals. Bottom two panels are cohesive energies for different defect configurations and different functionals. For the bottom panels, the solid lines denote the cohesive energy for pristine diamond without any defects using both PBE and HSE06 functionals.

determine which charge state is most stable at each Fermi level. This information is important for understanding the behavior of the defects in diamond under different doping conditions. For example, it provides information on the effect of different atomic species on the defects' charge stability. Here, the negative charge states act as electron acceptors and require compensatory electron donors in the system, such as substitutional N that have a deep donor level located 1.7 eV below the conduction band minimum [323, 324].

7.3.3 Electronic Structure

In this section, we present a detailed analysis of the electronic structure of the defects using group theory and DFT calculations. Both defects of interest, $^{141}PrV_2$ and $^{229}PaV_2$, are part of the C_{2v} symmetry point group. Using this, we derive a defect molecular orbital diagram to make predictions for the optical transitions and fine structure. First, we calculate the spin-polarized level structure of the single-electron orbitals using DFT and derive which irreducible representation of C_{2v} they belong to by applying the respective symmetry operators to the calculated wave functions. Figure 7.4 shows the single-electron orbital levels obtained from the DFT calculations. From these single electron orbitals, we construct the many electron (molecular) orbital configurations shown in Figure 4. This diagram displays the single-electron Kohn-Sham energy levels and their corresponding irreducible representations, allowing possible optical transitions to be identified. From the results, the +1 and -1 charge states features S=1 spin triplets; the neutral charge state has a S=3/2 quartet; and the -2 and -3 charge states feature an S=1/2 doublet and S=0 singlet, respectively. With this, we can identify charge states of interest based on their spin. In particular, we are interested in defect states with unpaired electrons in the ground state. This ensures that the defect is optically active and provides hyperfine coupling between a nuclear and electron spin, enabling the use of well-developed quantum control schemes to detect a nuclear-Schiff moment. Specifically, nuclear spin state preparation and read out is most easily facilitated using interactions with laser light via the hyperfine coupling with a surrounding electron [326–328]. Moreover, these nuclear hyperfine states could provide potentially hour long coherence times as this has been shown in other defects with nuclear spin [70, 329], further increasing the sensitivity of the measurement [330]. Given this, we limit our focus to the +1, 0, -1, and -2 charge states, leaving out the -3 charge state, which has no unpaired electrons. Importantly, it should be noted that there have been successful nuclear Schiff moment experiments which did not use hyperfine coupling [331], raising the possibility for future studies and control schemes for the -3 charge state. Among the remaining charge states of interest, we choose to further analyze the -1 and -2 charge states as they are more likely to form within natural diamond while also falling within Fermi level regions that the negatively charged NV center does.

One additional observation from the Kohn-Sham orbitals is that the defect ions introduce

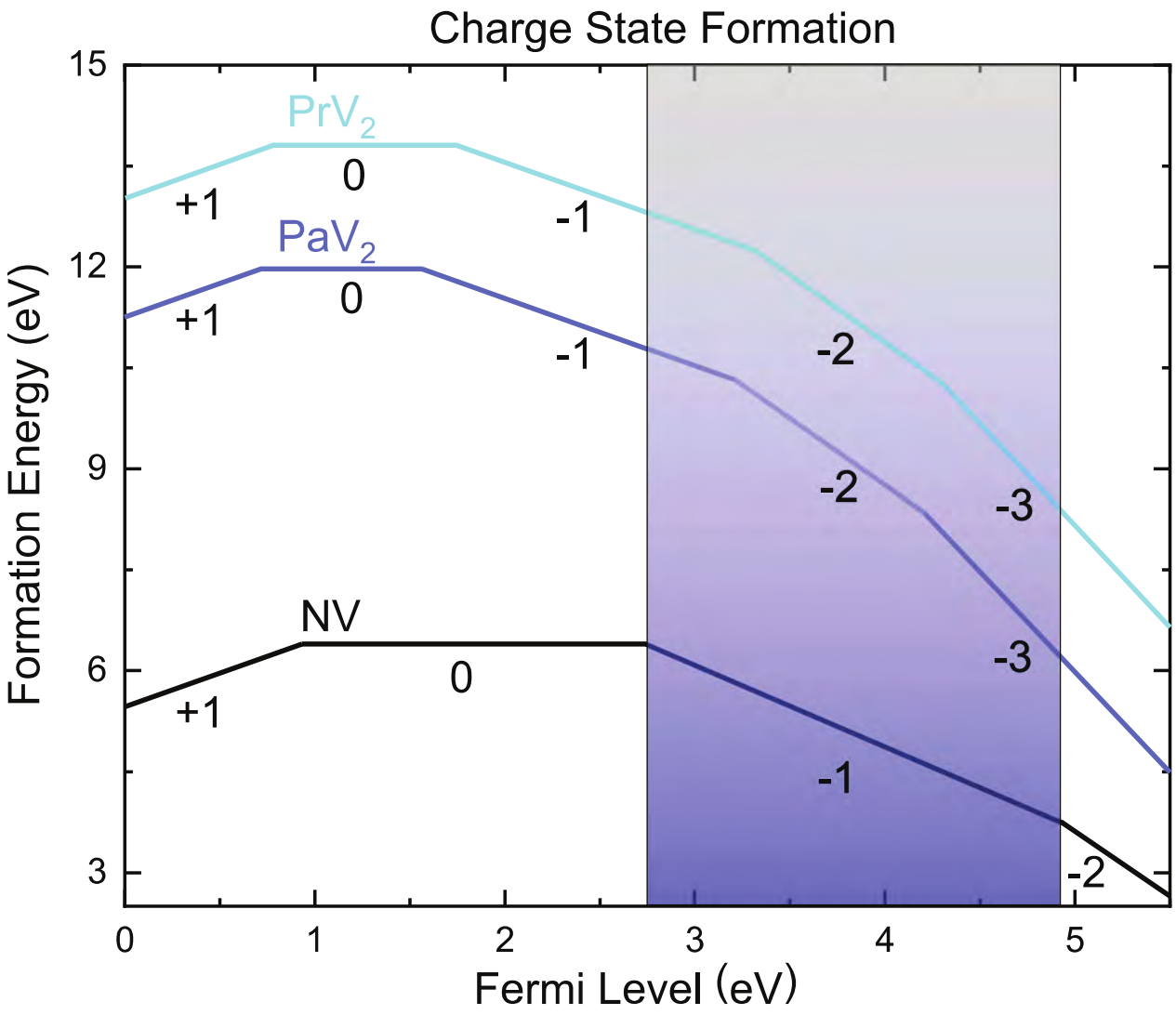

Figure 7.3 Charged formation energy as a function of Fermi level for PaV_2 and PrV_2 defects in diamond. Additionally, formation energies calculated by [325] for the NV center in diamond are included for comparison.

occupied bands within the band gap of diamond. This differs from other color centers in diamond such as certain group-IV or nickel vacancies where the Kohn-Sham orbitals are situated below the valence band edge [332, 333]. For $^{229}PaV_2$ and $^{141}PrV_2$, however, both the ground and excited state levels for the minority spin channel are located within the band gap. This localization of the defect states from the bulk bands reduces the probability of single-photon transitions from the defect to bulk states during defect-defect transitions, potentially enhancing the excitation efficiency for the studied centers.

In general, our goal is to identify electronic structures featuring ground and excited state spin and orbital configurations leading to qualitatively identical interaction, splitting patterns and optical transitions for both $^{141}PrV_2$ and $^{229}PaV_2$ so that the stable $^{141}PrV_2$ defect can be used as a test bed for method development. To identify these transitions, we first need to know which optical transitions are electric dipole allowed. In C_{2v}, the dipole moment vector transforms as (B_1, B_2, A_1). With that, we can calculate the matrix elements for various transitions using the irreducible symmetry representation to determine which transitions are allowed. Because the electric dipole operator does not act on the spin part of the wavefunction, we only consider non-spin flipping excitations within the spin up and spin down channels, respectively, to identify possible optically allowed transitions. Based on ground and excited state wavefunctions, we calculate transition dipole moments to determine the strength of certain transitions. Using this, transitions which match for both $^{141}PrV_2$ and $^{229}PaV_2$ and which have a TDM > 1 Debye were selected for further study. The results are displayed in Table 7.1 along with the calculated ZPL for each transition.

	Spin Channel	Transition	ZPL (nm)	TDM (Debye)
$^{229}PaV_2^{2-}$	up	$^2A_1 \rightarrow {}^2B_2$	553	1.36
$^{141}PrV_2^{2-}$	up	$^2A_1 \rightarrow {}^2B_2$	731	2.88
	down	$^2A_1 \rightarrow {}^2B_2$	1763	1.05
$^{229}PaV_2^{1-}$	down	$^3B_2 \rightarrow {}^3A_2$	1294	6.64
$^{141}PrV_2^{1-}$	down	$^3B_2 \rightarrow {}^3A_2$	1378	7.71

Table 7.1 Matching optical transitions for the −2 and −1 charge states for $^{229}PaV_2$ and $^{141}PrV_2$ defects. Spin channel refers to whether a spin up or down electron was promoted to a higher band (i.e., excited state). Transition shows the symmetry of the ground and excited state. TDM is the transition dipole moment, which corresponds to the strength of the transition.

We start our analysis with the -1 charge states for both defects, which have $^3B_2 \rightarrow {}^3A_2$ transitions. Because both defects have C_{2v} symmetry, the states that the single electron orbitals can take on can transform like (A_1, A_2, B_1, B_2). These are all orbital singlets, and thus the orbital angular momentum, L, is zero for these states [171, 334]. As a result, the spin orbit coupling which is proportional to $L \cdot S$ is zero. Consequently, there is no energy splitting from spin-orbit coupling.

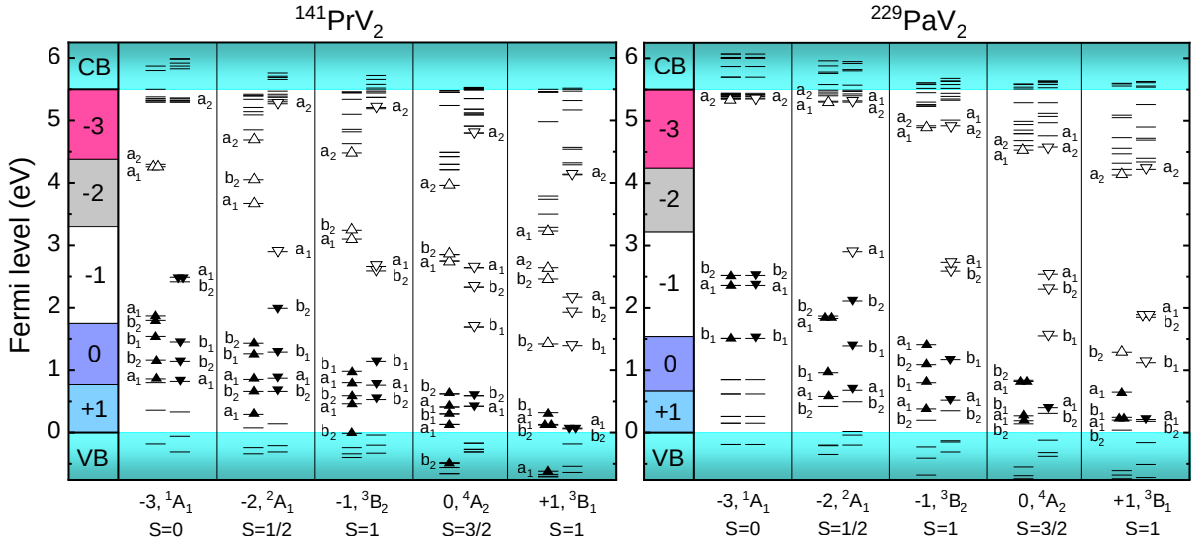

Figure 7.4 Ground state electronic structure for the charge states of $^{229}PaV_2$ and $^{141}PrV_2$. The single-electron orbitals are labeled with their corresponding irreducible representations.

The ground state $^3B_2$ features an $S = 1$ spin triplet, and ^{229}Pa nuclear spin $I = \frac{5}{2}$, leading to the fine and hyperfine structure shown in Figure 7.6. Five interactions were considered when analyzing the possible spin state splittings: the electron-electron magnetic dipolar interaction **D**, the hyperfine interaction **A**, the nuclear quadrupole interaction **Q**, and the electronic and nuclear Zeeman interactions:

$$\hat{H} = \mu_B g_e \vec{B} \cdot \vec{S} + \mu_N g_n \vec{B} \cdot \vec{I} + \vec{S} \cdot \mathbf{D} \cdot \vec{S} + \vec{S} \cdot \mathbf{A} \cdot \vec{I} + \vec{I} \cdot \mathbf{Q} \cdot \vec{I}, \tag{7.4}$$

where μ_B and μ_N are the Bohr and nuclear magnetons, $\vec{B}$ is the magnetic field vector, g_e and g_n are the electron and nuclear g-factors, and $\vec{S}$ and $\vec{I}$ are the total electron and nuclear spin angular momenta.

In the principle axis coordinates, the latter three terms in Eq. (3.1) can be written as:

$$\hat{H}_D = \mathbf{D}[S_z^2 - \frac{1}{3}S(S+1)] + \frac{E}{2}(S_+^2 + S_-^2) \tag{7.5}$$

$$\hat{H}_Q = \frac{eQ_I V_{zz}}{4I(2I-1)}[3I_z^2 - I(I+1) + \eta(I_+^2 + I_-^2)] \tag{7.6}$$

$$\hat{H}_A = A_{zz}S_z I_z + A_{xx}S_x I_x + A_{yy}S_y I_y \tag{7.7}$$

where $D = \frac{3}{2}D_z$, $E = \frac{D_x - D_y}{2}$, Q_I is the nuclear quadrupole moment, e is the electric charge, and $\eta = (V_{xx} - V_{yy})/V_{zz}$ is an asymmetric coefficient [335]. It should be noted that VASP has been found to underestimate the zero-field tensor, **D**, even when using hybrid functionals, so the values

may be larger than what was calculated [336]. The quadrupole for ^{229}Pa has not been experimentally measured, so the theoretically calculated value from [337] was used. The results of the DFT calculations are presented in Table 7.2 for the defect ions of interest. With these calculated tensor parameters, we use the free software EasySpin [338] to simulate the level structure both with and without an applied magnetic field (see Figures 7.5 and 7.6).

For the level structure, we start by looking at the zero-field splitting. The axial component of this interaction splits the $m_s = 0$ and $m_s = \pm 1$ states while the rhombic anisotropy from the E term can split the $m_s = 1$ and $m_s = -1$ states. The quadrupole interaction then splits all three of these branches further into $m_I = \pm\frac{1}{2}, \pm\frac{3}{2}, \pm\frac{5}{2}$ levels. From there, the hyperfine interaction splits the nuclear sublevels further. In this case, the hyperfine interaction is anisotropic, which results in more zero-field splitting. For brevity, we have combined the splittings due to the quadrupole and hyperfine interactions in the figures. When a magnetic field is applied in the z-direction, the electronic and nuclear Zeeman terms split both the electronic and nuclear sublevels further as can be seen in Figures 7.5 and 7.6.

The -2 charge state has one unpaired electron and therefore has spin $S = \frac{1}{2}$ due to the half-occupied molecular orbital that can be spin up or down, resulting in a spin multiplicity of 2. The ground state has the electronic configuration $[a_1]^2[b_2]^2[b_1]^2[a_1]^1[b_2]^2$, which transforms as the irreducible representation A_2 based on the direct product of the irreducible representations that constitute the state. Similar to the -1 transitions, the excited and ground states are orbital singlets, resulting in the absence of Jahn-Teller instability and spin-orbit coupling. Similarly, there is no spin-spin interaction because there is only one unpaired electron. Thus, we start our analysis with the application of a magnetic field, which lifts the degeneracy of the $m_s = \pm\frac{1}{2}$ states for both the ground and excited states, as they are both spin doublets. The electronic Zeeman interaction term was given above. Similar to the -1 charge state, there are 6 splittings for each branch from the nuclear Zeeman and magnetic hyperfine interaction terms, which split the $m_I = \pm\frac{1}{2}, \pm\frac{3}{2}, \pm\frac{5}{2}$ levels. See Figure 7.5 for the full level structure along with calculated values.

7.3.4 Potential Measurement Scheme

Here, we attempt to provide a general description of how a measurement using this defect could be carried out. In a typical nuclear Schiff moment search using diamagnetic atoms, a small bias magnetic field is applied to provide a quantization axis for the nuclear spin states. The magnitude of the magnetic field is chosen to be large enough to overwhelm residual magnetic fields but small enough to be generated by a low current source that can be made very stable in time. Once polarized, the nuclear spins can be readily oriented perpendicular to the magnetic field causing them to precess. This precession frequency is straightforward to measure and provides direct access to the energy

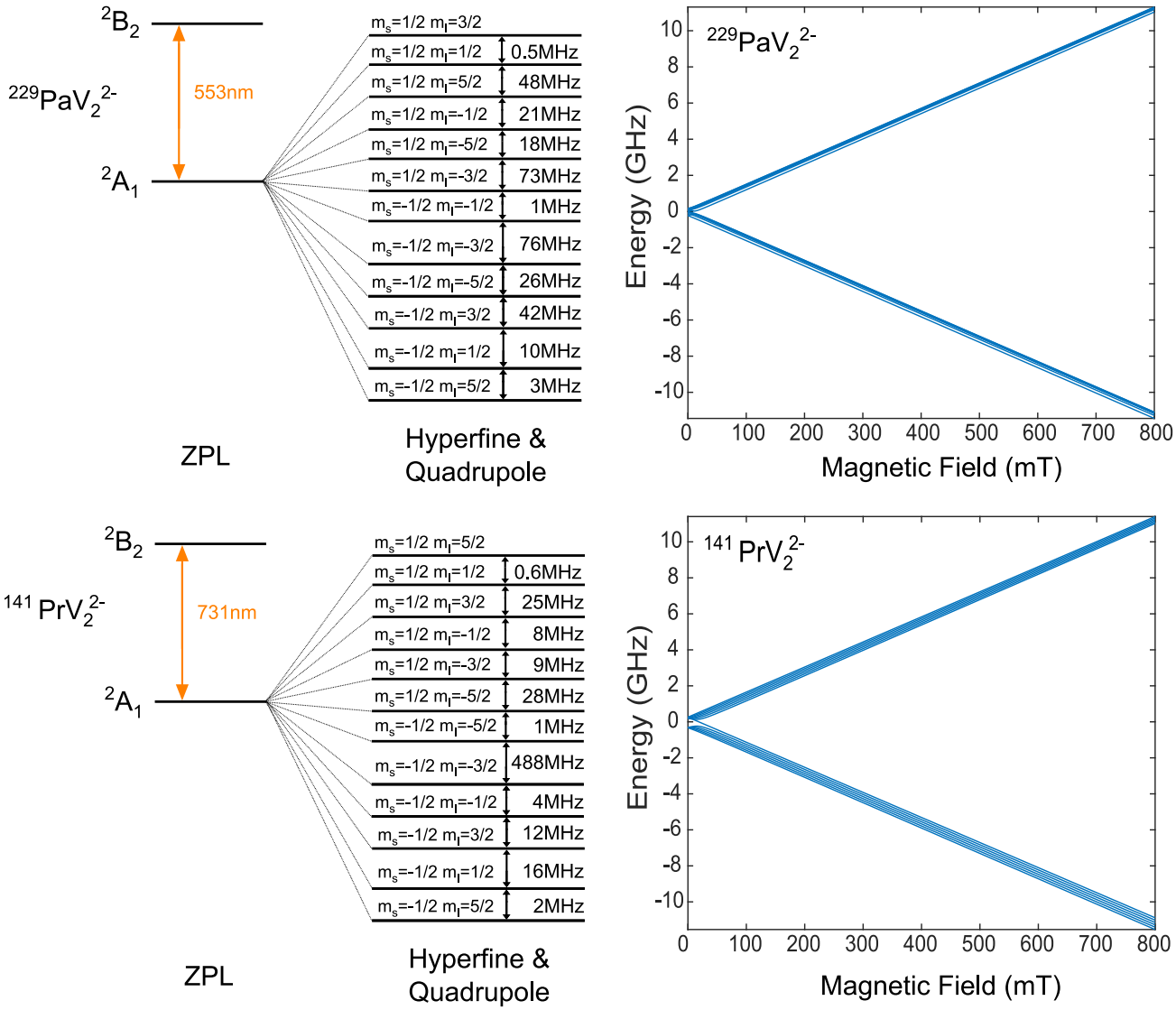

Figure 7.5 Electronic level structure with and without an applied magnetic field in the z-direction for the -2 charge states of $^{229}PaV_2$ and $^{141}PrV_2$. The magnetic field plots were simulated using EasySpin [338].

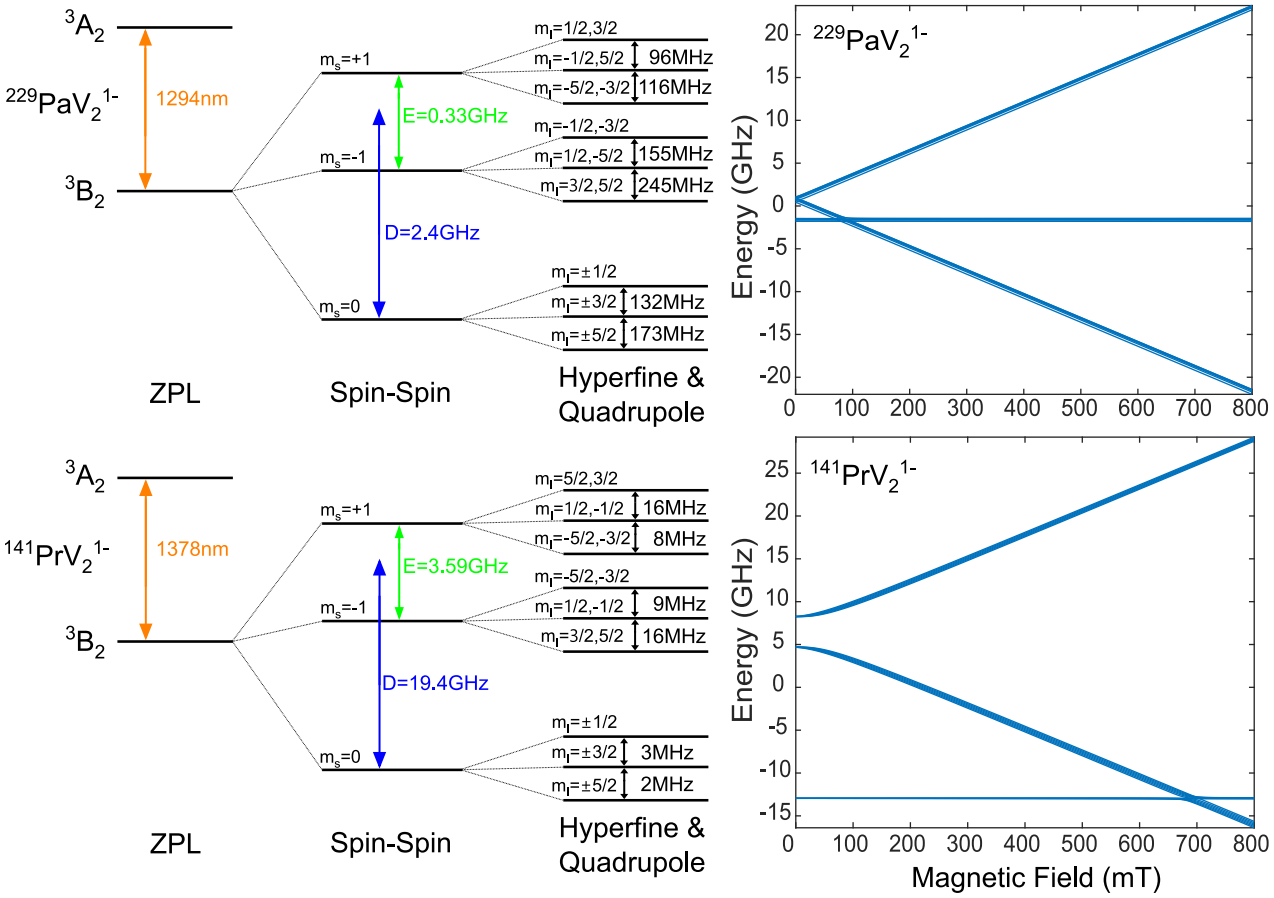

Figure 7.6 Electronic level structure with and without an applied magnetic field in the z-direction for the -1 charge states of $^{229}PaV_2$ and $^{141}PrV_2$. The magnetic field plots were simulated using EasySpin [338].

difference between two nuclear spin states. If there were a non-zero nuclear Schiff moment, then this would induce an atomic electric dipole moment (EDM) which would couple to an external electric field causing a shift in both the energy levels and the spin precession frequency. The shift due to the EDM can then be isolated by flipping the direction of the electric field relative to the magnetic field from parallel to antiparallel. This measurement protocol crucially relies on the magnetic field being very uniform and very stable to minimize systematic effects.

For the case of isotopes embedded in optical crystals, in this case diamond, the quantization axis is provided by the internal structure and symmetry of the defect itself. The energy difference between the two nuclear spin states can be measured using RF spectroscopy. The electric field "reversal" in this case is realized by studying two sub-ensembles of defects with dipole moments oriented along opposite crystal directions (e.g. $\langle 111 \rangle$ and $\langle \bar{1}\bar{1}\bar{1} \rangle$. The general idea is to measure the energy difference between two nuclear spin states for the two sub-ensembles separately and then to subtract them to isolate the component due to the EDM. More rigorous discussions of schemes for how this measurement protocol could be carried out in similar systems have been articulated in [276, 330]. It should also be noted that preferential alignment of groups of defects has been demonstrated for NV centers in diamond and could potentially be applied here [339].

	Sym.	A_{xx}	A_{yy}	A_{zz}	V_{xx}	V_{yy}	V_{zz}	D_x	D_y	D_z
$^{229}PaV_2^{2-}$	$^2A_1$	-76.5	-71.6	89.2	422	81.2	-504	–	–	–
$^{141}PrV_2^{2-}$	$^2A_1$	179	152	208	-199	-135	334	–	–	–
$^{229}PaV_2^{1-}$	$^3B_2$	62.8	1.45	75.9	750	119	-870	-713	-898	1611
$^{141}PrV_2^{1-}$	$^3B_2$	113	99.2	121	491	16.9	-507	-4696	-8255	12951

Table 7.2 Ground-state symmetry labels, hyperfine coupling parameters (A_{xx}, A_{yy}, A_{zz}) in MHz, electric field gradient tensor components (V_{xx}, V_{yy}, V_{zz}) in V/Å^2, and zero-field splitting tensor components (D_x, D_y, D_z) (for $S = 1$) in MHz for the -2 and -1 charge states. All quantities were calculated using the HSE06 functional except the zero-field splitting tensor, which was computed using the PBE functional.

7.3.5 Estimated EDM Sensitivity

To provide a first estimate of the sensitivity of these defects for nuclear Schiff moment and EDM measurements, we focus on the effective internal field generated by their non-inversion symmetric structure. To do this, we first attempt to estimate the differential dipole moment, $\Delta\mu$, and polarizability, $\Delta\alpha$, between the ground and excited states. We take an approach proposed by [330,

340] where the Stark shift of the ZPL can be modeled by:

$$\Delta E_{\mathrm{ZPL}} = -\frac{1}{\epsilon_s}\Delta\mu E - \frac{1}{2\epsilon_s^2}\Delta\alpha E^2, \tag{7.8}$$

where E is an applied electric field perturbing the defect, and ϵ_s is the static dielectric constant of the material which we take as 5.7 for diamond [256]. Using this, we calculate the ZPL at varying applied electric field strengths and fit the equation above to the resulting ZPL energy changes. We performed these calculations for both the -1 and -2 charge state for the $^{229}PaV_2$ defects. The VASP applied electric field is in units of eV/Å, so the resulting $\Delta\mu$ is initially in units of eÅ and $\Delta\alpha$ is in units of m^2e/V. We also provide these values in the other typically quoted units of Debye for differential dipole moment and a_0^3 for differential polarizability (see Table 7.3).

With these values in hand, we can make an estimate for the internal effective electric field within the crystal. To do this, we use the following equation:

$$E_{\mathrm{eff}}^{\mathrm{electron}} = \left(\frac{1}{4\pi\epsilon_0}\right)\left(\frac{\Delta\mu}{Z_{\mathrm{scale}}^3}\right), \tag{7.9}$$

where, $\epsilon_0 = 8.85 \times 10^{-12}$ [F/m] is the permittivity of free space, and $Z_{scale} = 1$Å is a length scale estimate for the volume. Importantly, the dipole moments used in the equation for differential dipole moment are not the EDM that is measured for fundamental symmetry breaking. It is the overall induced dipole because of the effective electric field within the non-inversion symmetric defect. With this, we can obtain a rough estimate for the effective electric field experienced by an electron within the defect. This estimate for the effective electric field is for the electrons, but for nuclear Schiff moment experiments, the relevant quantity is the effective electric field for the nucleus. In order to translate the effective electric field from the electrons to the nucleus, we referred to typical calculations for the effective internal electric field in polar diatomic molecules. In molecules of this type, the effective electric field for electron EDM is 10 GV/cm while the effective electric field for the nuclear Schiff moment is 0.1 GV/cm. One example of these calculations are for RaF [341]. We apply this heuristic for the calculations presented for Pa ions in diamonds by dividing the value we found for electrons by 100 to get an estimate for the nucleus. Lastly, it should be noted that the method used to calculate the effective electric field tends to overestimate the effective electric field strength by a factor of 10 [340].

Outside of these values for an effective field and differential polarizability, the defects have several other advantages. One such advantage is that the angular momentum is zero, so this greatly reduces their coupling to the lattice, enabling narrow optical linewidths. Furthermore, in the case of the -1 charge state, it features a spin-1 triplet, which should extend its coherence time because there will be limited coupling to the spin-1/2 bath within diamond, similar to the NV center.

	$\Delta\mu$		$\Delta\alpha$		$E_{\text{eff}}^{\text{electron}}$	$E_{\text{eff}}^{\text{nucleus}}$
	(eÅ)	(D)	(Å^{2}e/V)	(a_0^3)	(MV/cm)	(MV/cm)
$^{229}PaV_2^{2-}$	0.065	0.313	1.536	148.47	94	0.94
$^{229}PaV_2^{1-}$	0.105	0.503	0.458	44.27	151	1.51

Table 7.3 Differential dipole moments and polarizabilities in two unit systems (VASP output units and commonly quoted units). Also shown are the effective electric fields experienced by the electron and the shielded field experienced by the nucleus.

7.4 Conclusion

We have identified the $^{229}PaV_2$ defect in diamond as a promising candidate for tests of fundamental symmetry violations. It lacks inversion symmetry, which allows for heightened EDM sensitivity and can also inhabit a number of negatively-charged states, which have similar Fermi levels to the NV center, enabling co-magnetometry with NV centers. Multiple optical transitions which can be captured with laser spectroscopy techniques were identified. Furthermore, a large effective electric field was calculated. Moreover, while production of ^{229}Pa will occur at the Facility for Rare Isotope Beams, we have also identified a stable lanthanide-containing defect in the form of $^{141}PrV_2$ defects in diamond, for which we have identified ground to excited state configurations and transitions that are qualitatively identical to those of the $^{229}PaV_2$. This will facilitate experimental method development. While not considered here, the effect of applied electric fields or strain could also serve to enhance the dipole moment and the Hamiltonian terms should be explored in the future. Overall, this work establishes the concept of using rare isotopes embedded within diamond for tests of fundamental symmetries. Additionally, it highlights the potential of applying well-developed quantum control schemes to the search for a nuclear Schiff moment. This approach may also be applicable to other more stable isotopes which may also have octupole deformations [342, 343] in other types of optical crystals [330]. Additionally, there are similar proposals that can be found in [330].

Chapter 8

Summary and Outlook

8.1 Summary

This thesis has introduced the NiV^- as a strong candidate for use in both quantum networking and quantum computing applications. It has confirmed the electronic structure of the NiV^-, consisting of an excited-state orbital singlet with spin $1/2$ and a ground-state orbital doublet with spin $1/2$, with a large spin-orbit splitting in the ground state. Coherence measurements have shown that this large ground state splitting is sufficient to make phonon-induced decoherence not a problem at 1.65K. In addition, the NiV^- was shown to possess excellent optical properties, including a large Debye-Waller factor of 0.62 and lifetime-limited optical linewidths. Charge-state control of the NiV^- was also demonstrated using a Fermi-level-engineered all-diamond p-i-p device operated at cryogenic temperatures. With this, the local charge state could be probed and the NiV^{2-} was identified as the dark state, which in the absence of charge state control, becomes populated under resonant excitation. Coherent population trapping was achieved with the lowest spin sublevels in both the p-i-p sample as well as the nanopillar sample. Moreover, coherent all-optical control was achieved using two-photon Raman transitions and Rabi oscillations and Ramsey fringes were both observed with a $T_2^* = 286$ ns extracted. This time was extended further by using a Hahn-Echo sequence to achieve a $T_2^{\text{echo}} = 126\,\mu$s. This shows that at 1.65 K, the dominant limitation is not phonon-induced decoherence, but rather slowly varying magnetic-field noise arising from the ^{13}C nuclear spin bath.

8.2 Outlook

This outlook section reviews multiple different natural next steps and future directions for the NiV. It starts with extending the coherence time further using CPMG dynamical decoupling techniques, and then goes into deterministic creation of NiV^- centers; then it moves to improved charge-state stabilization techniques, cavity coupling, and increased photon collection efficiency.

Next, it discusses single-shot readout and reconfigurable nodes enabled by fast-switching magnetic-field topologies. After that, it turns to quantum frequency conversion and the generation of indistinguishable photons, followed by coupling to nearby nuclear spins. Finally, it closes with a discussion of early quantum networking applications which could be used with the NiV.

8.2.1 Extending Coherence Times with CPMG or Isotopic Purification

Given that the Hahn-Echo sequence was able to extend the coherence time, it is natural to expect a similar lengthening by extending the sequence with even more refocusing π pulses used in CPMG sequences. These should be performed at longer delay times and the corresponding coherence times should be measured. Scaling of the coherence time with the number of π pulses could also be extrapolated from this to determine theoretical limits of coherence time. Phonon-induced decoherence is expected to become an issue again at tens of ms, but this could be measured quantitatively using longer and longer CPMG sequences. Furthermore, the source of different noise types can be inferred based on the fits. Moreover, different dynamical decoupling sequences could be explored beyond CPMG. In particular, the XY family of sequences [344, 345], which use combinations of π-pulses around different axes (x-rotation, then y-rotation). Because these pulses use different rotation axes, they are more resilient to pulse length errors. In addition to CPMG, removing the ^{13}C nuclear spin bath by growing with isotopically enriched ^{12}C pre-cursors can also extend coherence times. Indeed, by removing the source of the noise, shorter DD sequences will likely go further in terms of extending the time.

8.2.2 Deterministic creation of NiV^-

Another area to explore is the deterministic creation of NiV centers. This is an important aspect for any qubit type, but especially because most scalable architectures for solid state qubits require the use of nanophotonic structures and precise placement of defects within cavities. One method is simply to create a certain defect density, either by CVD growth or ion implantation and then create structures throughout the sample. However, the resulting location of the defects will be random and as such coupling to the cavity may be worse. Laser writing is a promising approach which may be able to achieve an advantage over this. It has much higher spatial resolution (diffraction limited) than ion implantation and creation of defects in pre-fabricated structures has already been demonstrated [210, 346]. The main requirement for laser writing to work is that the impurity atom already be within the substrate material, ideally isolated and taking up either a substitutional or interstitial position. This is preferred because the laser writing process can break the bonds and cause a nearby vacancy to migrate over, forming the vacancy complex. In principle, this should be possible for nickel which has a substitutional defect that has been observed experimentally in

optical and electrical studies [171, 183, 347–349]. The Ni_s has been associated with a 2.56 eV absorption line [171] and it has been shown that the concentration of this absorption compared to NiV^- absorption can be varied by changing the concentration of nitrogen getter during diamond synethesis [155]. As such, it may be possible to preferentially grow samples with predominantly Ni_s with low amounts of NiV contained within. Importantly, different techniques may be recommended or should be explored as doping with nitrogen can introduce substitutional nitrogen or P_1 centers, which can limit spin coherence times owing to their electron spin S = $1/2$ [350]. Regardless, there may be other mechanisms by which subsitutional Ni can be formed over the vacancy complex.

8.2.3 Charge State Stabilization

Another area, which is slightly more developed but which might benefit from continued research is in the stabilization of the NiV^- charge state. While the all-diamond p-i-p structure already provides effective charge-state stabilization. New device architectures such as p-i-n diodes for example, could be of interest, as they offer larger ranges over which Fermi level can be tuned. Indeed, while the p-i-p device can only bring the Fermi level down, a p-i-n diode can do that and also bring it up. This could potentially increase the probability for stabilizing a wider range of NiV emitters based on their placement with respect to the diode. Additionally, it may also provide a stronger knob for adjusting the ZPL frequency via the DC Stark effect, potentially easing the requirement for indistinguishable photons. Furthermore, by determining the bias voltage values which correspond to NV charge state switching within these diodes, this could provide a way to calculate the actual charge transition levels for the NiV^-. This would be similar to what has been done in [252]. Importantly; however, reliable n-type doping in diamond remains incredibly difficult because donor activation energies are large (0.6 eV for phosphorus) and P-doped growth has a tendency to create compensating defects [251, 351, 352], leading to very low free carrier densities even at room temperature. At cryogenic temperatures, this problem may become even more severe, potentially limiting conduction and reducing the effectiveness of an n-type contact layer. Because of this, it remains an open question whether p-i-n devices can outperform p-i-p structures under the low-temperature conditions needed for NiV experiments.

An additional question is how to integrate such charge control architectures into nanophotonic structures such as nanopillars, waveguides, and cavities in a scalable way that allows for many nodes on a single chip. There is already substantial literature on embedding diode structures into quantum dot and color center platforms, which provides a useful starting point for this effort. For example growth of p, i, and n-type layers vertically and then dry etching to create pillars, with mesa structures attached nearby to electrically contact the devices. Overall, there remain ample open questions to be explored with regard to charge state stability for defects in devices.

8.2.4 Cavity Coupling and Increasing Collection Efficiency

Another important issue, alluded to above, is coupling the NiV to photonic structures. In emission based schemes this is critical because it enhances collection efficiencies (already low in diamond) and decreases excited state lifetimes through the Purcell effect [173]. In absorption based schemes, this is also needed to ensure incoming photons interact with the defect and get absorbed. Without such cavities, the probability of a single photon being absorbed by the defect is quite low. Cavities built around the defect ensure the photon can reflect within and increase the number of interactions, greatly improving the probability for absorption. Additionally, in emission, the mode of the cavity can determine many of the outgoing photon properties, effectively ensuring that indistinguishable photons are produced. The degree to which it improves this coupling probability is referred to as the quality factor of the cavity. There are a few general guidelines for designing cavities. For enhancement of the spontaneous emission rate, via the Purcell effect, one wants a maximum $Q/V^{1/2}$, where V is the mode volume of the cavity, and Q is the quality factor [353]. For strong coupling needed for absorption schemes, which rely on cavity quantum electrodynamics, maximizing $g/\kappa \sim Q/V^{1/2}$ where g is the defect-cavity coupling rate and κ is the cavity leak rate. Additionally maximizing $g/\gamma \sim 1/V^{1/2}$, where γ is the defect decay rate, is also important [353]. Because the wavelength in a dielectric is shortened by a factor of the index of refraction λ/n, the smallest volume light can be confined in a 3D volume is roughly $V = (\frac{\lambda}{n})^3$, where $n = 2.4$ in diamond. For short wavelengths, this can make achieving the smallest mode volume challenging because the nanofabrication required is more challenging. Because the NiV has a ZPL wavelength at 883 nm, this requirement is relaxed compared to shorter wavelength defects like SiV and NV. While much proof-of-principle work has been done with defects in diamond [173, 354, 355], this has yet to be extended to NiV and as such provides a large opportunity for exploration. Without it, entanglement generation rates will be limited by coupling efficiency.

Another question is the degree to which proximity to surfaces interrupts NiV functionality. One problem, which can arise is surface spins often associated with carbon dangling bonds and other paramagnetic defects, could fluctuate more rapidly than the surrounding ^{13}C nuclear spin bath and therefore contribute additional dephasing. Additionally, spectral diffusion and or charge state switching could become more of a problem, so ensuring the cavities can be built alongside charge state control mechanisms is critical. However, given that long coherence times could be achieved within the p-i-p sample in which the NiVs wer =e roughly 50 nm from the surface, it is a good indicator that integration into photonic structures won't prove a problem. Additionally, the defects remained functional within nanopillars with average distances to the surface at around 200 nm.

Something else potentially worth attempting to measure is the quantum efficiency of the NiV. In particular, determining the degree to which non-radiative decay channels dominate emission compared to radiative rates. As we are interested in radiative rates, if this can be improved, it

should be pursued. The measured count rates are not dissimilar to what has been measured in other defects in diamond at the single emitter level, especially considering that the current experiments are performed in bulk diamond and that standard detectors are usually much less efficient in the near-infrared than at visible wavelengths. At the same time, because the NiV optical transition occurs at lower energy than many other diamond defects, non-radiative channels may play a comparatively larger role. Directly measuring the quantum efficiency of the defect would therefore provide an important measure.

8.2.5 Single Shot Readout and Reconfigurable Nodes

A central requirement of quantum applications is the ability to perform high-fidelity single shot readout, ideally in a way which does not destroy the coherence of the system. For the NiV, optical spin pumping is easy with an off-axis magnetic field. The question, then is how to switch that off-axis magnetic field off so that the system reverts to its purely cycling transitions. This is how high fidelity readout is done in other diamond defects [117, 145, 356]. This could be realized using fast switching circuits which can quickly turn on and off an in-plane magnetic field. For an NiV aligned to the $\langle 111 \rangle$ direction, this should already be relatively aligned with the direction of the magnetic field and as such the excited state spin quantization axis should not have tilted too much to the point in which single shot readout is impossible with just a magnetic field applied in the upward direction. Then, an in-plane magnetic field could be applied which tilts the excited state spin quantization axis and enables optical spin pumping, and superposition preparation between the two spin ground states. In this way, a quickly reconfigurable node can be achieved which can be switched between spin pumping and cycling. This is something which is challenging for the SiV and heavier group-IV centers because to achieve efficient spin pumping requires slightly larger in-plane fields and so making devices becomes more challenging. Additionally, modifying either the off-cut angle or introducing an angle to ensure the on-axis field is as on-axis as possible to ensure that high fidelity single shot readout can be achieved could also be a solution.

8.2.6 Quantum Frequency Conversion and Indistinguishable Photons

Another avenue which needs to be explored for NiV to be useful in any quantum network is the efficiency with which the ZPL photons, useful for two photon interference, can be quantum frequency converted to the telecom-c band. As mentioned in Chapter 1, this can in theory be done in a low-noise regime via difference frequency generation in which 883nm is mixed with a 2050 nm tunable Thulium laser to produce 1550 nm light. Coherence maintaining frequency conversion of similar wavelengths with internal efficiencies exceeding 90% have been achieved before [357]. The main requirement are a good nonlinear crystal which can be used for proper phase matching.

Something else to explore is the degree to which two photon interference can be achieved and the number of tuning knobs which are available should one have two spectrally distinguishable NiV's. The Thulium laser can in theory be tuned over nm ranges, allowing for a control parameter to achieve indistinguishable photons. Additionally cavity integration to some extent solves this issue because only photons with a resonant frequency dependent on the size of the cavity will actually constructively interfere and be able to escape the cavity. Another more direct approach is DC Stark tuning, in which an applied electric field shifts the optical transition frequency of the emitter. While these approaches do nothing to eliminate the underlying inhomogeneous distribution, they do provide practical means to compensate for it. Encouragingly, we also observe cases where two spatially separated emitters have resonance frequencies that differ by only a few hundred MHz, as shown in Fig. 8.1. This detuning is well within the range typically achievable by DC Stark tuning, indicating that suitable pairs of spectrally compatible emitters can be found even without active tuning. This was observed in the p-i-p sample of which no high-pressure high temperature annealing was performed and as such suggests that it can be possible even without the highest degree of annealing. Looking forward, alternative fabrication approaches such as laser writing of defects may further suppress lattice damage and potentially reduce the inhomogeneous distribution even more, possibly relaxing annealing requirements. Ongoing efforts to reduce this inhomogeneous broadening, for example through optimized growth and annealing protocols [358], are therefore directly relevant to improving the scalability of NiV^--based quantum photonic platforms.

8.2.7 Coupling to Nuclear Spins

Another area of exploration is how to couple NiVs to long-lived nuclear spin states. This is an important advantage that solid state spins have access to, namely, that electron spins can interface readily with nearby nuclear spins. This allows the use of a fast electron spin for interaction with incoming light and transmission of quantum states while the nuclear spins can serve as long lived memories owing to their 3-orders of magnitude smaller magnetic moment and hence much more isolated spin state. This can be used in quantum computing applications or quantum networking situations in which quantum states or entanglement needs to be stored. Interfacing with nuclear spins has been demonstrated with NV centers, SiV centers, GeV centers and SnV centers using both ^{13}C nuclear spins and also isotopes of the impurity defect. The upside of using isotopes of the impurity defect is the electron spin comes inherently packaged with a nuclear spin with a relatively well-defined coupling strength. Nickel has multiple stable isotopes with some featuring non-zero nuclear spin values. For example, ^{61}Ni is a stable isotope with a nuclear spin $I = 3/2$.

One challenge with coupling these systems is that while nuclear spins feature long spin coherence times, electron spin coherence times are much shorter. The coupling between the two can thus

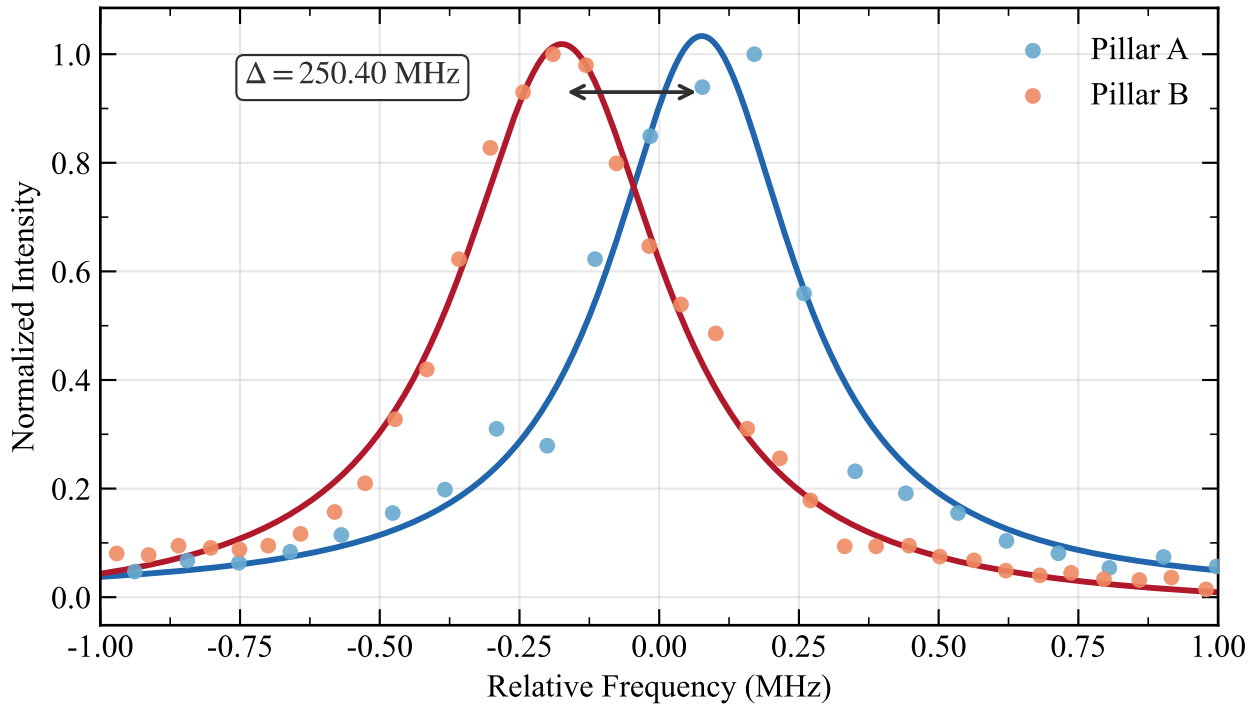

Figure 8.1 Resonant PLE spectra for two distinct emitters in different pillars which are close in resonant frequency, with the extracted delta between the two peak centers shown in the figure. This was taken at 1.6 K and a power of 4 μW of resonant light along with 1 μW of green light was used. This was taken in the p-i-p sample.

erode the long spin coherence time of the nuclear spin eventually causing it to be closer to that of the electron spin. Hence, methods related to charge state switching between states which have zero electron spin and the charge state with an electron spin are of interest. In particular, using the non-zero electron spin state to perform coupling and transmission of quantum states or entanglement and then whenever the nuclear spins are employed as quantum memories, the charge state is switched to one featuring zero electron spin state or a different spin state which weakens the coupling in a predictable fashion. This can allow the nuclear spin to remain coherent for the longer timescale it has available to it. This could be applicable to NiV in the sense that it is incredibly easy to turn it off or convert it to the dark NiV^{2-} state which is optically dark and features a S=0 spin state in the ground state [171]. Hence, turning the bias voltage off could enable switching to this charge state and because it has no electron spin, there would be no accelerated decoherence from the nuclear spin.

8.2.8 Alternative Charge States

It has already been mentioned in Chapter 1 that the neutral NiV^0 has a spin-1 ground state and as such may feature similar electronic properties to the NV. While it is challenging to identify these neutral defects and requires careful doping. There may be potential to observe it in the boron-doped regions of the p-i-p device and or by application of bias voltage.

8.2.9 Conclusion

In summary, there are many avenues of future research potential which can be explored with the NiV^-. Whether it is extending the coherence times or exploring different noise sources or creating NiVs deterministically with laser writing, the list is filled with opportunity.

APPENDIX

Test Appendix

REFERENCES

[1] Jonathan P Dowling and Gerard J Milburn. "Quantum technology: the second quantum revolution". In: *Philosophical Transactions of the Royal Society of London. Series A: Mathematical, Physical and Engineering Sciences* 361.1809 (2003), pp. 1655–1674.

[2] Bengt Nordén. "Quantum entanglement: facts and fiction–how wrong was Einstein after all?" In: *Quarterly Reviews of Biophysics* 49 (2016), e17.

[3] Peter W Shor. "Polynomial-time algorithms for prime factorization and discrete logarithms on a quantum computer". In: *SIAM review* 41.2 (1999), pp. 303–332.

[4] James R. Powell. "The Quantum Limit to Moore's Law". In: *Proceedings of the IEEE* 96.8 (Aug. 2008), pp. 1247–1248. ISSN: 0018-9219, 1558-2256. DOI: 10.1109/JPROC.2008.925411. URL: http://ieeexplore.ieee.org/document/4567410/ (visited on 04/25/2023).

[5] Andreas Bayerstadler et al. "Industry quantum computing applications". In: *EPJ Quantum Technology* 8.1 (2021), p. 25.

[6] Christian L Degen, Friedemann Reinhard, and Paola Cappellaro. "Quantum sensing". In: *Reviews of modern physics* 89.3 (2017), p. 035002.

[7] Zheshen Zhang and Quntao Zhuang. "Distributed quantum sensing". In: *Quantum Science & Technology* 6.4 (2021), p. 043001.

[8] Ryan S. Cassel, William G. Tobias, and Bonnie L. Marlow. *Quantum vs. Classical Complementary PNT: Are Quantum Sensors the Next Big Thing for PNT, or Are They Overhyped?* Tech. rep. Updated March 2023. MITRE, Feb. 2023. URL: https://www.mitre.org/sites/default/files/2024-06/PR-23-0577-Quantum-vs-Classical-Complementary-PNT.pdf.

[9] Vittorio Giovannetti, Seth Lloyd, and Lorenzo Maccone. "Quantum-enhanced measurements: beating the standard quantum limit". In: *Science* 306.5700 (2004), pp. 1330–1336.

[10] Stephanie Wehner, David Elkouss, and Ronald Hanson. "Quantum internet: A vision for the road ahead". In: *Science* 362.6412 (2018), eaam9288.

[11] Barry M Leiner et al. "The past and future history of the Internet". In: *Communications of the ACM* 40.2 (1997), pp. 102–108.

[12] Antonio Acín et al. "The quantum technologies roadmap: a European community view". In: *New Journal of Physics* 20.8 (Aug. 2018), p. 080201. ISSN: 1367-2630. DOI: 10.1088/1367-2630/aad1ea. URL: https://iopscience.iop.org/article/10.1088/1367-2630/aad1ea (visited on 04/25/2023).

[13] Brian Barrett. *You're Not Ready for Quantum Cracking*. Accessed 2026-03-31. Wired. June 2025. URL: https://www.wired.com/story/youre-not-ready-quantum-cracks/.

[14] Wing H Wong. "Timing attacks on RSA: revealing your secrets through the fourth dimension". In: *XRDS: Crossroads, The ACM Magazine for Students* 11.3 (2005), pp. 5–5.

[15] Charles H Bennett and Gilles Brassard. "Quantum cryptography: Public key distribution and coin tossing". In: *Theoretical computer science* 560 (2014), pp. 7–11.

[16] William K Wootters and Wojciech H Zurek. "The no-cloning theorem". In: *Physics Today* 62.2 (2009), pp. 76–77.

[17] Daniel J Lum et al. "Quantum enigma machine: Experimentally demonstrating quantum data locking". In: *Physical Review A* 94.2 (2016), p. 022315.

[18] Harry Buhrman et al. "Quantum fingerprinting". In: *Physical review letters* 87.16 (2001), p. 167902.

[19] David D Awschalom et al. "Challenges and opportunities for quantum information hardware". In: *Science* 390.6777 (2025), pp. 1004–1010.

[20] Anne Broadbent, Joseph Fitzsimons, and Elham Kashefi. "Universal blind quantum computation". In: *2009 50th annual IEEE symposium on foundations of computer science*. IEEE. 2009, pp. 517–526.

[21] Isaac L Chuang. "Quantum algorithm for distributed clock synchronization". In: *Physical review letters* 85.9 (2000), p. 2006.

[22] Peter Komar et al. "A quantum network of clocks". In: *Nature Physics* 10.8 (2014), pp. 582–587.

[23] Harry Buhrman, Richard Cleve, and Wim Van Dam. "Quantum entanglement and communication complexity". In: *SIAM Journal on Computing* 30.6 (2001), pp. 1829–1841.

[24] Daniel Gottesman, Thomas Jennewein, and Sarah Croke. "Longer-baseline telescopes using quantum repeaters". In: *Physical review letters* 109.7 (2012), p. 070503.

[25] Arian J Stolk et al. "Metropolitan-scale heralded entanglement of solid-state qubits". In: *Science advances* 10.44 (2024), eadp6442.

[26] Shi-Hai Wei et al. "Towards real-world quantum networks: a review". In: *Laser & Photonics Reviews* 16.3 (2022), p. 2100219.

[27] Koji Azuma et al. "Quantum repeaters: From quantum networks to the quantum internet". In: *Reviews of Modern Physics* 95.4 (2023), p. 045006.

[28] Maximilian Ruf et al. "Quantum networks based on color centers in diamond". en. In: *Journal of Applied Physics* 130.7 (Aug. 2021), p. 070901. ISSN: 0021-8979, 1089-7550. DOI: 10.1063/5.0056534. URL: https://aip.scitation.org/doi/10.1063/5.0056534 (visited on 05/11/2022).

[29] Anasua Chatterjee et al. "Semiconductor qubits in practice". en. In: *Nature Reviews Physics* 3.3 (Mar. 2021), pp. 157–177. ISSN: 2522-5820. DOI: 10.1038/s42254-021-00283-9. URL: http://www.nature.com/articles/s42254-021-00283-9 (visited on 07/27/2022).

[30] Evan Meyer-Scott, Christine Silberhorn, and Alan Migdall. “Single-photon sources: Approaching the ideal through multiplexing”. en. In: *Review of Scientific Instruments* 91.4 (Apr. 2020), p. 041101. ISSN: 0034-6748, 1089-7623. DOI: 10.1063/5.0003320. URL: https://pubs.aip.org/aip/rsi/article/1030773 (visited on 04/25/2023).

[31] Marco Petrovich et al. “Broadband optical fibre with an attenuation lower than 0.1 decibel per kilometre”. In: *Nature Photonics* 19.11 (2025), pp. 1203–1208.

[32] ME Lines. “Scattering losses in optic fiber materials. I. A new parametrization”. In: *Journal of applied physics* 55.11 (1984), pp. 4052–4057.

[33] Junqiu Liu et al. “High-yield, wafer-scale fabrication of ultralow-loss, dispersion-engineered silicon nitride photonic circuits”. In: *Nature communications* 12.1 (2021), p. 2236.

[34] Gerd Keiser. “Fiber optic communication networks”. In: *Fiber Optic Communications*. Springer, 2021, pp. 507–575.

[35] P. Kumar. “Quantum frequency conversion”. In: *Optics Letters* 15.24 (1990), pp. 1476–1478. DOI: 10.1364/OL.15.001476.

[36] Sebastian Zaske et al. “Visible-to-telecom quantum frequency conversion of light from a single quantum emitter”. In: *Physical review letters* 109.14 (2012), p. 147404.

[37] Matthias Bock et al. “High-fidelity entanglement between a trapped ion and a telecom photon via quantum frequency conversion”. In: *Nature communications* 9.1 (2018), p. 1998.

[38] Anshuman Singh et al. “Quantum frequency conversion of a quantum dot single-photon source on a nanophotonic chip”. In: *Optica* 6.5 (2019), pp. 563–569.

[39] Jason S. Pelc et al. “Long-wavelength-pumped upconversion single-photon detector at 1550 nm: performance and noise analysis”. In: *Optics Express* 20.17 (2012), pp. 19075–19084. DOI: 10.1364/OE.20.019075.

[40] Jason S. Pelc et al. “Influence of domain disorder on parametric noise in quantum frequency converters”. In: *Optics Letters* 36.6 (2011), pp. 864–866. DOI: 10.1364/OL.36.000864.

[41] Jason S Pelc et al. “Long-wavelength-pumped upconversion single-photon detector at 1550 nm: performance and noise analysis”. In: *Optics express* 19.22 (2011), pp. 21445–21456.

[42] V Krutyanskiy et al. “Polarisation-preserving photon frequency conversion from a trapped-ion-compatible wavelength to the telecom C-band”. In: *Applied Physics B* 123.9 (2017), p. 228.

[43] C. K. Hong, Z. Y. Ou, and L. Mandel. “Measurement of subpicosecond time intervals between two photons by interference”. en. In: *Physical Review Letters* 59.18 (Nov. 1987), pp. 2044–2046. ISSN: 0031-9007. DOI: 10.1103/PhysRevLett.59.2044. URL: https://link.aps.org/doi/10.1103/PhysRevLett.59.2044 (visited on 04/25/2023).

[44] Frédéric Bouchard et al. “Two-photon interference: the Hong–Ou–Mandel effect”. In: *Reports on Progress in Physics* 84.1 (Jan. 2021), p. 012402. ISSN: 0034-4885, 1361-6633. DOI: 10.1088/1361-6633/abcd7a. URL: https://iopscience.iop.org/article/10.1088/1361-6633/abcd7a (visited on 04/25/2023).

[45] T. Gerrits et al. “Spectral correlation measurements at the Hong-Ou-Mandel interference dip”. en. In: *Physical Review A* 91.1 (Jan. 2015), p. 013830. ISSN: 1050-2947, 1094-1622. DOI: 10.1103/PhysRevA.91.013830. URL: https://link.aps.org/doi/10.1103/PhysRevA.91.013830 (visited on 04/25/2023).

[46] C Lang et al. “Correlations, indistinguishability and entanglement in Hong–Ou–Mandel experiments at microwave frequencies”. In: *Nature Physics* 9.6 (2013), pp. 345–348.

[47] Xiang-Bin Wang. “Beating the photon-number-splitting attack in practical quantum cryptography”. In: *Physical review letters* 94.23 (2005), p. 230503.

[48] Alison E Rugar et al. “Quantum photonic interface for tin-vacancy centers in diamond”. In: *Physical Review X* 11.3 (2021), p. 031021.

[49] Johannes Borregaard, Anders Søndberg Sørensen, and Peter Lodahl. “Quantum networks with deterministic spin–photon interfaces”. In: *Advanced Quantum Technologies* 2.5-6 (2019), p. 1800091.

[50] Ravitej Uppu et al. “On-chip deterministic operation of quantum dots in dual-mode waveguides for a plug-and-play single-photon source”. en. In: *Nature Communications* 11.1 (July 2020), p. 3782. ISSN: 2041-1723. DOI: 10.1038/s41467-020-17603-9. URL: https://www.nature.com/articles/s41467-020-17603-9 (visited on 04/25/2023).

[51] Farzan Jazaeri et al. “A review on quantum computing: From qubits to front-end electronics and cryogenic MOSFET physics”. In: *2019 MIXDES-26th International Conference" Mixed Design of Integrated Circuits and Systems"*. IEEE. 2019, pp. 15–25.

[52] John Hannegan et al. “C-band single photons from a trapped ion via two-stage frequency conversion”. In: *Applied Physics Letters* 119.8 (2021).

[53] Jacob P Covey, Harald Weinfurter, and Hannes Bernien. “Quantum networks with neutral atom processing nodes”. In: *npj Quantum Information* 9.1 (2023), p. 90.

[54] Jacob P Covey et al. “Telecom-band quantum optics with ytterbium atoms and silicon nanophotonics”. In: *Physical Review Applied* 11.3 (2019), p. 034044.

[55] John Clarke and Frank K Wilhelm. “Superconducting quantum bits”. In: *Nature* 453.7198 (2008), pp. 1031–1042.

[56] P. Krantz et al. “A quantum engineer’s guide to superconducting qubits”. en. In: *Applied Physics Reviews* 6.2 (June 2019), p. 021318. ISSN: 1931-9401. DOI: 10.1063/1.5089550. URL: http://aip.scitation.org/doi/10.1063/1.5089550 (visited on 01/04/2023).

[57] Mohammad Mirhosseini et al. “Superconducting qubit to optical photon transduction”. In: *Nature* 588.7839 (2020), pp. 599–603.

[58] Youpeng Zhong et al. “Deterministic multi-qubit entanglement in a quantum network”. In: *Nature* 590.7847 (2021), pp. 571–575.

[59] Aaron Somoroff et al. “Millisecond coherence in a superconducting qubit”. In: *Physical Review Letters* 130.26 (2023), p. 267001.

[60] Matthew Reagor et al. “Quantum memory with millisecond coherence in circuit QED”. In: *Physical Review B* 94.1 (2016), p. 014506.

[61] Roberto Stassi, Mauro Cirio, and Franco Nori. "Scalable quantum computer with superconducting circuits in the ultrastrong coupling regime". In: *npj Quantum Information* 6.1 (2020), p. 67.

[62] Anasua Chatterjee et al. "Semiconductor qubits in practice". In: *Nature Reviews Physics* 3.3 (2021), pp. 157–177.

[63] L. M. K. Vandersypen et al. "Interfacing spin qubits in quantum dots and donors—hot, dense, and coherent". en. In: *npj Quantum Information* 3.1 (Dec. 2017), p. 34. ISSN: 2056-6387. DOI: 10.1038/s41534-017-0038-y. URL: http://www.nature.com/articles/s41534-017-0038-y (visited on 12/16/2022).

[64] Guido Burkard et al. "Semiconductor spin qubits". In: *Reviews of Modern Physics* 95.2 (2023), p. 025003.

[65] Sébastien Pezzagna and Jan Meijer. "Quantum computer based on color centers in diamond". en. In: *Applied Physics Reviews* 8.1 (Mar. 2021), p. 011308. ISSN: 1931-9401. DOI: 10.1063/5.0007444. URL: https://aip.scitation.org/doi/10.1063/5.0007444 (visited on 05/26/2022).

[66] Gary Wolfowicz et al. "Quantum guidelines for solid-state spin defects". In: *Nature Reviews Materials* 6.10 (2021), pp. 906–925.

[67] Yu-Chen Chen et al. "Laser writing of coherent colour centres in diamond". In: *Nature Photonics* 11.2 (2017), pp. 77–80.

[68] Shane M Eaton et al. "Quantum micro–nano devices fabricated in diamond by femtosecond laser and ion irradiation". In: *Advanced Quantum Technologies* 2.5-6 (2019), p. 1900006.

[69] Nir Bar-Gill et al. "Solid-state electronic spin coherence time approaching one second". In: *Nature communications* 4.1 (2013), p. 1743.

[70] Peter Christian Maurer et al. "Room-temperature quantum bit memory exceeding one second". In: *Science* 336.6086 (2012), pp. 1283–1286.

[71] Mohamed H Abobeih et al. "One-second coherence for a single electron spin coupled to a multi-qubit nuclear-spin environment". In: *Nature communications* 9.1 (2018), p. 2552.

[72] Manjin Zhong et al. "Optically addressable nuclear spins in a solid with a six-hour coherence time". In: *Nature* 517.7533 (2015), pp. 177–180.

[73] Gang Zhang et al. "Material platforms for defect qubits and single-photon emitters". In: *Applied Physics Reviews* 7.3 (2020), p. 031308.

[74] JR Weber et al. "Quantum computing with defects". In: *Proceedings of the National Academy of Sciences* 107.19 (2010), pp. 8513–8518.

[75] Yihuang Xiong et al. "Midgap state requirements for optically active quantum defects". In: *Materials for Quantum Technology* 4.1 (2024), p. 013001.

[76] Lee C Bassett et al. "Quantum defects by design". In: *Nanophotonics* 8.11 (2019), pp. 1867–1888.

[77] GD Fuchs et al. "A quantum memory intrinsic to single nitrogen–vacancy centres in diamond". In: *Nature Physics* 7.10 (2011), pp. 789–793.

[78] Mark E Turiansky et al. “Rational design of efficient defect-based quantum emitters”. In: *APL Photonics* 9.6 (2024).

[79] Milos Toth and Igor Aharonovich. “Single Photon Sources in Atomically Thin Materials”. en. In: *Annual Review of Physical Chemistry* 70.1 (June 2019), pp. 123–142. ISSN: 0066-426X, 1545-1593. DOI: 10.1146/annurev-physchem-042018-052628. URL: https://www.annualreviews.org/doi/10.1146/annurev-physchem-042018-052628 (visited on 12/16/2022).

[80] Ananth Kamath and Philippe Guyot-Sionnest. “The “energy gap law” for mid-infrared nanocrystals”. In: *The Journal of Chemical Physics* 160.20 (2024).

[81] Chanaprom Cholsuk, Sujin Suwanna, and Tobias Vogl. “Comprehensive scheme for identifying defects in solid-state quantum systems”. In: *The Journal of Physical Chemistry Letters* 14.29 (2023), pp. 6564–6571.

[82] Leslie Allen Riseberg and H-W_ Moos. “Multiphonon orbit-lattice relaxation of excited states of rare-earth ions in crystals”. In: *Physical Review* 174.2 (1968), p. 429.

[83] Xiaojing Xia et al. “Quantum point defects for solid-state laser refrigeration”. In: *Advanced Materials* 33.23 (2021), p. 1905406.

[84] Chris JH Wort and Richard S Balmer. “Diamond as an electronic material”. In: *Materials today* 11.1-2 (2008), pp. 22–28.

[85] Kazuhiro Kuruma et al. “Engineering phonon-qubit interactions using phononic crystals”. In: *arXiv preprint arXiv:2310.06236* (2023).

[86] Sounak Mukherjee et al. “A Telecom O-Band Emitter in Diamond”. en. In: *Nano Letters* 23.7 (Apr. 2023), pp. 2557–2562. ISSN: 1530-6984, 1530-6992. DOI: 10.1021/acs.nanolett.2c04608. URL: https://pubs.acs.org/doi/10.1021/acs.nanolett.2c04608 (visited on 04/25/2023).

[87] Jakub Cajzl et al. “Erbium ion implantation into diamond–measurement and modelling of the crystal structure”. In: *Physical Chemistry Chemical Physics* 19.8 (2017), pp. 6233–6245.

[88] Yu Jin et al. “Photoluminescence spectra of point defects in semiconductors: Validation of first-principles calculations”. en. In: *Physical Review Materials* 5.8 (Aug. 2021), p. 084603. ISSN: 2475-9953. DOI: 10.1103/PhysRevMaterials.5.084603. URL: https://link.aps.org/doi/10.1103/PhysRevMaterials.5.084603 (visited on 03/09/2023).

[89] N. Somaschi et al. “Near-optimal single-photon sources in the solid state”. en. In: *Nature Photonics* 10.5 (May 2016), pp. 340–345. ISSN: 1749-4885, 1749-4893. DOI: 10.1038/nphoton.2016.23. URL: http://www.nature.com/articles/nphoton.2016.23 (visited on 04/25/2023).

[90] Taras Plakhotnik, Marcus W Doherty, and Neil B Manson. “Electron-phonon processes of the nitrogen-vacancy center in diamond”. In: *Physical Review B* 92.8 (2015), p. 081203.

[91] Artur Lozovoi et al. “Detection and modeling of hole capture by single point defects under variable electric fields”. In: *Nano Letters* 23.10 (2023), pp. 4495–4501.

[92] Maximilian Ruf et al. “Quantum networks based on color centers in diamond”. In: *Journal of Applied Physics* 130.7 (2021).

[93] Sébastien Pezzagna and Jan Meijer. "Quantum computer based on color centers in diamond". In: *Applied Physics Reviews* 8.1 (2021).

[94] MW Doherty et al. "Theory of the ground-state spin of the NV- center in diamond". In: *Physical Review B—Condensed Matter and Materials Physics* 85.20 (2012), p. 205203.

[95] Gopalakrishnan Balasubramanian et al. "Ultralong spin coherence time in isotopically engineered diamond". In: *Nature materials* 8.5 (2009), pp. 383–387.

[96] Nabeel Aslam et al. "Quantum sensors for biomedical applications". In: *Nature Reviews Physics* (2023), pp. 1–13.

[97] William F Koehl et al. "Room temperature coherent control of defect spin qubits in silicon carbide". In: *Nature* 479.7371 (2011), pp. 84–87.

[98] AM Tyryshkin et al. "Coherence of spin qubits in silicon". In: *Journal of Physics: Condensed Matter* 18.21 (2006), S783.

[99] Abram L Falk et al. "Polytype control of spin qubits in silicon carbide". In: *Nature communications* 4.1 (2013), p. 1819.

[100] Steven Prawer and Igor Aharonovich. *Quantum information processing with diamond: principles and applications*. Elsevier, 2014.

[101] Gordon Davies and MF Hamer. "Optical studies of the 1.945 eV vibronic band in diamond". In: *Proceedings of the Royal Society of London. A. Mathematical and Physical Sciences* 348.1653 (1976), pp. 285–298.

[102] JoHoNo Loubser and JoA van Wyk. "Electron spin resonance in the study of diamond". In: *Reports on Progress in Physics* 41.8 (1978), p. 1201.

[103] NRS Reddy, NB Manson, and ER Krausz. "Two-laser spectral hole burning in a colour centre in diamond". In: *Journal of Luminescence* 38.1-6 (1987), pp. 46–47.

[104] E Van Oort, NB Manson, and M Glasbeek. "Optically detected spin coherence of the diamond NV centre in its triplet ground state". In: *Journal of Physics C: Solid State Physics* 21.23 (1988), p. 4385.

[105] A Gruber et al. "Scanning confocal optical microscopy and magnetic resonance on single defect centers". In: *Science* 276.5321 (1997), pp. 2012–2014.

[106] Fedor Jelezko et al. "Observation of coherent oscillations in a single electron spin". In: *Physical review letters* 92.7 (2004), p. 076401.

[107] L Childress et al. "Coherent dynamics of coupled electron and nuclear spin qubits in diamond". In: *Science* 314.5797 (2006), pp. 281–285.

[108] Yi Chou, Shang-Yu Huang, and Hsi-Sheng Goan. "Optimal control of fast and high-fidelity quantum gates with electron and nuclear spins of a nitrogen-vacancy center in diamond". en. In: *Physical Review A* 91.5 (May 2015), p. 052315. ISSN: 1050-2947, 1094-1622. DOI: 10.1103/PhysRevA.91.052315. URL: https://link.aps.org/doi/10.1103/PhysRevA.91.052315 (visited on 09/08/2022).

[109] Kay D Jahnke et al. "Electron–phonon processes of the silicon-vacancy centre in diamond". In: *New Journal of Physics* 17.4 (2015), p. 043011.

[110] Alessandro Lunghi and Stefano Sanvito. “How do phonons relax molecular spins?” In: *Science advances* 5.9 (2019), eaax7163.

[111] Lilian Childress and Ronald Hanson. “Diamond NV centers for quantum computing and quantum networks”. In: *MRS bulletin* 38.2 (2013), pp. 134–138.

[112] Christoph E. Nebel, ed. *Diamond for quantum applications*. Semiconductors and semimetals volume 103-104. OCLC: on1127115033. Amsterdam: Academic Press, 2020. ISBN: 978-0-12-820240-1 978-0-323-85024-7.

[113] LC Bassett et al. “Electrical Tuning of Single Nitrogen-Vacancy Center Optical Transitions Enhanced<? format?> by Photoinduced Fields”. In: *Physical review letters* 107.26 (2011), p. 266403.

[114] CT Nguyen et al. “Quantum network nodes based on diamond qubits with an efficient nanophotonic interface”. In: *Physical review letters* 123.18 (2019), p. 183602.

[115] C Santori et al. “Nanophotonics for quantum optics using nitrogen-vacancy centers in diamond”. In: *Nanotechnology* 21.27 (2010), p. 274008.

[116] Wei Hu, Zhenyu Li, and Jinlong Yang. “Surface and size effects on the charge state of NV center in nanodiamonds”. In: *Computational and Theoretical Chemistry* 1021 (2013), pp. 49–53.

[117] Lucio Robledo et al. “High-fidelity projective read-out of a solid-state spin quantum register”. In: *Nature* 477.7366 (2011), pp. 574–578.

[118] Gerald Waldherr et al. “Quantum error correction in a solid-state hybrid spin register”. In: *Nature* 506.7487 (2014), pp. 204–207.

[119] Hannes Bernien et al. “Heralded entanglement between solid-state qubits separated by three metres”. In: *Nature* 497.7447 (2013), pp. 86–90.

[120] Yuki Doi et al. “Pure negatively charged state of the NV center in n-type diamond”. In: *Physical Review B* 93.8 (2016), p. 081203.

[121] Philipp Neumann et al. “Single-shot readout of a single nuclear spin”. In: *science* 329.5991 (2010), pp. 542–544.

[122] G Waldherr et al. “Dark states of single nitrogen-vacancy centers in diamond unraveled by single shot NMR”. In: *Physical review letters* 106.15 (2011), p. 157601.

[123] Tobias Lühmann, Jan Meijer, and Sébastien Pezzagna. “Charge-assisted engineering of color centers in diamond”. In: *physica status solidi (a)* 218.5 (2021), p. 2000614.

[124] MV Hauf et al. “Chemical control of the charge state of nitrogen-vacancy centers in diamond”. In: *Physical Review B—Condensed Matter and Materials Physics* 83.8 (2011), p. 081304.

[125] Hayate Yamano et al. “Charge state stabilization of shallow nitrogen vacancy centers in diamond by oxygen surface modification”. In: *Japanese journal of applied physics* 56.4S (2017), 04CK08.

[126] IM Morris et al. “Lifetime-limited and tunable emission from single charge-stabilized nickel vacancy centers in diamond”. In: *Physical Review Letters* 135.4 (2025), p. 043602.

[127] Y Doi et al. “Deterministic electrical charge-state initialization of single nitrogen-vacancy center in diamond”. In: *Physical Review X* 4.1 (2014), p. 011057.

[128] Bernhard Grotz et al. “Charge state manipulation of qubits in diamond”. In: *Nature communications* 3.1 (2012), p. 729.

[129] Romana Schirhagl et al. “Nitrogen-vacancy centers in diamond: nanoscale sensors for physics and biology”. In: *Annual review of physical chemistry* 65.1 (2014), pp. 83–105.

[130] Hannes Bernien et al. “Two-photon quantum interference from separate nitrogen vacancy centers in diamond”. In: *Physical Review Letters* 108.4 (2012), p. 043604.

[131] Matteo Pompili et al. “Realization of a multinode quantum network of remote solid-state qubits”. In: *Science* 372.6539 (2021), pp. 259–264.

[132] Steffen Steinert et al. “High sensitivity magnetic imaging using an array of spins in diamond”. In: *Review of scientific instruments* 81.4 (2010), p. 043705.

[133] MV Gurudev Dutt et al. “Quantum register based on individual electronic and nuclear spin qubits in diamond”. In: *Science* 316.5829 (2007), pp. 1312–1316.

[134] Bas Hensen et al. “Loophole-free Bell inequality violation using electron spins separated by 1.3 kilometres”. In: *Nature* 526.7575 (2015), pp. 682–686.

[135] Elke Neu et al. “Single photon emission from silicon-vacancy colour centres in chemical vapour deposition nano-diamonds on iridium”. In: *New Journal of Physics* 13.2 (2011), p. 025012.

[136] Christian Hepp et al. “Electronic Structure of the Silicon Vacancy Color Center in Diamond”. en. In: *Physical Review Letters* 112.3 (Jan. 2014), p. 036405. ISSN: 0031-9007, 1079-7114. DOI: 10.1103/PhysRevLett.112.036405. URL: https://link.aps.org/doi/10.1103/PhysRevLett.112.036405 (visited on 05/11/2022).

[137] Benjamin Pingault et al. “All-Optical Formation of Coherent Dark States of Silicon-Vacancy Spins in Diamond”. en. In: *Physical Review Letters* 113.26 (Dec. 2014), p. 263601. ISSN: 0031-9007, 1079-7114. DOI: 10.1103/PhysRevLett.113.263601. URL: https://link.aps.org/doi/10.1103/PhysRevLett.113.263601 (visited on 05/11/2022).

[138] Jonas N. Becker et al. “All-Optical Control of the Silicon-Vacancy Spin in Diamond at Millikelvin Temperatures”. en. In: *Physical Review Letters* 120.5 (Jan. 2018), p. 053603. ISSN: 0031-9007, 1079-7114. DOI: 10.1103/PhysRevLett.120.053603. URL: https://link.aps.org/doi/10.1103/PhysRevLett.120.053603 (visited on 05/11/2022).

[139] Romain Debroux et al. “Quantum control of the tin-vacancy spin qubit in diamond”. In: *Physical Review X* 11.4 (2021), p. 041041.

[140] Johannes Görlitz et al. “Spectroscopic investigations of negatively charged tin-vacancy centres in diamond”. In: *New Journal of Physics* 22.1 (Jan. 2020), p. 013048. ISSN: 1367-2630. DOI: 10.1088/1367-2630/ab6631. URL: https://iopscience.iop.org/article/10.1088/1367-2630/ab6631 (visited on 06/11/2022).

[141] Takayuki Iwasaki et al. “Tin-vacancy quantum emitters in diamond”. In: *Physical review letters* 119.25 (2017), p. 253601.

[142] Takayuki Iwasaki et al. “Germanium-vacancy single color centers in diamond”. In: *Scientific reports* 5.1 (2015), p. 12882.

[143] Johannes Görlitz et al. “Coherence of a charge stabilised tin-vacancy spin in diamond”. In: *npj Quantum Information* 8.1 (2022), p. 45.

[144] C Adambukulam et al. “Hyperfine Spectroscopy and Fast, All-Optical Arbitrary State Initialization and Readout of a Single, Ten-Level Ge 73 Vacancy Nuclear Spin Qudit in Diamond”. In: *Physical Review Letters* 132.6 (2024), p. 060603.

[145] Denis D Sukachev et al. “Silicon-vacancy spin qubit in diamond: a quantum memory exceeding 10 ms with single-shot state readout”. In: *Physical review letters* 119.22 (2017), p. 223602.

[146] CT Nguyen et al. “An integrated nanophotonic quantum register based on silicon-vacancy spins in diamond”. In: *Physical Review B* 100.16 (2019), p. 165428.

[147] Zheng Wang et al. “Microwave heating effect on diamond samples of nitrogen-vacancy centers”. In: *ACS omega* 7.35 (2022), pp. 31538–31543.

[148] Isaac Harris et al. “Group-III quantum defects in diamond are stable spin-1 color centers”. In: *Physical Review B* 102.19 (2020), p. 195206.

[149] Matthew E Trusheim et al. “Lead-related quantum emitters in diamond”. In: *Physical Review B* 99.7 (2019), p. 075430.

[150] Emilio Corte et al. “Magnesium-vacancy optical centers in diamond”. In: *ACS photonics* 10.1 (2022), pp. 101–110.

[151] Peng Wang et al. “Transform-limited photon emission from a lead-vacancy center in diamond above 10 K”. In: *Physical Review Letters* 132.7 (2024), p. 073601.

[152] BL Green et al. “Neutral silicon-vacancy center in diamond: Spin polarization and lifetimes”. In: *Physical review letters* 119.9 (2017), p. 096402.

[153] Zi-Huai Zhang et al. “Neutral silicon vacancy centers in undoped diamond via surface control”. In: *Physical Review Letters* 130.16 (2023), p. 166902.

[154] Zi-Huai Zhang et al. “Neutral Silicon-Vacancy Centers in Diamond via Photoactivated Itinerant Carriers”. In: *Physical Review Applied* 19.3 (2023), p. 034022.

[155] Simon C. Lawson and Hisao Kanda. “An annealing study of nickel point defects in high-pressure synthetic diamond”. en. In: *Journal of Applied Physics* 73.8 (Apr. 1993), pp. 3967–3973. ISSN: 0021-8979, 1089-7550. DOI: 10.1063/1.352861. URL: http://aip.scitation.org/doi/10.1063/1.352861 (visited on 08/23/2022).

[156] Alexander Yelisseyev and Hisao Kanda. “Optical centers related to 3d transition metals in diamond”. In: *New diamond and frontier carbon technology* 17.3 (2007), pp. 127–178.

[157] Alexander M Zaitsev. *Optical properties of diamond: a data handbook*. Springer Science & Business Media, 2013.

[158] Vladimir Nadolinny, Andrey Komarovskikh, and Yuri Palyanov. “Incorporation of large impurity atoms into the diamond crystal lattice: EPR of split-vacancy defects in diamond”. In: *Crystals* 7.8 (2017), p. 237.

[159] JHN Loubser and WP Van Ryneveld. “Electron spin resonance of nickel in synthetic diamonds”. In: *Nature* 211.5048 (1966), pp. 517–517.

[160] MI Samoilovich, GN Bezrukov, and VP Butuzov. “Electron paramagnetic resonance of nickel in synthetic diamond”. In: *Soviet Journal of Experimental and Theoretical Physics Letters* 14 (1971), p. 379.

[161] JE Lowther. “Nickel defect centers in diamond”. In: *Physical Review B* 51.1 (1995), p. 91.

[162] R Larico et al. “An ab initio investigation on nickel impurities in diamond”. In: *Physica B: Condensed Matter* 340 (2003), pp. 84–88.

[163] Rolando Larico et al. “Isolated nickel impurities in diamond: A microscopic model for the electrically active centers”. In: *Applied physics letters* 84.5 (2004), p. 720.

[164] Rolando Larico et al. “Nickel impurities in diamond: a FP-LAPW investigation”. In: *Computational materials science* 30.1-2 (2004), pp. 62–66.

[165] Thomas Chanier and Adam Gali. “Ab initio characterization of a Ni-related defect in diamond: The W8 center”. In: *Physical Review B—Condensed Matter and Materials Physics* 87.24 (2013), p. 245206.

[166] Maria Helena Nazaré, AJ Neves, and Gordon Davies. “Optical studies of the 1.40-eV Ni center in diamond”. In: *Physical Review B* 43.17 (1991), p. 14196.

[167] G Davies, AJ Neves, and MH Nazaré. “Nickel isotope effects in the 1.4 eV centre in synthetic diamond”. In: *Europhysics Letters* 9.1 (1989), p. 47.

[168] L Paslovsky and JE Lowther. “Optical dichroism of nickel in diamond”. In: *Journal of Physics: Condensed Matter* 4.3 (1992), p. 775.

[169] JM Baker. “Do isolated interstitial nickel atoms occur in diamond? A re-examination of the electronparamagnetic resonance defects NIRIM-1 and NIRIM-2”. In: *Journal of Physics: Condensed Matter* 15.39 (2003), S2929.

[170] R Larico et al. “Electronic properties and hyperfine fields of nickel-related complexes in diamond”. In: *Physical Review B—Condensed Matter and Materials Physics* 79.11 (2009), p. 115202.

[171] Gergő Thiering and Adam Gali. “Magneto-optical spectra of the split nickel-vacancy defect in diamond”. en. In: *Physical Review Research* 3.4 (Oct. 2021), p. 043052. ISSN: 2643-1564. DOI: 10.1103/PhysRevResearch.3.043052. URL: https://link.aps.org/doi/10.1103/PhysRevResearch.3.043052 (visited on 05/11/2022).

[172] AJ Stolk et al. “Telecom-band quantum interference of frequency-converted photons from remote detuned nv centers”. In: *PRX Quantum* 3.2 (2022), p. 020359.

[173] Eric Bersin et al. “Telecom networking with a diamond quantum memory”. In: *PRX Quantum* 5.1 (2024), p. 010303.

[174] Elisa Londero et al. “Identification of nickel-vacancy defects by combining experimental and ab initio simulated photocurrent spectra”. In: *Physical Review B* 97.24 (2018), p. 241202.

[175] Emilie Bourgeois et al. “Photoelectric detection of electron spin resonance of nitrogen-vacancy centres in diamond”. In: *Nature Communications* 6.1 (2015), p. 8577.

[176] Michal Gulka et al. “Pulsed Photoelectric Coherent Manipulation and Detection of N-V Center Spins in Diamond”. In: *Physical review applied* 7.4 (2017), p. 044032.

[177] Emilie Bourgeois, Michal Gulka, and Milos Nesladek. “Photoelectric detection and quantum readout of nitrogen-vacancy center spin states in diamond”. In: *Advanced Optical Materials* 8.12 (2020), p. 1902132.

[178] Petr Siyushev et al. “Photoelectrical imaging and coherent spin-state readout of single nitrogen-vacancy centers in diamond”. In: *Science* 363.6428 (2019), pp. 728–731.

[179] Hiroki Morishita et al. “Room temperature electrically detected nuclear spin coherence of NV centres in diamond”. In: *Scientific reports* 10.1 (2020), p. 792.

[180] Michal Gulka et al. “Room-temperature control and electrical readout of individual nitrogen-vacancy nuclear spins”. In: *Nature Communications* 12.1 (2021), p. 4421.

[181] Brendon C Rose et al. “Observation of an environmentally insensitive solid-state spin defect in diamond”. In: *Science* 361.6397 (2018), pp. 60–63.

[182] Carlo Bradac et al. “Quantum nanophotonics with group IV defects in diamond”. en. In: *Nature Communications* 10.1 (Dec. 2019), p. 5625. ISSN: 2041-1723. DOI: 10.1038/s41467-019-13332-w. URL: https://www.nature.com/articles/s41467-019-13332-w (visited on 01/04/2023).

[183] Thomas Chanier, CE Pryor, and Michael E Flatte. “Substitutional nickel impurities in diamond: Decoherence-free subspaces for quantum information processing”. In: *Europhysics Letters* 99.6 (2012), p. 67006.

[184] Christopher J Foot. *Atomic physics*. Vol. 7. Oxford university press, 2005.

[185] Dieter Suter. *The physics of laser-atom interactions*. 19. Cambridge University Press, 1997.

[186] Goran Lindblad. “On the generators of quantum dynamical semigroups”. In: *Communications in mathematical physics* 48.2 (1976), pp. 119–130.

[187] Vittorio Gorini, Andrzej Kossakowski, and Ennackal Chandy George Sudarshan. “Completely positive dynamical semigroups of N-level systems”. In: *Journal of Mathematical Physics* 17.5 (1976), pp. 821–825.

[188] DF James and Jonathan Jerke. “Effective Hamiltonian theory and its applications in quantum information”. In: *Canadian Journal of Physics* 85.6 (2007), pp. 625–632.

[189] Norman F Ramsey. “A molecular beam resonance method with separated oscillating fields”. In: *Physical Review* 78.6 (1950), p. 695.

[190] Anthony Mark Fox. *Quantum optics: an introduction*. Vol. 15. Oxford university press, 2006.

[191] Leonard Mandel, Emil Wolf, and Jeffrey H Shapiro. *Optical coherence and quantum optics*. 1996.

[192] Edward B Flagg et al. “Resonantly driven coherent oscillations in a solid-state quantum emitter”. In: *Nature Physics* 5.3 (2009), pp. 203–207.

[193] Robert H Webb. “Confocal optical microscopy”. In: *Reports on progress in physics* 59.3 (1996), p. 427.

[194] Christian Hepp. "Electronic structure of the silicon vacancy color center in diamond". en. In: (2014). Publisher: Universität des Saarlandes. DOI: 10.22028/D291-23020. URL: https://publikationen.sulb.uni-saarland.de/handle/20.500.11880/23076 (visited on 06/02/2022).

[195] Ariful Haque and Sharaf Sumaiya. "An overview on the formation and processing of nitrogen-vacancy photonic centers in diamond by ion implantation". In: *Journal of Manufacturing and Materials Processing* 1.1 (2017), p. 6.

[196] S Lagomarsino et al. "Creation of silicon-vacancy color centers in diamond by ion implantation". In: *Frontiers in Physics* 8 (2021), p. 601362.

[197] R Kalish et al. "Ion-implantation-induced defects in diamond and their annealing: experiment and simulation". In: *physica status solidi (a)* 174.1 (1999), pp. 83–99.

[198] Jason M Smith et al. "Colour centre generation in diamond for quantum technologies". In: *Nanophotonics* 8.11 (2019), pp. 1889–1906.

[199] Jonas Nils Becker et al. "Ultrafast all-optical coherent control of single silicon vacancy colour centres in diamond". en. In: *Nature Communications* 7.1 (Dec. 2016), p. 13512. ISSN: 2041-1723. DOI: 10.1038/ncomms13512. URL: http://www.nature.com/articles/ncomms13512 (visited on 05/11/2022).

[200] Roman A Khmelnitsky et al. "Damage accumulation in diamond during ion implantation". In: *Journal of Materials Research* 30.9 (2015), pp. 1583–1592.

[201] Brad Slepetz and Miklos Kertesz. "Divacancies in diamond: a stepwise formation mechanism". In: *Physical Chemistry Chemical Physics* 16.4 (2014), pp. 1515–1521.

[202] R Kalish et al. "The nature of damage in ion-implanted and annealed diamond". In: *Nuclear Instruments and Methods in Physics Research Section B: Beam Interactions with Materials and Atoms* 148.1-4 (1999), pp. 626–633.

[203] Gemological Institute of America. *HPHT and CVD Diamond Growth Processes*. n.d. URL: https://www.gia.edu/hpht-and-cvd-diamond-growth-processes (visited on 04/11/2026).

[204] Jean-Charles Arnault, Samuel Saada, and Victor Ralchenko. "Chemical vapor deposition single-crystal diamond: a review". In: *physica status solidi (RRL)–Rapid Research Letters* 16.1 (2022), p. 2100354.

[205] Rafael R Gattass and Eric Mazur. "Femtosecond laser micromachining in transparent materials". In: *Nature photonics* 2.4 (2008), pp. 219–225.

[206] Richard D Simmonds et al. "Three dimensional laser microfabrication in diamond using a dual adaptive optics system". In: *Optics express* 19.24 (2011), pp. 24122–24128.

[207] Yu-Chen Chen et al. "Laser writing of individual nitrogen-vacancy defects in diamond with near-unity yield". In: *Optica* 6.5 (2019), pp. 662–667.

[208] Yu-Chen Chen et al. "Laser writing of scalable single color centers in silicon carbide". In: *Nano letters* 19.4 (2019), pp. 2377–2383.

[209] Andrew R Kirkpatrick et al. "Deterministic laser-writing of nitrogen-vacancy centres in high purity diamond". In: *Materials for Quantum Technology* 5.4 (2025), p. 041002.

[210] Anchita Addhya et al. “Photonic-cavity-enhanced laser writing of color centers in diamond”. In: *Nano Letters* 24.36 (2024), pp. 11224–11231.

[211] Birgit JM Hausmann et al. “Single-color centers implanted in diamond nanostructures”. In: *New Journal of Physics* 13.4 (2011), p. 045004.

[212] R. Larico et al. “Electronic properties and hyperfine fields of nickel-related complexes in diamond”. en. In: *Physical Review B* 79.11 (Mar. 2009), p. 115202. ISSN: 1098-0121, 1550-235X. DOI: 10.1103/PhysRevB.79.115202. URL: https://link.aps.org/doi/10.1103/PhysRevB.79.115202 (visited on 08/23/2022).

[213] Gergő Thiering and Adam Gali. “Ab initio magneto-optical spectrum of group-IV vacancy color centers in diamond”. In: *Physical Review X* 8.2 (2018), p. 021063.

[214] Gergő Thiering and Adam Gali. “Magneto-optical spectra of the split nickel-vacancy defect in diamond”. In: *Physical Review Research* 3.4 (2021), p. 043052.

[215] Christian Hepp et al. “Electronic structure of the silicon vacancy color center in diamond”. In: *Physical Review Letters* 112.3 (2014), p. 036405.

[216] Audrius Alkauskas et al. “First-principles theory of the luminescence lineshape for the triplet transition in diamond NV centres”. In: *New Journal of Physics* 16.7 (July 2014), p. 073026. ISSN: 1367-2630. DOI: 10.1088/1367-2630/16/7/073026. URL: https://iopscience.iop.org/article/10.1088/1367-2630/16/7/073026 (visited on 01/24/2023).

[217] J. O. Orwa et al. “Nickel related optical centres in diamond created by ion implantation”. en. In: *Journal of Applied Physics* 107.9 (May 2010), p. 093512. ISSN: 0021-8979, 1089-7550. DOI: 10.1063/1.3357374. URL: http://aip.scitation.org/doi/10.1063/1.3357374 (visited on 05/12/2022).

[218] Katharina Senkalla et al. “Germanium vacancy in diamond quantum memory exceeding 20 ms”. In: *Physical Review Letters* 132.2 (2024), p. 026901.

[219] A Kalachev et al. “Raman quantum memory based on an ensemble of silicon-vacancy centers in diamond”. In: *Laser Physics* 29.10 (2019), p. 104001.

[220] Bing Dong et al. “Temperature dependence of optical centers in Ib diamond characterized by photoluminescence spectra”. In: *Diamond and Related Materials* 116 (2021), p. 108389.

[221] Carsten Arend et al. “Photoluminescence excitation and spectral hole burning spectroscopy of silicon vacancy centers in diamond”. In: *Physical Review B* 94.4 (2016), p. 045203.

[222] A Dharmasiri et al. “Near-infrared optical thermometry of nickel color centers in diamond”. In: *Optics Letters* 50.3 (2025), pp. 968–971.

[223] Nabeel Aslam et al. “Photo-induced ionization dynamics of the nitrogen vacancy defect in diamond investigated by single-shot charge state detection”. In: *New Journal of Physics* 15.1 (2013), p. 013064.

[224] JO Orwa et al. “Nickel related optical centres in diamond created by ion implantation”. In: *Journal of applied physics* 107.9 (2010).

[225] Matthew E. Trusheim et al. “Transform-Limited Photons From a Coherent Tin-Vacancy Spin in Diamond”. en. In: *Physical Review Letters* 124.2 (Jan. 2020), p. 023602. ISSN: 0031-9007, 1079-7114. DOI: 10.1103/PhysRevLett.124.023602. URL: https://link.aps.org/doi/10.1103/PhysRevLett.124.023602 (visited on 05/11/2022).

[226] Prashun Gorai. “Beginner’s guide to interpreting defect and defect level diagrams”. In: *PRX Energy* 4.3 (2025), p. 032001.

[227] Simon M Sze, Yiming Li, and Kwok K Ng. *Physics of semiconductor devices*. John wiley & sons, 2021.

[228] Ádám Gali. “Recent advances in the *ab initio* theory of solid-state defect qubits”. en. In: *Nanophotonics* 12.3 (Feb. 2023), pp. 359–397. ISSN: 2192-8606, 2192-8614. DOI: 10.1515/nanoph-2022-0723. URL: https://www.degruyter.com/document/doi/10.1515/nanoph-2022-0723/html (visited on 03/08/2023).

[229] Alan T Collins. “The Fermi level in diamond”. In: *Journal of Physics: Condensed Matter* 14.14 (2002), p. 3743.

[230] DB Radishev et al. “Investigation of NV centers charge states in CVD diamond layers doped by nitrogen and phosphorous”. In: *Journal of Luminescence* 239 (2021), p. 118404.

[231] JO Orwa et al. “An upper limit on the lateral vacancy diffusion length in diamond”. In: *Diamond and related materials* 24 (2012), pp. 6–10.

[232] Chikara Shinei et al. “Change in charge state of NV center caused by monovacancy formation”. In: *Diamond and Related Materials* 140 (2023), p. 110523.

[233] JP Goss et al. “Donor and acceptor states in diamond”. In: *Diamond and related materials* 13.4-8 (2004), pp. 684–690.

[234] A Pu, V Avalos, and S Dannefaer. “Negative charging of mono-and divacancies in IIa diamonds by monochromatic illumination”. In: *Diamond and related materials* 10.3-7 (2001), pp. 585–587.

[235] Peter Deák et al. “Formation of NV centers in diamond: A theoretical study based on calculated transitions and migration of nitrogen and vacancy related defects”. en. In: *Physical Review B* 89.7 (Feb. 2014), p. 075203. ISSN: 1098-0121, 1550-235X. DOI: 10.1103/PhysRevB.89.075203. URL: https://link.aps.org/doi/10.1103/PhysRevB.89.075203 (visited on 02/15/2023).

[236] L Rino, AJ Neves, and Hisao Kanda. “Nickel–nitrogen complexes in synthetic diamond: the 1.660 eV luminescence system”. In: *Physica B: Condensed Matter* 340 (2003), pp. 94–98.

[237] Karl Johnston and Alison Mainwood. “Properties of nickel nitrogen complexes in diamond: stability and electronic structure”. In: *Diamond and related materials* 12.3-7 (2003), pp. 516–520.

[238] Konstantin Iakoubovskii et al. “ESR and optical evidence for a Ni vacancy center in CVD diamond”. In: *Physical Review B* 62.24 (2000), p. 16587.

[239] Simon C Lawson, Hisao Kanda, and Masami Sekita. “New nickel-related optical absorption in high-pressure synthetic diamond”. In: *Philosophical Magazine B* 68.1 (1993), pp. 39–46.

[240] Manuel Rieger et al. “Fast optoelectronic charge state conversion of silicon vacancies in diamond”. In: *Science Advances* 10.8 (2024), eadl4265.

[241] Elke Neu, Mario Agio, and Christoph Becher. “Photophysics of single silicon vacancy centers in diamond: implications for single photon emission”. In: *Optics express* 20.18 (2012), pp. 19956–19971.

[242] SC Kitson et al. “Intensity fluctuation spectroscopy of small numbers of dye molecules in a microcavity”. In: *Physical Review A* 58.1 (1998), p. 620.

[243] Christian Kurtsiefer et al. “Stable solid-state source of single photons”. In: *Physical review letters* 85.2 (2000), p. 290.

[244] Chunlang Wang. “A solid-state single photon source based on color centers in diamond”. PhD thesis. lmu, 2007.

[245] Lucio Robledo et al. “Control and Coherence of the Optical Transition of Single Nitrogen<? format?> Vacancy Centers in Diamond”. In: *Physical review letters* 105.17 (2010), p. 177403.

[246] Andrei Faraon et al. “Coupling of nitrogen-vacancy centers to photonic crystal cavities in monocrystalline diamond”. In: *Physical review letters* 109.3 (2012), p. 033604.

[247] Johannes Görlitz et al. “Spectroscopic investigations of negatively charged tin-vacancy centres in diamond”. In: *New Journal of Physics* 22.1 (2020), p. 013048.

[248] Alison E Rugar et al. “Narrow-linewidth tin-vacancy centers in a diamond waveguide”. In: *ACS Photonics* 7.9 (2020), pp. 2356–2361.

[249] Disheng Chen et al. “Optical gating of resonance fluorescence from a single germanium vacancy color center in diamond”. In: *Physical review letters* 123.3 (2019), p. 033602.

[250] Karin Groot-Berning et al. “Passive charge state control of nitrogen-vacancy centres in diamond using phosphorous and boron doping”. In: *physica status solidi (a)* 211.10 (2014), pp. 2268–2273.

[251] Milos Nesladek. “Conventional n-type doping in diamond: state of the art and recent progress”. In: *Semiconductor Science and Technology* 20.2 (2005), R19–R27.

[252] Tobias Lühmann et al. “Charge-state tuning of single SnV centers in diamond”. In: *ACS Photonics* 7.12 (2020), pp. 3376–3385.

[253] Lorenzo De Santis et al. “Investigation of the stark effect on a centrosymmetric quantum emitter in diamond”. In: *Physical Review Letters* 127.14 (2021), p. 147402.

[254] Mario Bertolotti. *Masers and lasers: an historical approach*. Crc Press, 2015.

[255] David A Harmin. “Theory of the Stark effect”. In: *Physical Review A* 26.5 (1982), p. 2656.

[256] Karl E Spear and John P Dismukes. *Synthetic diamond: emerging CVD science and technology*. Vol. 25. John Wiley & Sons, 1994.

[257] Ph Tamarat et al. “Stark shift control of single optical centers in diamond”. In: *Physical Review Letters* 97.8 (2006), p. 083002.

[258] Ph Tamarat et al. “Spin-flip and spin-conserving optical transitions of the nitrogen-vacancy centre in diamond”. In: *New Journal of Physics* 10.4 (2008), p. 045004.

[259] Emre Togan et al. “Quantum entanglement between an optical photon and a solid-state spin qubit”. In: *Nature* 466.7307 (2010), pp. 730–734.

[260] Louis Nicolas et al. “Sub-GHz linewidth ensembles of SiV centers in a diamond nanopyramid revealed by charge state conversion”. In: *ACS photonics* 6.10 (2019), pp. 2413–2420.

[261] Aedan Gardill et al. “Probing charge dynamics in diamond with an individual color center”. In: *Nano Letters* 21.16 (2021), pp. 6960–6966.

[262] RN Pereira et al. “Annealing study of the formation of nickel-related paramagnetic defects in diamond”. In: *Diamond and related materials* 11.3-6 (2002), pp. 623–626.

[263] James F Ziegler, Matthias D Ziegler, and Jochen P Biersack. “SRIM–The stopping and range of ions in matter (2010)”. In: *Nuclear Instruments and Methods in Physics Research Section B: Beam Interactions with Materials and Atoms* 268.11-12 (2010), pp. 1818–1823.

[264] Stefan Häußler et al. “Photoluminescence excitation spectroscopy of SiV- and GeV- color center in diamond”. In: *New Journal of Physics* 19.6 (2017), p. 063036.

[265] Peng Ji et al. “Multiple-photon excitation of nitrogen vacancy centers in diamond”. In: *Physical Review B* 97.13 (2018), p. 134112.

[266] Kevin Chia-lun Chen. “Lead-related quantum emitters in diamond”. PhD thesis. Massachusetts Institute of Technology, 2019.

[267] Young-Ik Sohn et al. “Controlling the coherence of a diamond spin qubit through its strain environment”. In: *Nature communications* 9.1 (2018), p. 2012.

[268] Berk Diler Kovos. “Transition Metal Ions as Optically Addressable Spin Qubits”. PhD thesis. The University of Chicago, 2021.

[269] Bartholomeus Machielse et al. “Quantum interference of electromechanically stabilized emitters in nanophotonic devices”. In: *Physical Review X* 9.3 (2019), p. 031022.

[270] A. D. Sakharov. “SPECIAL ISSUE: Violation of CP in variance, C asymmetry, and baryon asymmetry of the universe”. In: *Soviet Physics Uspekhi* 34 (May 1991), pp. 392–393. DOI: 10.1070/PU1991v034n05ABEH002497.

[271] James H Christenson et al. “Evidence for the 2 π Decay of the K 2 0 Meson”. In: *Physical Review Letters* 13.4 (1964), p. 138.

[272] T. E. Chupp et al. “Electric dipole moments of atoms, molecules, nuclei, and particles”. In: *Rev. Mod. Phys.* 91 (1 Jan. 2019), p. 015001. DOI: 10.1103/RevModPhys.91.015001.

[273] N. Auerbach, V. V. Flambaum, and V. Spevak. “Collective T - and P -Odd Electromagnetic Moments in Nuclei with Octupole Deformations”. In: *Phys. Rev. Lett.* 76 (23 June 1996), pp. 4316–4319. DOI: 10.1103/PhysRevLett.76.4316.

[274] V. Spevak, N. Auerbach, and V. V. Flambaum. “Enhanced T-odd, P-odd electromagnetic moments in reflection asymmetric nuclei”. In: *Phys. Rev. C* 56 (3 Sept. 1997), pp. 1357–1369. DOI: 10.1103/PhysRevC.56.1357.

[275] W. C. Haxton and E. M. Henley. “Enhanced T-Nonconserving Nuclear Moments”. In: *Phys. Rev. Lett.* 51 (21 Nov. 1983), pp. 1937–1940. DOI: 10.1103/PhysRevLett.51.1937.

[276] Jaideep Taggart Singh. "A new concept for searching for time-reversal symmetry violation using Pa-229 ions trapped in optical crystals". en. In: *Hyperfine Interactions* 240.1 (Dec. 2019), p. 29. ISSN: 0304-3843, 1572-9540. DOI: 10.1007/s10751-019-1573-z. URL: http://link.springer.com/10.1007/s10751-019-1573-z (visited on 02/14/2023).

[277] E Paige Abel et al. "Isotope harvesting at FRIB: additional opportunities for scientific discovery". In: *Journal of Physics G: Nuclear and Particle Physics* 46.10 (Aug. 2019), p. 100501. DOI: 10.1088/1361-6471/ab26cc. URL: https://dx.doi.org/10.1088/1361-6471/ab26cc.

[278] Mengnan Zou et al. "Proton radiation effects on carrier transport in diamond radiation detectors". In: *AIP advances* 10.2 (2020), p. 025004.

[279] C Bauer et al. "Radiation hardness studies of CVD diamond detectors". In: *Nuclear Instruments and Methods in Physics Research Section A: Accelerators, Spectrometers, Detectors and Associated Equipment* 367.1-3 (1995), pp. 207–211.

[280] T. Chakraborty et al. "CVD growth of ultrapure diamond, generation of NV centers by ion implantation, and their spectroscopic characterization for quantum technological applications". In: *Phys. Rev. Mater.* 3 (6 June 2019), p. 065205. DOI: 10.1103/PhysRevMaterials.3.065205. URL: https://link.aps.org/doi/10.1103/PhysRevMaterials.3.065205.

[281] Dhruba Das et al. "Diamond-The Ultimate Material for Exploring Physics of Spin-defects for Quantum Technologies and Diamontronics." In: *Journal of Physics D: Applied Physics* (2022).

[282] Sungkun Hong et al. "Nanoscale magnetometry with NV centers in diamond". In: *MRS bulletin* 38.2 (2013), pp. 155–161.

[283] P. E. Blöchl. "Projector augmented-wave method". en. In: *Physical Review B* 50.24 (Dec. 1994), pp. 17953–17979. ISSN: 0163-1829, 1095-3795. DOI: 10.1103/PhysRevB.50.17953. URL: https://link.aps.org/doi/10.1103/PhysRevB.50.17953 (visited on 04/02/2023).

[284] O. Bengone et al. "Implementation of the projector augmented-wave LDA+U method: Application to the electronic structure of NiO". en. In: *Physical Review B* 62.24 (Dec. 2000), pp. 16392–16401. ISSN: 0163-1829, 1095-3795. DOI: 10.1103/PhysRevB.62.16392. URL: https://link.aps.org/doi/10.1103/PhysRevB.62.16392 (visited on 04/02/2023).

[285] G. Kresse and J. Furthmüller. "Efficient iterative schemes for *ab initio* total-energy calculations using a plane-wave basis set". en. In: *Physical Review B* 54.16 (Oct. 1996), pp. 11169–11186. ISSN: 0163-1829, 1095-3795. DOI: 10.1103/PhysRevB.54.11169. URL: https://link.aps.org/doi/10.1103/PhysRevB.54.11169 (visited on 04/02/2023).

[286] John P. Perdew, Kieron Burke, and Matthias Ernzerhof. "Generalized Gradient Approximation Made Simple". en. In: *Physical Review Letters* 77.18 (Oct. 1996), pp. 3865–3868. ISSN: 0031-9007, 1079-7114. DOI: 10.1103/PhysRevLett.77.3865. URL: https://link.aps.org/doi/10.1103/PhysRevLett.77.3865 (visited on 04/02/2023).

[287] George Beridze and Piotr M. Kowalski. "Benchmarking the DFT+ *U* Method for Thermochemical Calculations of Uranium Molecular Compounds and Solids". en. In: *The Journal of Physical Chemistry A* 118.50 (Dec. 2014), pp. 11797–11810. ISSN: 1089-5639, 1520-5215. DOI: 10.1021/jp5101126. URL: https://pubs.acs.org/doi/10.1021/jp5101126 (visited on 04/02/2023).

[288] Danny E.P. Vanpoucke et al. "Can europium atoms form luminescent centres in diamond: A combined theoretical–experimental study". en. In: *Diamond and Related Materials* 94 (Apr. 2019), pp. 233–241. ISSN: 09259635. DOI: 10.1016/j.diamond.2019.02.024. URL: https://linkinghub.elsevier.com/retrieve/pii/S0925963518307544 (visited on 02/26/2023).

[289] Xin Tan et al. "Study of the structural stability and electronic structure of Ce-related defects in diamonds". en. In: *Optical Materials Express* 10.5 (May 2020), p. 1286. ISSN: 2159-3930. DOI: 10.1364/OME.387462. URL: https://opg.optica.org/abstract.cfm?URI=ome-10-5-1286 (visited on 02/26/2023).

[290] Andrew Magyar et al. "Synthesis of luminescent europium defects in diamond". In: *Nature communications* 5.1 (2014), p. 3523.

[291] Xin Tan et al. "Structural stability of Pr-related defects in diamond and electronic structure single photon source: A first-principles study". en. In: *AIP Advances* 8.10 (Oct. 2018), p. 105202. ISSN: 2158-3226. DOI: 10.1063/1.5050412. URL: https://aip.scitation.org/doi/10.1063/1.5050412 (visited on 02/27/2023).

[292] Jochen Heyd, Gustavo E. Scuseria, and Matthias Ernzerhof. "Hybrid functionals based on a screened Coulomb potential". en. In: *The Journal of Chemical Physics* 118.18 (May 2003), pp. 8207–8215. ISSN: 0021-9606, 1089-7690. DOI: 10.1063/1.1564060. URL: http://aip.scitation.org/doi/10.1063/1.1564060 (visited on 04/02/2023).

[293] Aliaksandr V. Krukau et al. "Influence of the exchange screening parameter on the performance of screened hybrid functionals". en. In: *The Journal of Chemical Physics* 125.22 (Dec. 2006), p. 224106. ISSN: 0021-9606, 1089-7690. DOI: 10.1063/1.2404663. URL: http://aip.scitation.org/doi/10.1063/1.2404663 (visited on 04/02/2023).

[294] Peter Deák et al. "Accurate defect levels obtained from the HSE06 range-separated hybrid functional". en. In: *Physical Review B* 81.15 (Apr. 2010), p. 153203. ISSN: 1098-0121, 1550-235X. DOI: 10.1103/PhysRevB.81.153203. URL: https://link.aps.org/doi/10.1103/PhysRevB.81.153203 (visited on 02/20/2023).

[295] Adam Gali. "Identification of individual C 13 isotopes of nitrogen-vacancy center in diamond by combining the polarization studies of nuclear spins and first-principles calculations". en. In: *Physical Review B* 80.24 (Dec. 2009), p. 241204. ISSN: 1098-0121, 1550-235X. DOI: 10.1103/PhysRevB.80.241204. URL: https://link.aps.org/doi/10.1103/PhysRevB.80.241204 (visited on 04/02/2023).

[296] Danny E. P. Vanpoucke. "Linker Functionalization in MIL-47(V)-R Metal–Organic Frameworks: Understanding the Electronic Structure". en. In: *The Journal of Physical Chemistry C* 121.14 (Apr. 2017), pp. 8014–8022. ISSN: 1932-7447, 1932-7455. DOI: 10.1021/acs.jpcc.7b01491. URL: https://pubs.acs.org/doi/10.1021/acs.jpcc.7b01491 (visited on 04/02/2023).

[297] Thomas M. Henderson, Joachim Paier, and Gustavo E. Scuseria. "Accurate treatment of solids with the HSE screened hybrid". en. In: *physica status solidi (b)* 248.4 (Apr. 2011), pp. 767–774. ISSN: 03701972. DOI: 10.1002/pssb.201046303. URL: https://onlinelibrary.wiley.com/doi/10.1002/pssb.201046303 (visited on 04/02/2023).

[298] Alejandro J. Garza and Gustavo E. Scuseria. "Predicting Band Gaps with Hybrid Density Functionals". en. In: *The Journal of Physical Chemistry Letters* 7.20 (Oct. 2016), pp. 4165–4170. ISSN: 1948-7185, 1948-7185. DOI: 10.1021/acs.jpclett.6b01807. URL: https://pubs.acs.org/doi/10.1021/acs.jpclett.6b01807 (visited on 04/02/2023).

[299] Kevin Hendrickx et al. "Understanding Intrinsic Light Absorption Properties of UiO-66 Frameworks: A Combined Theoretical and Experimental Study". en. In: *Inorganic Chemistry* 54.22 (Nov. 2015), pp. 10701–10710. ISSN: 0020-1669, 1520-510X. DOI: 10.1021/acs.inorgchem.5b01593. URL: https://pubs.acs.org/doi/10.1021/acs.inorgchem.5b01593 (visited on 04/02/2023).

[300] A. Chaudhry et al. "First-principles study of luminescence in Eu 2 + -doped inorganic scintillators". en. In: *Physical Review B* 89.15 (Apr. 2014), p. 155105. ISSN: 1098-0121, 1550-235X. DOI: 10.1103/PhysRevB.89.155105. URL: https://link.aps.org/doi/10.1103/PhysRevB.89.155105 (visited on 04/02/2023).

[301] Kamil Czelej, Piotr Śpiewak, and Krzysztof J. Kurzydłowski. "Electronic structure of substitutionally doped diamond: Spin-polarized, hybrid density functional theory analysis". en. In: *Diamond and Related Materials* 75 (May 2017), pp. 146–151. ISSN: 09259635. DOI: 10.1016/j.diamond.2017.03.009. URL: https://linkinghub.elsevier.com/retrieve/pii/S0925963516306434 (visited on 04/02/2023).

[302] Giulio Di Palma et al. "The VN2 negatively charged defect in diamond. A quantum mechanical investigation of the EPR response". In: *Carbon* 159 (2020), pp. 443–450. ISSN: 0008-6223. DOI: https://doi.org/10.1016/j.carbon.2019.12.031. URL: https://www.sciencedirect.com/science/article/pii/S0008622319312667.

[303] Joel Davidsson et al. "First principles predictions of magneto-optical data for semiconductor point defect identification: the case of divacancy defects in 4H–SiC". In: *New Journal of Physics* 20.2 (Feb. 2018), p. 023035. DOI: 10.1088/1367-2630/aaa752. URL: https://dx.doi.org/10.1088/1367-2630/aaa752.

[304] D. W. Drumm et al. "Thermodynamic stability of neutral Xe defects in diamond". en. In: *Physical Review B* 82.5 (Aug. 2010), p. 054102. ISSN: 1098-0121, 1550-235X. DOI: 10.1103/PhysRevB.82.054102. URL: https://link.aps.org/doi/10.1103/PhysRevB.82.054102 (visited on 02/04/2023).

[305] Jakub Cajzl et al. "Erbium ion implantation into diamond – measurement and modelling of the crystal structure". en. In: *Physical Chemistry Chemical Physics* 19.8 (2017), pp. 6233–6245. ISSN: 1463-9076, 1463-9084. DOI: 10.1039/C6CP08851A. URL: http://xlink.rsc.org/?DOI=C6CP08851A (visited on 01/20/2023).

[306] Hannu-Pekka Komsa, Tapio T. Rantala, and Alfredo Pasquarello. "Finite-size supercell correction schemes for charged defect calculations". en. In: *Physical Review B* 86.4 (July 2012), p. 045112. ISSN: 1098-0121, 1550-235X. DOI: 10.1103/PhysRevB.86.045112. URL: https://link.aps.org/doi/10.1103/PhysRevB.86.045112 (visited on 04/02/2023).

[307] Christoph Freysoldt, Jörg Neugebauer, and Chris G. Van de Walle. "Fully *Ab Initio* Finite-Size Corrections for Charged-Defect Supercell Calculations". en. In: *Physical Review Letters* 102.1 (Jan. 2009), p. 016402. ISSN: 0031-9007, 1079-7114. DOI: 10.1103/PhysRevLett.102.016402. URL: https://link.aps.org/doi/10.1103/PhysRevLett.102.016402 (visited on 01/29/2023).

[308] Marco Arrigoni and Georg K.H. Madsen. "Spinney: Post-processing of first-principles calculations of point defects in semiconductors with Python". en. In: *Computer Physics Communications* 264 (July 2021), p. 107946. ISSN: 00104655. DOI: 10.1016/j.cpc.2021.107946. URL: https://linkinghub.elsevier.com/retrieve/pii/S0010465521000709 (visited on 03/24/2023).

[309] Hyeondeok Shin et al. "Cohesion energetics of carbon allotropes: Quantum Monte Carlo study". In: *The Journal of Chemical Physics* 140.11 (2014), p. 114702. DOI: 10.1063/1.4867544. eprint: https://doi.org/10.1063/1.4867544. URL: https://doi.org/10.1063/1.4867544.

[310] Christoph Freysoldt et al. "First-principles calculations for point defects in solids". en. In: *Reviews of Modern Physics* 86.1 (Mar. 2014), pp. 253–305. ISSN: 0034-6861, 1539-0756. DOI: 10.1103/RevModPhys.86.253. URL: https://link.aps.org/doi/10.1103/RevModPhys.86.253 (visited on 02/09/2023).

[311] Ravishankar Sundararaman and Yuan Ping. "First-principles electrostatic potentials for reliable alignment at interfaces and defects". en. In: *The Journal of Chemical Physics* 146.10 (Mar. 2017), p. 104109. ISSN: 0021-9606, 1089-7690. DOI: 10.1063/1.4978238. URL: http://aip.scitation.org/doi/10.1063/1.4978238 (visited on 02/16/2023).

[312] Anuj Goyal et al. "The Conundrum of Relaxation Volumes in First-Principles Calculations of Charged Defects in UO2". en. In: *Applied Sciences* 9.24 (Dec. 2019), p. 5276. ISSN: 2076-3417. DOI: 10.3390/app9245276. URL: https://www.mdpi.com/2076-3417/9/24/5276 (visited on 04/07/2023).

[313] Viktor Ivády et al. "Pressure and temperature dependence of the zero-field splitting in the ground state of NV centers in diamond: A first-principles study". In: *Phys. Rev. B* 90 (23 Dec. 2014), p. 235205. DOI: 10.1103/PhysRevB.90.235205. URL: https://link.aps.org/doi/10.1103/PhysRevB.90.235205.

[314] Koichi Momma and Fujio Izumi. "VESTA: a three-dimensional visualization system for electronic and structural analysis". In: *Journal of Applied crystallography* 41.3 (2008), pp. 653–658.

[315] Qijing Zheng. *QijingZheng/VaspBandUnfolding*. URL: https%20//github.com/QijingZheng/VaspBandUnfolding (visited on 04/25/2023).

[316] Xin Tan et al. “Principle study of the europium vacancy color center in a diamond”. en. In: *Optical Materials Express* 10.12 (Dec. 2020), p. 3277. ISSN: 2159-3930. DOI: 10.1364/OME.410064. URL: https://opg.optica.org/abstract.cfm?URI=ome-10-12-3277 (visited on 02/26/2023).

[317] Alison Mainwood. “Nitrogen and nitrogen-vacancy complexes and their formation in diamond”. en. In: *Physical Review B* 49.12 (Mar. 1994), pp. 7934–7940. ISSN: 0163-1829, 1095-3795. DOI: 10.1103/PhysRevB.49.7934. URL: https://link.aps.org/doi/10.1103/PhysRevB.49.7934 (visited on 04/02/2023).

[318] Xin Tan et al. “First-principle study on the influence of common impurities in diamond on the electronic structure of Ce-related defects”. In: *Optical Materials Express* 11.10 (2021), pp. 3421–3430.

[319] Takayoshi Fujimura et al. “Structural stability and optical properties of Ni complex defects in diamond”. en. In: *Diamond and Related Materials* 128 (Oct. 2022), p. 109280. ISSN: 09259635. DOI: 10.1016/j.diamond.2022.109280. URL: https://linkinghub.elsevier.com/retrieve/pii/S0925963522004629 (visited on 03/02/2023).

[320] Malaya K Nayak and Rajat K Chaudhuri. “Ab initio calculation of P, T-odd effects in YbF molecule”. In: *Chemical physics letters* 419.1-3 (2006), pp. 191–194.

[321] Manfred Fiebig et al. “The evolution of multiferroics”. In: *Nature Reviews Materials* 1.8 (2016), pp. 1–14.

[322] Isaac Harris et al. “Group-III quantum defects in diamond are stable spin-1 color centers”. en. In: *Physical Review B* 102.19 (Nov. 2020), p. 195206. ISSN: 2469-9950, 2469-9969. DOI: 10.1103/PhysRevB.102.195206. URL: https://link.aps.org/doi/10.1103/PhysRevB.102.195206 (visited on 01/13/2023).

[323] A Mainwood. “Substitutional impurities in diamond”. In: *Journal of Physics C: Solid State Physics* 12.13 (July 1979), pp. 2543–2549. ISSN: 0022-3719. DOI: 10.1088/0022-3719/12/13/018. URL: https://iopscience.iop.org/article/10.1088/0022-3719/12/13/018 (visited on 04/10/2023).

[324] Koji Kobashi. *Shift of Fermi level by substitutional impurity-atom doping in diamond and cubic- and hexagonal-boron nitrides*. 2014. arXiv: 1406.6204 [cond-mat.mtrl-sci].

[325] Ádám Gali. “Ab initio theory of the nitrogen-vacancy center in diamond”. In: *Nanophotonics* 8.11 (2019), pp. 1907–1943. DOI: doi:10.1515/nanoph-2019-0154. URL: https://doi.org/10.1515/nanoph-2019-0154.

[326] Michael Bishof et al. “Improved limit on the ^{225}Ra electric dipole moment”. In: *Phys. Rev. C* 94 (2 Aug. 2016), p. 025501. DOI: 10.1103/PhysRevC.94.025501. URL: https://link.aps.org/doi/10.1103/PhysRevC.94.025501.

[327] B. Graner et al. “Reduced Limit on the Permanent Electric Dipole Moment of ^{199}Hg”. In: *Phys. Rev. Lett.* 116 (16 Apr. 2016), p. 161601. DOI: 10.1103/PhysRevLett.116.161601. URL: https://link.aps.org/doi/10.1103/PhysRevLett.116.161601.

[328] T. A. Zheng et al. "Measurement of the Electric Dipole Moment of ^{171}Yb Atoms in an Optical Dipole Trap". In: *Phys. Rev. Lett.* 129 (8 Aug. 2022), p. 083001. DOI: 10.1103/PhysRevLett.129.083001. URL: https://link.aps.org/doi/10.1103/PhysRevLett.129.083001.

[329] Manjin Zhong et al. "Optically addressable nuclear spins in a solid with a six-hour coherence time". In: *Nature* 517.7533 (Jan. 2015), pp. 177–180. ISSN: 1476-4687. DOI: 10.1038/nature14025. URL: https://doi.org/10.1038/nature14025.

[330] Harish D Ramachandran and Amar C Vutha. "Nuclear T-violation search using octopole-deformed nuclei in a crystal". In: *Physical Review A* 108.1 (2023), p. 012819.

[331] N. Sachdeva et al. "New Limit on the Permanent Electric Dipole Moment of ^{129}Xe Using ^{3}He Comagnetometry and SQUID Detection". In: *Phys. Rev. Lett.* 123 (14 Oct. 2019), p. 143003. DOI: 10.1103/PhysRevLett.123.143003. URL: https://link.aps.org/doi/10.1103/PhysRevLett.123.143003.

[332] Gerg ő Thiering and Adam Gali. "Ab Initio Magneto-Optical Spectrum of Group-IV Vacancy Color Centers in Diamond". In: *Phys. Rev. X* 8 (2 June 2018), p. 021063. DOI: 10.1103/PhysRevX.8.021063. URL: https://link.aps.org/doi/10.1103/PhysRevX.8.021063.

[333] Gergő Thiering and Adam Gali. "The (eg ⊗ eu) ⊗ Eg product Jahn–Teller effect in the neutral group-IV vacancy quantum bits in diamond". In: *npj Computational Materials* 5.1 (Feb. 2019), p. 18. ISSN: 2057-3960. DOI: 10.1038/s41524-019-0158-3. URL: https://doi.org/10.1038/s41524-019-0158-3.

[334] Omid Golami et al. "*Abinitio* and group theoretical study of properties of a carbon trimer defect in hexagonal boron nitride". In: *Phys. Rev. B* 105 (18 May 2022), p. 184101. DOI: 10.1103/PhysRevB.105.184101. URL: https://link.aps.org/doi/10.1103/PhysRevB.105.184101.

[335] Hao Tang et al. "First-principles calculation of the temperature-dependent transition energies in spin defects". In: *The Journal of Physical Chemistry Letters* 14.13 (2023), pp. 3266–3273.

[336] Marcin Roland Zemła, Kamil Czelej, and Jacek A Majewski. "Graphene–Iron (II) Phthalocyanine Hybrid Systems for Scalable Molecular Spintronics". In: *The Journal of Physical Chemistry C* 124.50 (2020), pp. 27645–27655.

[337] VV Flambaum and AJ Mansour. "Enhanced magnetic quadrupole moments in nuclei with octupole deformation and their C P-violating effects in molecules". In: *Physical Review C* 105.6 (2022), p. 065503.

[338] Stefan Stoll and Arthur Schweiger. "EasySpin, a comprehensive software package for spectral simulation and analysis in EPR". In: *Journal of magnetic resonance* 178.1 (2006), pp. 42–55.

[339] Christian Osterkamp et al. "Engineering preferentially-aligned nitrogen-vacancy centre ensembles in CVD grown diamond". In: *Scientific reports* 9.1 (2019), pp. 1–7.

[340] Marianne Etzelmüller Bathen, Lasse Vines, and José Coutinho. "First-principles calculations of Stark shifts of electronic transitions for defects in semiconductors: the Si vacancy in 4H-SiC". In: *Journal of Physics: Condensed Matter* 33.7 (2020), p. 075502.

[341] A. D. Kudashov et al. “Ab initio study of radium monofluoride (RaF) as a candidate to search for parity- and time-and-parity–violation effects”. In: *Phys. Rev. A* 90 (5 Nov. 2014), p. 052513. DOI: 10.1103/PhysRevA.90.052513. URL: https://link.aps.org/doi/10.1103/PhysRevA.90.052513.

[342] V. V. Flambaum and H. Feldmeier. “Enhanced nuclear Schiff moment in stable and metastable nuclei”. In: *Phys. Rev. C* 101 (1 Jan. 2020), p. 015502. DOI: 10.1103/PhysRevC.101.015502. URL: https://link.aps.org/doi/10.1103/PhysRevC.101.015502.

[343] V. V. Flambaum and V. A. Dzuba. “Electric dipole moments of atoms and molecules produced by enhanced nuclear Schiff moments”. In: *Phys. Rev. A* 101 (4 Apr. 2020), p. 042504. DOI: 10.1103/PhysRevA.101.042504. URL: https://link.aps.org/doi/10.1103/PhysRevA.101.042504.

[344] Terry Gullion, David B Baker, and Mark S Conradi. “New, compensated carr-purcell sequences”. In: *Journal of Magnetic Resonance (1969)* 89.3 (1990), pp. 479–484.

[345] Alexandre M Souza, Gonzalo A Álvarez, and Dieter Suter. “Robust dynamical decoupling”. In: *Philosophical Transactions of the Royal Society A: Mathematical, Physical and Engineering Sciences* 370.1976 (2012), pp. 4748–4769.

[346] Aaron M Day et al. “Laser writing of spin defects in nanophotonic cavities”. In: *Nature Materials* 22.6 (2023), pp. 696–702.

[347] DM Hofmann et al. “Acceptor level of substitutional Ni in diamond”. In: *Physical Review B* 50.23 (1994), p. 17618.

[348] J Isoya, H Kanda, and Y Uchida. “EPR studies of interstitial Ni centers in synthetic diamond crystals”. In: *Physical Review B* 42.16 (1990), p. 9843.

[349] J P Goss et al. “The lattice location of Ni in diamond: a theoretical study”. In: *Journal of Physics: Condensed Matter* 16.25 (June 2004), pp. 4567–4578. ISSN: 0953-8984, 1361-648X. DOI: 10.1088/0953-8984/16/25/014. URL: https://iopscience.iop.org/article/10.1088/0953-8984/16/25/014 (visited on 08/23/2022).

[350] Reinis Lazda et al. “Cross-relaxation studies with optically detected magnetic resonances in nitrogen-vacancy centers in diamond in external magnetic field”. In: *Physical Review B* 103.13 (2021), p. 134104.

[351] A Reznik, C Uzan-Saguy, and R Kalish. “Effects of point defects on the electrical properties of doped diamond”. In: *Diamond and Related Materials* 9.3-6 (2000), pp. 1051–1056.

[352] Hiromitsu Kato et al. “n-type diamond growth by phosphorus doping on (0 0 1)-oriented surface”. In: *Journal of Physics D: Applied Physics* 40.20 (2007), pp. 6189–6200.

[353] Dirk Englund, Ilya Fushman, and Jelena Vuckovic. “General recipe for designing photonic crystal cavities”. In: *Optics express* 13.16 (2005), pp. 5961–5975.

[354] Kazuhiro Kuruma et al. “Coupling of a single tin-vacancy center to a photonic crystal cavity in diamond”. In: *Applied Physics Letters* 118.23 (2021), p. 230601.

[355] Anna Tchebotareva et al. “Entanglement between a diamond spin qubit and a photonic time-bin qubit at telecom wavelength”. In: *Physical review letters* 123.6 (2019), p. 063601.

[356] Roland Nagy et al. “High-fidelity spin and optical control of single silicon-vacancy centres in silicon carbide”. In: *Nature communications* 10.1 (2019), pp. 1–8.

[357] Benjamin Kambs et al. “Low-noise quantum frequency down-conversion of indistinguishable photons”. In: *Optics express* 24.19 (2016), pp. 22250–22260.

[358] Rémi Blinder et al. “Reducing inhomogeneous broadening of spin and optical transitions of nitrogen-vacancy centers in high-pressure, high-temperature diamond”. In: *Communications Materials* 5.1 (2024), p. 224.